Hall A 12 GeV Upgrade

Pre-Conceptual Design Report

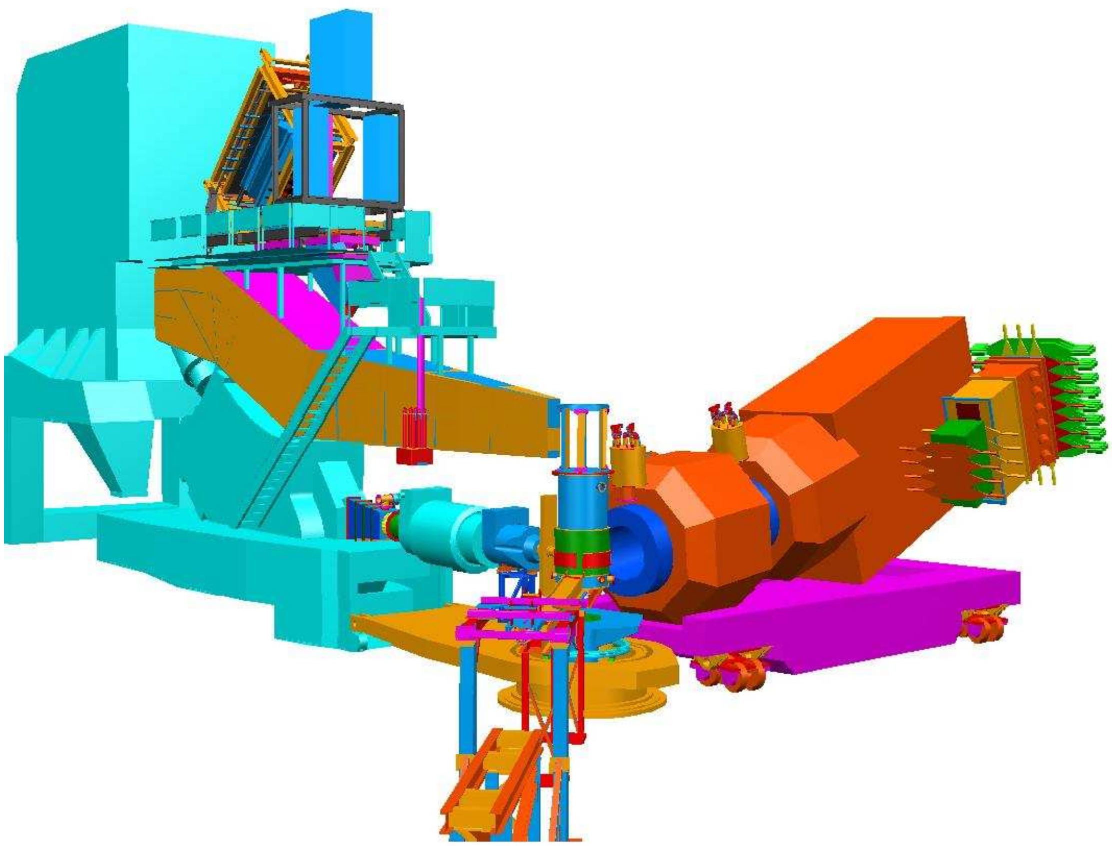

December 3, 2002

Contributors to the Hall A pCDR

J. Arrington, R.J. Holt, P.E. Reimer, and K. Wijesooriya
Argonne National Laboratory (Argonne, IL)

K. Aniol
California State University-Los Angeles (Los Angeles, CA)

L. Todor
Carnegie Mellon University (Pittsburgh, PA)

T. Averett, C. Carlson, K. Griffioen, F. Gross, and V. Sulkosky
College of William and Mary (Williamsburg, VA)

D. Lhuillier and F. Sabatie
DAPNIA/SPhN (Saclay, France)

D. Dutta and H. Gao
Duke University (Durham, NC)

W. Boeglin, P. Markowitz, and M. Sargsian
Florida International University (Miami, FL)

F. Garibaldi and G. Urciuoli
INFN/Sezione Sanita (Roma, Italy)

E. Voutier
ISN Grenoble (Grenoble, France)

A. Afanasev, P. Brindza, J.-P. Chen, E. Chudakov, R. Feuerbach, J. Gomez, J.-O. Hansen, D.W. Higinbotham, C.W. de Jager, J. LeRose, W. Melnitchouk, R. Michaels, S. Nanda, B. Reitz, A. Saha, G. Warren, and B. Wojtsekhowski
Jefferson Lab (Newport News, VA)

G.G. Petratos and A.T. Katramatou
Kent State University (Kent, OH)

W. Bertozzi, Z. Chai, S. Gilad, O. Gayou, R. Suleiman, H. Xiang, X. Zheng, and L.Y. Zhu
Massachusetts Institute of Technology (Cambridge, MA)

S. Jeschonnek
Ohio State University (Columbus, OH)

A. Radyushkin, C. Hyde-Wright, R. Schiavilla, P. Ulmer, and L.B. Weinstein
Old Dominion University (Norfolk ,VA)

R. Gilman, X. Jiang, and K. McCormick
Rutgers, The State University of New Jersey (New Brunswick, NJ)

S. Brodsky
Stanford Linear Accelerator Center (Menlo Park, CA)

V. Nelyubin
St. Petersburg Institute of Nuclear Physics (St. Petersburg, Russia)

S. Choi, Z.-E. Meziani, K. Slifer, and P. Solvignon
Temple University (Philadelphia, PA)

J. Jourdan
University of Basel (Basel, Switzerland)

P. Bertin
Universite de Clermont Ferrand (Aubiere, France)

J. Annand, D. Ireland, J. Kellie, K. Livingston, G. Rosner, and D. Watts
University of Glasgow (Glasgow, Scotland)

A. Thomas
University of Adelaide (Adelaide, Australia)

A. Nathan and J.-C. Peng
University of Illinois (Urbana-Champaign, IL)

S. Širca
University of Ljubljana (Ljubljana, Slovenia)

E. Beise, C.C. Chang, and X. Ji
University of Maryland (College Park, MD)

K.S. Kumar
University of Massachusetts (Amherst, MA)

G. Cates, A. Deur, R. Lindgren, N. Liyanage, B.E. Norum, and K. Wang
University of Virginia (Charlottesville, VA)

and

The Jefferson Lab Hall A Collaboration

Contents

Chapter 1

Introduction

Atomic structure was unraveled with the invention of Quantum Mechanics during the first half of the last century, while nuclear structure was elucidated with the grasp of non-relativistic many body physics in the 60's. However, at the next layer, the inner structure of the proton and neutron known as the building blocks of nuclear matter has challenged us for decades. This inner structure poses a wealth of fundamental questions which have a deep impact on our understanding of Nature and the universe we live in.

Quantum Chromodynamics (QCD) is a fundamental theory which we all believe describes the strong interaction. However, QCD is a strongly coupled relativistic quantum field theory and its solution when the interaction is strong has not been found yet. Therefore, exploring the structure of the proton and neutron in order to determine the parameters of QCD, solve it and understand it defines in itself a frontier area of modern nuclear physics.

At present times, the excitement in studying hadron structure comes from the great experimental and theoretical opportunities which present themselves before us. On the one hand rapid development in technological advances including high duty cycle and high luminosity lepton beams, polarized beams and targets and high precision detectors allows access to many observables with high precision which were impossible to measure previously. Jefferson Lab with 12 GeV will emerge as the main next generation facility to answer many important questions about the hadronic structure of matter. On the other hand our grasp of QCD physics in its non-perturbative (strong) regime has made steady progress. Particularly, large-scale Lattice QCD calculations will become feasible in the immediate future, thus allowing precision calculations of hadronic observables which can be compared with new data.

The interplay between new experiments and theoretical advances will drive the field to the stage where we can describe the quark-gluonic structure of hadronic matter to the same level as we presently account for the electronic structure of atoms. These new experiments which probe the hadronic matter through hard scattering and form factor measurements will answer questions of paramount importance about the quark-gluon substructure of hadronic matter. The goal is to measure with an unprecedented precision key observables needed to develop a quantitative understanding based on QCD of how quarks and gluons provide the binding and spin to the nucleon. These are also designed to take optimum advantage of the combined role of existing and planned detectors in Hall A at Jefferson Lab.

In this conceptual design report we present a program of experiments that clearly fit the class of experiments needed in this interplay and show the host of opportunities that will form a comprehensive program of physics aimed ultimately at enhancing significantly our understanding of the nuclear building blocks, the origin of the nucleon-nucleon force and testing the limits of the standard model of nuclear physics. In the executive summary we shall highlight the key experiments and show the importance of building the large-acceptance MAD spectrometer with its associated detectors in Hall A to achieve this goal.

Chapter 2

Executive Summary

Hall A at Jefferson Lab has a remarkable and fruitful experimental program using the Continuous Electron Beam Facility up to 6 GeV incident energy. Exciting results on the electromagnetic, electroweak and spin properties of the nucleon have provided a better insight to our present description of the nucleon, while at the same time triggering a wealth of questions of fundamental nature. New theoretical efforts with the goal of understanding how QCD works clearly call for experiments where the range of four-momentum and energy transfers is raised to a new kinematic domain. To this end its energy needs to be increased while maintaining high luminosity, duty cycle and quality of the incident beam. This in turn allows for smaller distance scales to be probed in order to advance our detailed knowledge of the building blocks of matter.

As the electron beam energy is raised to 11 GeV two major avenues of investigation in Hall A emerge naturally. The first addresses the structure of the nucleon while the second addresses the structure of hadrons in the nuclear medium. Each avenue forms a comprehensive physics program.

On the Structure of the Nuclear Building Blocks:

<u>Theme 1:</u> **- The quark-gluon structure of the nucleon in the valence quark region.**- Experiments designed to extract the spin- and flavor- dependent quark distribution functions of the nucleon; experiments designed to extract moments of the spin structure functions for direct comparison with Lattice QCD calculations.

<u>Theme 2:</u> **- Mapping components of the quark-gluon wave function using exclusive reactions.** - Elastic scattering on the nucleon, real Compton scattering (RCS), deep virtual Compton scattering (DVCS) on the proton are used to anchor the determination of specific components of the proton wave function. The theoretical framework is that of the generalized parton distributions (GDP's).

On the structure of Hadrons in the nuclear medium:

<u>Theme 3:</u> **Hadrons in the nuclear medium.** - Experiments designed to probe hadrons in the nuclear medium at small distances and with high precision. The aim is to investigate correlations, formation and propagation of hadrons in the nuclear medium using the theoretical framework of QCD.

Other Opportunities:

<u>Theme 4:</u> **Search for new physics in the electroweak sector using the nucleon as a laboratory.** -Deep inelastic scattering on the deuteron is used to search for physics beyond the standard model by performing a precision measurement of $\sin^2(\theta_W)$ at a momentum transfer far from the Z-pole.

2.1 The Valence Quark Structure of the Nucleon

2.1.1 Quark Flavor and Spin Decomposition in the Nucleon

Since the 70's unpolarized deep inelastic scattering (DIS) has proved to be a powerful and fruitful tool to probe the structure of the nucleon. Quarks/partons were discovered and identified as the substructure of the nucleon at SLAC. A major effort was then launched around the world for a detailed investigation of the quark and gluon momentum distributions within the quark-parton model. Subsequently, precisely measured scaling violations of the structure functions were successfully interpreted within the framework of perturbative QCD providing an important test of QCD as the theory of strong interactions. From these studies significant conclusions on the nucleon quark-gluon structure were drawn, among others, that sea quarks and gluons dominate the low x_{Bj} ($x_{Bj} \leq 0.4$) region of the momentum distribution while the three basic "valence" quarks cleanly populate the large x_{Bj} ($x_{Bj} \geq 0.4$) region.

In the 80's technical advances for producing polarized beams and polarized targets triggered a new experimental effort which focused on the spin structure of the nucleon. This effort culminated with the test of the Bjorken sum rule, a fundamental sum rule of QCD, and the determination of the quark contribution to the spin of the nucleon. Although a large experimental effort has gone into measuring the full kinematic regime, there has never been a facility where the valence quark region could be measured with precision . The statistical precision of the world data is quite poor for $x_{Bj} > 0.4$. While the valence quark momentum distribution is peaked around 0.3, it is nevertheless polluted by the sea quarks and the gluons. Therefore, a very clean and unambiguous contribution of the "valence quarks" can only be expected when x is larger than 0.5. Unfortunately in this kinematic region the probability of finding any of the valence quarks becomes rather small leading to a poor statistical determination of key observables. Taking advantage of the energy upgrade and the unprecedented polarized luminosity in Hall A, this situation will be improved dramatically. A detailed mapping of the spin structure function of the proton and neutron as a function of the scale probed is expected to have a profound impact on our understanding of the structure of the nucleon.

For example, in most dynamical models of the nucleon, its polarization asymmetry $A_1^{n,p}$, which reflects the quark spin wave-function, is expected to be large and positive in the valence quark region. At large momentum transfers the asymmetry $A_1^{n,p}$ is expected to approach 1 when $x_{Bj} \to 1$. This reflects that in the valence region the struck quark which carries most of the nucleon momentum, carries also all of its spin. A detailed examination of the present neutron data shows no sign of the expected behavior (see Figure 2.1). However, a dramatic improvement can be achieved in the measurement of the neutron asymmetry using the 11 GeV polarized beam and a polarized ^3He target combined with the proposed MAD spectrometer in Hall A as shown in Figure 2.1.

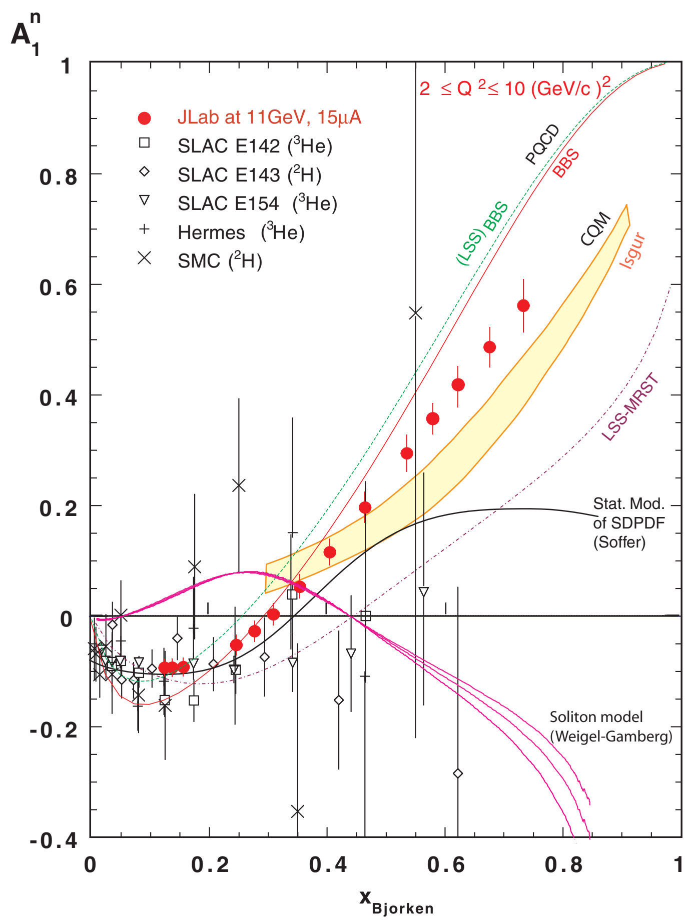

Figure 2.1: A measurement of the neutron polarization asymmetry A_1^n, determined by the spin structure of the valence quarks made possible by the combination of an 11 GeV beam and the MAD spectrometer in Hall A. The shaded area represents a range of valence quark models; the solid line is a prediction of a pQCD light-cone quark model.

Values of x_{Bj} greater than 0.8 cannot be reached at 11 GeV due to kinematics limitations nor can they be reached at the high-energy facilities due to the luminosity limitation. However, when the validity of duality between the spin distribution measured in DIS and the one measured in the resonance region has been verified, values of $A_1^{n,p}$ for x_{Bj} up to 0.9

can be achieved. The measurements described in section 3.1.6 are important to understand how to reconcile a constituent quark picture of the nucleon with the one involving current quarks and gluons.

The knowledge of the polarization asymmetries $A_1^{n,p}$ allows a flavor decomposition of the valence quark spin distributions assuming a value for the ratio d/u. In the constituent quark model it is expected that $\Delta u/u \to 1$ while $\Delta d/d \to -1/4$ when $x_{Bj} \to 1$. A different result is obtained in the quark-parton model when pQCD quark helicity conservation is used, namely $\Delta u/u \to 1$ while $\Delta d/d \to 1$. These predictions can be tested and spin distributions extracted in a comprehensive analysis if one complements the inclusive data with semi-inclusive asymmetry measurements of charged pions on the proton, deuterium and ^3He.

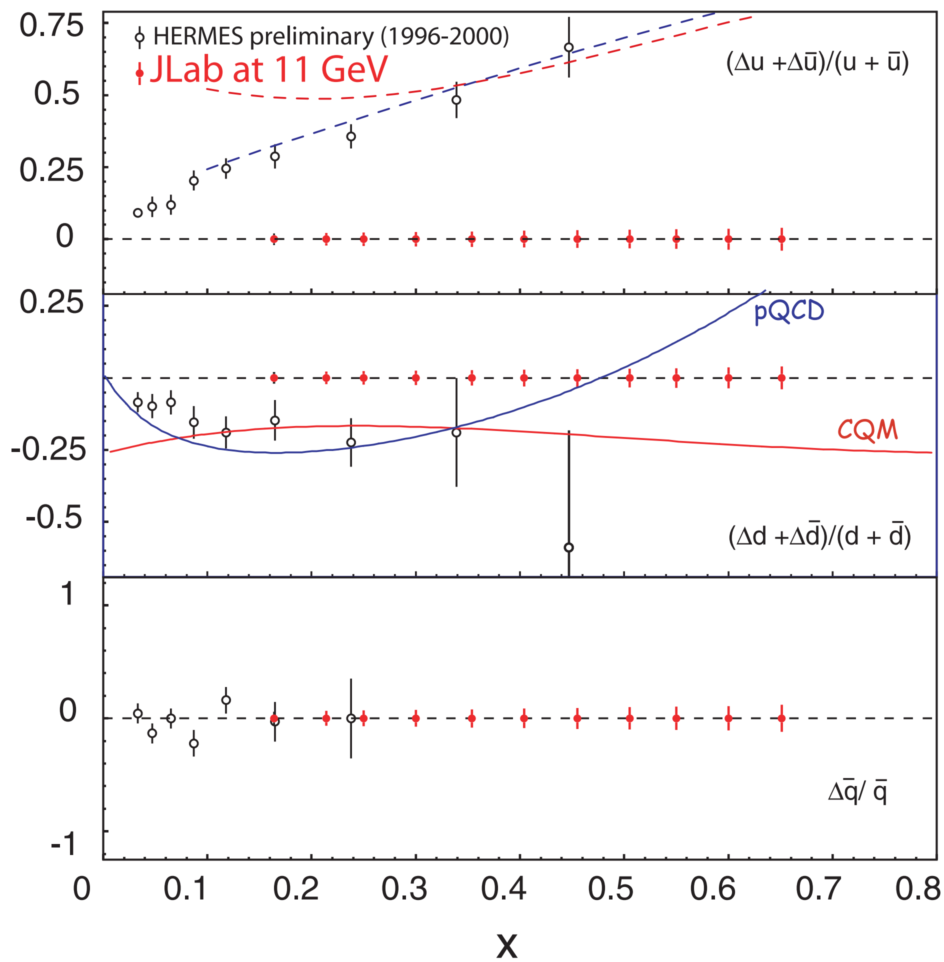

Figure 2.2: A semi-inclusive measurement of π^+ and π^- production on the proton and ^3He allows a spin and flavor decomposition of the nucleon spin quark distributions. Factorization is assumed but will be tested and quantified by several additional measurements.

Figure 2.2 shows the level of precision achievable in determining the valence quark distributions using the 11 GeV beam and the MAD spectrometer in Hall A. Factorization of the quark distributions and the fragmentation functions has been assumed. The validity of this assumption will be tested in a separate series of studies.

2.1.2 Color Electric and Magnetic Polarizabilities

In inclusive polarized lepton-nucleon deep-inelastic scattering, one can access two spin-dependent structure functions of the nucleon, g_1 and g_2. While g_1 can be understood in terms of the Feynman parton model which describes the scattering in terms of *incoherent* parton scattering, g_2 can not. However, g_2 is extremely interesting because it provides a unique opportunity to study the quark-gluon correlations in the nucleon which are otherwise inaccessible. According to the optical theorem, g_2 is the imaginary part of the spin-dependent Compton amplitude for the process

$$\gamma^*(+1) + N(1/2) \rightarrow \gamma^*(0) + N(-1/2),$$

where γ^* and N denote a virtual photon and a nucleon, respectively, and the numbers in parentheses are their helicities. Thus this Compton scattering involves the t-channel helicity exchange $+1$. When it is factorized in terms of parton sub-processes, the intermediate partons must carry this helicity exchange. Because of chirality conservation in vector coupling, massless quarks in perturbative processes can not produce a helicity flip. Nevertheless, in QCD this helicity exchange may occur in the following two ways: first, single-quark scattering in which the quark carries one unit of orbital angular momentum through its transverse momentum wave function; second, quark scattering with an additional transversely-polarized gluon from the nucleon target. The two mechanisms are combined in such a way to yield a gauge-invariant result. Consequently, g_2 provides a direct probe of the quark-gluon correlations in the nucleon wave function. Particularly interesting physics is contained in the second moment in x of a linear combination of g_1 and g_2,

$$d_2(Q^2) = 2\int_0^1 x^2[g_1(x,Q^2) + 3g_2(x,Q^2)]dx \tag{2.1}$$

This specific combination of g_1 and g_2 filters out the free quark scattering interaction exposing the higher twist or quark-gluon interaction. The $d_2(Q^2)$ matrix element is a twist-three matrix element which is related to a certain quark-gluon correlation, and describes how the gluon field inside the nucleon responds when the latter is polarized. Due to parity conservation, a color magnetic field $\vec{B}$ can be induced along the nucleon polarization and a color electric field $\vec{E}$ in the plane perpendicular to the polarization. In fact d_2 can be written as

$$d_2 = (2\chi_B + \chi_E)/3 \ . \tag{2.2}$$

where χ_B and χ_E are the gluon-field polarizabilities defined in the rest frame of the nucleon using the color-singlet operators $O_B = \psi^\dagger g\vec{B}\psi$ and $O_E = \psi^\dagger\vec{\alpha}\times g\vec{E}\psi$:

$$\chi_{B,E}2M^2\vec{S} = \langle PS|O_{B,E}|PS\rangle \ . \tag{2.3}$$

where M is the nucleon mass and $\vec{S}$ its spin.

Our goal is to gain insight into the gluon fields inside the nucleon and the structure of QCD through precision measurements of d_2 for both the proton and the neutron and a direct comparison of these measurements with Lattice QCD. Presently $d_2^{p,n}$ has been evaluated using state of the art computers in the framework of Lattice QCD. The proton d_2 world data have a comparable but better precision than the lattice QCD calculation. This situation might change soon with the rapid increase of computing speed. On the other hand, the lattice QCD calculation of the neutron d_2 is one of few quantities where the lattice QCD calculation has a better precision than the experimental data. Lattice QCD offers a powerful tool to investigate our understanding of the nucleon by direct comparison of quantities like d_2. The present results are very encouraging but much experimental progress needs to be achieved for a definitive comparison with the data. We show in Fig. 2.3 how the upgrade could impact on the present situation on the neutron. The improvement is rather impressive and will prove to be powerful as both the calculations and the experiments reach new precision levels.

2.1.3 Other semi-inclusive experiments

Beyond what has been described above, the 12 GeV upgrade will allow a series of critical experiments which will be performed to address different facets of hadron structure. These experiments should have an impact on our overall understanding of the structure of hadrons. Some of them are highlighted below.

- *Light quark sea asymmetry in the nucleon*

  In the past decade one of the surprises in the investigation of the nucleon was the discovery that the sea quark distributions in the proton are not flavor symmetric. The explanation of the symmetry of the sea in $u\bar{u}$ and $d\bar{d}$ at high Q^2 was prompted by the belief that the dominant contributing process is gluon bremsstrahlung into $q\bar{q}$ pairs. This was found to be naive and that there is an excess of $\bar{d}$ quarks over $\bar{u}$ in the proton. Interpretation of this asymmetry has focused on the non-perturbative aspect of QCD through the role of chiral symmetry breaking and the pion cloud associated with the proton. While the overall asymmetry is believed to be understood from basic principles, the magnitude and x_{Bj} distribution of this asymmetry are still under investigation. Complementing the Drell-Yan data with precision data of semi-inclusive charged-pion electro-production on hydrogen and deuterium targets in the range $0.1 < x_{Bj} < 0.45$ will prove to be a powerful constraint for models of the nucleon. Since an important assumption in extracting the parton distributions is factorization of the DIS process and the fragmentation process, the validity of this hypothesis will be checked. The 11 GeV upgrade and luminosity achievable in Hall A are keys to perform experimental studies of the x_{Bj} and z dependence of the pion production cross sections in order to allow an independent determination of parton distributions and fragmentation functions, thus of factorization properties.

- *The pion structure function*

The role played by the pion in QCD is unique since it is considered to be the pseudo-Goldstone boson responsible for chiral symmetry breaking. While crucial, this symmetry breaking is not fully understood and the pion is not light enough to be identified as a Goldstone boson. The pion also mediates the long-range nucleon-nucleon force responsible for the existence of nuclear matter. Similar to the case of the nucleon, the pion mass must be understood in terms of the underlying degrees of freedom of QCD. It is thus natural to ask *what is the structure of the pion itself*. In the framework of the quark-parton model the pion substructure has been investigated at HERA with unexpected results. It is found that first, the quark momentum distribution shape in the sea region has the same shape as that of the nucleon and second, the pion sea quark distribution has about 1/3 the magnitude of the nucleon sea distribution at odds with quark counting rules. This latter result is puzzling given our perhaps naive expectation that the sea distribution should be about 2/3 that in the proton. Furthermore, the valence quark distribution as $x_{Bj} \to 1$ extracted from the Drell-Yan results of FNAL experiment E615 does not behave as predicted by pQCD. Using the 11 GeV beam and the MAD spectrometer in coincidence with a low-energy neutron detector in Hall A, high precision DIS data from the pion cloud surrounding a proton (Sullivan process) will be obtained at $Q^2 = 3.0$ and 1.5 $(GeV/c)^2$ ranging between 0.25 and 0.8 in x. This experiment should confirm/refute the observations of E165 and yield a better insight in our description of the pion.

- *Transversity*

The nucleon structure function $h_1(x, Q^2)$ is a quantity not yet measured with high precision. In the QPM this distribution is expressed in terms of the incoherent sum of the flavor-dependent transversity distributions $\delta q_i(x, Q^2)$. The zeroth moment of this distribution represents the net transverse polarization of quarks in a transversely polarized nucleon. Due to its chiral-odd nature this distribution cannot be accessed in inclusive experiments. Therefore, in order to measure it, the process must be described by two chiral-odd objects. In semi-inclusive pion production using a nucleon target transversely polarized with respect to the virtual photon direction, it is argued that a chiral-odd fragmentation function (responsible for the pion production) combined with a chiral-odd transversity distribution (describing the initial spin state of the struck quark) would lead to a measurable azimuthal asymmetry. Such an asymmetry has been observed by the HERMES collaboration. Unfortunately, since the target polarization had only a small component transverse to the direction of the photon, their use of a longitudinally polarized target led to large statistical uncertainties in the result. Precision measurements of the azimuthal asymmetry using polarized hydrogen, deuterium and helium-3 targets over the valence quark region of x_{Bj} (initial fractional momentum of struck quark), and wide range of z (fractional momentum of the produced pion) keeping the four-momentum transfer of the virtual photon Q^2 in the scaling regime ($Q^2 > 1 GeV^2$) and the invariant mass of the undetected final state above the resonance region ($W > 2$ GeV)) is of paramount importance. This would allow to test the factorization of the initial and final state of the reaction and subsequently extract for the first time the transversity distribution. While questions of interpretation of the reaction mechanism are presently open, there is a consensus that *precision* measurement are the only path to resolve them and determine the transverse spin structure of the nucleon with sufficient confidence. Last but not least transversity may teach us about the breaking of chiral symmetry in QCD because in the limit of zero quark masses transversity can not be defined. This transversity perhaps is linked to chiral symmetry breaking and mass generation in QCD. Unlike helicity it is a quantity free of gluon anomaly.

2.2 Exclusive reactions

A mapping of the quark-gluon wave function of the nucleon is the ultimate goal for a complete understanding of nucleon structure. While this goal is a difficult challenge, a few experiments have been designed to give data in limited but important regions of the nucleon system phase space. Among these experiments those we consider to be performed in Hall A are *the measurement of elastic form factors of the nucleon*, *the measurement of wide angle Compton scattering (WACS)* and *deep virtual Compton scattering (DVCS)*. The data provided by these experiments combined with the recently articulated generalized parton distribution (GDP) framework will anchor our interpretation of the nucleon structure in terms of the underlying degrees of freedom. One should keep in mind, however, that this framework is unifying only in a regime where the factorization theorem is valid. The 12 GeV energy upgrade provides the kinematics flexibility to test the degree of validity of the factorization picture in order to take the appropriate venue for a reliable description of the nucleon response under the electromagnetic probe.

- *Nucleon elastic scattering form factors*

  In the early sixties measurements of the nucleon elastic form factors formed the ground for discovering its compositeness. Over the last forty years a Fourier analysis of the measurements in a large range of momentum transfer (Q^2) provided a detailed picture of the spatial charge and magnetization distributions. Although absolute values of these form factors could not be obtained using the degrees of freedom of QCD, the Q^2 dependence has been evaluated in pQCD the last twenty years. The poor precision of the data obtained using mainly the Rosenbluth method seemed rather consistent with those predictions. However, the latest precision measurements of the proton ratio G_E^p/G_M^p via $p(\vec{e},e'\vec{p})$ from Jefferson Lab show an unexpected Q^2 dependence in contrast with the pQCD predictions. These results might be suggesting the importance of the transverse momentum of quarks and its contribution to the total angular momentum of the nucleon regardless of the probed scale. The GDP's provide a universal framework to describe the nucleon observables such as the elastic form factors. These latter are expressed as the zero-th moments of GDP's similar or complementary to those used in WACS.

$$F_1 = \int dx \sum_f e_f H_f(x, \xi = 0, Q^2) \qquad (2.4)$$

$$F_2 = \int dx \sum_f e_f E_f(x, \xi = 0, Q^2) \tag{2.5}$$

where f refers to the different quark flavors. Thus, nucleon elastic form factors belong to the list of observables critical for the determination of the nucleon wave-function. The present limit in Q^2 of the polarization transfer measurements can be increased using the 12 GeV beam from 6 to 13 $(GeV/c)^2$.

- *Wide Angle Compton Scattering*

  In the framework of the GDP's an extended number of observables including the elastic form factors are needed to determine the nucleon wave function. As an example real Compton scattering (RCS) offers new measurable quantities that are linked to the GDP's through inverse moments in the variable x. These new form factors are basic quantities that require understanding as we explore the structure of the nucleon. In the perturbative QCD approach, the RCS amplitude is described by scattering from the elementary 3-quark Fock-state of the proton, with the perturbative exchange of two gluons, to balance the momentum transfer. This formalism is rigorous at asymptotic energies, but it is not clear where the asymptote lies. In the Feynman mechanism, the scattering amplitude is dominated by the photon scattering on a single quark, and the momentum transfer is absorbed by the non-perturbative wave function of the nucleon.

  The real Compton scattering cross section interpreted in the framework of the GDP's reads:

$$\frac{d\sigma}{dt} = \frac{d\sigma}{dt}|_{KN}[f_V R_V^2(t) + (1 - f_V) R_A^2(t)] \tag{2.6}$$

$$R_V(t) = \int \frac{dx}{x} e_f^2 H_f(x, \xi = 0, t) \tag{2.7}$$

$$R_A(t) = \int \frac{dx}{x} e_f^2 \tilde{H}_f(x, \xi = 0, t) \tag{2.8}$$

  where $t = (q - q')^2$ is the momentum transfer, x is the fraction of longitudinal momentum carried by the struck quark. At high energies this cross section is factorized as the Klein-Nishina cross section on a single quark times moments of the GPD's of the struck quark in the proton. Until recently RCS observables have not been explored experimentally with high precision[] because of limitations in the luminosity of the available facilities. Experiment E99-114 has set a new record in the experimental precision of the RCS cross section in the kinematic range in s and $Q^2 = -t$. The proposed upgrade will provide the unique opportunity to extend this measurement to a range of s from 12 to 19 GeV^2 and Q^2 up to 10 GeV^2 when combining the MAD spectrometer and doubling the size of the present calorimeter. Figure 2.4 shows the achievable precision in the proposed measurement and discrimination between the pQCD and GDP's approach.

  The goal of the RCS program in Hall A is to provide rigorous tests of these detailed reaction mechanisms, so that we may extract structure information with confidence. The structure information will reveal how the transverse profile of the parton densities in the proton varies with longitudinal momentum fraction.

- *Deeply Virtual Compton Scattering*

  When the initial photon is virtual instead of real as in the RCS the process it is identified as Virtual Compton scattering. Another variable, the virtual photon 4-momentum (Q^2), can be dialed by the choice of electron scattering kinematics. If Q^2 and s, the total invariant mass, are chosen large enough but t small, the process is known as Deeply Virtual Compton Scattering. The large Q^2 is necessary for a clean interpretation of the scattering amplitude as a convolution of a perturbative kernel with a set of ground-state quark matrix elements known as the GPD's. Unlike RCS, VCS interferes with the Bethe-Heitler process. However, the latter can be used as an amplifier and filter of the DVCS signal. While more information can be accessed varying Q^2 and s, this process is challenging experimentally. The task in such an experiment is first to isolate the process $ep \to ep\gamma$ from competing $ep \to ep\pi^\circ$,$ep \to eN^*\gamma$...channels. This in turns requires a combination of resolution and over-complete detection of all reaction products. Using a polarized electron beam and in the DVCS limit the electron beam helicity cross section difference is

  $$d^5\sigma(\vec{e}p \to ep\gamma) - d^5\sigma(\vec{e}p \to p\gamma) = \frac{1}{\tilde{s}\tilde{u}}[A\sin\phi + B\sin 2\phi + C\sin 3\phi]$$

  where A is the twist-two interference term of the elastic form factors in the BH amplitude, B is a twist-three term such that the ratio B/A is expected to scale as $1/\sqrt{Q^2}$. C is a gluon GPD and is believed to be negligible at JLab kinematics.

  The experiment is performed by detecting the scattered electrons in the MAD spectrometer, the photons in a thousand-element PbF_2 calorimeter and the recoil protons in an one-hundred-element scintillator array (solid angle 0.75 sr). With a luminosity of $10^{37}/\mathrm{cm}^2/\mathrm{s}$ one would measure at several kinematics in Q^2, x and t, with each x point requiring 400 hours at this luminosity for a significant statistical accuracy.

- *Photopion production*

  In DIS, scaling of the nucleon structure function $F_2(x, Q^2)$ with respect to the 4-momentum transfer Q^2 was key to identify the quark/partons as the constituents of nucleon. When the coverage in 4-momentum transfer was increased and precision of the data improved, scaling violations were observed but successfully described in pQCD. The scaling concept is also used in exclusive reactions to explore the transition region. For example, the onset of scaling has been observed at a surprisingly low momentum transfer (1 GeV^2) in the reduced differential cross section of photodisintegration of the deuteron at 90° c.m. scattering angle whereas hadron helicity conservation predictions tend not to agree with polarization observables in the same range of momentum transfer. An unexpected large spin correlation coefficient A_{NN} was measured in pp scattering suggesting contrary to the pQCD predictions that it is four times more likely for protons to scatter when their spin are both parallel and normal to the scattering plane than when they are anti-parallel at the largest momentum transfer measured ($p_T^2 \approx (\mathrm{GeV/c})^2$, $\theta_{cm} = 90°$). A detailed study using helicity observables has proved to be challenging but is believed to be a promising venue for a better grasp of the phenomena occurring in this region. Probing the onset of scaling by measuring the reduced differential cross sections in photopion production off the nucleon in $p(n)(\gamma, \pi^{\pm})n(p)$ with respect to the center of mass energy $\sqrt{s}$ allows a complementary approach in investigating this puzzle and the transition region. This process is motivated by the recent observation that the reduced cross section seems to "*oscillate*" around the scaling predictions of pQCD (originally known as quark counting rules obtained from dimensional analysis). The transition region seems to be rich with phenomena that perhaps mix the long-range and short-range properties of the strong interaction. If this is true, unexplained phenomena as described above and others would be understood within the interference concept. With the 11 GeV CEBAF upgrade combined with the MAD spectrometer in Hall A the reduced cross section at a C.M. angle of 90° would be measured as a function of $\sqrt{s}$ up to 22 GeV^2, thus doubling range in $\sqrt{s}$ of the present planned measurement in Hall A. This range will then includes the crossing of the J/ψ threshold production allowing the test of other possible reaction mechanisms. The statistical precision of the measurement and its resolution in $\sqrt{s}$ would be more than adequate to observe the oscillatory behavior and its dampening around the scaling prediction of pQCD.

- *J/Ψ production near threshold*

  The production of charmonium near threshold offers a new opportunity in our investigation of QCD dynamics. In contrast to diffractive charm production at high energy which tests the gluon structure function at small x, this reaction close to the threshold ($x \approx 1$) is sensitive to multi-quark, gluonic and hidden color correlations in nucleon and nuclei. Because of threshold kinematics of this reaction all quarks including the two heavy quarks resulting from the photon probe $\bar{c}c$ fluctuation must be in a small volume. The result is five quarks involved in the reaction mechanism which implies that perhaps three-gluon exchange may dominate the reaction over two- or one-gluon exchange thus opening the way to study correlations between valence quarks.

  The available precision and range of the t dependence of the cross section measurements from SLAC and Cornell near threshold leave open the question of what gluon exchange dominates the cross section at threshold. Since the data used a photon energy starting at $E_\gamma = 12$ GeV up to 21 GeV there is a large crucial gap between threshold and $E_\gamma =$ 12 GeV. With precision data from an upgraded CEBAF 12 GeV beam the three-gluon exchange might be resolved from the two-gluon exchange interpretation of the J/ψ photoproduction cross section.

  When this production is studied on few-body nuclei, gluon exchange might occur between the $\bar{c}c$ pair and colored three-quark clusters thus revealing the hidden color part of the nuclear wave function. This is a domain of short-range nuclear physics where nucleons lose their identity. Near threshold, various interpretations of the reaction mechanism lead to a drastically different understanding of the short-range behavior of nuclear matter.

The experimental program on the nucleon and nuclei would be carried using MAD and HRS spectrometers. This setup would have enough mass resolution for background rejection and t resolution for removing the coherent J/Ψ production on nuclei.

2.2.1 Hadrons in the Nuclear Medium

- *Elastic Form Factors*

  In the last forty years, the description of nuclear matter using meson-nucleon degrees of freedom has been very rewarding. This approach has offered a very efficient framework for explaining and predicting many electromagnetic properties of nuclei. The framework has earned the name "standard model" of nuclear physics. Elastic form factors of nuclei have provided a powerful test ground for this standard model. Sophisticated non-relativistic calculations have successfully described the charge and magnetization distributions of few-body nuclei like ^{3}He and ^{3}H at low momentum transfer. Information on the bulk properties of nuclei such as charge radii and magnetic radii has been obtained but also the shape of the probability distribution of charge and magnetization has been determined. At high momentum transfers it is expected that the perturbative quark counting rule picture would provide a better description of these form factors. In the case of the simplest nucleus, the deuteron, the data at the highest possible values of momentum transfer seem consistent with both the quark counting rule picture and meson-nucleon picture. In order to resolve these two pictures it is essential to extend the measurement of elastic form factors on few-body systems to the highest momentum transfers possible. Figure 2.5 shows an example of a possible extension of the ^{3}He elastic form factor which would double the Q^2 range of existing measurements. ¿From examining the present data it is not clear what picture would emerge as the measurement is extended to $Q^2 \approx 5.6$ GeV^2. Resolving this situation in light nuclei is essential to our broad understanding of nuclear matter.

  Hall A with an 11 GeV electron beam would be an ideal place to perform measurements of the form factors of light nuclei including ^{2}D, ^{3}He and ^{4}He. These will test the limits of the nuclear standard model and discover the expected transition region where quark-gluon degrees of freedom becomes more appropriate for the description of the few-body nuclear systems.

- *Color transparency*

  One of the powerful predictions of QCD is the existence of color transparency (CT). This phenomenon relies on the fact that when a hard scattering occurs it samples a small transverse-size point-like configuration (PLC) in the proton. This configuration is a color-singlet object, thus expected to interact weakly with the rest of the proton at high energies. Finally, assuming a large coherence length at high energies one expects that the scattering states are frozen during the collision. Signs of CT effects are expected to emerge in the quasi-elastic $A(e,e'p)A-1$ process if the energy and momentum transfers are large enough that the ejected nucleon travels through the nucleus in point-like configurations. The transparency defined as the measured cross section divided by the plane-wave impulse-approximation cross section, where final state interactions are neglected, is expected to start to rise towards unity at the onset of CT as the momentum transfer becomes sufficiently large. At present, measurements of this process at SLAC and JLab while reaching $Q^2 \approx 8$ (GeV/c)^2 are consistent with calculations that do not include CT. But because they are not sufficiently accurate nor at high enough Q^2 these data cannot rule out several of the realistic CT models.

The importance of CT has prompted a search of a variety of measurements that might be more sensitive to the clean determination of the effect. It is suggested that one way to observe the onset of CT in nuclei is to compare the $(e, e'p)$ cross section where recoil momenta are large ($p_{recoil} \approx 400$ MeV/c) to the cross section where recoil momenta are small ($p_{recoil} \leq 200$ MeV/c). Large nuclear recoil momenta originate from the ejected nucleon re-scattering with other nucleons of the recoil nucleus. At large recoil momenta the cross section is dominated by re-scattering while at low momenta single scattering dominates the cross section but Glauber screening is important. The ratio of these cross sections is expected to decrease as the momentum transfer reaches the onset of CT. The use of light nuclei provides a fertile ground for complete calculations with very good initial wave functions and an Eikonal approximation which accounts for all orders of re-scattering.

Another way to increase the sensitivity in the search for CT is to measure the ejected proton polarization in a polarized quasi-free reaction on nuclei $(\vec{e}, e'\vec{p})$. In this case both CT as well as nuclear filtering (NF) are investigated in the same experiment. Here it is expected that the normal component of the induced polarization, which is produced solely by final state re-scattering would vanish at the onset of CT. The sideway and longitudinal components of the proton polarization which are known as polarization transfer components can also be used to look for the onset of CT. These two components give us access to the ratio of the electromagnetic form factors of the nucleon $\mu G_E/G_M$ inside the nucleus. This ratio is expected to change when it is compared to the free proton ratio at the CT onset.

A promising reaction to enhance the sensitivity of the CT search is pion photoproduction in the nuclear medium. As discussed earlier the cross section of the elementary process $\gamma n \to \pi^- p$ has been predicted to oscillate around the counting rule predictions. This oscillation is expected to be the manifestation of the interference between long- and short-range amplitudes of quark interactions. Configurations where large quark separations are present tend not to propagate in the nuclear medium compared to configurations with small quark separation, it is expected thus that the oscillation phenomenon is suppressed and is known as NF. This effect would manifest itself as a 180° out of phase oscillation in the ratio of the nuclear cross section to the free cross section scaled by the number of protons (known as transparency). At the same time as NF is studied, CT can be investigated in light nuclei because the expansion time of the PLC to a full proton needs not to happen within the size of the nucleus. Thus taking a light nucleus one might expect to see CT at a lower Q^2 than a heavier nucleus where NF would dominate.

Using the 11 GeV CEBAF beam in Hall A the precision of the data can be improved by at least a factor of 2 while doubling the range of momentum transfer accessible $Q^2 \approx 18$ (GeV/c)^2 where the size of CT models predictions is appreciable. A full program of CT study will include medium weight (^{56}Fe, ^{12}C) and light nuclei (^2H, ^{3}He and ^{4}He) where the wave function of these nuclei is much better known and a reasonable calculation of the final state interaction according to conventional Glauber theory can be performed.

- *Short-range correlations via inclusive $A(e,e')X$ at $x > 1$*

When electron scattering off a nucleus is described as scattering off moving quarks, the fraction of momentum carried by the struck quark can be larger than that carried by a quark in a nucleon. In fact the struck quark can carry up to the full momentum of the nucleus. When scattering off a nucleon, the Bjorken variable x represents the fraction of momentum carried by the struck quark which can be as large as unity. Assuming we keep this definition of x when considering the scattering off a nucleus, then x can be greater than unity reaching values as high as A, the atomic number of the nucleus. In a hadronic description of the nucleus and low momentum transfer the region of the cross section above $x = 1$ is dominated by nucleon-nucleon short-range correlations. In this description one expects that as the momentum transfer increases, the cross section falls at least at the rate the nucleon form factors or faster. As the momentum transfer becomes considerably larger, the process enters the deep inelastic scattering regime (DIS). Thus instead of the coherent nucleonic contribution, the quark scattering contribution totally dominates the process. The scattering is believed to occur on a superfast quark since it must carry a momentum larger that that of quarks in the nucleon. When this regime is reached it is reasonable to expect the onset of scaling like in DIS at low x. This is a regime where short-range two-body correlations are interpreted in terms of the basic degrees of freedom of QCD.

The present data from JLab experiment E89-008 have not yet displayed the onset of scaling perhaps because the data are not at sufficiently high Q^2 (7 GeV^2). With the CEBAF upgrade it is proposed to measure F_2 on several nuclear targets up to $Q^2 = 25$ GeV^2 at $x = 1.5$ including deuterium which is crucial for identifying two-body versus multi-body correlations by comparison with $A > 2$ targets. Measurements of F_2 at these large Q^2 are then feasible in a reasonable beam time period in Hall A due to the large solid angle and large momentum acceptance of the MAD spectrometer

2.2.2 Search for New Physics in the Electroweak Sector

As discussed above, the 12 GeV upgrade offers a unique opportunity to measure nucleon observables in order to deepen our grasp of its electromagnetic and spin structure within QCD. Nevertheless, it is important to take advantage of this occasion to explore other sectors of physics, in this case of physics beyond the Standard Model of the electroweak sector. The measurement of parity violating asymmetry in deep inelastic scattering off the deuteron would allow the extraction of the relative strength of the SU(2) and U(1) coupling, namely a function of the weak mixing angle θ_W. The expected precision and the value of Q^2 of the proposed measurement will help resolve the present ambiguity in the Q^2 evolution of this coupling constant. Existing data of θ_W from Atomic parity violation and neutrino deep inelastic scattering off iron (NuTeV) at a Q^2 value similar to the proposed experiment have resulted in a puzzle that Jefferson Lab can help resolve. The planned Moller scattering experiment (SLAC E158) and approved Q_{Weak} experiment at JLab are also precision experiments which should help towards a resolution of this puzzle. But more importantly those planned experiments and the proposed experiment will offer sensitivity to different "new physics scenarios" in case strong deviations from the standard model are observed. The CEBAF polarized electron beam has proved to be of superior quality for parity violating experiments. A program of DIS parity measurements, using 11 GeV beam with the Hall A MAD spectrometer, can determine $\sin^2\theta_W$ at a $Q^2 \approx 3$ (GeV/c)^2 to an 0.5% relative uncertainty, which is better than that of the NuTeV experiment. The physics scenario needed to resolve any observed deviation from the Standard Model with an extension of it is truly complementary to that provided by the other planned experiments.

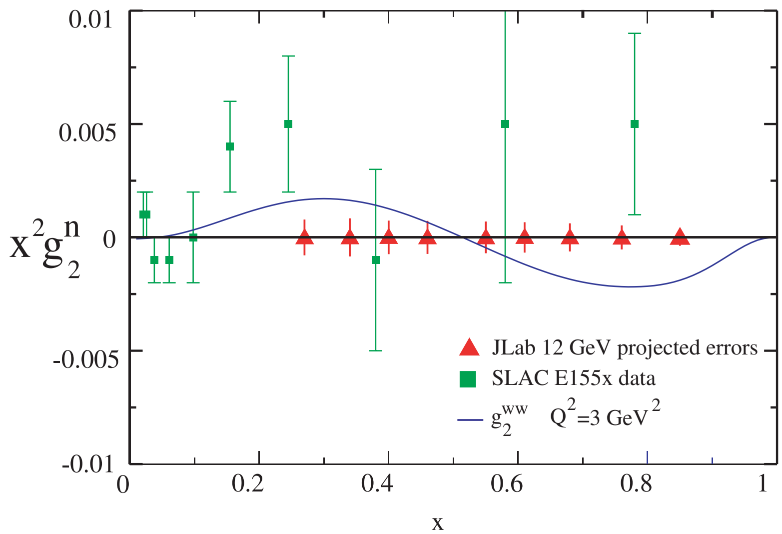

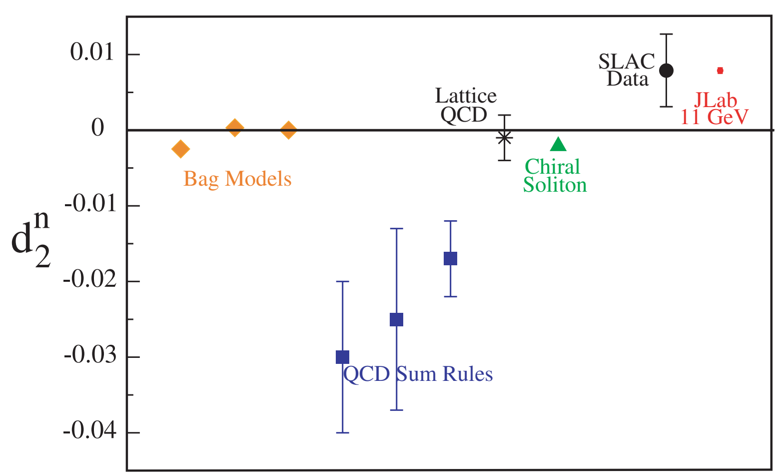

Figure 2.3: a) g_2 spin structure function measured in Hall A using the 11 GeV electron beam and the MAD spectrometer. Neutron d_2 matrix element compared to nucleon models and to state of the art Lattice QCD calculations

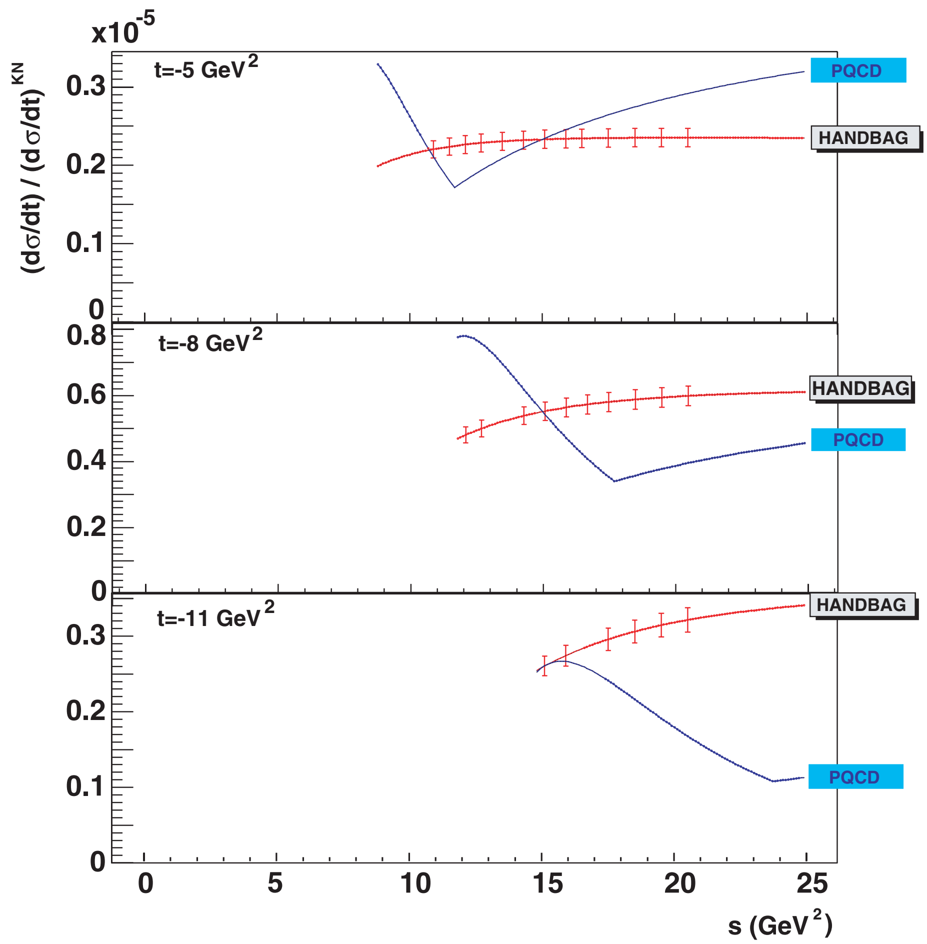

Figure 2.4: Ratio of the differential $\gamma p \rightarrow \gamma p$ cross section to the Klein-Nishina process on an elementary point-charge e, as a function of s at three values of t. The "pQCD" and "Handbag" curves are described in the text. All projected data points are $\pm 5\%$ bins in t and $\pm 2.5\%$ bins in s. The data can be obtained at three incident electron energies 6.6, 8.8, and 11.0 GeV, and the configuration described in the Exclusive Reactions section. A total of 1000 production hours is required.

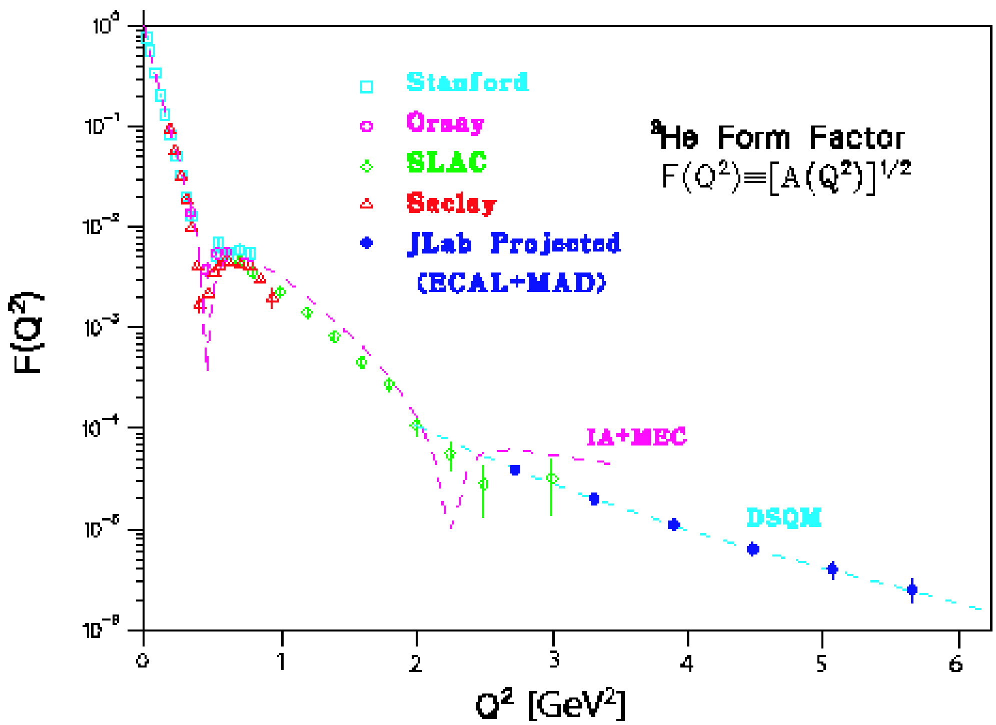

Figure 2.5: Projected data for the ^{3}He form factor $F(Q^2)$ with an 11 GeV JLab beam. Also shown are existing data and predictions of the standard model (IA+MEC) [1] and the dimensional-scaling quark model (DSQM) [2]

Chapter 3

Physics Program

3.1 Inclusive Structure

3.1.1 Valence Quark Structure of the Nucleon

One of the most fundamental properties of the nucleon is the structure of its valence quark distributions. Unlike sea quarks, which at high Q^2 are largely generated in perturbative QCD through gluon bremsstrahlung and subsequent splitting into quark–antiquark pairs, valence quarks are entirely non-perturbative, and therefore more directly reflect the structure of the QCD ground state.

Experimentally, most of the recent studies of nucleon structure have emphasized the small-x_{Bj} region populated mainly by sea quarks (x_{Bj} being the fraction of momentum of the nucleon carried by the quark), while the valence quark structure has for some time now been thought to be understood. Three decades of deep inelastic and other high-energy scattering experiments have provided a detailed map of the nucleon's quark distributions over a large range of kinematics, with one major exception — the deep valence region, at very large x_{Bj}, $x_{Bj} \geq 0.5 - 0.6$. In this region the valence structure of the nucleon can be probed most directly, since sea quark distributions, which must be subtracted from the measured cross sections to reveal the valence structure, are negligibly small beyond $x_{Bj} \sim 0.3$. It is both surprising and unfortunate that the large-x_{Bj} region has been so poorly explored experimentally. Indeed, one of the recommendation of the recent report on *Key Issues in Hadronic Physics*, which identified the future goals of the field of hadronic physics, was that "new experiments that eliminate this problem are a high priority" [3].

This situation is clearly evident in the valence u and d quark distributions, which are usually obtained from measurements of the proton and neutron structure functions, F_2^p and F_2^n, respectively, which at leading order are defined as the charge-squared weighted sums of the quark and antiquark distributions of various flavors ($q = u, d, s \cdots$):

$$F_2(x_{Bj}) \;=\; 2x_{Bj}F_1(x_{Bj}) \;=\; x_{Bj}\sum_q e_q^2\left(q(x_{Bj}) + \bar{q}(x_{Bj})\right) \; . \tag{3.1}$$

While the u quark distribution is relatively well constrained by the F_2^p data for $x_{Bj} < 0.8$, the absence of free neutron targets has left large uncertainties in the d quark distribution beyond

$x_{Bj} \sim 0.5$ arising from incomplete understanding of the nuclear medium modifications in the deuteron, from which F_2^n is extracted. For instance, whether or not one corrects for Fermi motion and binding (off-shell) effects in the deuteron, the extracted $R^{np} \equiv F_2^n/F_2^p$ ratio can differ by $\sim 50\%$ already at $x_{Bj} \sim 0.75$ [4, 5].

These large uncertainties have prevented answers to such basic questions as why the d quark distribution at large x_{Bj} appears to be smaller (or "softer") than the u, softer even than what would be expected from flavor symmetry. Furthermore, since the precise $x_{Bj} \to 1$ behavior of the d/u ratio is a critical test of the mechanism of spin-flavor symmetry breaking, the large errors on the current data preclude any definitive conclusions about the fundamental nature of quark-gluon dynamics in the valence quark region. From another perspective, knowledge of quark distributions at large x_{Bj} is also essential for determining high energy cross sections at collider energies, such as in searches for new physics beyond the standard model [6], where structure information at $x_{Bj} \sim 0.6 - 0.8$ feeds down to lower x_{Bj} at higher values of Q^2 through perturbative Q^2 evolution.

In addition, at fixed Q^2 since the region of large x_{Bj} corresponds to low hadron final state mass, W, the physics of nucleon structure functions at large x_{Bj} is closely connected to the physics governing $N \to N^*$ transition form factors. Through quark-hadron duality, which relates averages of nucleon resonance contributions at low Q^2 to scaling structure functions at high Q^2 [7, 8], measurement of structure functions at large x_{Bj} can also reveal important information about the structure of the excited states of the nucleon.

The need for reliable large x_{Bj} data is even more pressing for spin-dependent quark distributions. Spin degrees of freedom allow access to information about the structure of hadrons which are not available through unpolarized processes. Spin-dependent quark distributions are usually extracted from measurements of the spin-polarization asymmetry, A_1, which is approximately given by the ratio of spin-dependent to spin-averaged structure functions,

$$A_1(x_{Bj}) \approx \frac{g_1(x_{Bj})}{F_1(x_{Bj})} , \tag{3.2}$$

where, to leading order,

$$g_1(x_{Bj}) = \sum_q e_q^2 \left(\Delta q(x_{Bj}) + \Delta\bar{q}(x_{Bj})\right) , \tag{3.3}$$

with Δq defined as the difference between quark distributions with spin aligned and anti-aligned with the spin of the nucleon, $\Delta q = q^\uparrow - q^\downarrow$. The first spin structure function experiments at CERN [9] on the moment, or integral, of g_1, suggested that the total spin carried by quarks was very small, or even zero, prompting the so-called "proton spin-crisis". A decade of subsequent measurements of spin structure functions using proton, deuteron and ^{3}He targets have determined the total quark spin much more accurately, with the current world average value being $\sim 20 - 30\%$ [10], which is still considerably less than the value expected from the simple quark model in which valence quarks carry all of the proton spin.

While the spin fractions carried by quarks and gluons (or generically, partons) are obtained by integrating the spin-dependent parton momentum distributions, the distributions themselves, as a function of the momentum fraction x_{Bj}, contain considerably more information about the quark-gluon dynamics than do their integrals. Furthermore, spin-dependent distributions are generally even more sensitive than spin-averaged ones to the quark-gluon dynamics responsible for spin-flavor symmetry breaking. Considerable progress has been made in measuring spin-dependent structure functions over the last decade, especially in the small x_{Bj} region. However, as for the unpolarized structure functions, relatively little attention has been paid to the pure valence region at large x_{Bj}. The lack of data in the valence region is particularly glaring in the case of the neutron, where there is no information at all on the polarization asymmetry A_1^n for $x_{Bj} \geq 0.4$. This is even more unfortunate given that there are rigorous QCD predictions for the behavior of A_1 as $x_{Bj} \to 1$ which have never been tested.

3.1.2 Theoretical Predictions for Large-x_{Bj} Distributions

The simplest model of the proton, polarized in the $+z$ direction, has three quarks described by a wave function which is symmetric in spin and flavor [11]:

$$\begin{aligned} |p\uparrow\rangle &= \frac{1}{\sqrt{2}}\,|u\uparrow(ud)_{S=0}\rangle + \frac{1}{\sqrt{18}}\,|u\uparrow(ud)_{S=1}\rangle - \frac{1}{3}\,|u\downarrow(ud)_{S=1}\rangle \\ &\quad - \frac{1}{3}\,|d\uparrow(uu)_{S=1}\rangle - \frac{\sqrt{2}}{3}\,|d\downarrow(uu)_{S=1}\rangle\,, \end{aligned} \tag{3.4}$$

where $q\uparrow\downarrow$ represents the active quark which undergoes the deep inelastic collision, and $(qq)_S$ denotes the two-quark configuration with spin S that is a spectator to the scattering. (The neutron wave function can be obtained by simply interchanging the u and d quarks.) On the basis of exact spin-flavor symmetry, which is described by the group SU(6), the $S = 0$ and $S = 1$ "diquark" states contribute equally, giving rise to simple relations among the quark distributions, such as $u = 2d$ and $\Delta u = -4\Delta d$, which in terms of the structure functions correspond to:

$$R^{np} \equiv F_2^n/F_2^p = \frac{2}{3}; \quad A_1^p = 5/9; \quad \text{and} \quad A_1^n = 0. \tag{3.5}$$

In nature spin-flavor SU(6) symmetry is, of course, broken. It has been known for some time that the d quark distribution is softer than the u quark distribution, which reflects the fact that the neutron to proton ratio R^{np} deviates strongly from the SU(6) expectation beyond $x_{Bj} \sim 0.4$. On the other hand, the data for the polarization asymmetries A_1 are so poor in the valence region that it is presently not possible to discern whether the SU(6) predictions are borne out for the spin-dependent distributions.

A number of models have been developed for quark distributions which incorporate mechanisms for the breaking of the SU(6) symmetry, some of which can be linked directly to phenomena such as the hyperfine splitting of the baryon and meson mass spectra. Feynman and others [11, 14, 15] observed that there was a correlation between the nucleon and Δ mass difference and the suppression of R^{np} at large x_{Bj}. A quark hyperfine interaction, such as that due to one-gluon exchange, instantons or pion exchange, which can induce a higher energy for the $S = 1$ spectator "diquark" in Eq. (3.4), will necessarily give rise to a larger

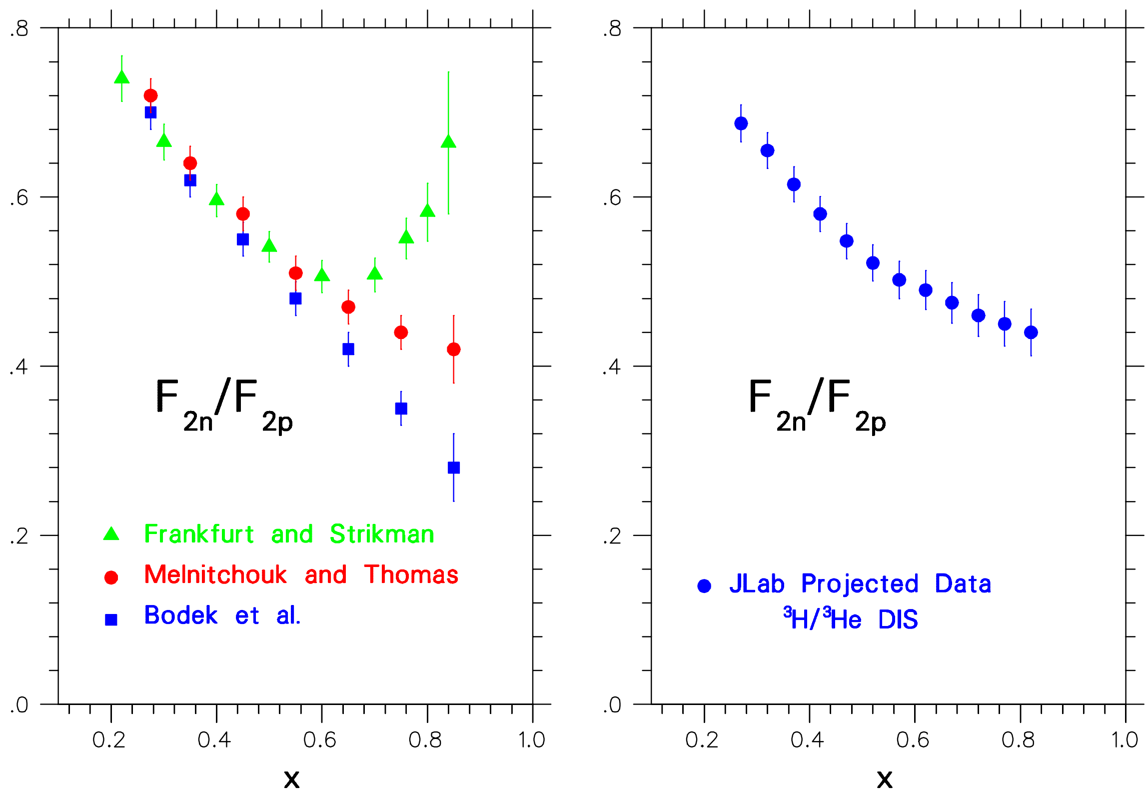

Figure 3.1: Ratio R^{np} of neutron to proton structure functions as a function of x_{Bj}, extracted from the SLAC data on the deep inelastic proton and deuteron structure functions. The left panel represents R^{np} extracted according to different prescriptions for accounting for nuclear effects in the deuteron: Fermi smearing only (blue squares) [4, 12], Fermi motion and nuclear binding corrections (red circles) [5], and assuming the nuclear EMC effect in the deuteron scales with nuclear density (green triangles) [13]. The right panel shows the projected errors for the proposed ^{3}H and ^{3}He JLab experiment.

mass for the Δ, since the quark wave function for the Δ has all "diquark" configurations with $S = 1$ [16]. If the $S = 0$ states are dominant at large x_{Bj}, Eq.(3.4) implies that the d quark distribution will be suppressed relative to the u in the valence quark region. This same mechanism will also lead to specific predictions for the polarization asymmetries as $x_{Bj} \to 1$:

$$R^{np} \to \frac{1}{4}; \quad A_1^p \to 1; \quad \text{and} \quad A_1^n \to 1 \ . \tag{3.6}$$

More radical non-perturbative models of SU(6) breaking, such as those which include instantons as important degrees of freedom, predict dramatically different behavior for A_1^n as $x_{Bj} \to 1$, namely that it goes to a value close to zero [17].

Perturbative QCD, on the other hand, predicts that the dominant components of the proton valence wave function at large x_{Bj} are those associated with states in which the total "diquark" spin projection, S_z, is zero [18]. Consequently, scattering from a quark polarized in the opposite direction to the proton polarization is suppressed relative to the helicity-aligned configuration. From Eq.(3.4) this leads to the predictions in the $x_{Bj} \to 1$ limit:

$$R^{np} \to \frac{3}{7}; \quad A_1^p \to 1; \quad \text{and} \quad A_1^n \to 1 \ . \tag{3.7}$$

The novelty of these predictions, especially for A_1, is that they follow essentially directly from perturbative QCD in the limit as $Q^2 \to \infty$ and $x_{Bj} \to 1$. However, it is not *a priori* clear at which x_{Bj} and Q^2 the transition from non-perturbative dynamics to perturbative QCD takes place, so that experimental guidance on this issue is needed.

Arguments based on local quark-hadron duality allow one to relate the $x_{Bj} \to 1$ behavior of structure functions to the large Q^2 behavior of elastic form factors [19], independent of model assumptions about the underlying dynamics. Since the structure functions are dominated by the magnetic form factor, G_M, at large Q^2, the ratios of structure functions are predicted to be particularly simple [20]:

$$R^{np} \to \left.\frac{d(G_M^n)^2/dQ^2}{d(G_M^p)^2/dQ^2}\right|_{Q^2\to\infty}; \quad A_1^p \to 1; \quad \text{and} \quad A_1^n \to 1 \ . \tag{3.8}$$

Once again, while these predictions are expected to be accurate at large Q^2, it is not known at which Q^2 values local duality will be valid, and this can only be established experimentally.

While the trend of the existing R^{np} data is consistent with models with broken SU(6) symmetry, because of uncertainties in the extraction procedure associated with nuclear corrections, they cannot discriminate between the competing mechanisms of SU(6) breaking, as evident from Figure 3.1. For the asymmetries $A_1^{n,p}$, while we do not expect the SU(6) predictions to be accurate, the existing measurements at high x_{Bj} lack the precision to even distinguish any of the predictions from the naive SU(6) result.

3.1.3 Neutron to Proton Structure Function Ratio, F_2^n/F_2^p

If the nuclear EMC effect (the modification of the free nucleon structure function in the nuclear environment) in deuterium were known, one could apply nuclear smearing corrections directly to the deuterium data to obtain the free neutron F_2^n. However, the EMC effect in the deuteron requires knowledge of the free neutron structure function itself, so the argument becomes cyclic. The best way to reliably determine R^{np}, free of the large uncertainties associated with nuclear corrections at large x_{Bj}, is through simultaneous measurements of the inclusive ^{3}He and ^{3}H structure functions, maximally exploiting the mirror symmetry of $A = 3$ nuclei. Regardless of the absolute value of the nuclear EMC effect in ^{3}He or ^{3}H, the differences between these will be small — on the scale of charge symmetry breaking in the nucleus.

In the absence of a Coulomb interaction, and in an isospin symmetric world, the properties of a proton (neutron) bound in the ^{3}He nucleus would be identical to that of a neutron (proton) bound in the ^{3}H nucleus. If, in addition, the proton and neutron distributions in ^{3}He (and in ^{3}H) were identical, the neutron structure function could be extracted with no nuclear corrections, regardless of the size of the EMC effect in ^{3}He or ^{3}H individually.

In practice, ^{3}He and ^{3}H are of course not perfect mirror nuclei — their binding energies for instance differ by some 10% — and the proton and neutron distributions are not quite identical. However, the $A = 3$ system has been studied for many years, and modern realistic $A = 3$ wave functions are known to rather good accuracy. Using these wave functions, together with a nucleon spectral function, the difference in the EMC effects for the ^{3}He and ^{3}H nuclei has been shown [21, 22, 23, 24, 25, 26] to be less than 2% for $x_{Bj} < 0.8 - 0.85$. More importantly, the actual model dependence of this difference is less than 1% for all x_{Bj} values accessible experimentally with an 11 GeV beam. Possible effects beyond the impulse approximation (in which electrons scatter incoherently from individual nucleons in the nucleus), such as scattering from hypothetical six-quark clusters in the nucleus, have also been considered [25, 26], and found to give small corrections for $x_{Bj} \lesssim 0.8 - 0.85$.

By performing the tritium and helium measurements under identical conditions, the ratio of the deep inelastic cross sections for the two nuclei can be measured with 1% experimental uncertainty (SLAC Experiments E139 [27] and E140 [28, 29] have quoted 0.5% uncertainties for measurements of ratios of cross sections). The proposed kinematics are illustrated in Table 3.1.3, and the expected cross sections, counting rates and beam times are given in Table 3.1.3.

Deep inelastic scattering with the proposed 11 GeV JLab electron beam can therefore provide precise measurements for the $F_2^{^3\mathrm{He}}/F_2^{^3\mathrm{H}}$ ratio, from which R^{np} can be extracted essentially free of nuclear corrections at the 1% level over the entire range $0.10 \leq x_{Bj} \leq 0.82$. In addition, it will for the first time enable the size of the EMC effect to be determined in $A = 3$ nuclei, which to date has been measured only for $A \geq 4$ nuclei. The key issue for this experiment will be the availability of a high-density tritium target, comparable with the previously used Saclay [30] and MIT-Bates [31] tritium targets. The quality of the projected data is highlighted in Figure 3.1.

3.1.4 Proton Spin Structure: A_1^p at Large x_{Bj}

After a decade of experiments at CERN, SLAC and DESY [32], our knowledge of the spin structure of the proton is rather impressive, as illustrated in Fig. 3.2 for the polarization

x	W^2 [(GeV/c)^2]	Q^2 [(GeV/c)^2]	E' (GeV)	θ (deg)	π/e
0.82	4.0	13.8	2.00	46.6	52
0.77	4.7	12.9	2.10	43.8	43
0.72	5.5	11.9	2.20	41.0	36
0.67	6.2	10.9	2.35	37.8	27
0.62	6.9	9.8	2.55	34.4	19
0.57	7.6	8.9	2.65	32.1	19
0.52	8.3	8.1	2.75	29.9	18
0.47	9.0	7.2	2.85	27.7	19
0.42	9.6	6.3	3.00	25.2	18
0.37	10.2	5.5	3.10	23.1	19
0.32	10.7	4.6	3.30	20.6	18
0.27	11.2	3.8	3.50	18.1	18
0.22	11.6	3.0	3.65	15.8	19

Table 3.1: Helium/Tritium DIS Kinematics with $\mathbf{E} = 11$ GeV.

asymmetry A_1^p. At low and medium x_{Bj} ($x_{Bj} < 0.4$) the various data sets are consistent with each other and show a definite rise with x_{Bj}. At higher x_{Bj} ($x_{Bj} > 0.4$), however, the errors become significantly larger, and the trend is no longer clear: the current data cannot distinguish between a pure SU(6) symmetric scenario, in which $A_1^p \to 5/9$, and the pQCD limit, $A_1^p \to 1$. With an 11 GeV beam and the MAD spectrometer in Hall A, Jefferson Lab will provide a unique facility for closing this gap in our knowledge of A_1^p.

In order to unambiguously extract the A_1 asymmetry from data, two beam-target asymmetries must be measured: one with the target polarization oriented longitudinally with respect to the electron beam ($A_{\|}$) and one oriented transversely ($A_{\perp}$):

$$A_{\|} = \frac{\sigma^{\downarrow\Uparrow} - \sigma^{\uparrow\Uparrow}}{\sigma^{\downarrow\Uparrow} + \sigma^{\uparrow\Uparrow}} \qquad \text{and} \qquad A_{\perp} = \frac{\sigma^{\downarrow\Rightarrow} - \sigma^{\uparrow\Rightarrow}}{\sigma^{\downarrow\Rightarrow} + \sigma^{\uparrow\Rightarrow}} \ , \tag{3.9}$$

where $\sigma^{\uparrow\Uparrow}$ ($\sigma^{\uparrow\Downarrow}$) is the cross section for the beam and target helicities parallel (anti-parallel), and $\sigma^{\downarrow\Rightarrow}$ ($\sigma^{\uparrow\Rightarrow}$) is the cross section for scattering an electron polarized parallel (anti-parallel) to the beam direction from a transversely polarized target. These observed asymmetries can then be related to the virtual photon-absorption asymmetries, A_1 and A_2:

$$A_1 = \frac{\sigma^T_{1/2} - \sigma^T_{3/2}}{\sigma^T_{1/2} + \sigma^T_{3/2}} = \frac{A_{\|}}{D(1+\eta\zeta)} + \frac{\eta A_{\perp}}{d(1+\eta\zeta)} \ , \tag{3.10}$$

x	$\sigma(^3\text{He})$ (nb/sr/GeV)	$\sigma(^3\text{H})$ (nb/sr/GeV)	^{3}He Rate (Events/h)	^{3}H Rate (Events/h)	^{3}He Time (h)	^{3}H Time (h)
0.82	0.0146	0.0117	15500	12500	10.3	12.8
0.77	0.0308	0.0240	35500	27700	4.5	5.8
0.72	0.0639	0.0491	80100	61600	2.0	2.6
0.67	0.130	0.0996	180000	138000	0.9	1.2
0.62	0.261	0.202	402000	312000	0.5	0.5
0.57	0.463	0.364	776000	610000	0.5	0.5
0.52	0.801	0.639	1430000	1140000	0.5	0.5
0.47	1.35	1.10	2510000	2040000	0.5	0.5
0.42	2.35	1.95	4580000	3800000	0.5	0.5
0.37	3.89	3.30	7840000	6650000	0.5	0.5
0.32	7.00	6.07	15000000	13000000	0.5	0.5
0.27	12.8	11.3	29100000	25800000	0.5	0.5
0.22	23.3	21.1	55300000	50100000	0.5	0.5

Table 3.2: Cross sections, counting rates and beam times for ^{3}He/^{3}H DIS measurements.

$$A_2 = \frac{\sigma^{LT}}{\sigma^T_{1/2} + \sigma^T_{3/2}} = \frac{\zeta A_\parallel}{D(1+\eta\zeta)} + \frac{A_\perp}{d(1+\eta\zeta)} \ , \tag{3.11}$$

where $\sigma^T_{1/2(3/2)}$ is the virtual photo-absorption transverse cross section for total helicity of the photon and nucleon of 1/2 (3/2), and σ^{LT} is the interference between the transverse and longitudinal photon-nucleon amplitudes. The factor D is a depolarization factor ($0 \le D \le 1$), which gives the projection of the target polarization along the direction of the three-momentum transfer, $D = (1-\epsilon E'/E)/(1+\epsilon R)$, where $\epsilon^{-1} = 1 + 2[1 + Q^2/4M^2 x^2_{Bj}] \tan^2\theta/2$, and $R + 1 = (1 + 4M^2 x^2_{Bj}/Q^2)F_2/[2x_{Bj}F_1]$. The other kinematic factors are given by $\eta = \epsilon Q/(E - \epsilon E')$, $d = D\sqrt{2\epsilon/(1+\epsilon)}$, and $\zeta = \eta(1+\epsilon)/2\epsilon$.

We propose a measurement to constrain the large x_{Bj} behavior of A^p_1 in Hall A using the MAD spectrometer and a NH_3 target. The MAD spectrometer is ideally suited for this experiment because of its large acceptance. The target, built by the University of Virginia (UVa), has been used in several previous spin structure measurements. Measurement of both the parallel and perpendicular asymmetry for two central spectrometer settings will cover a range of x_{Bj} of between 0.4 and 0.8. As seen in Fig. 3.2, this will provide the best measurements of A^p_1 available in this region.

The proposed kinematics and times are listed in Table 3.3. The time for the perpendicular measurements was chosen so that the statistical uncertainty in $A_\perp$ contributed to about one-third of the statistical error in the extracted A_1^p. For all measurements, we required that $Q^2 > 2$ GeV^2/c^2 where very little Q^2 dependence in A_1^p has been observed [33], and that the invariant mass $W > 2$ GeV for deep inelastic scattering.

We have been conservative in our estimates of the experiment performance in estimating our uncertainties. We assumed a beam polarization of 80% and an average target polarization of 80%. We assumed a luminosity for the current NH_3 target of 10^{35}/cm^2/s and a dilution factor of 0.15. It is quite likely that improvement in target technology will allow us to increase the luminosity, but our uncertainty estimates use existing capabilities.

To estimate the systematic uncertainties, we can use as a guide the SLAC experiment E143, which used the same target and a similar setup [34]. For E143 the leading systematic uncertainty for the high x_{Bj} measurements was due to uncertainty in $R(x_{Bj}, Q^2)$. This experiment will be less sensitive to R than E143 because of the larger scattering angles, so we expect about a 2.6% uncertainty from R. The target polarization will contribute about 2.5% to the uncertainty, the dilution factor, f, which is defined as the ratio of polarized nucleons to the total number of nucleons in the target, to about 1.6%, and radiative correction to about 2%. The beam polarization will contribute 1-2%, depending on the polarimetry available in Hall A at the time of the measurement. Adding these uncertainties in quadrature, we can expect an approximately 5% systematic uncertainty in these measurements, which is comparable to the statistical uncertainties.

Table 3.3: List of proposed kinematics. Under Rates, the range of rates for the x_{Bj} bins is shown in Fig. 3.2.

Setting	Range of x_{Bj}	θ	E' (GeV)	Time (h)	Target Field	Rate (1/h)
1	0.6-0.8	36^o	2.75	1000	$\parallel$	18-53
2	0.6-0.8	36^o	2.75	100	$\perp$	18-53
3	0.4-0.6	25^o	3.30	200	$\parallel$	647-760
4	0.4-0.6	25^o	3.30	20	$\perp$	647-760

Compared to the other halls at Jefferson Lab, the MAD spectrometer in Hall A is the preferred means to measure A_1^p. To extract A_1^p independently of a model (for A_2), it is necessary to measure both $A_\parallel$ and $A_\perp$. This is only possible in Hall A and Hall C because the large transverse field of the NH_3 target introduces significant complications in CLAS. To go to the largest x_{Bj} possible at Jefferson Lab, it is necessary to go to large scattering angles. Since the acceptance of MAD is significantly larger than either the HMS or the planned SHMS in Hall C, MAD is the preferred spectrometer to conduct this experiment. Thus, the combination of the 11 GeV electron beam energy at an upgraded Jefferson Lab coupled with the MAD spectrometer and the UVa NH_3 target will allow us to dramatically extend our understanding of A_1^p at large x_{Bj}.

3.1.5 Neutron Spin Structure, A_1^n

While data on R^{np} and A_1^p give some indication of the large-x_{Bj} behavior of the valence quark distributions at $x_{Bj} \lesssim 0.6$, the experimental situation for the neutron A_1^n at large x_{Bj} has been totally unclear. Until the recently completed measurement (JLab Hall A Collaboration E99-117[35]), the statistical precision of the data did not even allow a meaningful statement about the qualitative behavior of A_1^n for $x_{Bj} > 0.4$. Although still preliminary, the measurement at JLab Hall A produced interesting results up to $x_{Bj} \simeq 0.61$ with much improved precision. The experiment proposed here is to use the 11 GeV JLab electron beam to perform a precision measurement of A_1^n, utilizing the Hall A polarized ^{3}He target and the proposed MAD spectrometer. Because the neutron in ^{3}He carries almost 90% of the nuclear spin, polarized ^{3}He is an ideal source of polarized neutrons [36].

The experiment involves measurement of the polarization asymmetry, $A_1^{^3\mathrm{He}}$, obtained by scattering polarized electrons from a polarized ^{3}He target with the beam and target helicities parallel and anti-parallel (see Eq. (3.10)). The neutron asymmetry A_1^n is extracted from $A_1^{^3\mathrm{He}}$ after correcting for residual nuclear effects in ^{3}He associated with Fermi motion and binding, using modern three-body wave functions [37, 38, 39, 40, 41]. In addition to the use of the polarized ^{3}He target, other polarized targets (ND_3 and NH_3) will be used for cross checks for the investigation of the nuclear effects.

Table 3.4: Comparison of the figure of merit (FOM) for large x_{Bj} measurements of the A_1^n structure function at HERA, SLAC and JLab.

Expt. Name	E_i (GeV)	E' (GeV)	θ (deg.)	x_{Bj} bin	Q^2 $(\mathrm{GeV/c})^2$	D	f	Rate (Hz)	FOM (10^{-4})
HERMES	35.0	17.0	5.2	0.60-0.70	9.1	0.22	0.50	0.05	2
SLAC E143	29.13	25.5	7.0	0.60-0.70	9.1	0.29	0.84	0.3	10
JLab	11.0	4.4	25	0.60-0.70	8.5	0.67	0.80	2.7	1000

An example of the kinematics relevant for this experiment is given in Table 3.4. To illustrate the improvement of the projected results obtainable with JLab at 11 GeV compared with previously measured data from other facilities we introduce a figure of merit (FOM) $= D^2 \times \mathrm{Rate} \times f^2$, which allows a meaningful comparison between different laboratories. Here "Rate" takes into account the use of the proposed MAD spectrometer, and f is the dilution factor. Table 3.4 shows the comparison between the relevant parameters at competitive existing laboratories at comparable, large x_{Bj} and Q^2. Note that with increasing beam energy the depolarization factor decreases. The lowest beam energy, therefore, which guarantees access to the large-x_{Bj} region in the DIS region is optimal. JLab at 11 GeV would enable access to $x_{Bj} \lesssim 0.8$ at $W \approx 2$ GeV.

While this cut in W would allow the deep inelastic continuum to be cleanly accessed, one may extend the measurements of A_1^n to even larger x_{Bj} by using quark-hadron duality in the resonance region, $W < 2$ GeV. If duality is observed to hold for the spin-dependent g_1 structure function as well as it does for the unpolarized F_2 structure function [8], averaging over small regions of W will suppress the high twist contributions associated with the low-lying resonances, and enable the dominant scaling component of A_1 to be measured out to $x_{Bj} \simeq 0.95$. This will be discussed in more detail in the next Section.

3.1.6 Duality in Spin Structure Functions

Thirty years ago, Bloom and Gilman [7] found that the inclusive F_2 structure function measured in the nucleon resonance region at low values of invariant mass (W) generally follows a global scaling curve that describes high W data in the DIS region. Furthermore, this resonance–DIS duality also holds locally; the equivalence of the averaged resonance and scaling structure functions appears to hold for each resonance. More recently, high-precision data on the F_2 structure function from Jefferson Lab [8] have confirmed the earlier observations, demonstrating that duality works remarkably well down to rather low values of Q^2 [~ 0.5 (GeV/c)^2].

This duality between the resonance region, which may be described by constituent quark models, and the scaling region, which is governed by pQCD, hints a common origin for both regions. Understanding duality therefore gives insight into the transition from the scaling region of asymptotic freedom to the resonance region dominated by confinement.

In QCD, Bloom-Gilman duality can be formulated in terms of the operator product expansion (OPE) of QCD moments of structure functions [19]. In this approach, contributions are organized according to powers of $1/Q^2$, or according to the "twist" of certain local operators, where twist is defined as the difference between the mass dimension and the spin of the operator. The leading terms are associated with free quark scattering, and are responsible for the scaling of the structure function. The higher order $1/Q^2$ terms, the so-called higher twist terms, involve interactions between quarks and gluons and hence reflect elements of confinement dynamics. The weak Q^2 dependence exhibited by the low moments of F_2 means that, surprisingly, the non-leading, $1/Q^2$-suppressed, interaction terms do not play a major role even at low Q^2 [≈ 1 (GeV/c)^2]. Since the higher order $1/Q^2$ terms are expected to be most pronounced at low values of Q^2, this weak Q^2 dependence of the low moments indicates that higher order $1/Q^2$ terms either cancel each other or have small coefficients.

Although the OPE formalism allows us to organize hadronic observables in terms of an asymptotic expansion, it does not tell us *a priori* why certain matrix elements are small or cancel. While the origins of duality still remains a mystery, the new precision data on F_2 structure function from Jefferson Lab [8] have stimulated a considerable amount of theoretical activity on Bloom-Gilman duality [42, 43, 44, 45, 46, 47, 48]. These theoretical efforts have addressed the origins of duality not only for the F_2 structure function of the proton, but also for the neutron and for the spin dependent structure functions. It is vital for our understanding of duality and its practical exploitation that the spin and flavor dependence of duality be established empirically.

The best overlap between DIS and resonance regions is over the moderate to high x_{Bj} range between 0.1 and 0.75. As described elsewhere in this document, the DIS spin structure function measurements of neutron and proton possible with the 12 GeV beam at Jefferson Lab will provide the most precise DIS spin data over this x_{Bj} range. There has been very little spin structure data available in the resonance region until recently. This is especially true for the neutron due to the lack of a free neutron target. A few Jefferson Lab experiments that were completed recently or will run in the near future in Halls A, B, and C will provide precision spin structure data for the proton and the neutron over the Q^2 range of 0.2–5 (GeV/c)^2 and the x_{Bj} range of 0.1–0.7 [49]. With the availability of an 11 GeV beam, however, these spin structure measurements for the proton and the neutron can be extended up to $Q^2 \approx 10$ (GeV/c)^2 and $x_{Bj} \approx 0.95$ in the resonance region. These data, combined with the precision high x_{Bj} spin structure function data in the DIS region at larger W, can be used for a stringent test of parton-hadron duality for spin structure functions.

Measurement of neutron (polarized ^{3}He) spin structure functions in the resonance region

The 11 GeV electron beam combined with the polarized ^{3}He target in Hall A and the MAD spectrometer provides the best opportunity to measure neutron spin structure function data in the resonance region up to very high values of x_{Bj}. In an experiment similar to the extraction of A_1^n in the DIS region described in section 3.1.5, parallel and perpendicular cross section asymmetries for electron scattering off polarized ^{3}He will be used to extract virtual photon asymmetries A_1, A_2 and spin structure functions g_1 and g_2 for the neutron in the resonance region. The high luminosity available from the Hall A polarized ^{3}He target combined with the 30 msr solid angle of the MAD spectrometer allows for a precision extraction of these quantities up to $x_{Bj} \sim 0.95$ in roughly 900 hours. An example of the kinematics, electron rates and expected uncertainties for this experiment is shown in Table 3.5. The

E_0 (GeV)	θ_e (degrees)	E$'$ (GeV)	Q^2 (GeV)^2	$\bar{x}_{Bj}$ at Δ	Rate Hz	ΔA_1^n	Time Hours
6.0	12.5	4.8	2.01	0.75	29	0.04	15
6.0	18.5	4.4	2.74	0.81	7	0.05	25
6.0	22.5	3.9	3.60	0.85	2	0.06	49
8.0	18.5	5.4	4.50	0.88	1.4	0.06	83
8.0	22.5	4.8	5.79	0.89	0.3	0.075	147
10.0	18.5	6.3	6.61	0.91	0.3	0.075	193
11.0	18.5	6.7	7.71	0.93	0.2	0.08	308

Table 3.5: Kinematics, rates and statistical uncertainties for the proposed measurements. A 100 MeV momentum bin has been used for the rate calculations. Due to the MAD momentum acceptance of $\sim \pm 15\%$, each momentum setting considered here contains 15-20 100 MeV bins. The rates and the uncertainties given are for the bin with the lowest rate of a given momentum setting. For the rate calculations we have assumed a beam current of 15 μA.

Q^2/W phase-space covered by this experiment is given in Figure 3.3. Figure 3.4 shows the expected data for the three resonance regions compared to the available world data and the projected DIS data with 11 GeV beam at Jefferson Lab.

The total measurement time as given in Table 1 is 820 hours. This beam time allows for almost complete coverage of the resonance region in Q^2 ($2 < Q^2 < 8.5$ (GeV/c)^2), in x_{Bj} ($0.4 < x_{Bj} < 0.95$), and in W ($1.0 < W < 2.2$ GeV).

Measurement of proton spin structure functions in the resonance region

Section 3.1.4 discussed the possibility of high precision extraction A_1^p in the DIS region using the UVa polarized NH_3 target and the MAD spectrometer in Hall A. The overall figure of merit for polarized protons from the UVa NH_3 target is only about a factor of 2 less than the figure of merit for polarized neutrons from the Hall A polarized ^{3}He target. As a result the UVa polarized NH_3 target combined with the MAD spectrometer can be used to extract proton spin structure functions in the resonance region at the same kinematic settings as for the neutron given in the previous section with statistical errors only about $\sqrt{2}$ times worse than those shown for A_1^n in figure Fig. 3.4.

Testing spin and flavor dependence of duality and its applications

The spin structure function measurements in the resonance and the DIS regions discussed in this document will allow for a stringent test of quark-hadron duality for spin structure functions of both neutron and proton. In the case of neutron (polarized ^{3}He) and separately in the case of proton, the DIS and resonance data for the duality test will be obtained using the identical beam, target and spectrometer setup. This will eliminate many systematic uncertainties in the comparison of structure functions in the two regions.

While it is interesting in its own right to test duality predictions for spin structure functions, such a test can lead to very important applications. With a good understanding of duality between DIS and resonance regions one can use the resonance spin structure data to access the very high x_{Bj} region ($x_{Bj} > 0.75$), which will not be accessible in any other experiment in the foreseeable future. Figures 3.5,3.6 show the possibilities of extending the A_1^n and A_1^p higher x_{Bj} by relaxing the invariant mass cut to $W < 1.5$ GeV and $W < 1.2$ GeV given that duality holds for spin structure functions. This data will allow a well restricted extrapolation of both A_1^n and A_1^p to $x_{Bj} = 1$ for the first time.

3.1.7 Higher Twists and the g_2^n Structure Function

While the g_1 structure function has a simple interpretation in the quark-parton model in terms of quark helicity distributions, and has been the focus of extensive experimental programs over the last decade, there have been few dedicated experimental studies of the g_2 structure function. The g_2 structure function is related to the transverse polarization of the nucleon, and although it does not have a simple quark-parton model interpretation, it contains important information about quark-gluon correlations within the nucleon.

As discussed in the preceding Section, in QCD the quark-gluon correlations are associated with higher twist operators, which are suppressed by additional factors of $1/Q$ relative to the leading twist (twist-2) contribution (which is associated with free quark scattering). At large values of Q^2, QCD allows one to relate the moments of spin structure functions to the matrix elements of operators of given twist. Because the leading twist-2 operator contributes to both g_1 and g_2, it is possible to express the twist-2 part of g_2, known as g_2^{WW}, in terms of g_1 as follows [50]:

$$g_2^{WW}(x_{Bj}, Q^2) = -g_1(x_{Bj}, Q^2) + \int_{x_{Bj}}^{1} dy \frac{g_1(y, Q^2)}{y} \ . \tag{3.12}$$

The simplest twist-3 matrix element which contains information on quark-gluon correlations is given by:

$$d_2(Q^2) \;\; = \;\; \int_0^1 dx_{Bj} \; x_{Bj}^2 \left[2g_1(x_{Bj}, Q^2) + 3g_2(x_{Bj}, Q^2)\right] \ . \tag{3.13}$$

Note that because of the x_{Bj}^2 weighting in Eq.(3.13), d_2 is dominated by the large-x_{Bj} behavior of g_1 and g_2. The physical significance of d_2 is that it reflects the response of a quark to the polarization of the gluon color field in the nucleon, $d_2 = (2\chi_B + \chi_E)/3$, with χ_B (χ_E) the gluon-field polarizability in response to a color magnetic (electric) field $\vec{B}$ ($\vec{E}$) [51].

Published data for g_2 were obtained from experiments E142-E155 at SLAC [52, 53], and the SMC experiment at CERN [54]. Using results from the most recent experiment at SLAC [53], which measured g_2 for proton and deuteron, values for g_2 for the neutron were extracted and are shown in Fig. 3.7. Note that the SLAC data vary in Q^2 from $0.8 - 8.4$ GeV^2 over the measured x_{Bj} range. The curve labeled "g_2^{WW}" represents the leading twist contribution to g_2 [50] at fixed $Q^2 = 3$ GeV^2, calculated from a fit to world data on g_1 [53]. Using these data, a non-zero positive value for d_2^n has been extracted that is in disagreement with all of the theoretical calculations [55, 56, 57, 58, 59, 60, 61, 62], see Fig. 3.8. However, in most cases, the disagreement is less than 1σ, and the size of the experimental error does not allow one to make a conclusive statement about the importance of higher-twist effects in the nucleon. On the other hand, considerable progress has been made recently in calculating matrix elements from first principles in QCD using lattice techniques. The lattice results from the QCDSF Collaboration [63] are in agreement with the better determined proton d_2, but underestimate somewhat the neutron data. A striking feature of the neutron d_2 lattice calculations is that the error is significantly smaller than the current experimental error, and will become even smaller with the next generation of lattice simulations which will be performed over the next 2-3 years [64].

A 12 GeV JLab experiment will make a factor of 10 statistical improvement in the error on d_2^n by taking advantage of the high-luminosity 11 GeV beam and the large acceptance MAD spectrometer. Precision data for g_2^n will be obtained in the range $0.2 < x_{Bj} < 0.9$ at fixed $Q^2 = 3$ GeV^2, with special focus on the high-x_{Bj} region which dominates d_2. Projected statistical errors for $x_{Bj}^2 g_2^n$ and d_2^n are shown in Figs. 3.7 and 3.8 respectively. The expected statistical error on d_2 for this experiment is 2.5×10^{-4} for 100 hours of beam. The other significant feature of the JLab measurement is the ability to measure at fixed Q^2. Measurements at fixed Q^2 are essential to accurately quantifying higher twist effects. Because g_2 is sensitive to gluon exchange, even at moderately large Q^2, and is not easily interpreted in terms of simple parton models, its Q^2 evolution is not well known. The data from SLAC used to obtain d_2^n cover an order of magnitude in Q^2 over the measured x_{Bj} range, making it difficult to cleanly extract higher twist effects from other sources of Q^2 dependence. In addition, the SLAC data in the high-x_{Bj} region, which dominates d_2^n, are at $Q^2 \simeq 8$ GeV^2, which further suppresses higher twist effects relative to the leading twist contribution.

A complete program for studying g_2 at JLab will also include measurements of d_2^n at $Q^2 = 4$ and 5 GeV^2 with similar precision to those shown in Figs. 3.7 and 3.8. These additional measurements will provide information on the Q^2 evolution of the higher twist effects and allow further study the behavior of g_2 at high x_{Bj} where there is significant contribution from the resonance region. To achieve similar statistical precision at $Q^2 = 4$ and 5 GeV^2 would require an additional 250 and 800 hours of beam, respectively.

3.1.8 High Energy Behavior of g_1

The large x_{Bj} region is crucial for determining higher moments of structure functions, and testing the behavior of valence quark distributions in the limit $x_{Bj} \to 1$. On the other hand, an 11 GeV electron beam will also enable one to probe the region of larger W, which is important in constraining structure functions at small x_{Bj}.

The high-energy behavior of the g_1 structure function of the nucleon is important for testing fundamental QCD sum rules, such as the Bjorken sum rule [65], which relates structure functions measured at high Q^2 to the axial vector charge of the nucleon measured in weak neutron β decay. Another fundamental sum rule which relates differences of cross sections for absorption of a real photon ($Q^2 = 0$) to the nucleon's anomalous magnetic moment, κ, is the Gerasimov-Drell-Hearn (GDH) sum rule [66],

$$\int_{\nu_{th}}^{\infty} \frac{d\nu}{\nu}(\sigma_{1/2} - \sigma_{3/2}) \quad = \quad -\frac{2\pi^2\alpha\kappa^2}{M^2} \ , \tag{3.14}$$

where $\sigma_{3/2}$ ($\sigma_{1/2}$) is the scattering cross section for a photon with spin parallel (anti-parallel) to the spin of the nucleon. The GDH sum rule is derived from general principles of causality, Lorentz and electromagnetic gauge invariance, and unitarity, together with an unsubtracted dispersion relation for the spin dependent part of the Compton amplitude. Its violation would provide important challenges to our understanding of nucleon spin structure in QCD [67]. Data from ELSA and MAMI [68] up to energies of ≈ 2 GeV indicate that the sum rule is converging to a value which is 2σ above the GDH prediction. Clearly it will be important to establish whether, and at which energies, this sum rule is saturated.

A generalization of the GDH sum rule to finite Q^2 allows one to make contact with parton model sum rules such as the Bjorken sum rule, and study the transition from $Q^2 = 0$ to large Q^2. The generalized GDH integral can be defined as:

$$I(Q^2) \quad = \quad \frac{2M^2}{Q^2} \int_0^1 dx_{Bj} \ g_1(x_{Bj}, Q^2) \ . \tag{3.15}$$

In the limit $Q^2 \to 0$ one recovers the GDH sum rule, Eq. (3.14), $I(Q^2) \to -\kappa^2/4$. While the low-energy part of the integrand in $I(Q^2)$ (namely, $g_1 \propto \sigma_{1/2} - \sigma_{3/2}$) is dominated by the resonance region, the high-energy part is very sensitive to Regge dynamics, such as the nature of Pomeron. A number of predictions exist for the high energy behavior of $\sigma_{1/2} - \sigma_{3/2}$, ranging from a constant in the case of a scalar Pomeron, to a $\sim \ln \nu / \nu$ dependence for non-perturbative two-gluon exchange (soft Pomeron) [69], to $\sim 1/\ln^2 \nu$ behavior for a two-Pomeron cut contribution [70]. While there exist some data to constrain the extrapolations to high ν in the perturbative region at larger $Q^2(\sim 10\ \mathrm{GeV}^2)$, nothing at all is known about the Q^2 dependence of this quantity at low Q^2, especially in the preasymptotic regime. At a 12 GeV JLab one can measure the Q^2 dependence of the Regge description and study the transition between Regge dynamics and perturbative QCD.

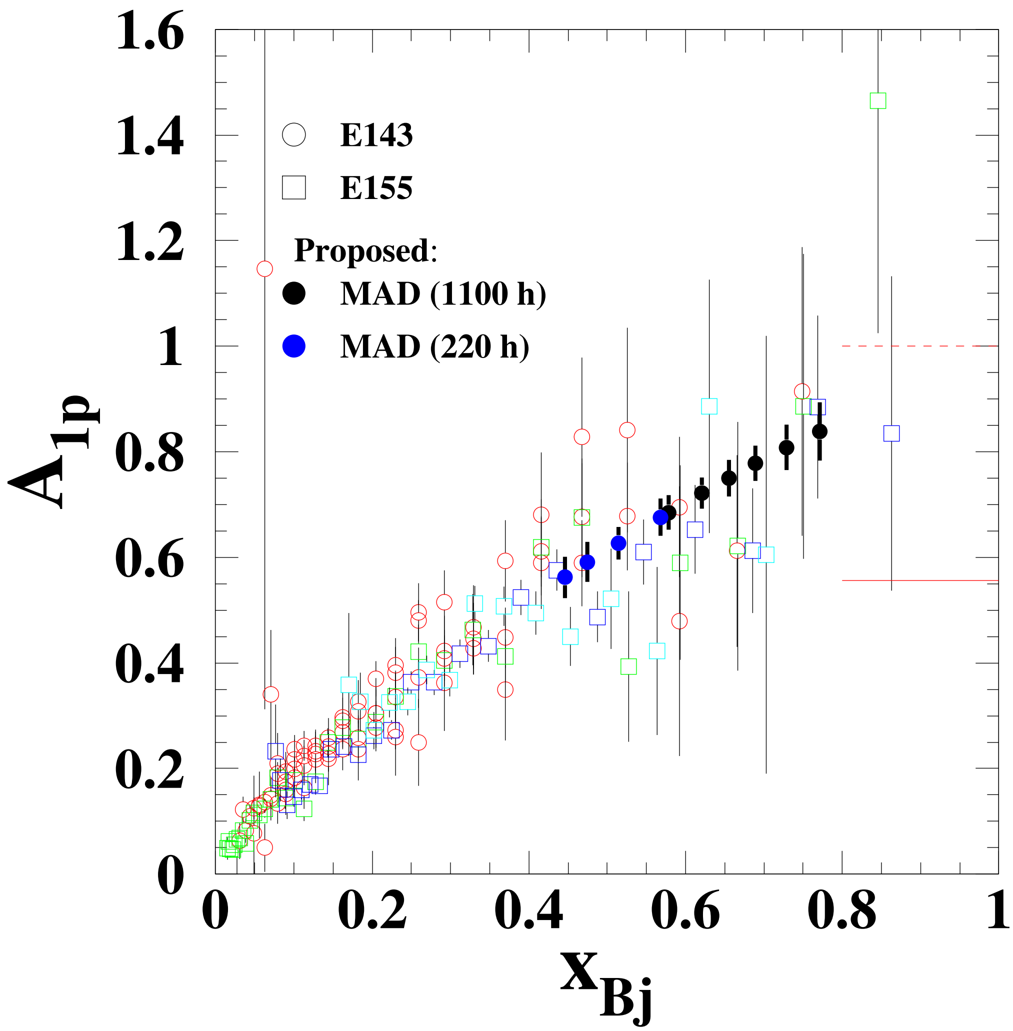

Figure 3.2: A_1^p from SLAC E143 and E155 experiments and projected errors for Hall A with an 11 GeV electron beam and the MAD spectrometer. Only statistical errors are shown. The dashed red line on the right side of the graph shows the pQCD limit for A_1^p as $x_{Bj} \to 1$; the solid line is the limit for SU(6) symmetry preserving models.

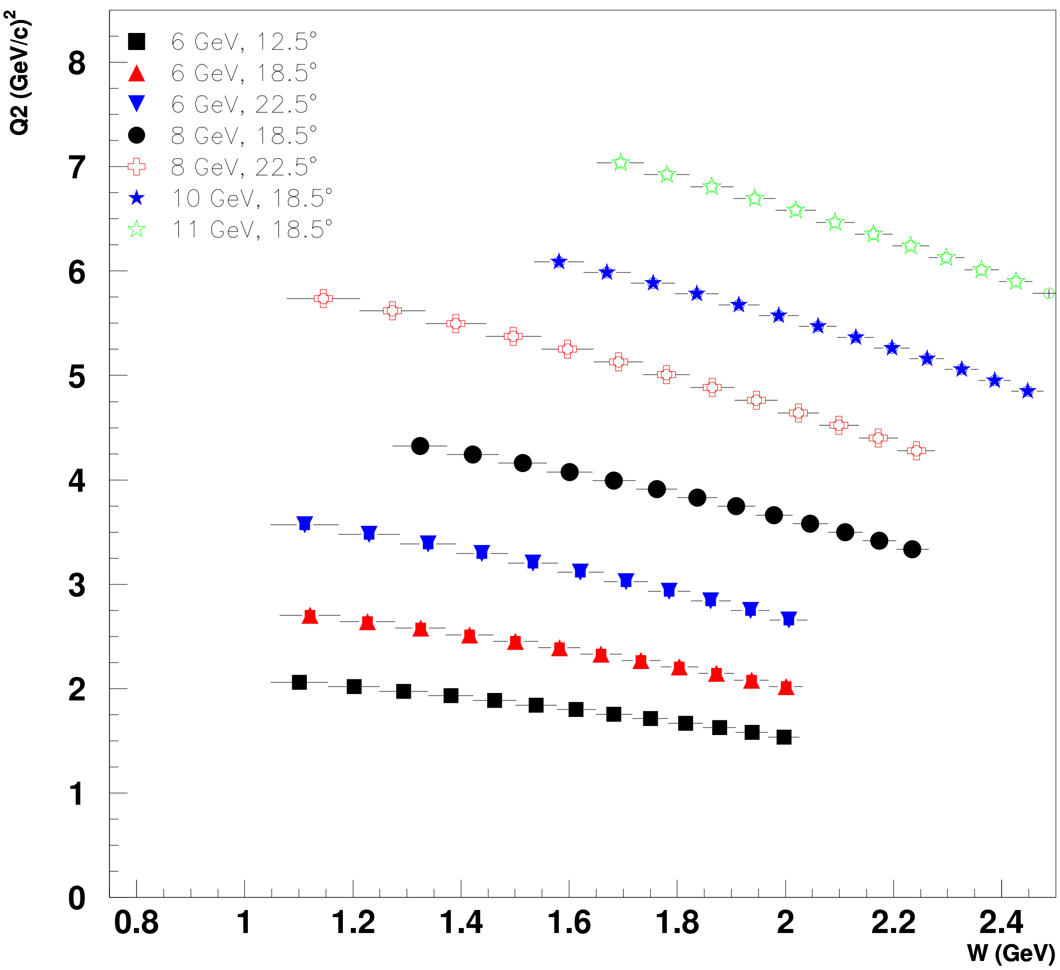

Figure 3.3: The proposed Q^2 and W coverage for spin structure function measurements of the proton and the neutron in the resonance region using the 11 GeV beam and the MAD spectrometer.

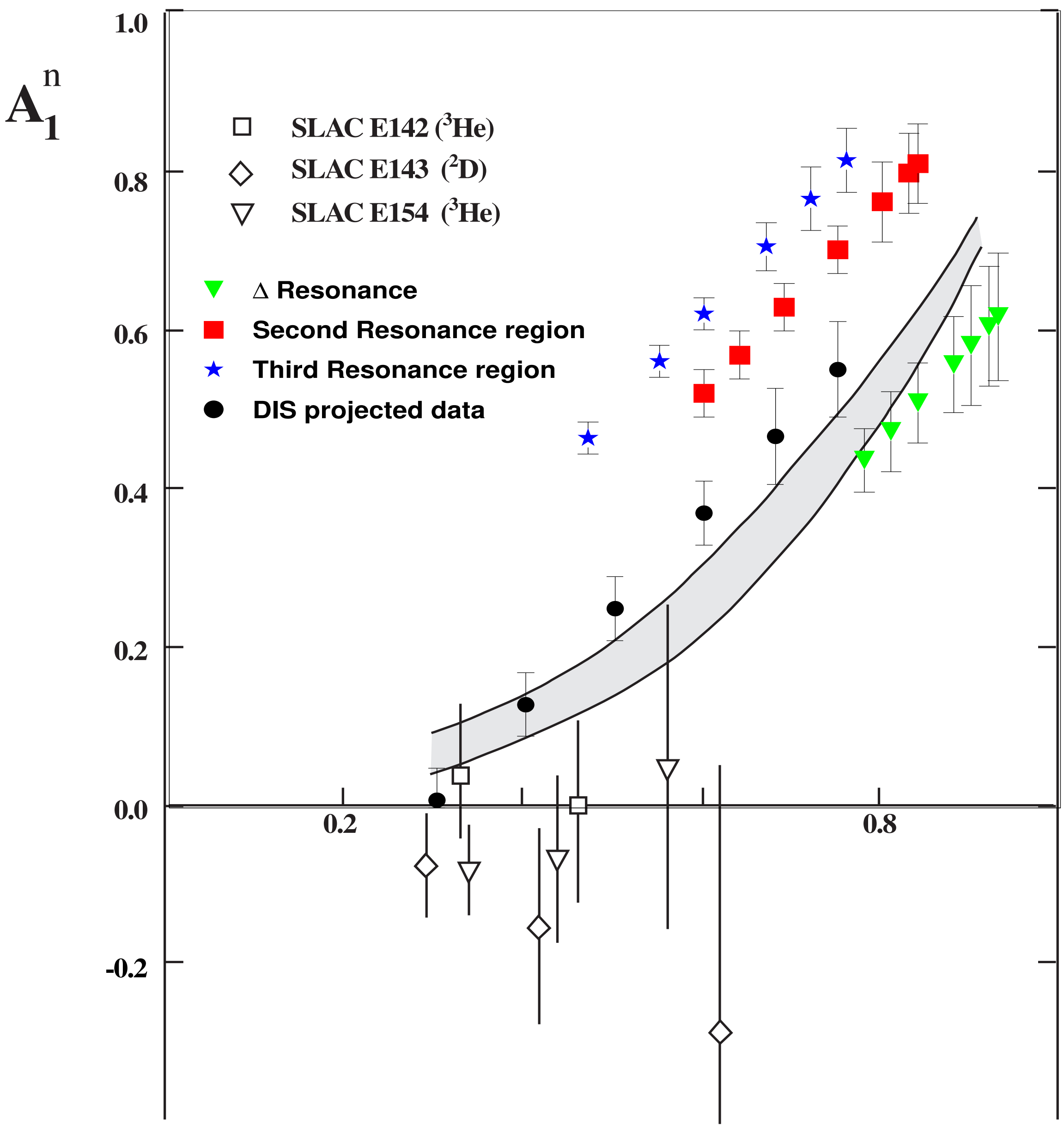

Figure 3.4: The projected data for the proposed measurement in the three resonance regions. Note that the values of A_1^n for the three resonance regions have been shifted by different offsets to ensure clarity. The solid circles show the projected data for DIS with 12 GeV beam at Jefferson Lab.

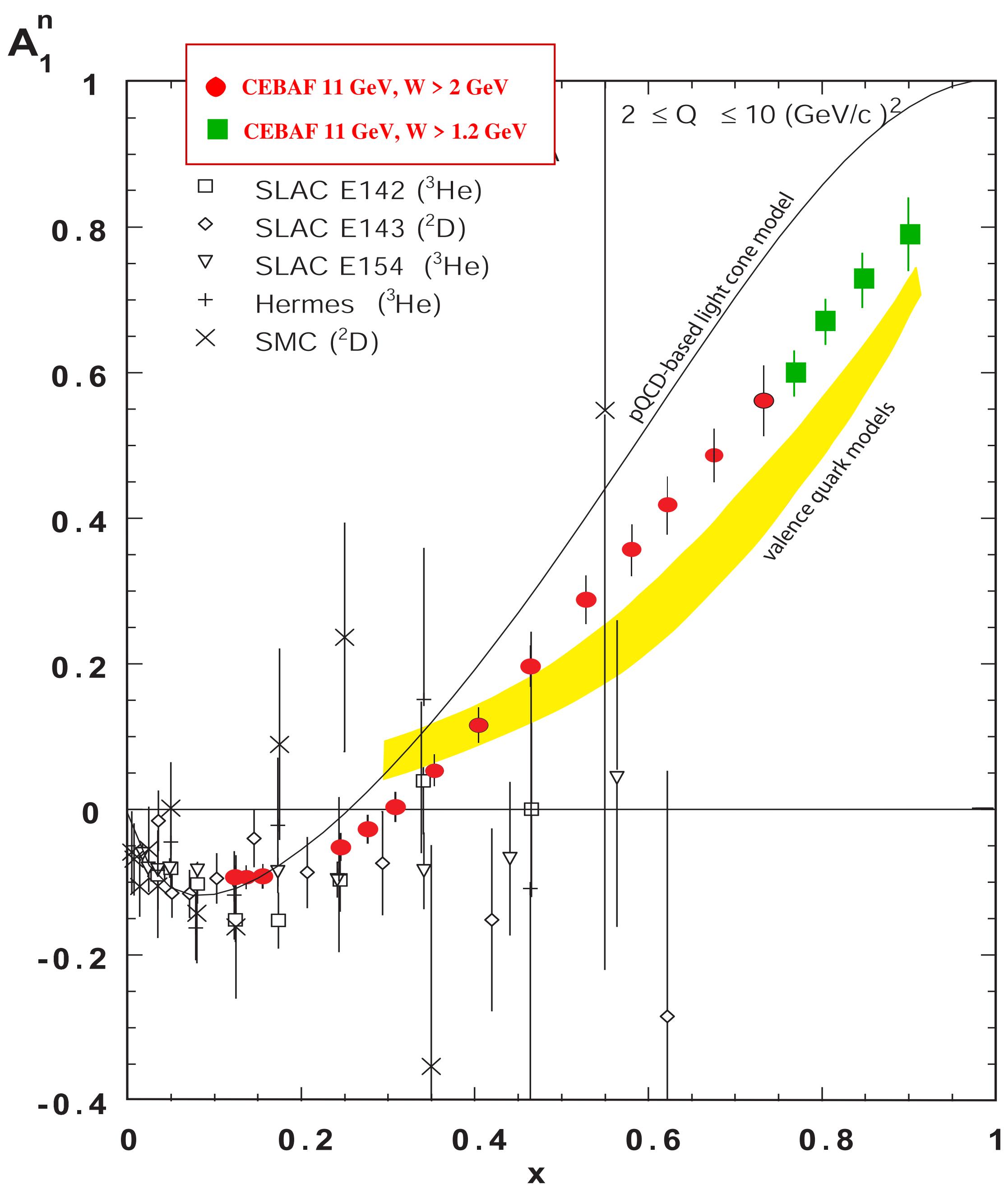

Figure 3.5: Projected data for a measurement of A_1^n in the large x_{Bj} region. The red filled circles are for the data in the DIS region ($W > 2$ GeV), while the filled diamonds show the possibility of extending the measurement to higher x_{Bj} by relaxing the invariant mass cut.

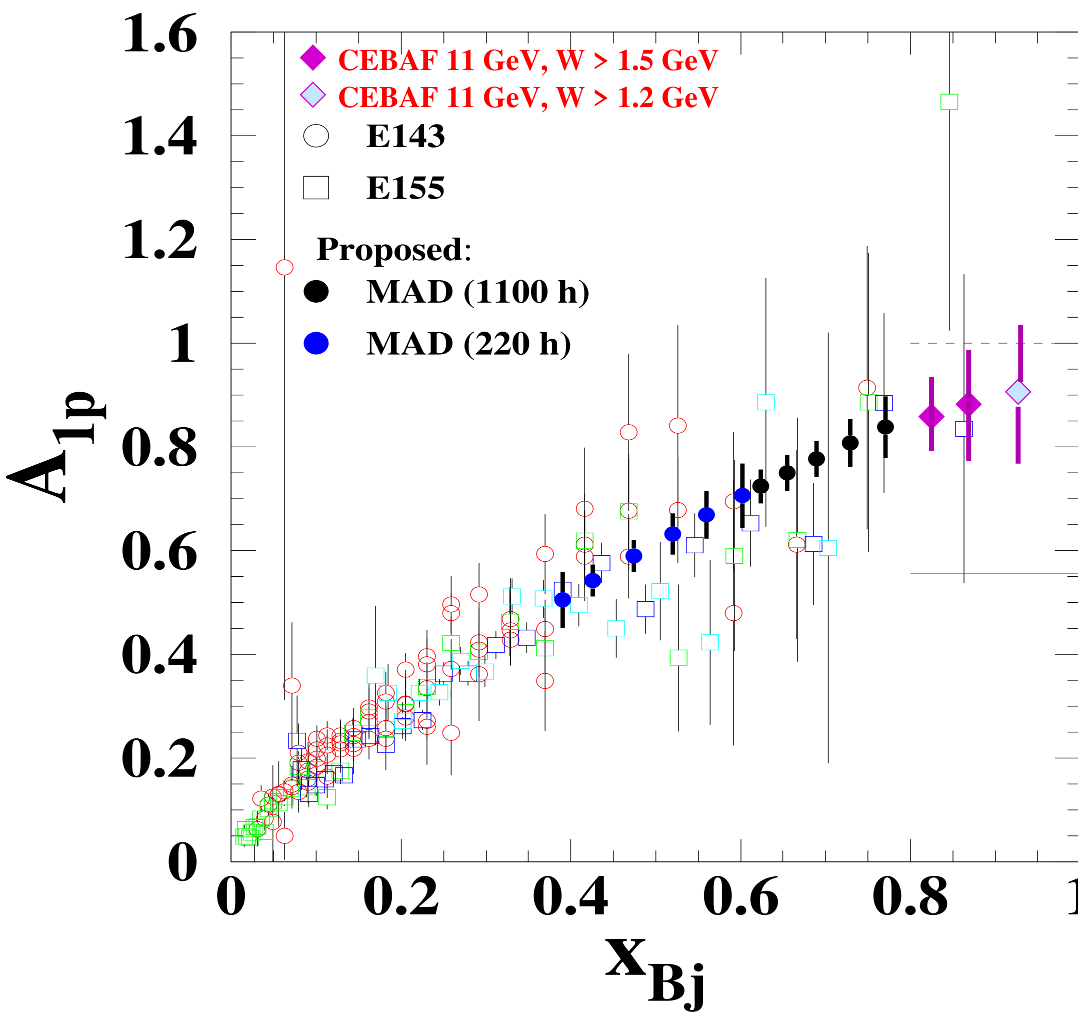

Figure 3.6: Projected data for a measurement of A_1^p in the large x_{Bj} region. The filled circles are for the data in the DIS region ($W > 2$ GeV), while the filled diamonds show the possibility of extending the measurement to higher x_{Bj} by relaxing the invariant mass cut.

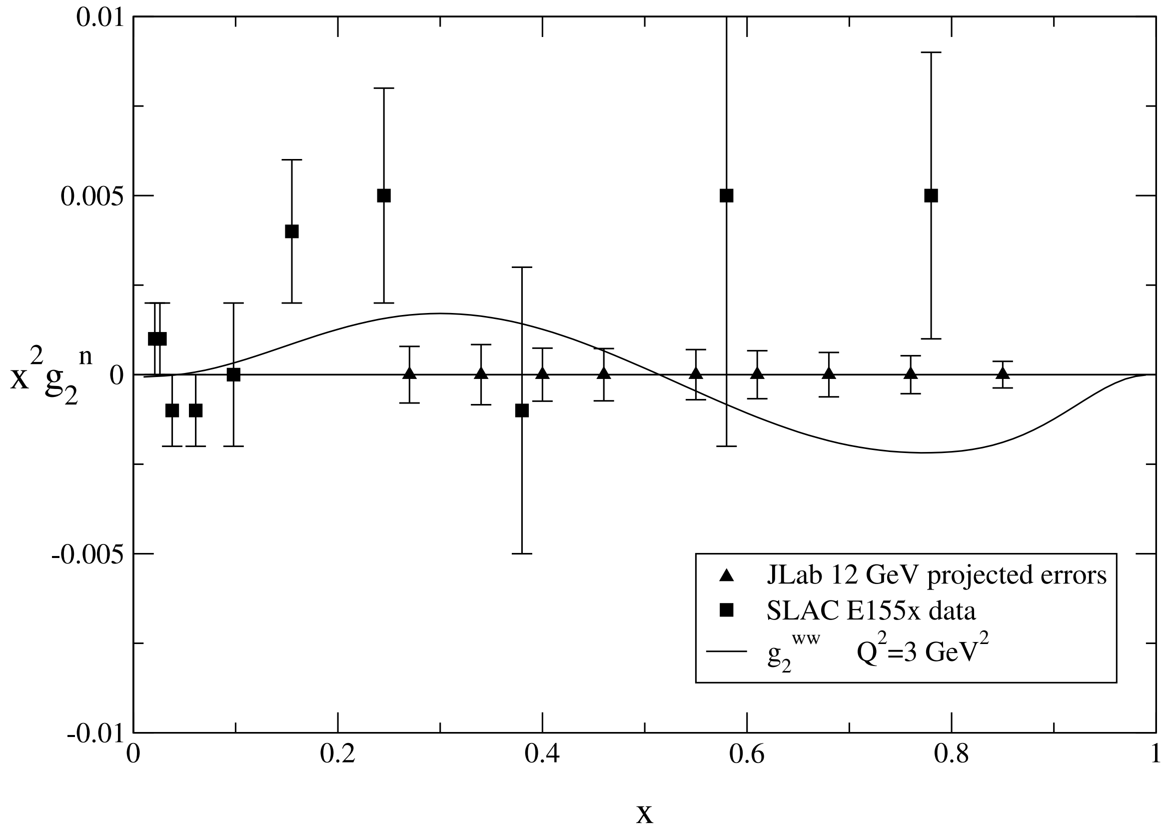

Figure 3.7: Measure values for $x_{Bj}^2 g_2^n$ from experiment E155x at SLAC and projected errors from a 12 GeV measurement at Jefferson Lab. Also shown is the twist-2 prediction, g_2^{WW}.

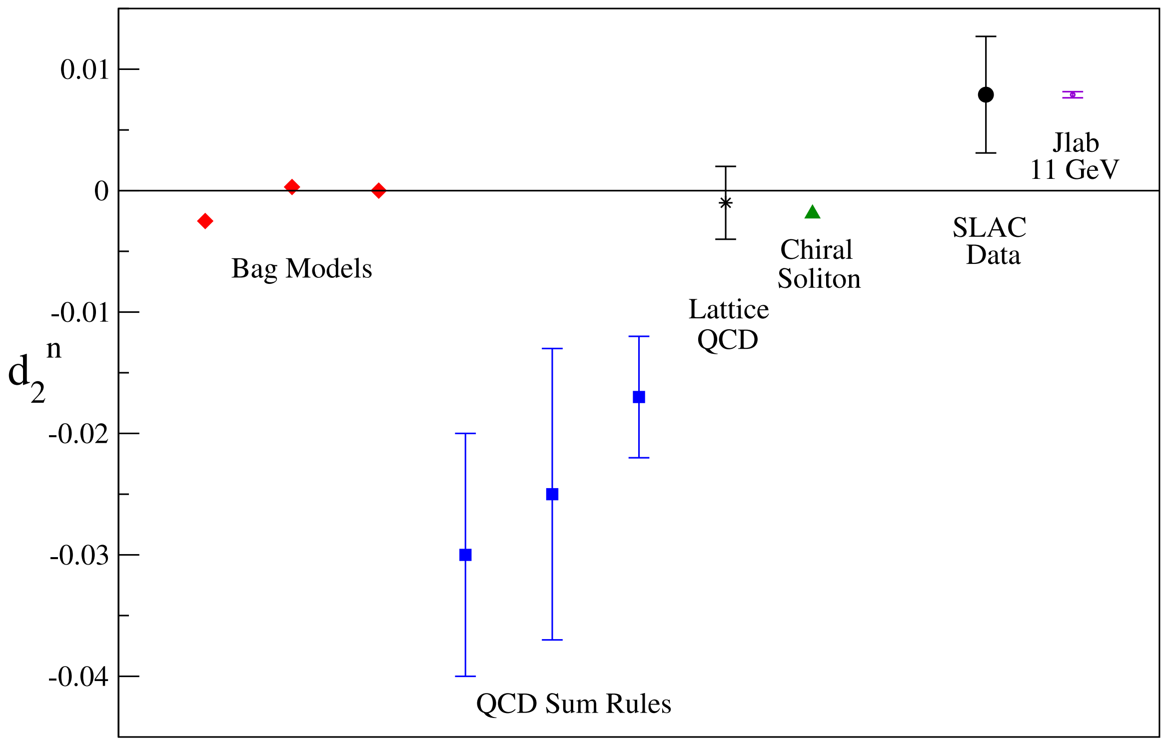

Figure 3.8: Various theoretical models for the neutron twist-3 matrix element d_2^n along with the measured value from SLAC and the expected error from a measurement at 12 GeV at Jefferson Lab (shown at the value of the SLAC measurement).

3.2 Semi-inclusive processes

3.2.1 Introduction

Semi-inclusive deep inelastic scattering, in which a hadron h is detected in the final state in addition to the scattered electron, offers a tremendous opportunity for determining the spin and flavor structure of the nucleon, as well as extracting information on new distributions which are not accessible in inclusive scattering. A comprehensive program of semi-inclusive measurements in Hall A with a 12 GeV CEBAF has the potential to significantly enrich our understanding of the workings of QCD at relatively low energy.

In the quark-parton model, the cross section for the process $eN \to e'hX$ is given as a product of quark distribution functions in the nucleon, $q(x_{Bj})$, and quark fragmentation functions $D_q^h(z)$ [71],

$$\frac{d\sigma^{eN\to e'hX}}{dx_{Bj}dz} \equiv Y_N^h(x_{Bj}, z) \;\; \propto \;\; \sum_q e_q^2 \; q(x_{Bj}) \; D_q^{(}z) \; , \tag{3.16}$$

where e_q is the charge of quark flavor q. The kinematic variable $z = E_h/\nu$ is the fraction of the energy of the struck quark carried by the produced hadron in the target rest frame. Measurements of specific hadronic final states allow for spin and flavor separation of quark distribution functions [72, 73, 74], providing sensitive tests for the quark structure of the nucleon. In addition, an entire family of new quark distribution functions, such as those sensitive to T-odd effects which cannot be observed in inclusive reactions, become accessible in semi-inclusive experiments [75].

The probability that the produced meson originated from the struck quark, and not from a $q\bar{q}$ pair produced from the vacuum, can be maximized by restricting measurements to large values of z. In this way high momentum fragments of deep-inelastic nucleon breakup statistically tag the underlying quark structure. On the other hand, semi-inclusive cross sections at large values of x_{Bj} and z are small, requiring the highest possible luminosity, while the detection of two particles in the final state requires an electron beam with a high duty cycle. These factors make Hall A at a 12 GeV CEBAF a unique facility for studying semi-inclusive electroproduction reactions.

One of the most important and exciting discoveries of the past decade concerning the structure of the nucleon came with the observation that the sea quarks in the proton are not symmetric, but that there is a significant excess of $\bar{d}$ antiquarks over $\bar{u}$ in the proton [76, 77, 78, 79]. Naive expectations from gluon bremsstrahlung into $q\bar{q}$ pairs, which is the dominant process of sea quark creation at high Q^2, were that this perturbatively generated sea would be equally populated by $u\bar{u}$ and $d\bar{d}$ pairs. The large asymmetry observed between $\bar{u}$ and $\bar{d}$ highlighted the crucial role played by non-perturbative physics in both the valence and sea structure of the proton. Many theoretical explanations of this effect focussed on the role of dynamical chiral symmetry breaking and the associated pion cloud of the nucleon in the generation of the flavor asymmetry [80]. Since the long-range structure of the proton is dominated by the emission and reabsorption of a virtual π^+, $p \to n + \pi^+ \to p$, scattering from the virtual π^+ meson, which contains a valence $\bar{d}$ antiquark, will naturally lead to an excess of $\bar{d}$ over $\bar{u}$ in the proton [81]. Indeed, the existence of an asymmetry was subsequently demonstrated from QCD on the basis of chiral symmetry breaking, independent of dynamical assumptions about quark-gluon interactions [82].

On the other hand, the magnitude and x_{Bj} dependence of the $\bar{d} - \bar{u}$ asymmetry is more difficult to understand from QCD, especially at larger x_{Bj} ($x_{Bj} \sim 0.2 - 0.4$), where the asymmetry becomes smaller and the error bars larger. In particular, the downward trend of the $\bar{d}/\bar{u}$ ratio observed in the Drell-Yan data [79] presents a serious challenge to theoretical models [83], and other mechanisms may be necessary to accurately represent the shape of the asymmetry [84, 85]. For example, because there are more valence u quarks than d in the proton, the Pauli Exclusion Principle would suggest that creation of $u\bar{u}$ pairs should be suppressed relative to $d\bar{d}$ [86, 1]. The experimental asymmetry may then be a combination of two (or more) effects [84].

The best way to disentangle these effects on the antiquark distributions is to consider the spin dependence of the asymmetry. Since pions have spin zero, scattering from a virtual pion cloud of the nucleon will not contribute to the helicity distributions $\Delta\bar{u}$ or $\Delta\bar{d}$ (higher order contributions, or those associated with scattering from heavier, spin 1 mesons are negligibly small [87, 88, 89]). On the other hand, the effects of quark antisymmetrization are expected to be as large or larger in the spin-dependent asymmetry $\Delta\bar{u} - \Delta\bar{d}$ as in the unpolarized $\bar{d}-\bar{u}$ asymmetry [90, 91, 92]. Preliminary data from HERMES [93] suggests that the distributions $\Delta\bar{d}$ and $\Delta\bar{u}$ are rather small, and consistent with zero within overall errors. If confirmed, this would suggest that the dominant mechanism underlying the generation of the proton sea is associated with dynamical chiral symmetry breaking, and that effects from antisymmetrization may be small [94, 95, 96]. However, the errors on the difference $\Delta\bar{u} - \Delta\bar{d}$, which is most sensitive to non-perturbative effects such as meson clouds (perturbative contributions arising from gluon bremsstrahlung largely cancel in the difference) are rather large, and better quality data in the range $0.1 \leq x_{Bj} \leq 0.4$ would be extremely valuable in drawing firm conclusions. As illustrated below, measurement of semi-inclusive production of $\pi^{\pm}$ with unpolarized and polarized electron beam and target at 11 GeV JLab kinematics will significantly improve our knowledge of the x_{Bj} dependence of both the flavor asymmetry $\bar{d}/\bar{u}$ and the polarization asymmetries $\Delta\bar{u}$ and $\Delta\bar{d}$.

The role of dynamical chiral symmetry breaking in the structure of the nucleon can also be probed directly, by measuring the structure function of the pion in semi-inclusive DIS from a proton target with a spectator neutron. The x_{Bj} dependence of the quark distributions in the pion is an essential ingredient in models of the spin-flavor asymmetries in the proton sea. There are existing data from Drell-Yan measurements of π^- on heavy nuclei from Fermilab [97] and CERN [98]. More recently, measurements at HERA have attempted to access the pion structure function at very low x_{Bj}, with rather surprising findings that the total sea in the pion is significantly larger than expected [99]. At the same time there is an unresolved question about the consistency of the Drell-Yan data [97] with predictions for the $x_{Bj} \to 1$ behavior based on perturbative QCD [100], which appear to be borne out for the proton but not for the pion. It is crucial therefore to obtain accurate data on the valence and sea components of the pion structure function over a large range of x_{Bj}.

While Hall A at 11 GeV can make significant inroads into unraveling the spin and flavor content of the proton sea, a unique contribution can also be made in determining the behavior of the spin dependent valence distributions at large x_{Bj}. The large x_{Bj} behavior of spin dependent distributions dictates the $x_{Bj} \to 1$ limit of the inclusive polarization asymmetries A_1^n and A_1^p. Current data, however, are unable to distinguish between even the most basic SU(6) symmetric predictions, $A_1^n = 0$ and $A_1^p = 5/9$, and the expectations from pQCD, namely $A_1^n \to 1$, $A_1^p \to 1$ as $x_{Bj} \to 1$. Measurements of the asymmetries A_1^n and A_1^p at $x_{Bj} \leq 0.8$ at 11 GeV will enable one to clearly establish where the deviations from SU(6) appear.

On the other hand, non-perturbative models which incorporate SU(6) breaking typically lead to a suppression of d quarks relative to u [11, 15, 16]. Consequently, these models also predict that $A_1^{n,p} \to 1$ as $x_{Bj} \to 1$, making it difficult to discriminate between the broken SU(6) and pQCD behaviors from inclusive measurements alone. This is unfortunate, since the behavior of the polarized d quark distribution is predicted to be qualitatively different: $\Delta d/d \to 1$ in pQCD, but $\Delta d/d \to -1/3$ in broken SU(6), so that even the sign is unknown. By tagging $\pi^{\pm}$ mesons in the final state at large z, one can disentangle the individual Δu and Δd distributions at large x_{Bj}. There are indications from HERMES data of a positive trend for $\Delta u/u$ with increasing x_{Bj}, while $\Delta d/d$ appears to stay below zero out to $x_{Bj} \sim 0.4$. Semi-inclusive data from Hall A will enable measurements to be extended to $x_{Bj} \sim 0.8$, and more definitively test whether Δd stays negative, or starts to display the characteristic behavior predicted from pQCD.

If one in addition tags charged kaons in the final state, then the polarized strange component of the nucleon can be probed. A large negative value of Δs was postulated as an explanation for the small value of the total proton spin carried by quarks observed in inclusive g_1^p experiments, which subsequently prompted the so-called "spin-crisis" [9]. Preliminary semi-inclusive data from HERMES [93] suggest a rather small and even positive value of Δs, which would favor an explanation of the proton "spin-crisis" in terms of a large positive gluon polarization, or suggest the need to re-examine assumptions about SU(3) flavor symmetry made in the analysis. A small value of Δs would be compatible with the null results obtained thus far from MIT-Bates and the HAPPEX experiment in Hall A on the strange electric and magnetic form factors of the proton. It would also be consistent with the expectations from models of the nucleon in which the strangeness content is represented by a kaon cloud [101, 43, 102], which yield small values for both Δs and the strangeness form factors [103]. Measurement of $\Delta s/s$ in Hall A at 11 GeV would thus provide an important complementary set of experiments to the strangeness form factor program from parity-violating electron scattering at Jefferson Lab.

Although inclusive measurements can provide some information on the unpolarized and polarized quark distributions, information on the transversity distribution, $\delta q(x_{Bj}, Q^2)$, which gives the net transverse polarization of quarks in a transversely polarized nucleon, can only be obtained from reactions involving at least one additional hadron. While there exist a number of lattice calculations of the lowest moment of the transversity distribution [104], nothing is known about the transversity distribution empirically. Measurements of the transversity distribution would complete the determination of all the leading twist parton distributions in the nucleon. Because the transversity is chirally odd, its measurement requires an additional chirally odd amplitude in the process, such as a chiral odd fragmentation function in semi-inclusive scattering [105]. Observation of a single-spin azimuthal asymmetry in semi-inclusive pion production from a transversely polarized target would provide the first clear signal of the transversity distribution. Furthermore, since the transversity is believed to be valence quark dominated, its measurement in the region of medium and large x_{Bj} values is ideally suited for Jefferson Lab with an 11 GeV beam.

Before proceeding to the details of the proposed experiments, one needs to address the question of factorization at an energy upgraded JLab. At beam energies $\leq$ 11 GeV, one may question whether the quark-parton model is applicable for semi-inclusive reactions and whether the 'current fragmentation' and 'target fragmentation' regions can be cleanly separated. Indeed, it remains an open question, although recent experiments at HERMES [78] and Jefferson Lab [106, 107] indicate that factorization of the electroproduction cross sections and spin asymmetries into z-dependent fragmentation and x_{Bj}-dependent distribution parts does appear to take place at energies lower than previously believed. Another indication may come from theoretical calculations [108] of pion electroproduction at high transverse momentum, which points out that the estimated virtuality of the gluon exchanged in the short-range process at 11 GeV beam energy is equivalent to the one for the elastic pion form factor at $Q^2 \leq 35$ GeV^2. Such a large scale is probably sufficient for perturbative QCD to determine the dynamics of the process.

Ultimately the question of where factorization is valid must be resolved experimentally. Factorization can be easily tested by comparing the x_{Bj} dependence of the extracted quark distributions at several different values of z. In addition, one can test the z-independence of particular ratios of π^+ and π^- yields on proton and neutron targets in which the fragmentation dependence cancels if Eq. (3.16) holds. The degree to which this cancellation occurs, and factorization holds, can be accurately determined at an energy upgraded CEBAF. Moreover, with the large Q^2 range available with an 11 GeV beam it will be possible to accurately map out the transition from coherent production to the region where single quark fragmentation dominates, and clearly establish the limits of a partonic description of electroproduction. This will also enable one to test whether the concept of quark-hadron duality is valid in semi-inclusive reactions, which may then allow the analysis of the semi-inclusive cross sections in terms of single quark scattering and fragmentation to be extended to lower energies.

At a beam energy of 11 GeV, the accessible kinematic regions in the (x_{Bj}, Q^2) and (x_{Bj}, W^2) planes for an $(e, e'h)$ measurement are shown in Fig. 3.9(a) and (b). Constant electron angle (θ_e) lines are plotted from 10° to 60° in addition to the constant $\vec{q}$ angle (θ_q) lines. In order to stay in the deep inelastic region at the highest possible W, the center of the fragmentation cone will be limited to a very forward angle. A combination of the MAD spectrometer as the electron arm and the exiting HRS spectrometer (plus the SEPTUM magnet for 6° and 9° configuration) as the hadron arm will be a typical arrangement. While the capability for MAD to access 15° scattering angle while keeping a reasonable solid angle (15 msr) is preferred, more forward angle for the MAD spectrometer with a significantly reduced solid angle is necessary for certain physics cases.

The key experiments of the semi-inclusive program that can be performed using the combination of the Hall A high-resolution spectrometer and the planned MAD spectrometer include: a) Probing flavor asymmetry of the light-quark sea in the nucleon; b) Flavor separation of polarized distributions for the light and strange quarks in the nucleon; c) Studies of the pion structure functions; and d) Measuring transversity distributions of the nucleon, which are discussed in more detail in the following sections.

Before we discuss these key experiments, it is essential to demonstrate that factorization holds experimentally.

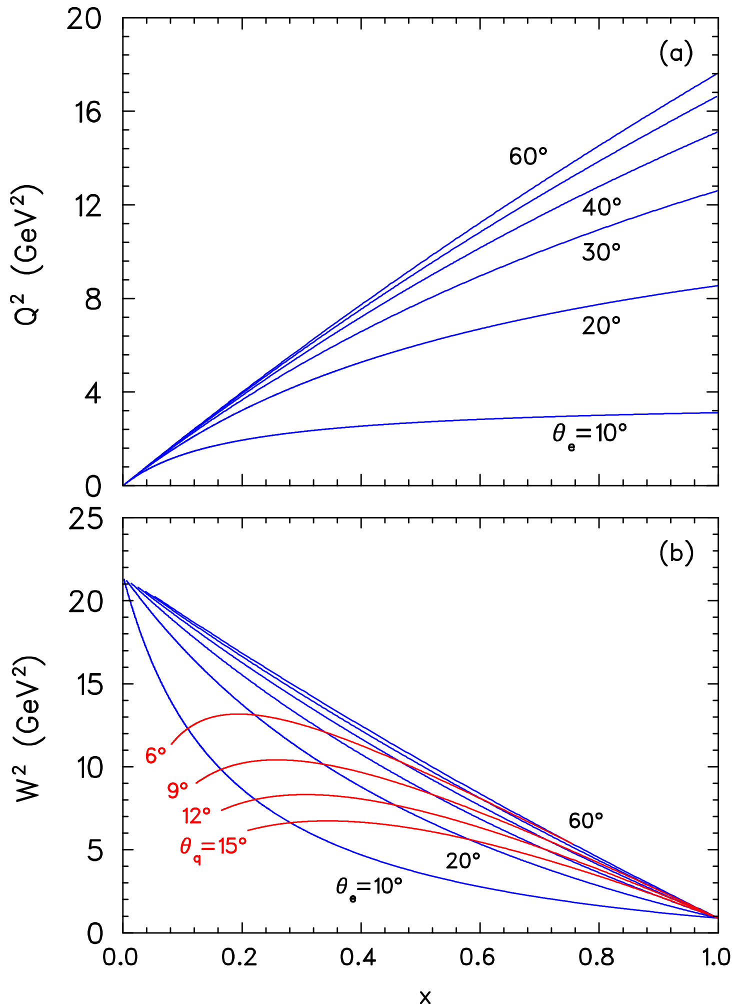

Figure 3.9: Accessible kinematic region for an $(e, e'h)$ measurement at 11 GeV.

3.2.2 Experimental demonstration of factorization

The demonstration of factorization should be the first step in the experimental program of semi-inclusive measurements. The extent to which factorization applies is an open question which can only be answered by experiment. Quantitative measurements on several clean observables should be made to give clear indications on how well factorization holds. If factorization can be shown to hold at a reasonable level, information on quark distributions can be extracted with confidence. In the case that an independent factorization applies between the virtual photon-quark hard scattering process and the hadronization of the struck quark, quark fragmentation functions can be shown to cancel each other in certain combinations of pion production ratios. The z-independent behavior of such ratios can serve as clear indications of the onset of factorization.

Assuming isospin symmetry and charge conjugation invariance, the number of light quark to charge pion fragmentation functions is reduced to two type: the favored (D^+) and the unfavored (D^-) fragmentation functions:

$$D^+ \equiv D_u^{\pi^+} = D_d^{\pi^-} = D_{\bar{u}}^{\pi^-} = D_{\bar{d}}^{\pi^+}, \tag{3.17}$$

$$D^- \equiv D_u^{\pi^-} = D_d^{\pi^+} = D_{\bar{u}}^{\pi^+} = D_{\bar{d}}^{\pi^-}, \tag{3.18}$$

and only one type of fragmentation function (D^0) for light quark to neutral pion fragmentation:

$$D^0 \equiv D_u^{\pi^0} = D_d^{\pi^0} = D_{\bar{u}}^{\pi^0} = D_{\bar{d}}^{\pi^0}. \tag{3.19}$$

Neglecting heavy quark contributions while considering the valence region only, in semi-inclusive $(e, e'\pi^\pm)$ reaction, if four independent yields ($Y_p^{\pi^+}, Y_p^{\pi^-}, Y_n^{\pi^+}$ and $Y_n^{\pi^-}$) are determined, two ratios can be formed in which the fragmentation functions cancel out:

$$t_1(x) = \frac{Y_p^{\pi^+}(x,z) + Y_p^{\pi^-}(x,z)}{Y_n^{\pi^+}(x,z) + Y_n^{\pi^-}(x,z)} = \frac{4u(x) + d(x) + 4\bar{u}(x) + \bar{d}(x)}{4d(x) + u(x) + 4\bar{d}(x) + \bar{u}(x)}, \tag{3.20}$$

$$t_2(x) = \frac{Y_p^{\pi^+}(x,z) - Y_p^{\pi^-}(x,z)}{Y_n^{\pi^+}(x,z) - Y_n^{\pi^-}(x,z)} = \frac{4u(x) - d(x) - 4\bar{u}(x) + \bar{d}(x)}{4d(x) - u(x) - 4\bar{d}(x) + \bar{u}(x)}. \tag{3.21}$$

We have left out the explicit Q^2 dependence for clarity. Furthermore, if π^0 events can be reconstructed with reasonable resolutions using a calorimeter, another z-independent ratio can be formed:

$$t_3(x) = \frac{Y_p^{\pi^0}(x,z)}{Y_n^{\pi^0}(x,z)} \equiv t_1(x). \tag{3.22}$$

Clearly, observation of the z-scaling behavior of t_1, t_2 and t_3 will be a strong indication of factorization.

With a polarized beam and a polarized target, double spin asymmetries can also be used as indications of factorization. For example, with a target polarized along $\vec{q}$ direction, double spin asymmetry of π^0 production ($A_{LL}^{\pi^0}$) should be independent of z and equal to the inclusive asymmetry A_1. Furthermore, one can form two helicity asymmetries from the yield sum and difference of charged pion production in which the fragmentation functions cancel out:

$$A_{LL}^+(x) = \frac{(Y^{\pi^+}(x,z) + Y^{\pi^-}(x,z))_{\lambda_e=+1} - (Y^{\pi^+}(x,z) + Y^{\pi^-}(x,z))_{\lambda_e=-1}}{(Y^{\pi^+}(x,z) + Y^{\pi^-}(x,z))_{\lambda_e=+1} + (Y^{\pi^+}(x,z) + Y^{\pi^-}(x,z))_{\lambda_e=-1}}, \tag{3.23}$$

$$A_{LL}^{-}(x) = \frac{(Y^{\pi^+}(x,z) - Y^{\pi^-}(x,z))_{\lambda_e=+1} - (Y^{\pi^+}(x,z) - Y^{\pi^-}(x,z))_{\lambda_e=-1}}{(Y^{\pi^+}(x,z) - Y^{\pi^-}(x,z))_{\lambda_e=+1} + (Y^{\pi^+}(x,z) - Y^{\pi^-}(x,z))_{\lambda_e=-1}}. \tag{3.24}$$

If factorization is strictly applied , both A_{LL}^{+} and A_{LL}^{-} should be independent of z. In addition, one expect that $A_{LL}^{+}(x) = A_{LL}^{\pi^0}(x) = A_1(x)$.

3.2.3 Probing the light quark sea flavor asymmetry with semi-inclusive charged pion production

A benchmark measurement for the semi-inclusive studies is the determination of the light quark sea flavor asymmetry in the nucleon [73]. By measuring π^+ and π^- DIS yields on hydrogen and deuterium targets, the HERMES collaboration demonstrated sensitivity to the sea flavor asymmetry comparable to the E866 measurement at Fermilab with the Drell-Yan process [78, 79], though in a very different Q^2 region. Nuclear corrections to the neutron distributions extracted from the deuteron data are typically less than 1–2% for $x_{Bj} \sim 0.1$–0.4 [84]. Defining the ratio $r(x_{Bj}, z)$ of the difference of $\pi^{\mp}$ yields for the proton and neutron,

$$r(x_{Bj}, z) \;=\; \frac{Y_p^{\pi^-}(x_{Bj}, z) - Y_n^{\pi^-}(x_{Bj}, z)}{Y_p^{\pi^+}(x_{Bj}, z) - Y_n^{\pi^+}(x_{Bj}, z)}\ , \tag{3.25}$$

the antiquark asymmetry can be determined via [73]:

$$\frac{\bar{d}(x_{Bj}) - \bar{u}(x_{Bj})}{u(x_{Bj}) - d(x_{Bj})} \;=\; \frac{J(z)(1 - r(x_{Bj}, z)) - (1 + r(x_{Bj}, z))}{J(z)(1 - r(x_{Bj}, z)) + (1 + r(x_{Bj}, z))}\ , \tag{3.26}$$

where $J(z) = 3/5(1+D^-/D^+)/(1-D^-/D^+)$, and D^+ and D^- are the favored and unfavored fragmentation functions, respectively, as defined in Eqs. (3.17,3.18) (Here and in subsequent equations the explicit Q^2 dependence of the quark distribution and fragmentation functions is omitted for clarity.) At large z the unfavored fragmentation is strongly suppressed, $D^- \ll D^+$. At an 11 GeV incident electron beam energy, Jefferson Lab has unique advantages to perform such a measurement: fixed targets allow significantly higher luminosity than available at HERMES, and the kinematics allow a probe of the high x_{Bj} region, where the asymmetry is poorly known. A precision determination of the asymmetry at high x_{Bj} will provide stringent constraints on nucleon structure models, which give rise to rather different predictions for $x_{Bj} > 0.3$ [84, 85].

An important assumption in the extraction of parton distributions is factorization of the deep-inelastic process, Eq. (3.16). In the sea flavor asymmetry measurement one will check the validity of this hypothesis by examining the dependence of the extracted parton distribution difference on the pion momentum fraction, z. With the high luminosity available at Jefferson Lab, a detailed separation of the x_{Bj} and z dependence of the pion production cross-section becomes possible, allowing independent determinations of parton distributions, fragmentation functions and factorization properties.

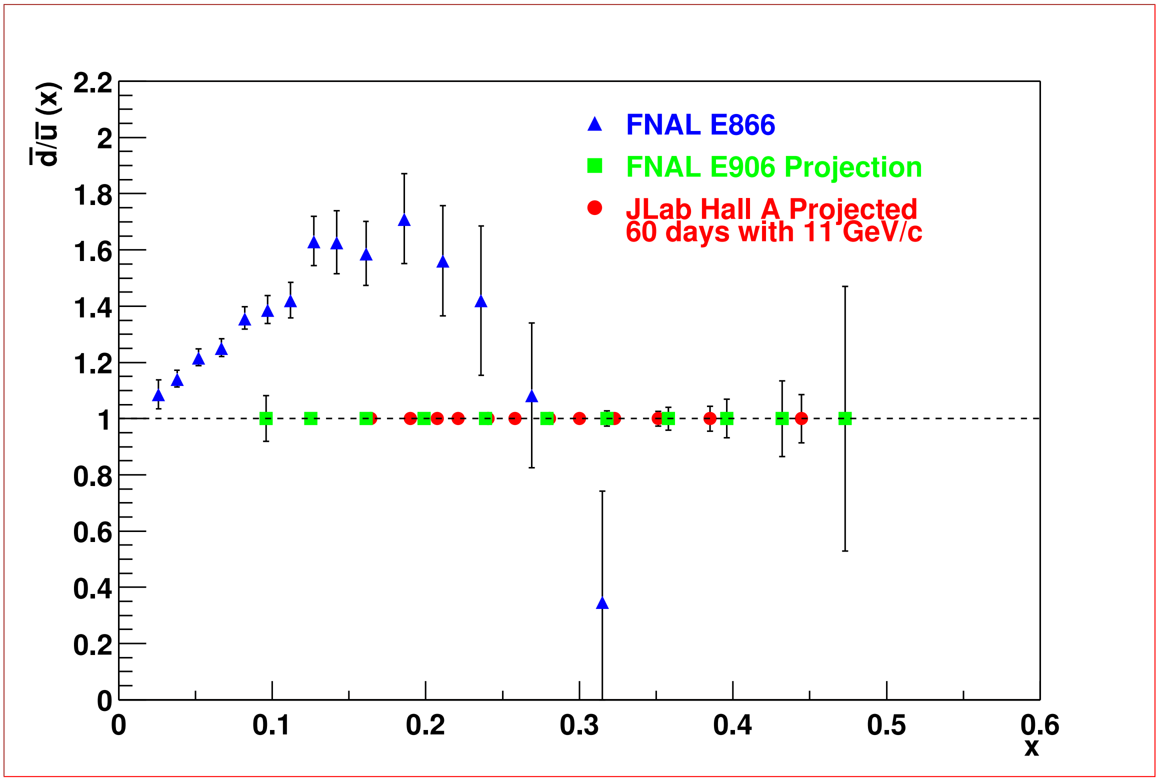

Figure 3.10: The projected precision of $\bar{d}/\bar{u}$ extractions at Hall A with an 11 GeV incident electron beam. The published measurement of E866 [79] as well as the E906 projection are plotted for comparison [109]. Only statistical uncertainties are shown.

The possible sensitivity at the Jefferson Lab Hall A with an 11 GeV/c beam has been explored. The projection uses a Monte Carlo [110] simulation based on the CTEQ low-Q^2 parton distribution parameterizations [111], the LUND string fragmentation model [112], and a model of the expected acceptance in Hall A. The measurement will scatter 70 μA of 11 GeV/c electron beam from a liquid hydrogen (deuterium) target with a target length of 30 cm corresponding to a thickness of 2(5) g/cm^2, giving a luminosity of 5.3(13)$\times 10^{38}$ Nucleons/cm^2. The proposed MAD spectrometer captures scattered electrons up to 7 GeV/c; it is positioned far forward at 12°, with a 6 msr solid angle acceptance. The MAD spectrometer magnet will be set to central momenta p_e= 4.5 and 6 GeV/c with an assumed $\pm$15% momentum window. These settings probe an average (x_{Bj}, Q^2 (GeV^2), W^2 (GeV^2)) of (0.21, 2.6, 10.5) and (0.36, 3.4, 7.0). Coincident pions will be detected in the Hadron arm HRS positioned at –12°. To allow a significant range in z, three hadron arm magnet settings may be used: p_π= 2.0, 3.0, and 3.8 GeV/c. The hadron momentum window covers $\pm$ 5%, and positive and negative pions are detected in separated runs. A ring imaging Čerenkov detector may separate pions cleanly from kaons and protons. The typical semi-inclusive DIS coincident pion rate from hydrogen in one of these configurations is 350 Hz with an average pion z of 0.53. Projected uncertainties on the extraction of $\bar{d}/\bar{u}$ are presented in Figure

3.10. A sixty-day measurement period, which incorporates nine days of calibration, target changes, and spectrometer magnet field value and polarity changes, is assumed. Also shown in Fig. 3.10 is the projection of a Drell-Yan measurement using the FNAL main injector at 120 GeV [109].

A study of the light quark sea flavor asymmetry in the high x_{Bj} region with precision significantly exceeding the E866 measurement is achievable in Jefferson Lab Hall A. Though the incident electron energy is lower than that available at HERMES, the larger scattering angle allows an exploration of a similar Q^2 range with higher precision. The average Jefferson Lab Q^2 is much smaller than the average of the E866 data and the possible future Drell-Yan measurements using the FNAL main injector, giving a sensitivity to possible Q^2 dependence in the sea flavor asymmetry. This measurement would allow a simple, high statistics exploration of factorization at 11 GeV/c. A successful measurement opens a window to considerably more physics opportunities. Further study of kaon production gives direct sensitivity to s quark and $\bar{s}$ antiquark distributions. Also, a detailed investigation of the x_{Bj} and z dependence of hadron yields from nuclear targets accesses both the quark flavor dependence of the EMC effect and also the influence of hadron attenuation in the nuclear medium. With polarized targets, the quark flavor structure of the nucleon spin distribution is accessible.

3.2.4 Probing the quark flavor structure of the nucleon spin distribution from $\vec{N}(\vec{e}, e'\pi^{\pm})$ process

While unpolarized semi-inclusive meson production provides a means of extracting spin-averaged quark and antiquark distributions in the nucleon, semi-inclusive production with a *polarized* beam on a *polarized* target offers the prospect of determining the spin-dependence of the individual quark species. Furthermore, by comparing semi-inclusive data with inclusive DIS measurement, one can directly test the degree to which flavor SU(3) symmetry holds in DIS processes. At large Q^2, the spin asymmetry A_1^h for the production of a hadron h by a polarized virtual photon on a polarized nucleon can be written [113]:

$$A_1^h(x_{Bj}, z) \quad = \quad P_e \cdot P_T \cdot \frac{y(1-\frac{1}{2}y)}{1-y+\frac{1}{2}y^2} \cdot \frac{\sum_q e_q^2\ \Delta q(x_{Bj}) D_q^h(z)}{\sum_q e_q^2\ q(x_{Bj}) D_q^h(z)}\ . \tag{3.27}$$

Measurement of π^+ and π^- (or $K^{\pm}$) mesons from proton or neutron targets, together with knowledge of the unpolarized distributions $q(x_{Bj})$, allows one then to extract from Eq. (3.27) information on the spin-dependent distributions $\Delta q(x_{Bj})$ and $\Delta\bar{q}(x_{Bj})$.

Assuming the use of the regular Hall C polarized NH_3 target and the Hall A polarized ^{3}He target in their standard configurations, a total of 1000 hour measurements on each target at $z = E_\pi/\nu = 0.40 \sim 0.5$ in each setting will yield statistical uncertainties on $A_1^{\pi^+}$ and $A_1^{\pi^-}$, as shown in Fig. 3.11. The measurement time is arranged such that similar statistical accuracies can be achieved for $A_1^{\pi^+}$ and $A_1^{\pi^-}$. The MAD spectrometer, as the electron arm, will be located at $15° \sim 23°$, at a central momentum of $3.20 \sim 4.54$ GeV/c. The geometrical acceptance of MAD is assumed to be $10 \sim 20$ msr, depending on its angle. The momentum acceptance of MAD is assumed to be ±10%. One existing Hall A HRS spectrometer, as the hadron arm, will be located at $6^\circ \sim 14.5^\circ$, at a central momentum of $1.60 \sim 4.30$ GeV/c. The geometrical acceptance of HRS is taken as 5 msr, and its momentum acceptance is taken as ±4.5%. The Q^2 range is $2.40 \sim 7.90$ GeV^2, the W range is $2.25 \sim 3.62$ GeV, and the W' range is $1.80 \sim 2.86$ GeV. The extraction of the neutron asymmetry from the ^{3}He asymmetry takes into account the standard nuclear corrections due to the polarization of the protons in ^{3}He and Fermi smearing and nuclear binding corrections, as in the case of the inclusive polarization asymmetries.

With the existing RICH detector in the HRS providing PID for charged kaons, asymmetries of $A_1^{K^+}$ and $A_1^{K^-}$ can be measured in the same setting, the statistical uncertainties will be about twice as large. Using the same data set, inclusive asymmetries can also be formed with high statistics, leaving the accuracy of the $A_1(p)$ and $A_1(^3\text{He})$ measurement dominated by systematic uncertainties. The large momentum acceptance and solid angle of the MAD spectrometer combined with the high density of the polarized targets will provide us the opportunity of high precision measurements of double-spin asymmetries. Assuming factorization has been demonstrated, the "purity" method which has been used by the HERMES collaboration can be used to extract the quark polarization distributions from the measured semi-inclusive asymmetries [113]. The expected statistical accuracies, based on 1000 hour measurements with each polarized target, are shown in Fig. 3.12 together with the HERMES published results [113] for comparison. Clearly, these measurements at a 12 GeV JLab would make significant inroads in our understanding of the distribution of quark and antiquark spin in the nucleon.

3.2.5 The pion structure function

As the pseudo-Goldstone boson associated with the spontaneous breaking of the chiral symmetry of QCD, the pion plays a special role in nuclear physics. It has long been known that the longest range part of the nucleon–nucleon force in nuclei is described by one pion exchange. Because of its small mass, the effects of the pion on hadron structure at large distances can be systematically quantified via chiral perturbation theory. On the other hand, because it is also an eigenstate of QCD, the pion itself has substructure which can be revealed by a high energy probe. Indeed, the deep inelastic scattering on the pion cloud of the nucleon leads to the observed excess of $\bar{d}$ antiquarks over $\bar{u}$ in the proton sea, as discussed above. An important related question is: What is the structure of the pion itself?

While the valence quark content of the pion is obviously different from that of the nucleon, an important question is whether the structure of the pion sea is similar to that of a nucleon. Recently, measurements of the pion structure function at very low x_{Bj} have been performed at HERA [99], which have led to two unexpected findings: (1) the sea in the pion has the same shape in x_{Bj} as the sea in the proton, and (2) the pion sea has approximately 1/3 of the magnitude of the sea in the proton. This latter result is especially surprising since from quark counting rules one expects the pion sea to be $\sim 2/3$ of that in the proton. Some chiral quark models [114] predict that the pion sea should in fact carry a larger momentum fraction than the proton sea.

At the same time, data on the structure of the pion at larger x_{Bj} has also left a number of unresolved puzzles. For instance, the $x_{Bj} \to 1$ behavior of the valence quark distributions in the pion is predicted from perturbative QCD to be $(1 - x_{Bj})^2$ [100], whereas pionic Drell-Yan data suggest an exponent ≈ 1 [97]. Recently a number of theoretical model analyses have attempted to explain the pion structure function in the valence region, using the Nambu–Jona-Lasinio model [115, 116], and the Dyson-Schwinger approach [117]. Typical agreement with the pion structure function is shown in Fig. 3.13, where the prediction from the Dyson-Schwinger calculation is compared with the Drell-Yan data. In a model-independent approach, several low moments of the pion structure function have also been determined in lattice QCD [118], and future calculations of higher moments may allow the structure of the pion to be understood from first principles.

In the meantime, however, new measurements of the pion structure function over a large range of x_{Bj} may shed light on these issues, both at large and small values of x_{Bj}. With the 12 GeV upgrade at Jefferson Lab measurements could be made in the valence region, and compared with existing pion Drell-Yan data, which would verify the technique used by the HERA experiments to measure the pion structure function. Furthermore knowledge of the pion structure function at high x_{Bj} may enable us to provide constraints on the pion form factor at high Q^2, which is difficult to access experimentally [119, 120].

The pion structure function can be measured by exploiting the Sullivan process [121], illustrated in Fig. 3.14, where the charge exchange reaction eliminates backgrounds from diffractive scattering. Contributions from the ρ or heavier mesons must also be accounted for before information on the pion structure function can be extracted, however, because of their higher masses these will be suppressed relative to the π. Furthermore, by restricting the kinematics to low t one can minimize the theoretical uncertainties in extrapolating to the pion pole.

The key to the experimental technique is to measure the low-energy outgoing neutron in coincidence with the scattered electron. A simulation of a possible experiment in Hall A with the 11 GeV beam, the MAD spectrometer, a neutron counter, a 4 cm LH2 target, and a 0.6 μA unpolarized beam for 25 days of beam time is shown in Fig. 3.15.

The MAD spectrometer to detect electrons in coincidence with the neutrons detected in a plastic scintillator detector is assumed. Two possible MAD angles (15° and 22°) to access two different Q^2 regions are discussed below.

MAD at 15°.

Assumed solid angle for MAD at 15° is 15 msr. Electron singles rates are expected to be about 80 Hz. Central electron momentum of 2.5 GeV/c and a momentum acceptance of ±15% is assumed. Accessible Q^2 is about 1.5 (GeV/c)^2. The expected e^-/π^- ratio is about 1/100 (in the worst case). For a 0.6 μA beam with 4 cm LH2 target, the real coincidence rates expected is 0.075 Hz and accidental coincidence rate in a 50 ns timing window is about 0.05 Hz, giving an estimated signal to noise ratio of about 1.5:1. Time used for the 15° points is 5 days. Figure. 3.16 gives the kinematic coverage at $Q^2 = 1.5$ (GeV/c)^2.

MAD at 22°.

Assumed solid angle for MAD at 22° is 21 msr. Electron singles rates are expected to be about 30 Hz. Central electron momentum of 2 GeV/c and a momentum acceptance of

$\pm 15\%$ is assumed. Accessible Q^2 is about 3.0 (GeV/c)^2. For a 0.6 μA beam with 4 cm LH2 target, the real coincidence rates expected is 0.01 Hz and accidental coincidence rate in a 50 ns timing window is about 0.02 Hz, giving an estimated signal to noise ratio of about 1:2. Time used for the 15° points is 20 days. Figure. 3.17 gives the kinematic coverage at $Q^2 = 3.0$ (GeV/c)^2.

3.2.6 Transversity measurements

In addition to the unpolarized and polarized quark distributions, $q(x_{Bj}, Q^2)$ and $\Delta q(x_{Bj}, Q^2)$, a third quark distribution, called transversity, is the remaining twist-2 distribution yet to be measured. This helicity-flip quark distribution, $\delta q(x_{Bj}, Q^2)$, can be described in QPM as the net transverse polarization of quarks in a transversely polarized nucleon. The corresponding structure function is given by

$$h_1(x_{Bj}, Q^2) = \frac{1}{2}\sum_i e_i^2 \delta q_i(x_{Bj}, Q^2). \tag{3.28}$$

Due to the chiral-odd nature of the transversity distribution, it can not be measured in inclusive DIS experiments. In order to measure $\delta q(x_{Bj}, Q^2)$, an additional chiral-odd object is required. For example, the double spin asymmetry, A_{TT}, for Drell-Yan cross section in transversely polarized pp collision, is sensitive to transversity since $A_{TT} \sim \sum_i e_i^2 \delta q_i(x_1)\delta \bar{q}_i(x_2)$. Such a measurement could be carried out at RHIC[122], although the anticipated effect is small, on the order of $1 - 2\%$.

Several other methods for measuring transversity have been proposed for semi-inclusive DIS. In particular, Collins suggested[105] that a chiral-odd fragmentation function in conjunction with the chiral-odd transversity distribution would lead to an observable single-spin azimuthal asymmetry in semi-inclusive pion production. An analysis of the jet structure in $Z^\circ \rightarrow 2$ jets decay suggested that the Collins function has a sizable magnitude[123].

The HERMES collaboration has recently measured[124, 125] single-spin azimuthal asymmetry for charged and neutral pion electroproduction. Using unpolarized positron beam on a longitudinally polarized hydrogen target, the cross section was found to have a sinϕ dependence, where ϕ is the azimuthal angle between the pion and the (e, e') scattering plane. This Single-Spin-Asymmetries (SSA) can be expressed as the analyzing power in the sinϕ moment, and the result is shown in Fig. 3.18 for π^+, π^-, and π° as a function of the pion fractional energy z, the Bjorken x_{Bj}, and the pion transverse momentum $P_\perp$. The sinϕ moment for an unpolarized (U) positron scattered off a longitudinally (L) polarized target contains two main contributions

$$\begin{aligned} \langle sin\phi \rangle \quad & \alpha \quad S_L \frac{2(2-y)}{Q\sqrt{1-y}} \sum_q e_q^2 x_{Bj} h_L^q(x_{Bj}) H_1^{\perp,q}(z) \\ & + \quad S_T(1-y) \sum_q e_q^2 x_{Bj} h_1^q(x_{Bj}) H_1^{\perp,q}(z), \end{aligned} \tag{3.29}$$

where S_L and S_T are the longitudinal and transverse components of the target spin orientation with respect to the virtual photon direction. For the HERMES experiment with a longitudinally polarized target, the transverse component is nonzero with a mean value of $S_T \approx 0.15$. The observed azimuthal asymmetry could be a combined effect of the h_1 transversity and the twist-3 h_L distribution. Figure 3.18 shows that a model calculation[126, 127] reproduces the z, x_{Bj}, and $P_\perp$ dependences of the π° asymmetry quite well. The striking difference between the π^+ and π^- analyzing power suggests that the Collins fragmentation function is sizable only when the flavor of the struck quark is present in the final hadron.

If the azimuthal asymmetry observed by HERMES is indeed caused by the h_1 transversity, a much larger asymmetry is expected for a transversely polarized target. An earlier SMC measurement had limited statistics and was inconclusive[128]. The HERMES Collaboration plans to measure the shape of $\delta u(x_{Bj})$ (and $H_1^{\perp,u}(z)$) using a transversely polarized proton target in 2002-03. A proposal to measure $\delta d(x_{Bj})$ using a transversely polarized deuterium target has also been discussed[129].

The 12 GeV upgrade at JLab offers several unique opportunities to study the nucleon transversity distributions. These opportunities include:

- The transversely polarized ^3He target at Hall-A could lead to an accurate measurement of the transversity distribution in the neutron. Such a measurement probes $\delta d(x_{Bj})$ in the proton, and is complementary to the measurement of $\delta u(x_{Bj})$ being pursued at HERMES using a transversely polarized hydrogen target. It is not yet certain whether HERMES will measure transversity using transversely polarized deuterium target. Clearly, it would be of much interest to compare the results obtained from a polarized deuterium versus a polarized ^3He target.

- The higher beam intensity and the lower beam energies at JLab would provide better sensitivities for exploring the transversity distributions at larger x_{Bj}. Since the transversity is expected to be a valence-quark effect, it is important to have a good coverage at the large x_{Bj} region.

- The kinematic coverage at JLab energies allows a detailed study of the Q^2 dependence of the azimuthal asymmetries. Since both the leading-twist and the higher-twist effects could contribute to the measured asymmetry, the Q^2 dependence could help disentangling these contributions.

To evaluate the feasibility for a transversity study at Hall-A, we have considered the following two experimental configurations:

- A measurement of $e^- +^3 \vec{He} \to e^{-\prime} + \pi^\pm + x$ with two magnetic spectrometers. The first spectrometer serves as a tagging spectrometer for detecting the scattered e^-, while the second spectrometer measures the charged pions produced in the semi-inclusive DIS process.

- A measurement of $e^- +^3 \vec{He} \to e^{-\prime} + \pi^\circ + x$ with a magnetic spectrometer and an electromagnetic calorimeter. The magnetic spectrometer again serves as a tagging spectrometer for the scattered e^-, while the electromagnetic spectrometer measures the π° through the $\pi^\circ \to \gamma\gamma$ decays. Note that the HERMES experiment [125] showed that the azimuthal asymmetry for π° is comparable to that of the π^+.

We recall first the kinematic cuts employed in the HERMES analysis [125]. They are $Q^2 > 1$ GeV^2, $W > 2$ GeV, $0.2 < Z < 0.7$, and $y < 0.85$. In Fig. 3.19 we show the kinematics plots for (e, e') scattering using 11 GeV electron beam. The three curves in each plot correspond to electron scattering angles at $12.5^\circ, 25.0^\circ$, and 37.5°, respectively. A broad range of spectrometer settings could be selected which satisfy the kinematic constraints imposed in the HERMES analysis.

The azimuthal asymmetry A_T for a transversely polarized target can be written as

$$A_T(x_{Bj}, y, z) = P_T\ D_{nn}\ \frac{\sum_q e_q^2 \delta q(x_{Bj}) H_1^{\perp(1)q}(z)}{\sum_q e_q^2 q(x_{Bj}) D_1^q(z)}, \tag{3.30}$$

where P_T is the target polarization and $D_{nn} = (1-y)/(1-y+y^2/2)$ is the transverse spin transfer coefficient. $D_1^q(z)$ is the unpolarized fragmentation function and $H_1^{\perp(1)q}(z)$ is the polarized fragmentation function integrated over k_T (with suitable weight)

$$H_1^{\perp(1)q}(z) = z^2 \int d^2k_T\ \frac{k_T^2}{2M_h^2}\ H_1^{\perp(1)q}(z, z^2k_T^2). \tag{3.31}$$

Collins suggested the following parameterization:

$$H_1^{\perp(1)q}(z, z^2k_T^2) = \frac{M_C\ M_h}{M_C^2 + k_T^2} D_1^q(z, z^2k_T^2). \tag{3.32}$$

Following Ref. [129], we choose $M_C = 0.7$ GeV and a Gaussian transverse momentum dependence for the fragmentation function

$$D_1^q(z, z^2K_T^2) = D_1^q(z)\frac{R^2}{\pi z^2} exp(-R^2k_T^2), \tag{3.33}$$

where $R^2 = z^2/b^2$, and $b^2 = 0.25$ GeV^2.

We have calculated A_T as a function of x, y and z for 11 GeV electron beam energy. Typical results of a 1000 hour measurement are shown in Fig. 3.20, where the z-dependence of A_T are plotted for $x_{Bj} = 0.2$, $Q^2 = 2.5\text{GeV}^2$ and $x_{Bj} = 0.3$, $Q^2 = 3.0\text{GeV}^2$ kinematics. We assume $\delta q(x_{Bj}) = \Delta q(x_{Bj})$ in this calculation. The AAC parameterization of the polarized nucleon structure functions were used for $\Delta q(x_{Bj})$, and the CTEQ5M parameterization were used for the unpolarized structure functions. For the fragmentation functions, the parameterization of Aubert et al. [130] was adopted. We assume a typical polarized $^{15}NH_3$ target with 80% polarization, and a ^3He target of 45% polarization. The dilution factors due to the unpolarized nucleons in the target material have been taken into account. It is interesting to note that the π^- production on a polarized ^{3}He target has a much larger asymmetry with an opposite sign compare to that of the π^+ asymmetry. This trend is very different from the situation of a polarized proton target due to the contribution of d-quark transversity $\delta d(x_{Bj})$ in the neutron.

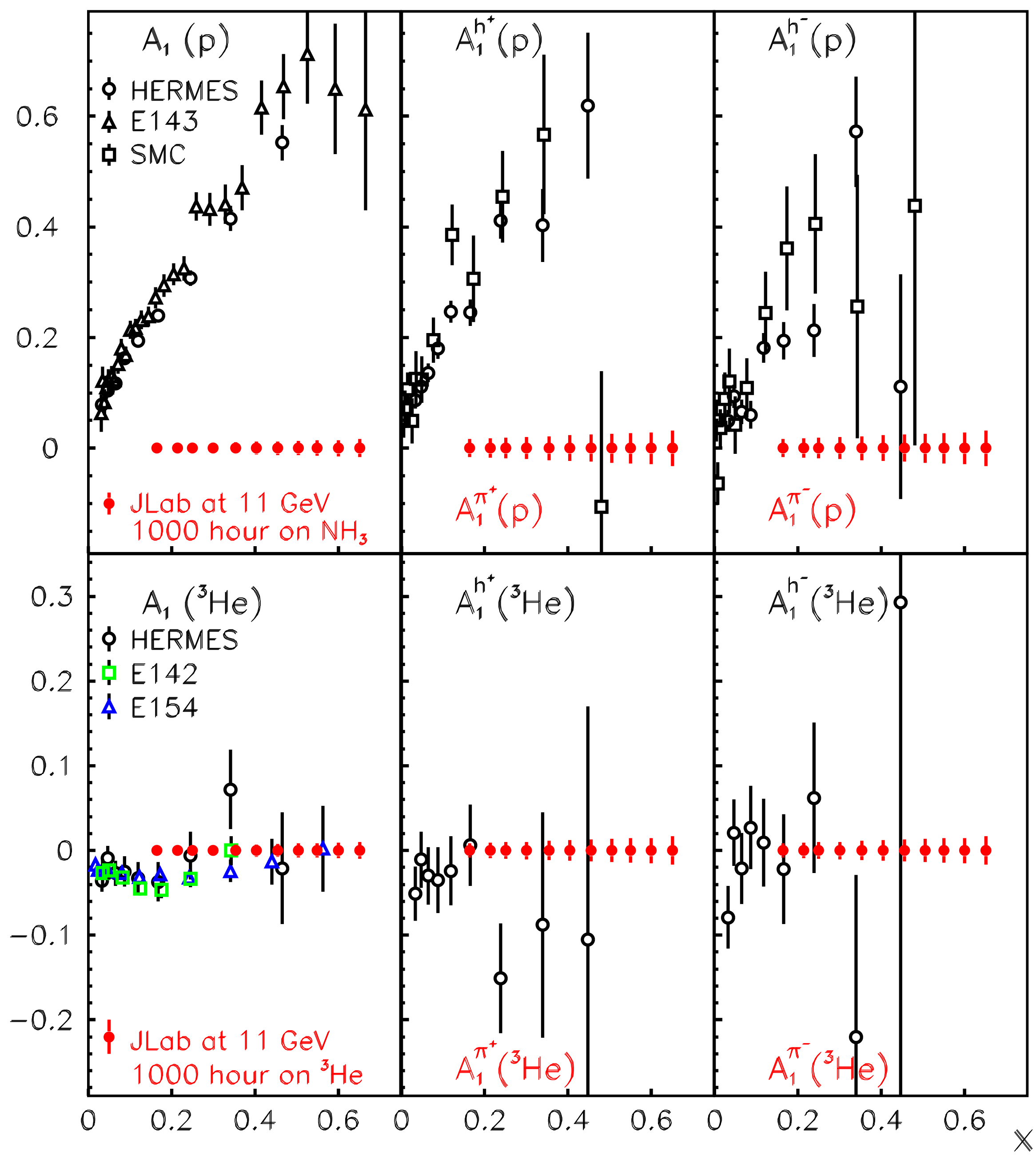

Figure 3.11: Expected semi-inclusive asymmetry measurements with polarized NH_3 and ^{3}He targets. 1000 hours of beam time is assumed for each target. Error bars are statistical only.

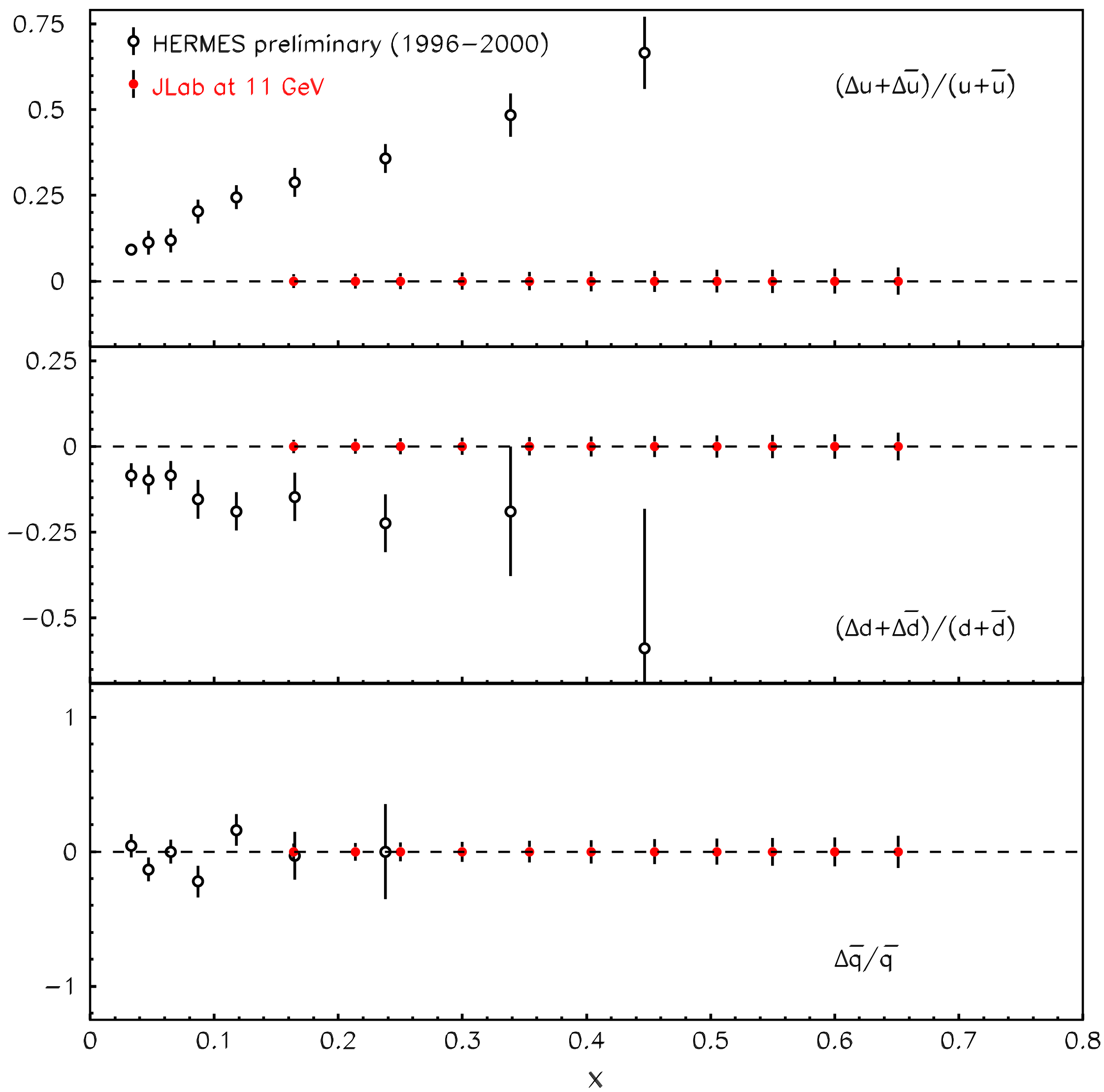

Figure 3.12: Expected results on $\frac{\Delta\bar{q}}{\bar{q}}$ from semi-inclusive asymmetry measurements with polarized NH_3 and ^3He targets. 1000 hours of beam time is assumed for each target. Error bars are statistical only.

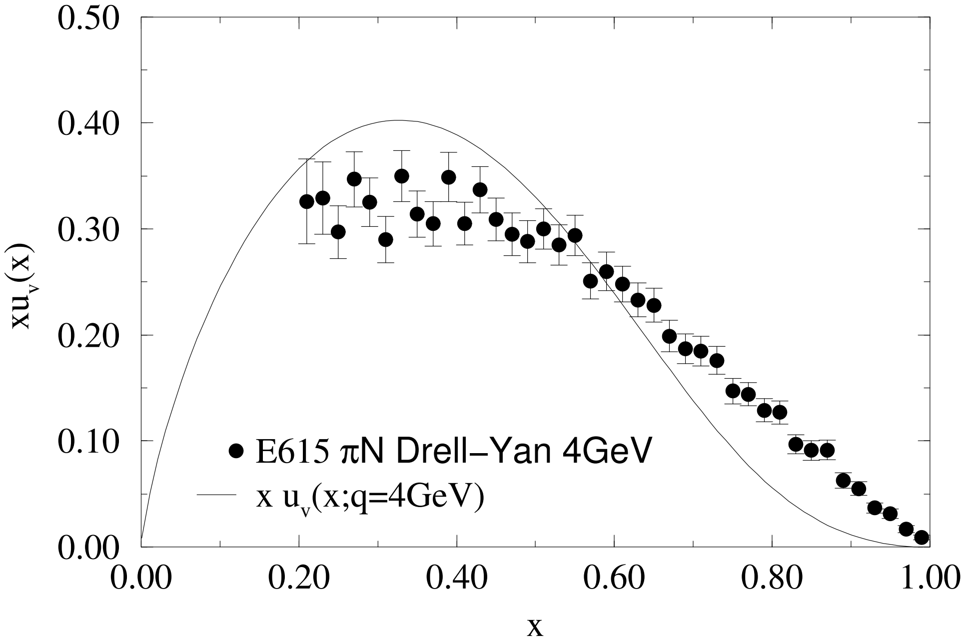

Figure 3.13: Existing data for the pion structure function from Drell-Yan scattering [97]. The solid curve represents a calculation of Hecht *et al.* [117], which is typical of treatments that describe the pion as a non pointlike bound state. There is a marked disagreement between the calculation and data at high x_{Bj}.

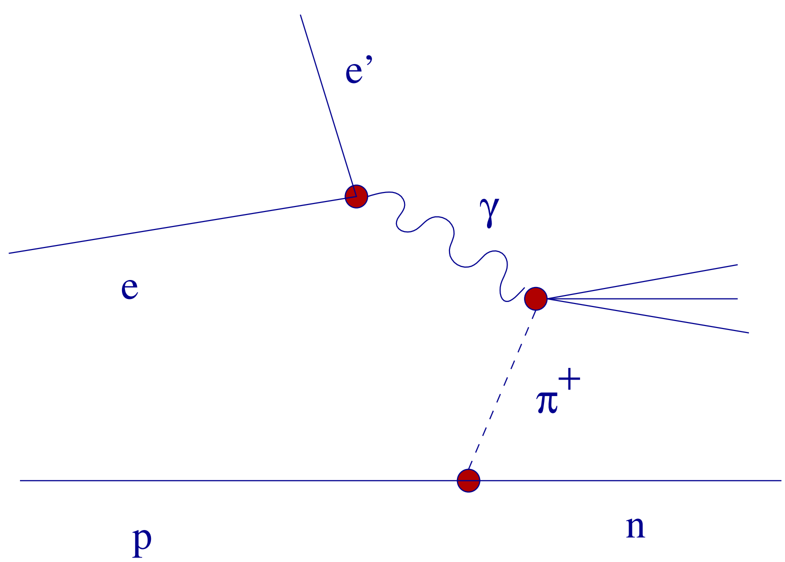

Figure 3.14: The Sullivan process: Deep inelastic scattering from the pion cloud surrounding a proton.

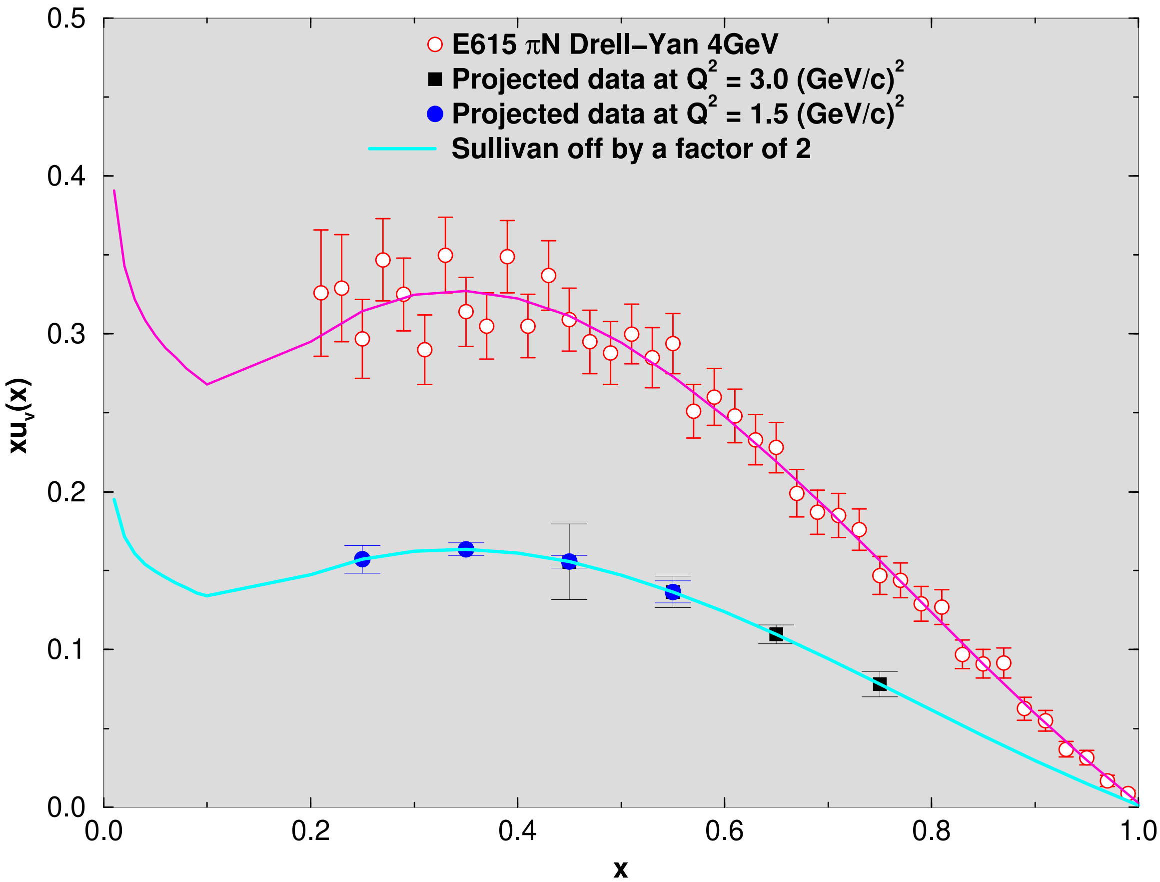

Figure 3.15: Simulated data for the pion structure function at two different Q^2 points (1.5, and 3.0 $(\text{GeV/c})^2$) using MAD spectrometer in coincidence with a low energy neutron detector at 11 GeV beam in Hall A.

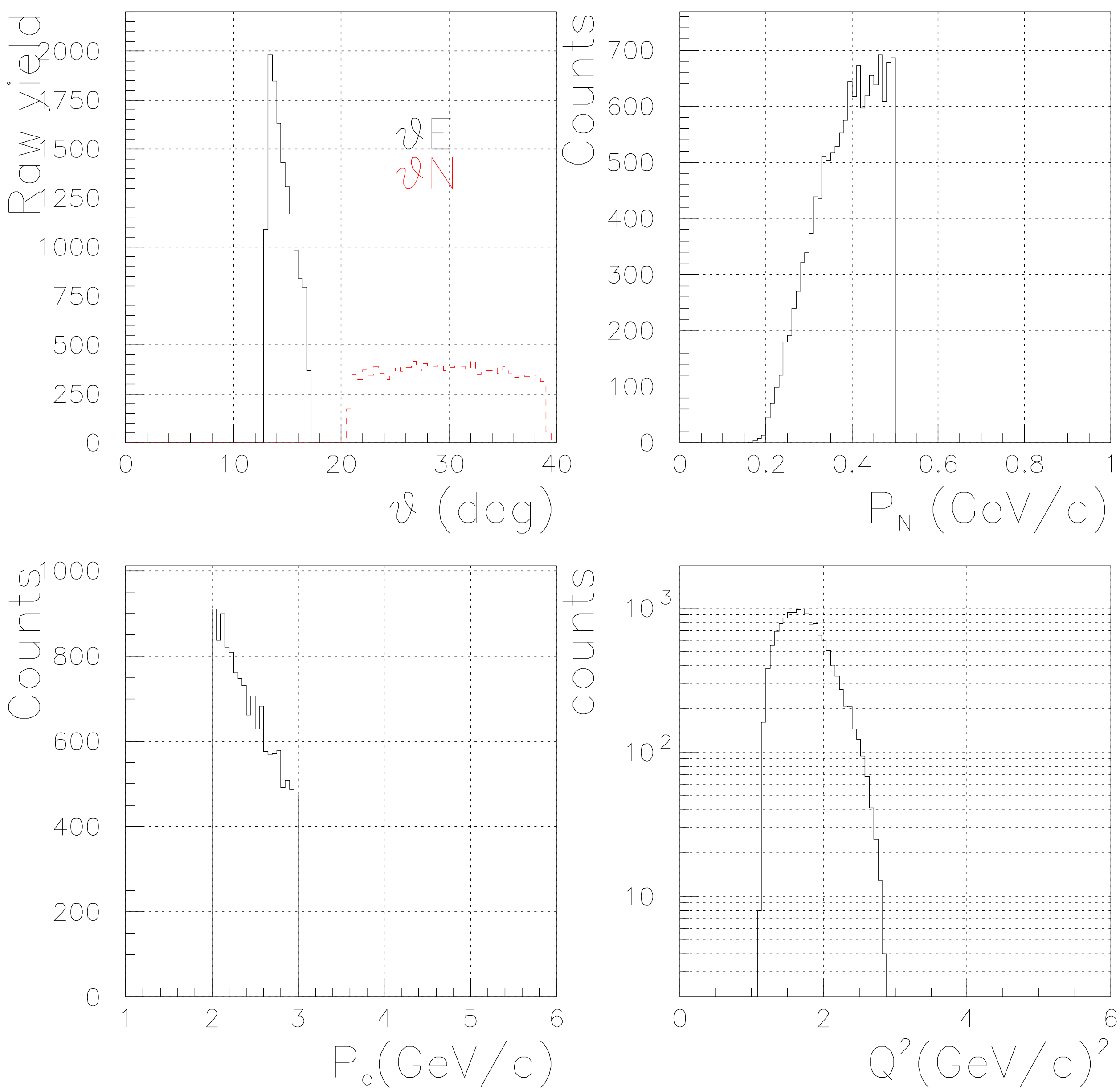

Figure 3.16: Simulated MAD kinematics at 15°. Top left gives the central angle for MAD and the neutron detector, top right gives the neutron momentum range accessed, bottom left gives the electron momentum range covered, and the bottom right gives the Q^2 range covered.

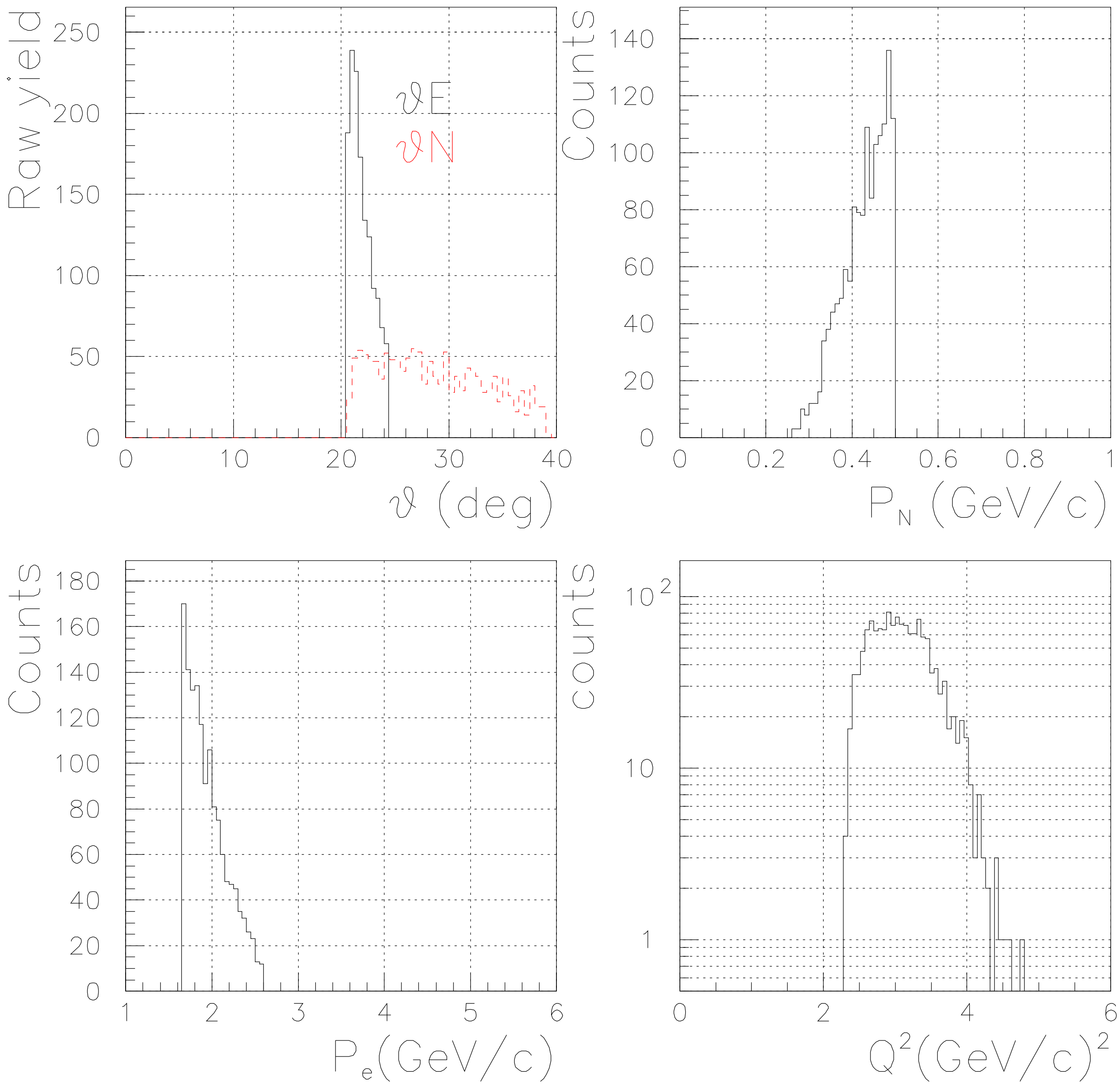

Figure 3.17: Simulated MAD kinematics at 22^0. Top left gives the central angle for MAD and the neutron detector, top right gives the neutron momentum range accessed, bottom left gives the electron momentum range covered, and the bottom right gives the Q^2 range covered.

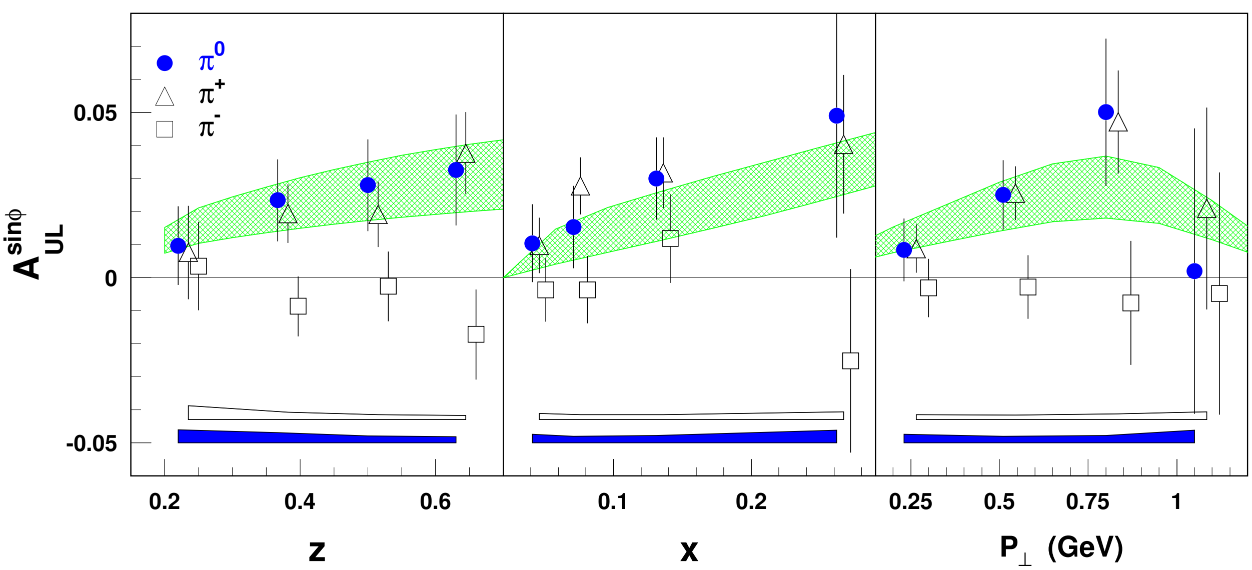

Figure 3.18: Analyzing power in the $\sin\phi$ moment from HERMES [124, 125]. Error bars include the statistical uncertainty only. The filled and open bands at the bottom of the panels represent the systematic uncertainties for neutral and charged pions, respectively. The shaded areas show a range of predictions of a model calculation applied to the case of π° electro-production [126, 127].

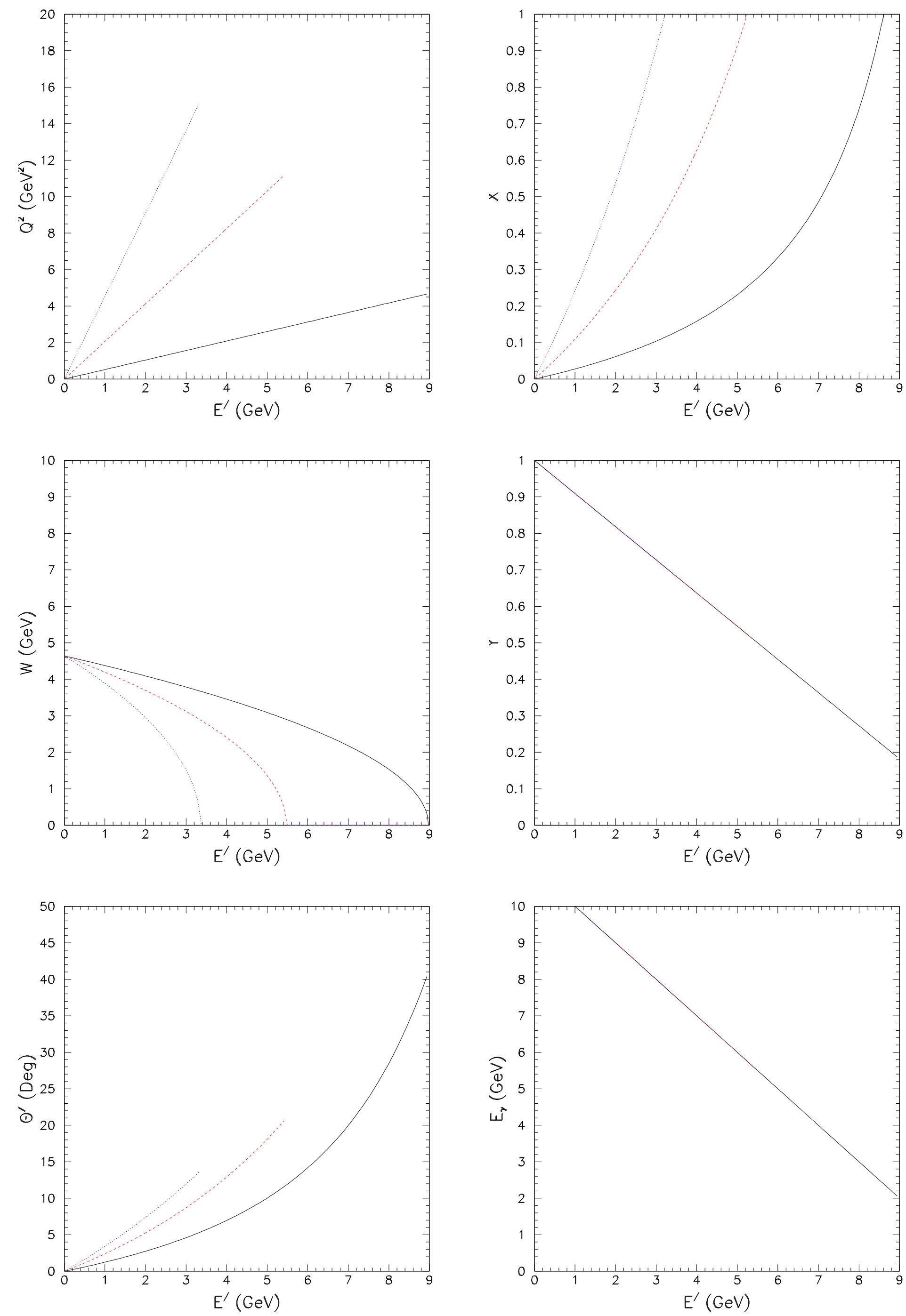

Figure 3.19: Kinematics plots for (e, e') scattering using 11 GeV electron beam. The solid, dashed, and dotted curves correspond to electron scattering angle at $12.5°, 25.0°$, and $37.5°$, respectively. E' is the energy of the scattered electron and θ' is the laboratory angle of the virtual photon.

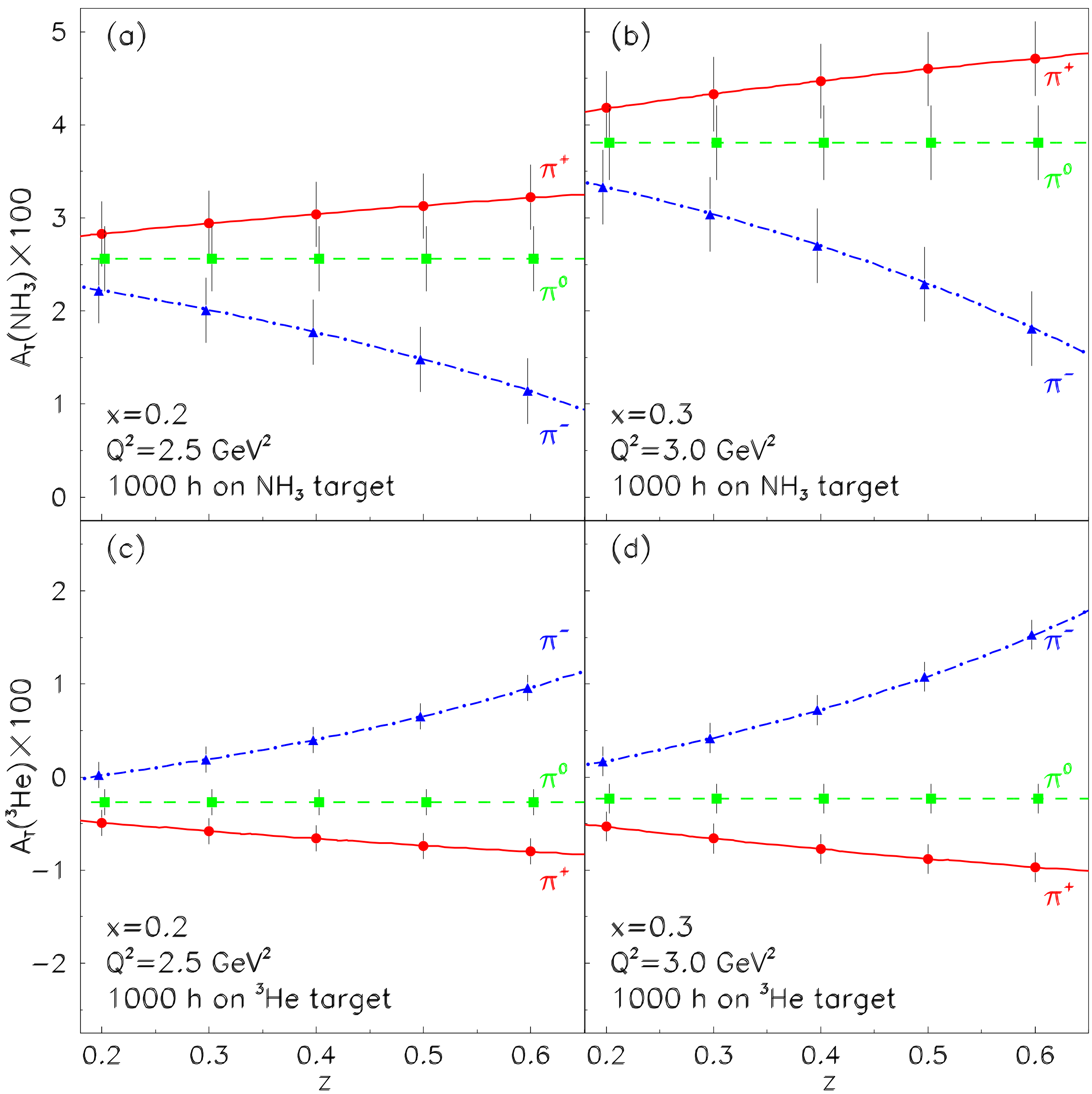

Figure 3.20: The expected precisions in transverse single-spin asymmetry measurements on a polarized $^{15}NH_3$ and a polarized ^3He target, for the kinematics of $x_{Bj} = 0.2$ and $x_{Bj} = 0.3$. 1000 hours of beam time is assumed for each target.

3.3 Exclusive Reactions

Exclusive electromagnetic reactions provide a unique opportunity for studying both the short distance structure of hadrons, and for extracting novel long-distance quark and gluon matrix elements of hadrons. Exclusive reactions of interest in Hall A include

- Elastic electron scattering on the proton
- Quasi-Elastic ${}^3\vec{H}e(\vec{e}, e'n)X$ scattering to extract the neutron $G_E(Q^2)/G_M(Q^2)$ ratio.
- Real Compton Scattering (RCS) at high perpendicular momentum transfer: $\gamma p \to \gamma p$.
- Deeply Virtual Compton Scattering (DVCS) $ep \to ep\gamma$, $ep \to eN^*\gamma$, and Deeply Virtual Meson production: $ep \to eNM$, $M = \pi$, η, ... Deep virtual scattering refers to the $Q^2 \gg \Lambda_{\rm QCD}$, $s \gg M^2$, and $-t \ll Q^2$ (also $-u \approx s$) kinematics.
- Meson photo-production and deuteron photo-disintegration at high perpendicular momentum.
- Virtual Compton Scattering below two pion threshold for the extraction of Generalized Polarizabilities at high Q^2.
- Virtual Compton Scattering at high t

Jefferson Lab at 6 GeV provides an unprecedented combination of high luminosity, low emittance, and high polarization. With this facility, we have greatly enhanced the precision of our measurements of exclusive reactions. For example, the measurements of the ratio G_{Ep}/G_{Mp} have radically changed our understanding of the charge and current densities inside the proton [131, 132]. The recent measurements of real Compton scattering, meson photo-production and deuteron photo-disintegration have vastly expanded the kinematic range and statistic precision of these high p_T reactions.

In addition to this experimental progress, the last decade has seen the emergence of a new theoretical framework for understanding exclusive reactions. A new QCD factorization theorem [133] requires that at sufficiently high momentum transfer Q^2, the deep virtual reactions factorize into the convolution of a hard scattering kernel with quark and gluon matrix elements (Generalized Parton Distributions) of the target (nucleon or nucleus)[134]. In the Deeply virtual meson production, the reaction kernel is also convoluted with the quark and gluon distribution amplitude of the final meson.

Measurements of Deeply Virtual electroproduction have two goals: Firstly, to test the range of validity of the factorization theorem. Secondly, if the theorem is valid in our accessible kinematics, to extract new information on quark correlations: For example, measurements of GPD at a single (x, ξ) point and variable t measure a correlation between longitudinal momentum and transverse position. This will enable us to form three dimensional pictures of the proton for the first time [135, 136]. The significance of these correlations is illustrated by X. Ji's sum rule of the vector GPDs yielding the total contribution of quark orbital angular momentum to the nucleon spin[137]. Although we cannot measure this sum

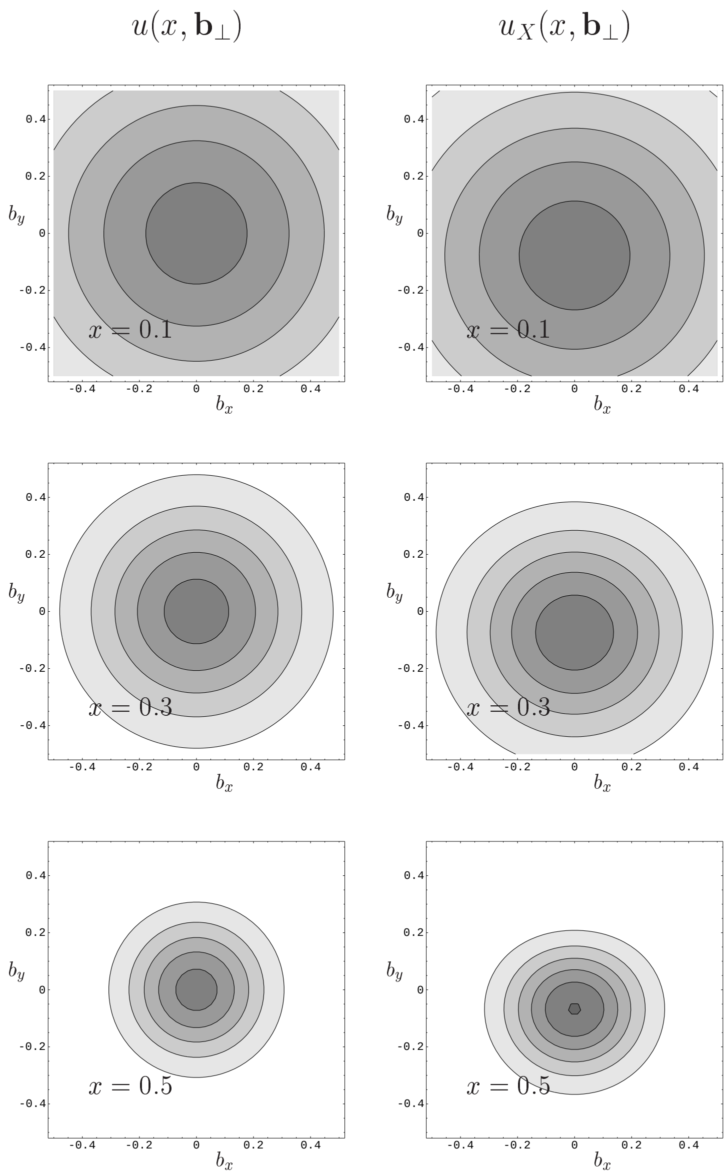

Figure 3.21: Up-quark probability distributions transverse to the proton center-of-momentum coordinate, in the infinite momentum frame (along $\hat{z}$), for three values of lightcone momentum xP^+. The left column $u(x, \mathbf{b}) = \mathcal{H}_u(x, \mathbf{b})$ is the up-quark probability distribution for an unpolarized proton. The right column $u_X(x, \mathbf{b}) = \mathcal{H}_u(x, \mathbf{b}) - [1/(2M)](\partial/\partial b_y)\mathcal{E}_u(x, \mathbf{b})$ is the probability distribution for a proton polarized in the x direction. $\mathcal{H}$ and $\mathcal{E}$ are the Fourier transforms with respect to $\Delta_\perp$ of $H(x, 0, t = -\vec{\Delta}_\perp^2)$ and $E(x, 0, t = -\vec{\Delta}_\perp^2)$, respectively.

rule directly, we can constrain models of the GPDs which in turn predict values of the sum rule ([138]).

Exclusive reactions at Jefferson Lab at 12 GeV will enable us to build a radically new picture of the proton. On very general grounds, we expect a correlation between the longitudinal and transverse variables of the form:

$$H_f(x, \xi, t) \approx q_f(x) e^{t(1-x)a^2/x} \tag{3.34}$$

where $q_f(x)$ is the forward parton distribution of flavor f and a is a parameter characterizing the transverse size. Neither the simple factorization, nor the Gaussian ansatz, are expected to be particularly accurate. What is important in Eq. 3.34 is the strong correlation between the t-dependence (transverse size) and the x-dependence (longitudinal momentum). At large x, the t-dependence becomes very soft: the proton is small in transverse impact parameter space. At small x, the t-dependence is very stiff: the proton swells.

Fig. 3.21 illustrates the physical significance of Eq. 3.34. The figure shows both the dramatic change in transverse profile as a function of longitudinal momentum (xP^+), and the spatial anisotropy introduced by $E(x, \xi, t)$, the proton helicity flip GPD. Neglecting strange quarks, the down quark GPDs are similar to Fig. 3.21, except the polarized d-quark distribution is distorted in the positive b_y direction. The electric dipole moment in the $-b_y$ direction implicit in the polarized distributions is a dynamical consequence of the kinematic relation that a boost perpendicular to the magnetic moment induces an electric dipole moment along $\vec{\mu} \times \vec{P}$.

The Hall A upgrade to 11 GeV beam offers crucial opportunities to greatly enhance the kinematic range accessible to exclusive reactions, while maintaining high statistical and systematic precision. This will provide comprehensive tests of factorization in processes such as DVCS, RCS, and high P_T meson production. By measuring the parton densities in transverse impact parameter space, with a variety of longitudinal momentum weightings, as described below these exclusive processes perform a form of tomography of the proton.

3.3.1 G_{Ep}/G_{Mp} at high Q^2

The simplest exclusive reaction is elastic electron scattering on the proton. The elastic form factors are the most fundamental quantities reflecting the composite structure of the hadrons. Furthermore, knowledge of the nucleon form factors is an important ingredient in the analysis of processes involving electromagnetic interactions with complex nuclei.

The elastic form factors measure the lowest (x^0) moments of the Generalized Parton Distributions:

$$F_1(Q^2) = \int dx \sum_f e_f H_f(x, \xi, -Q^2); \tag{3.35}$$

$$F_2(Q^2) = \int dx \sum_f e_f E_f(x, \xi, -Q^2). \tag{3.36}$$

Thus elastic electron scattering measures the current density in the transverse coordinate, averaged over longitudinal momentum.

The recent Jefferson Lab Hall A measurements of the ratio $\mu G_{Ep}/G_{Mp}$ [132],[131] have radically changed our understanding of the proton form factors. The data strongly prefer a scaling $F_{2p}/F_{1p} \propto 1/\sqrt{Q^2}$, contrary to previous hypotheses that F_2 would scale as F_1/Q^2. The MAD spectrometer in Hall A is well suited to extend these measurements of $\mu G_{Ep}/G_{Mp}$ to $Q^2 \leq 10$ (GeV/c)^2 with $P_{\max} = 6$ GeV/c. In fact, with the central momentum of the MAD at 6 GeV/c, the full solid angle acceptance is still achieved at nearly 7 GeV/c. Thus measurements to $Q^2 = 11$ (GeV/c)^2 are possible with the standard MAD. It is likely that these measurements can be extended to $Q^2 = 13.3$ (GeV/c)^2 if the maximum momentum of MAD is stretched to 8 GeV. This can be achieved by reducing the bend angle, which however would greatly increase the background of low energy particles in the focal plane detectors. We note that the overdetermined kinematics and asymmetry ratio of $p(\vec{e}, e'\vec{p})$ measurements will permit operation of the spectrometer at high background levels for these elastic measurements.

Fig. 3.22 shows the range in Q^2 we are able to determine the proton form factor ratio $\mu G_{Ep}/G_{Mp}$ with the large acceptance of the MAD spectrometer equipped with a Focal Plane Polarimeter and an electromagnetic calorimeter in Hall A. Table 3.3.1 shows us the kinematics and the estimated time necessary for the measurements.

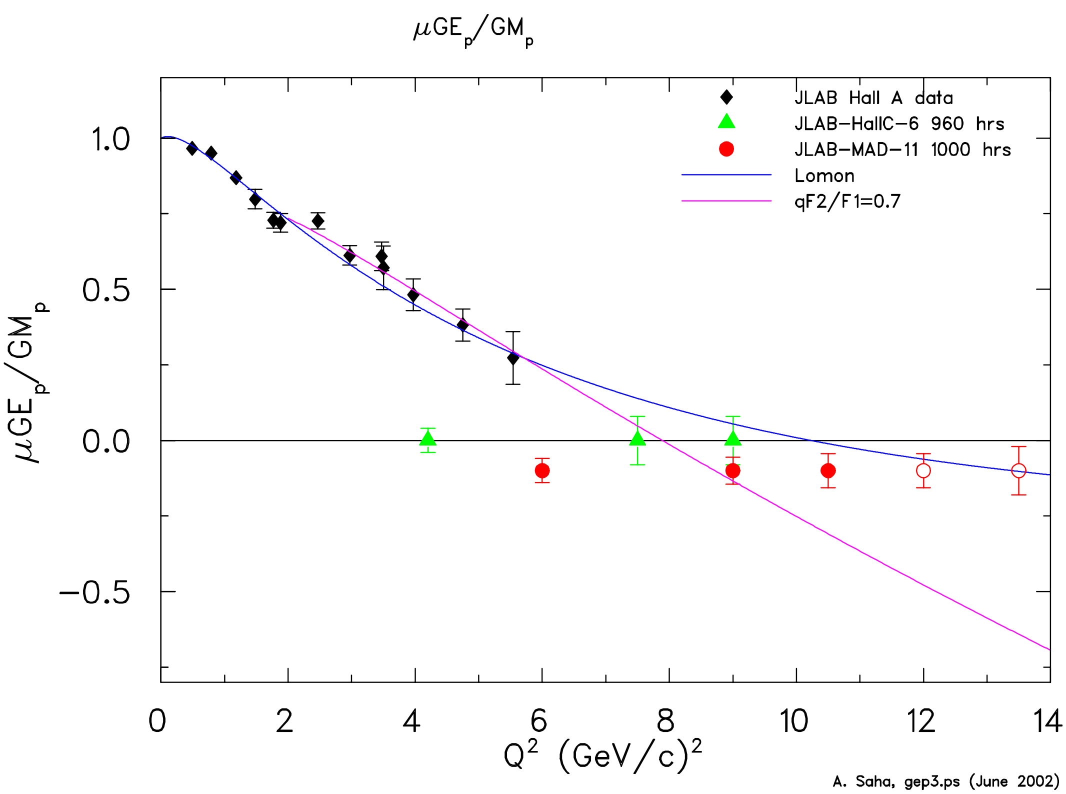

Figure 3.22: Form factor ratio $\mu G_{Ep}/G_{Mp}$ measured via $p(\vec{e}, e'\vec{p})$. The points labeled JLab–HallC are projected points with 6 and 11 GeV beam energy. The points labeled JLab-MAD-11 are projected points in Hall A with the MAD spectrometer.

The value of the FPP analyzing power does not enter the measurement of $\mu G_{Ep}/G_{Mp}$ but does enter into the error analysis. Measurements of the [CH_2] analyzing power up to 5.3 GeV/c (Q^2 = 8.3 (GeV/c)^2) at Dubna show that the fall off of the analyzing power with momentum is much more gradual than initially believed and that there is still an appreciable value of the analyzing power remaining at these values of momentum. We have assumed a constant value of the analyzing power for our error analysis (Figure of Merit $\epsilon A_y^2 = 1.2 * 10^{-3}$). It would be useful to obtain data on the analyzing power of CH_2 prior to the data taking at the highest values of Q^2. These projected results in Table 3.3.1 are very preliminary. Detailed simulation and estimation of systematic errors are necessary for more realistic projections.

Q^2 GeV^2	$k\sigma_{ep} * 10^{-10}$ ($b.GeV^2$)	E_f GeV	θ_e deg	$p(=q)$ GeV	θ_p deg	Jac. (e/p)	Calo $d\Omega_e$	MAD $d\Omega_p$	MAD $Sin\chi$	Δ $\frac{\mu G_{Ep}}{G_{Mp}}$	Time Hours
6.0	376.1	7.80	15.2	4.03	30.5	< 1		20	0.37	0.04	40
9.0	41.9	6.21	20.9	5.66	23.1	0.9	21	23	0.63	0.045	140
10.5	16.9	5.41	24.3	6.47	20.1	1.5	30	20	0.94	0.056	110
12.0	7.34	4.61	28.2	7.3	17.4	2.6	44	17	0.98	0.056	270
13.3	3.59	3.88	32.5	8.0	15.1	4.6	74	16	0.79	0.08	440

Table 3.6: Kinematics and Run Time Estimate for $p(\vec{e}, e'\vec{p})$ measurements of the ratio $G_{E\,p}(Q^2)/G_{M\,p}(Q^2)$, at $E_i = 11$ GeV.

3.3.2 Measurement of G_E^n at high Q^2

The neutron electric form factor G_E^n is the least well measured of the four nucleon Sachs form factors. The magnetic form factor of the proton G_M^p is measured over a wide range of Q^2 [139, 140]. The ratio G_{Ep}/G_{Mp} is discussed in a previous section. The neutron magnetic form factor G_M^n was recently studied in Hall B for Q^2 up to 4.8 (GeV/c)^2 [141].

Our present knowledge of the neutron electric form factor G_E^n, is displayed in fig. 3.23. The extraction of G_E^n at high momentum transfer from quasi elastic e – d scattering via the Rosenbluth separation technique leads to large uncertainties. The difficulties in measuring G_E^n at high Q^2 from cross section measurements arise from the small value of G_E^n compared to the magnetic contribution to the cross section (τG_M^n). In particular, the Rosenbluth measurements do not distinguish between a vanishing G_E^n and the most recent theoretical predictions [142]. Double polarization experiments at JLab and other facilities measured $G_E^n(Q^2)$ up to Q^2 = 1.5 (GeV/c)^2 [143]. R. Schiavilla, and I. Sick recently extracted G_E^n up to Q^2 = 1.7 (GeV/c)^2 from data on the deuteron quadrupole form factor $F_{2C}(Q^2)$ [144]. In JLab Hall A, there is one more double polarization $^3\overrightarrow{\mathrm{He}}(\vec{e}, e'n)X$ experiment approved to measure G_E^n up to 3.4 (GeV/c)^2 [145].

The MAD spectrometer together with JLab at beam energies above 6 GeV would provide the opportunity to extend the measurements of G_E^n to Q^2 = 5 (GeV/c)^2, by the double polarization $^3\overrightarrow{He}(\vec{e}, e'n)X$ technique. The existing high luminosity polarized ^{3}He target can be utilized. The MAD spectrometer is the appropriate device to detect the quasi elastically scattered electrons. Figure 3.24 shows the achievable statistical error in 30 days beam time using the MAD spectrometer in its forward angle (15°) configuration, compared to the MAD in its standard configuration, the BigBite spectrometer and the HRS spectrometers. The amount of beam time does not include the overhead time needed for polarization, energy, control and calibration measurements and assumes 100% efficiency. Furthermore a beam current of 15 uA, and 75% beam– and 40% target polarization are used for this estimate. For a given Q^2 and spectrometer, the figure of merit (FOM) has been optimized first. The FOM is maximized if the electrons are detected at small scattering angles. For the HRS, the best FOM is reached using the maximum central momentum of 4.3 GeV/c in the HRS. The BigBite spectrometer is the optimal device for medium values of the momentum transfer up to roughly 3 GeV/c due to its large solid angle of 95 msr (with an extended target). But because the momentum resolution for particles with momenta above 1.5 GeV/c is not sufficient, BigBite has to be operated at backward angles (and lower beam energies) to achieve high momentum transfers, which reduces the advantage of the large solid angle. For higher values of momentum transfer, the MAD spectrometer becomes superior. The maximum central momentum of 6 GeV/c allows the use of MAD at more forward angles increasing the cross section, and therefore the FOM, dramatically. The solid angle of 15 msr in this configuration is therefore still sufficient. All these estimates assume that the size of the neutron detector matches the angular acceptance of the MAD spectrometer. For Q^2=5 (GeV/c)^2 the appropriate scattering angle of the electrons would be 18°, the beam energy would be 8.65 GeV, and the scattered electrons would have a momentum of 6 GeV/c. Within 60 days plus overhead a measurement of G_E^n with an accuracy of 20% is possible.

3.3.3 Real Compton Scattering

Wide angle real Compton scattering (RCS, or WACS) at high energy is a natural extension of elastic electron scattering. The momentum transfer $t = (q-q')^2$ (q and q' are the incident and scattered photon four-momenta) plays the same role as Q^2 in $p(e, e'p)$. More specifically, the reaction mechanism is determined by the perpendicular momentum transfer to the proton:

$$p_\perp = \frac{s - M^2}{2\sqrt{s}} \sin\theta_{\gamma\gamma}^{CM}, \tag{3.37}$$

where $\theta_{\gamma\gamma}^{CM}$ is the photon scattering angle in the photon-proton Center of Mass. At asymptotically large $p_\perp$, the RCS scattering amplitude factorizes into a convolution of a perturbative reaction kernel with the distribution amplitude for the simplest 3-quark Fock-Space configuration of the proton.

At photon energies of 6–11 GeV, however, A. Radyushkin has suggested that the reaction kernel for WACS will be dominated by the simple Klein-Nishina process on a single quark, convoluted with the GPD of the quark in the proton [146]. Note that the GPD sums over all Fock-states of the proton. Neglecting the contribution of a gluon term, the RCS cross

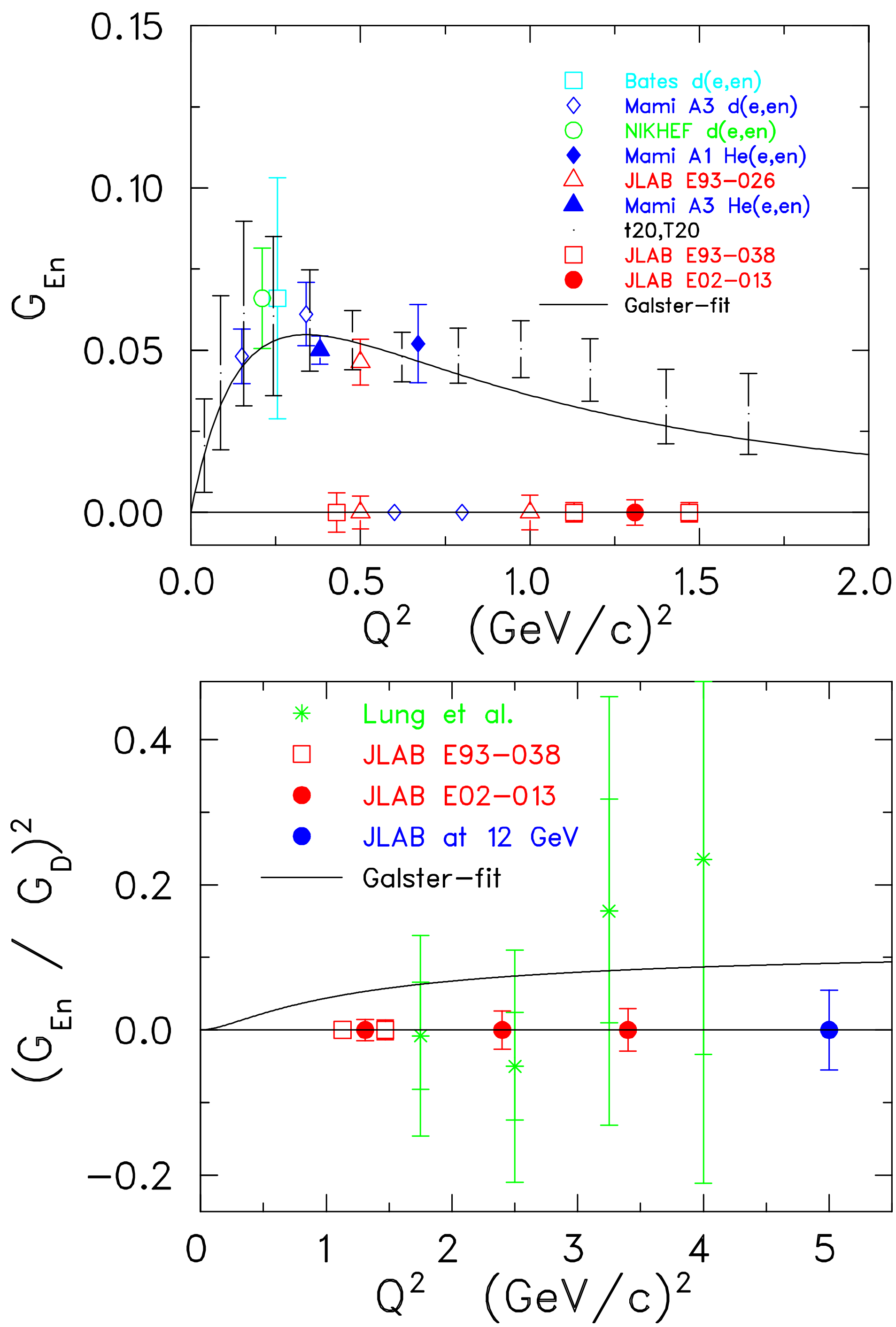

Figure 3.23: Available data on G_E^n. Top: data for $Q^2 \leq 2$ (GeV/c)^2. Bottom: data for $Q^2 \geq 1.0$ (GeV/c)^2. Because the Rosenbluth separation cannot determine the sign of G_E^n, the bottom figure shows the square of the ratio of G_E^n normalized to the dipole form factor G_D. The data points plotted with $G_E^n = 0$ are from planned experiments and from experiments which have run, but are unpublished.

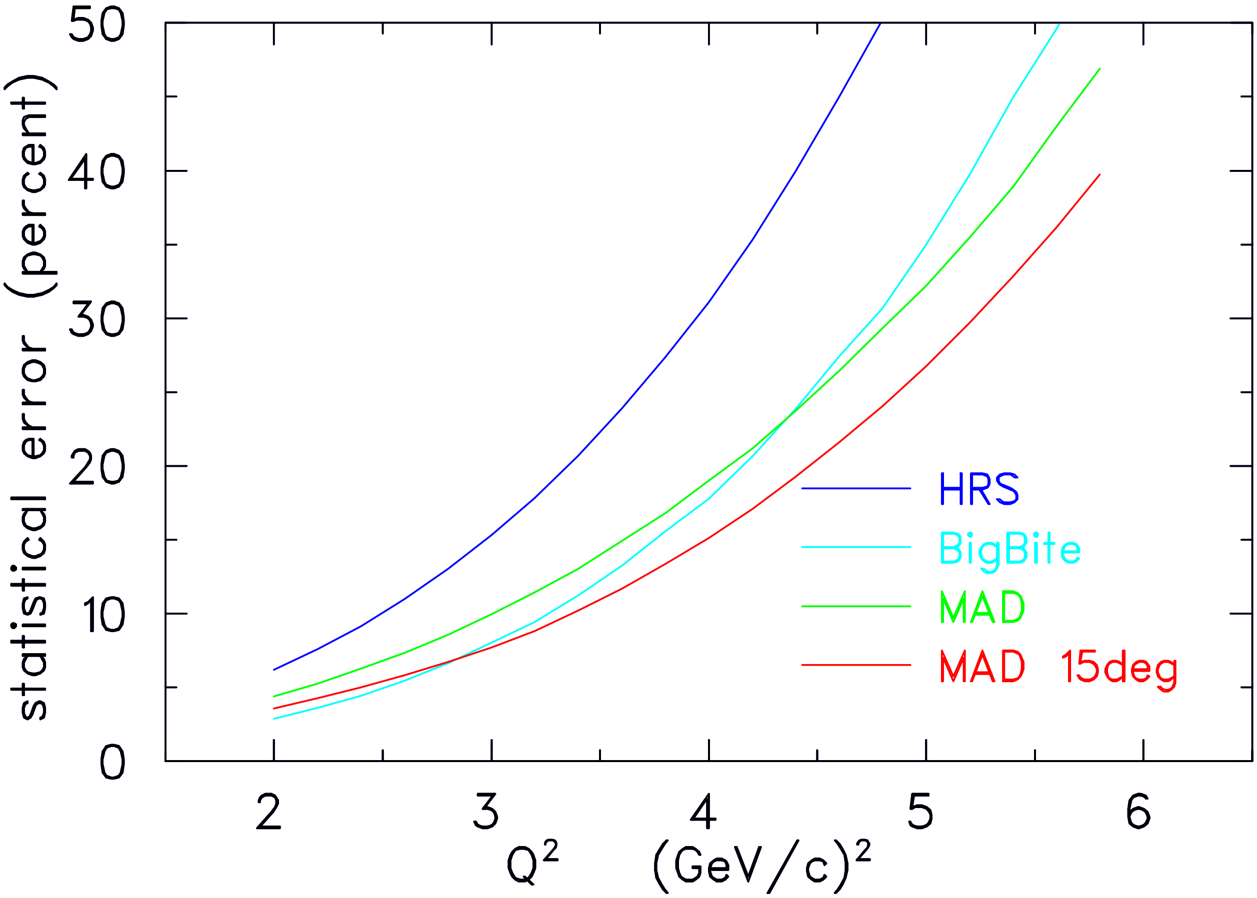

Figure 3.24: Statistical uncertainty in G_E^n obtainable in 30 days of beam time via the $^3\vec{H}e(\vec{e}, e'n)X$ reaction, utilizing different spectrometer setups.

section has the form [147]:

$$\frac{d\sigma}{dt} = \left.\frac{d\sigma}{dt}\right|_{\mathrm{KN}} \left[f_V \left(R_V^2(t) + \tau_C R_T^2(t)\right) + (1 - f_V) R_A^2(t)\right] \tag{3.38}$$

$$R_V(t) = \int \frac{dx}{x} e_f^2 H_f(x, \xi = 0, t) \tag{3.39}$$

$$R_T(t) = \int \frac{dx}{x} e_f^2 E_f(x, \xi = 0, t) \tag{3.40}$$

$$R_A(t) = \int \frac{dx}{x} e_f^2 \tilde{H}_f(x, \xi = 0, t), \tag{3.41}$$

where $d\sigma_{\mathrm{KN}}$ is the Klein-Nishina cross section for Compton scattering on a point fermion, $\tau_C = -t/4M^2$, and $0 < f_v < 1$ is a kinematic factor. Thus WACS samples the longitudinal momentum distribution with a $1/x$ weight, compared to the unit weighting of the quark momentum distribution in elastic electron scattering.

The experimental data on WACS were very limited until January 2002 when the JLab Hall A Collaboration (E99-114) took data up to 5.7 GeV at 1000 times higher luminosity

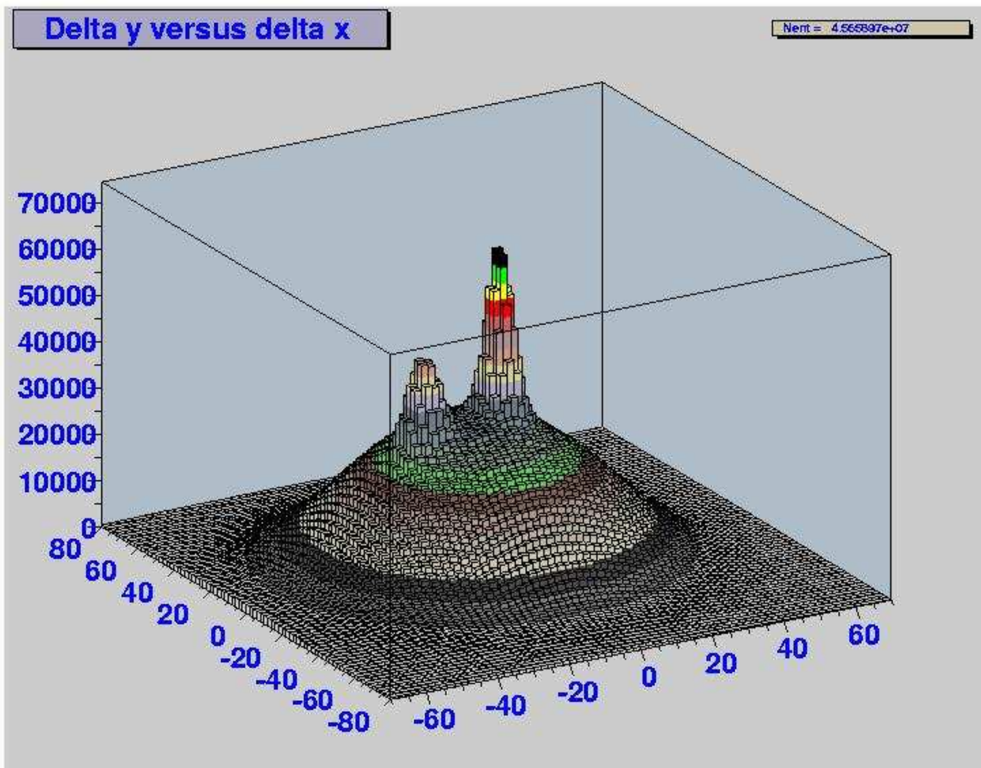

Figure 3.25: Coincidence $p(\gamma,\gamma' p)$, $p(\gamma,p\gamma)\gamma$, and $p(e,e'p)$ events from JLab Hall A Real Compton Scattering Experiment 99-114. The horizontal axes are the difference between the detected position (cm) of the photon (reconstructed in the calorimeter) and the position predicted from the proton momentum measured in the HRS, assuming the event is an exclusive Compton event. The peak at $(0,0)$ contains the $p(\gamma,\gamma' p)$ events. The dipole magnet in front of the calorimeter displaces the $p(e,e'p)$ peak to negative Δx. The broad background is $p(\gamma,p\gamma)X$ events, mostly $\gamma p \to p\pi^0$.

than the previous experiment of Shupe [148] from the late 1970s. With one month production running, the recent experiment achieved 5% statistics (including background subtraction) in 24 bins covering $5 \leq s \leq 11$ GeV^2 and $-0.5 \leq \cos\theta_{\gamma\gamma}^{CM} \leq 0.5$. The separation of the $p(\gamma,\gamma p)$ $p(e,e'p)$ and $p(\gamma,p\gamma)\gamma = p(\gamma,p)\pi^0$ channels is illustrated in Fig. 3.25. This recently completed experiment demonstrated that mixed electron-photon beam can be used in Compton scattering with very high data rate.

Kinematically, the 12 GeV upgrade, the MAD spectrometer, and a large calorimeter expands the range in s from 12 to 19 GeV^2, for $-t$ up to 10 GeV^2 (Fig. 3.26,3.27). The cross sections $d\sigma/dt$ at fixed $\theta_{\gamma\gamma}^{\rm CM}$ scale approximately as s^{-6} (However at fixed t, the cross sections scale approximately as s^{-2}). Thus by doubling the beam energy, the cross section at fixed $\theta_{\gamma\gamma}^{\rm CM}$ will decrease by a factor of $2^6 = 64$. However, the laboratory acceptance in t scales as $\Delta t = 2kk'\Delta\Omega^{\rm lab}$. Thus doubling the beam energy increases the t-acceptance 4-fold. We will also double the size of the calorimeter. This 8-fold increase in acceptance for the photon arm is nearly matched by the increased acceptance of MAD over the HRS. In addition, we can nearly double the luminosity. We can therefore measure the RCS process at $\theta_{\gamma\gamma}^{CM} = 60$, 75, 90, and 105° at incident electron energies of 6.6, 8.8 and 11 GeV with 7% statistics in two months of production running.

At fixed $\theta_{\gamma\gamma}^{CM}$, compared to the recent Hall A data, these new measurements up to 11 GeV can test the scaling behavior over a factor of 64 in the cross section. At fixed t, in the soft overlap mechanism (Eq. 3.38) the cross section falls by over a factor of four and the value of $p_{\perp}^2$ grows by more than a factor of four. Thus the Hall A detectors can provide a unique and powerful probe of quark dynamics in the simplest of exclusive processes beyond elastic electron scattering.

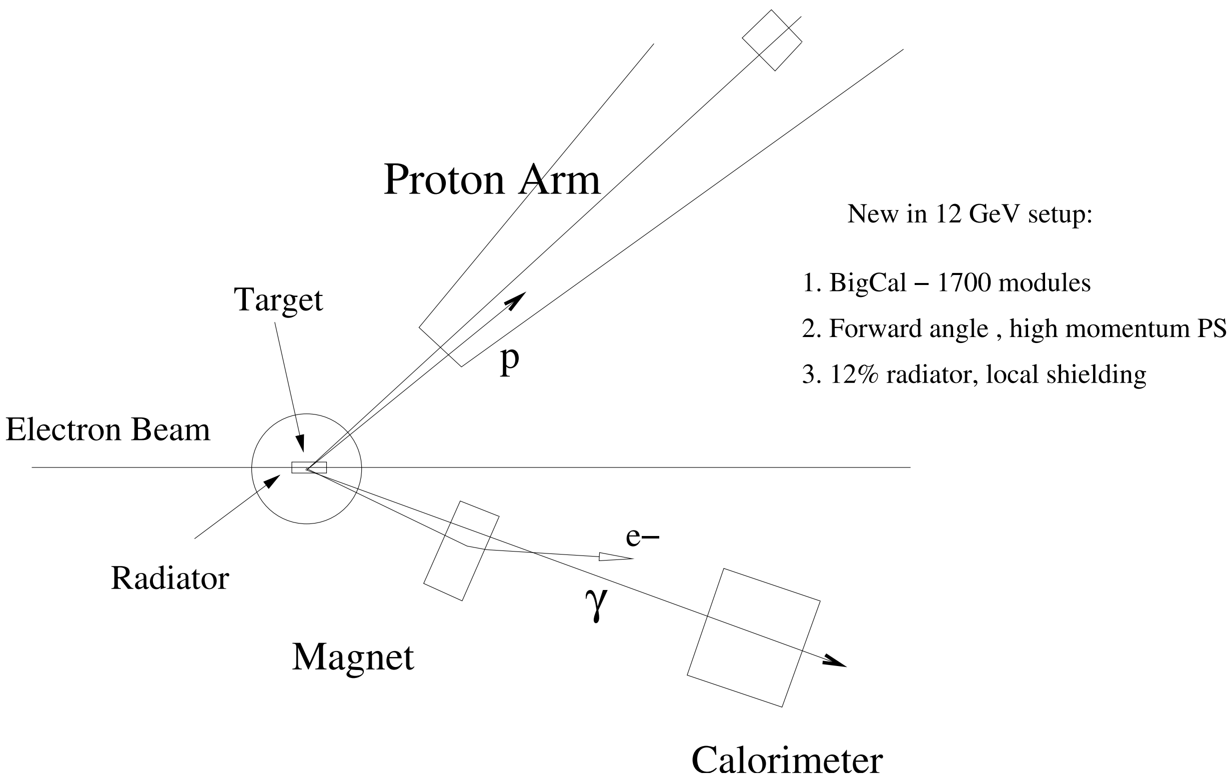

Figure 3.26: Experimental setup for RCS with 12 GeV CEBAF

3.3.4 Deeply Virtual Compton Scattering

Deeply virtual Compton scattering (DVCS) refers to the $ep \to ep\gamma$ reaction at large Q^2 and s, but small t (net momentum transfer to the proton). At sufficiently large Q^2, a factorization theorem predicts that the scattering amplitude is the convolution of a perturbative kernel with a set of ground-state quark matrix elements, called Generalized Parton Distributions (GPDs). The VCS process interferes coherently with the Bethe-Heitler (process), which can be used as both an amplifier and a filter for the DVCS amplitude. In particular, in JLab kinematics, the beam helicity interference is dominated by an interference between the BH amplitude and the imaginary part of the VCS amplitude.

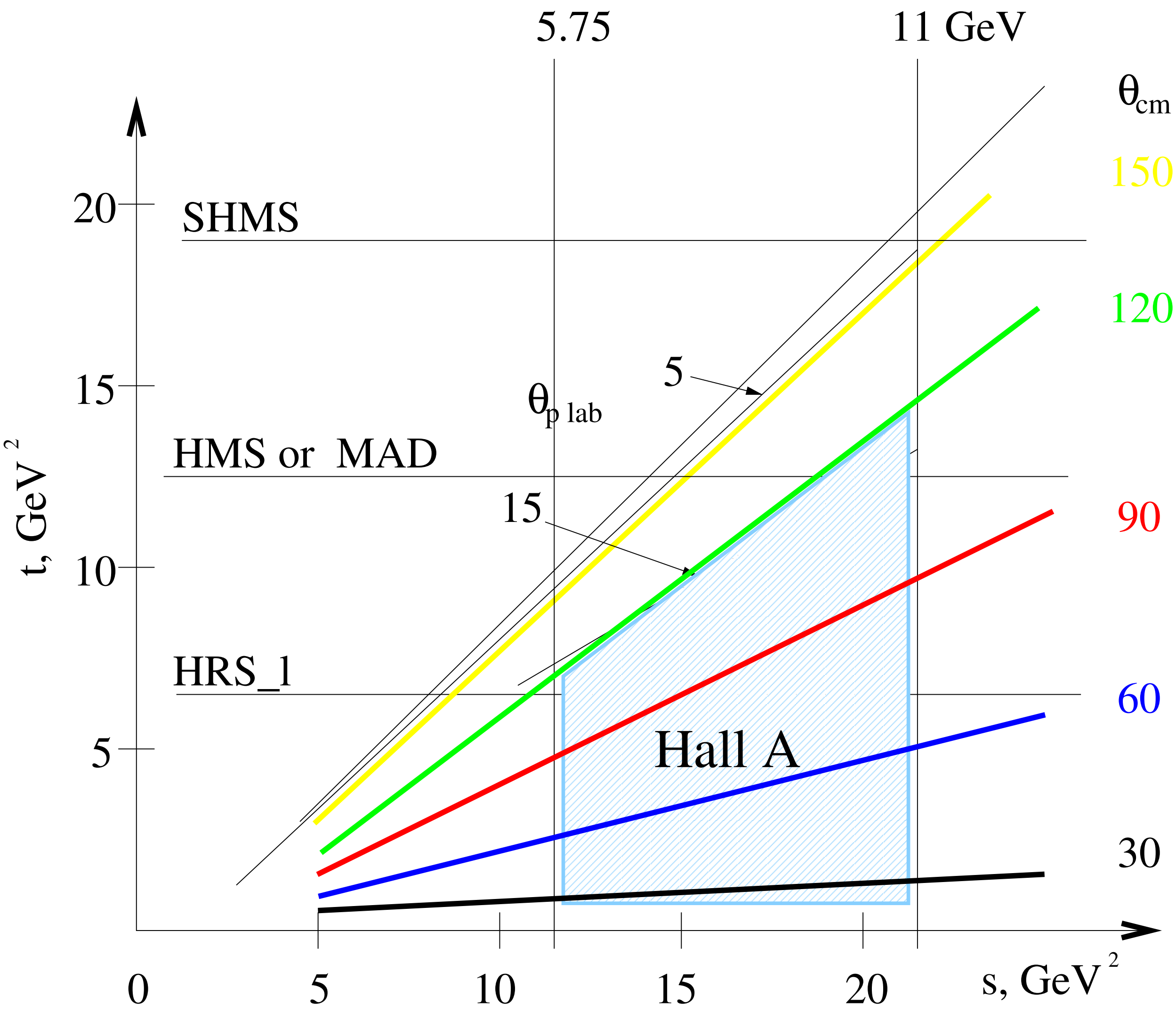

Figure 3.27: Kinematics of RCS with 12 GeV CEBAF

Hall A at 11 GeV can measure the DVCS process with high statistics up to the following limits in Q^2 as a function of $x_{\rm Bj}$:

$$
\begin{array}{lll}
x_{\rm Bj} = 0.20 & Q^2 \leq 2.5\ \text{GeV}^2 & (s \leq 11\ \text{GeV}^2) \\
x_{\rm Bj} = 0.35 & Q^2 \leq 6.0\ \text{GeV}^2 & (s \leq 11\ \text{GeV}^2) \\
x_{\rm Bj} = 0.50 & Q^2 \leq 7.0\ \text{GeV}^2 & (s \leq 8\ \text{GeV}^2)
\end{array}
$$

Isolation of the exclusive $ep \to ep\gamma$ channel from competing $ep \to ep\pi^0$, $ep \to eN^*\gamma \ldots$ channels requires a combination of resolution and overcomplete detection of all three reaction products. We propose to detect the scattered electron in the MAD spectrometer (taking advantage of its large acceptance), the photon in a 1000 element PbF_2 calorimeter, and the recoil protons in a 100 element scintillator array (solid angle 0.75 sr). Recent beam tests for E00-110 confirm that this configuration can operate at a luminosity of $10^{37}/\text{cm}^2/\text{s}$.

Fig. 3.28 illustrates the separation of the exclusive DVCS channel from the Deep Virtual π^0 and inelastic DVCS channels. The cross section estimates are obtained from [149].

In the DVCS limit, the beam helicity cross section difference is [150]:

$$d^5\sigma(\overrightarrow{e}p \to ep\gamma) - d^5\sigma(\overleftarrow{e}p \to ep\gamma) = \frac{1}{\tilde{s}\tilde{u}}\left[A\sin\phi + B\sin 2\phi + C\sin 3\phi\right]. \quad (3.42)$$

In Eq. 3.42, A is the leading order twist-two term resulting from the interference of the elastic form factors in the BH amplitude with a superposition of three GPDs. To leading order B is twist-three, and the ratio B/A is therefore predicted to scale as $1/\sqrt{Q^2}$. C is a gluon GPD, and is expected to be negligible in JLab kinematics. The factor $1/\tilde{s}\tilde{u} = 1/(2k \cdot q'\, 2k' \cdot q')$ is the interference of the electron propagators in the two BH terms.

Figs. 3.29 and 3.31 display the statistical precision of the measurement of the helicity dependent cross section as a function of t at high Q^2 for $x_{\rm Bj}$ centered at 0.35 and 0.50, respectively. The cross section estimates are from Guichon and Vanderhaeghen [151]. Figs. 3.30 and 3.32 display the statistical precision of the extraction of the A and B terms of Eq. 3.42 as a function of t. Each $x_{\rm Bj}$ point requires 400 hours at $10^{37}/\text{cm}^2/\text{s}$ luminosity to obtain the complete distribution in t. Equal or greater statistics can be obtained at the same $x_{\rm Bj}$ values and lower Q^2.

At fixed $x_{\rm Bj}$ the Q^2 dependence and the ratio B/A in each t-bin are independent tests of the QCD factorization theorem. The shape of the t-distribution for different values of x will measure the change in the transverse profile of the proton, as a function of longitudinal momentum, as suggested by Eq. 3.34 and Fig. 3.21.

At large $x_{\rm Bj}$, the minimum proton recoil momentum scales as $p' \approx x_{\rm Bj}M$. For $x_{\rm Bj} > 0.6$, the range of these protons is greater than 3 cm Fe. Thus measurements at large $x_{\rm Bj}$ can be accomplished with significant shielding on the proton array–allowing higher luminosity.

3.3.5 Polarizabilities at High Q^2

The Generalized Polarizabilities (GP) of the proton measure the spatial distribution of the distortion of the internal structure of proton under the influence of an external $E1$ or $M1$ electromagnetic field [152, 151]. The GPs are defined as the $s \to M^2$ limit of the (non-Born) Virtual Compton Scattering amplitude. The Dispersion Relation formalism of B. Pasquini, et al.[153] provides a practical method to extract the polarizabilities from the VCS data up to two-pion threshold. This requires parallel measurements of single pion electro-production at the same Q^2 through the resonance region. Generalized polarizabilities up to $Q^2 = 6.0$ GeV^2 can be extracted from $p(e, e'p\gamma)$ measurements using the MAD spectrometer and a compact PbF_2 calorimeter placed at either side of the spectrometer. Table 3.3.6 details a sample kinematics and count rate estimate.

The existing data on the magnetic polarizability illustrate the interplay in the proton between para- and dia-magnetism [154]. It is also clear that the generalized polarizabilities are not saturated by the nucleon resonances[153]. At high Q^2, the inelastic spectrum of the proton is dominated by quark degrees of freedom, even in the resonance region (duality).

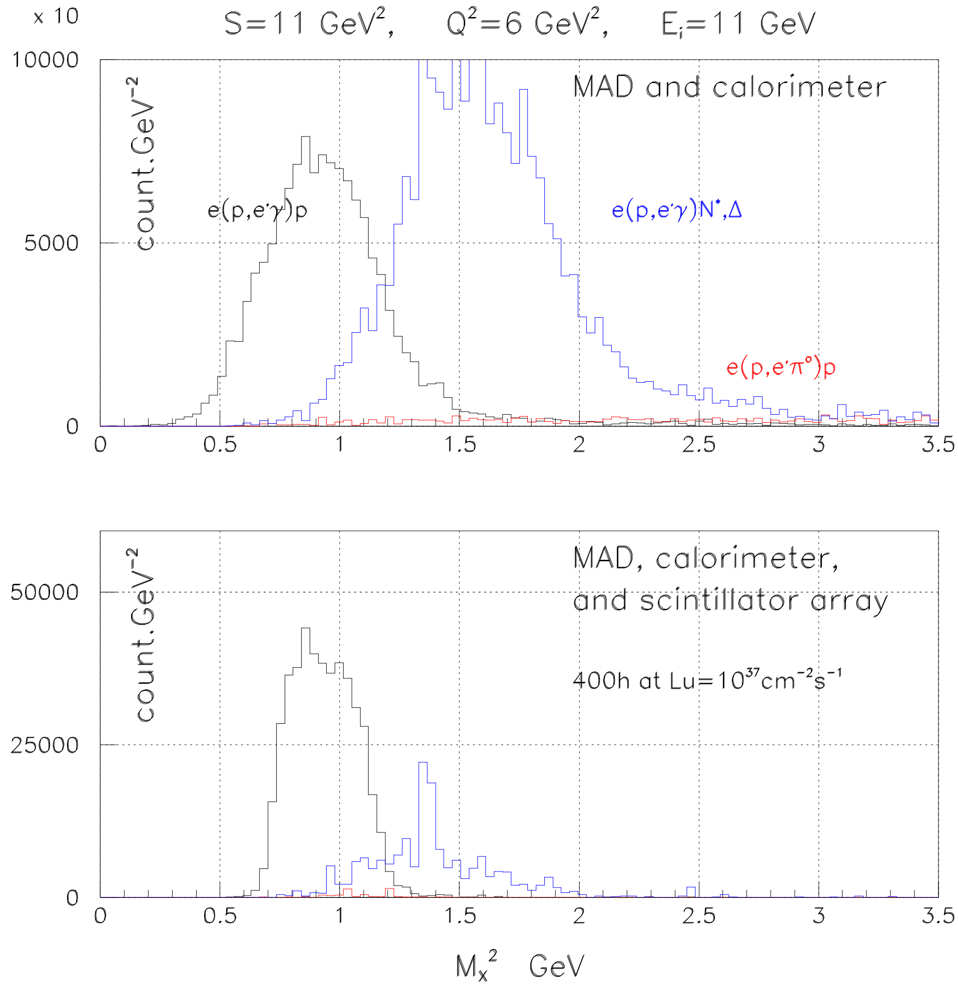

Figure 3.28: Missing Mass squared (GeV^2) distribution for the $p(e, e'\gamma)X$ reaction at $E_i = 11$ GeV, $Q^2 = 6.0$ GeV^2, and $s = 11$ GeV^2. The three curves are: $ep \to ep\gamma$ (Black); $ep \to e\Delta\gamma$ (Blue) $ep \to ep\pi^0$ (Red, almost 0). In both top and bottom, the electrons are detected in the MAD spectrometer, and the photons are detected in the proposed PbF_2 calorimeter (see text). For the $ep \to ep\pi^0$ events, only the leading photon is detected. In the bottom plot, the proton is detected in a scintillator array (see text) and a 2D cut is applied between the detected position of the proton and the position predicted by the $p(e, e'\gamma)p$ kinematics. For the simulation, the $ep \to e\Delta\gamma$ cross section (including both BH and DVCS processes) is set equal to the $ep \to ep\gamma$ cross section. In the plot, the $ep \to ep\pi^0$ cross section is amplified by a factor 20 relative to the model prediction, in order to make the π^0 yield visible on the plot.

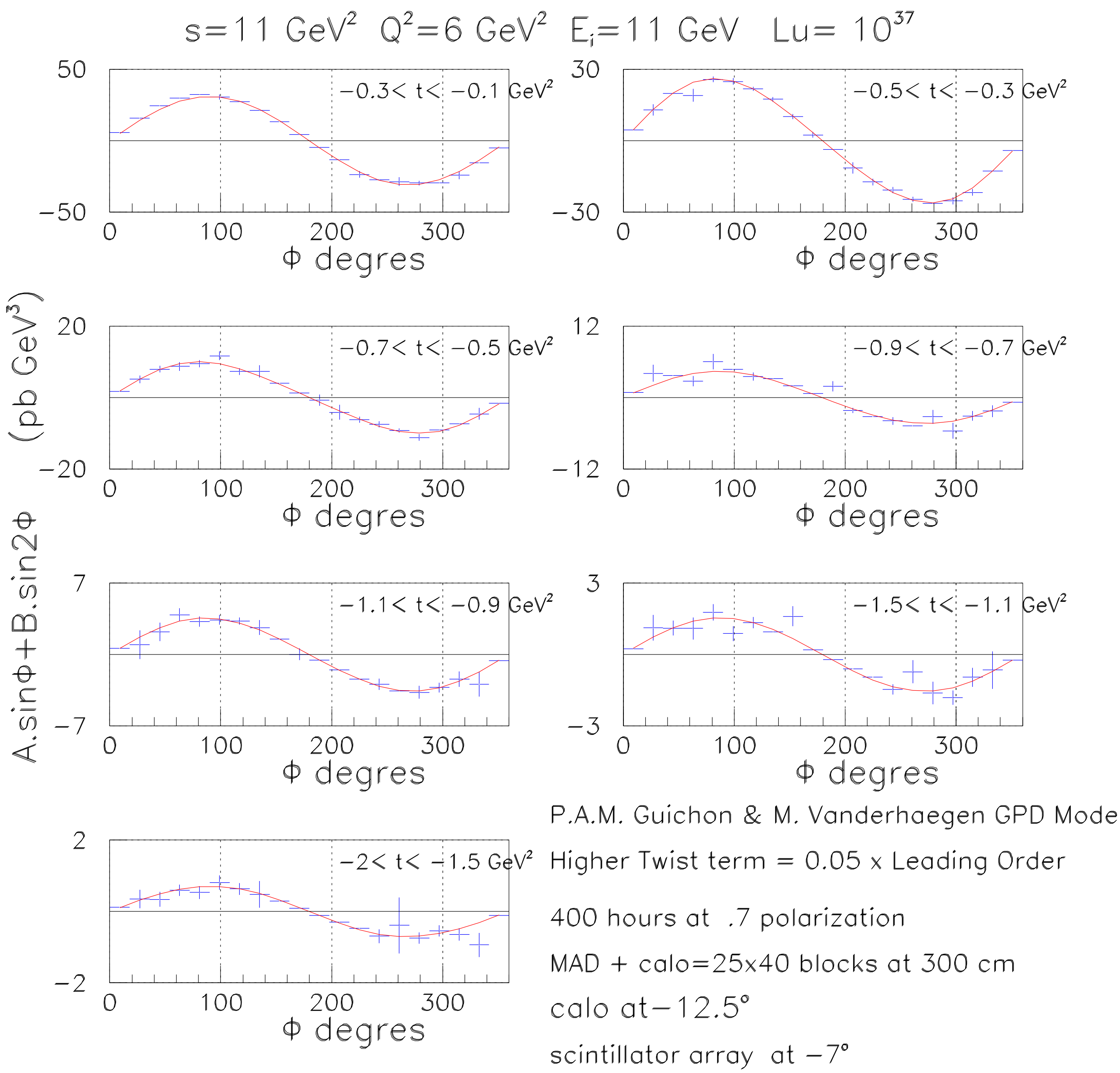

Figure 3.29: Helicity dependent cross sections $\tilde{s}\tilde{u}\,[d\sigma(\vec{e},e'p\gamma) - d\sigma(\vec{e},e'p\gamma)]$ at $\langle x_{\rm Bj}\rangle = 0.35$ in 7 bins in t, weighted by the Bethe-Heitler propagator $\tilde{s}\tilde{u}$. Statistics are for 400 hours at $\mathcal{L} = 10^{37}/\mathrm{cm}^2/\mathrm{s}$. The proton array is centered around the nominal $\vec{q}$ direction of $-7°$, but all active detector elements are more than 20° from the beam line. The Calorimeter is centered at $-12.5°$. The blue points are pseudo data (with error bars) distributed statistically around the values obtained in the simulation. The red curve is a Fourier fit to the pseudo data.

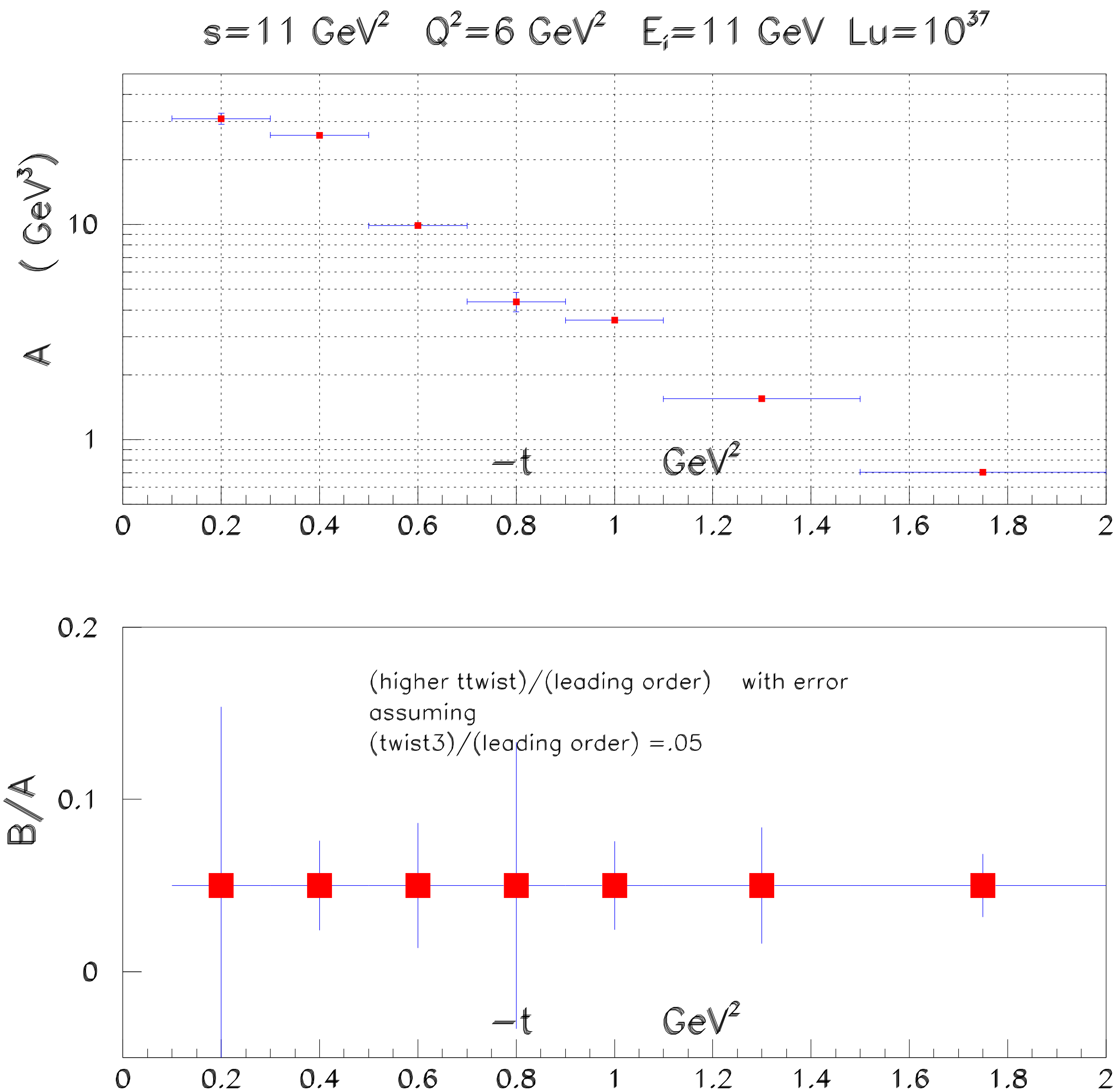

Figure 3.30: Anticipated precision of the extraction of the leading twist $\sin\phi$ and higher twist $\sin 2\phi$ terms as a function of t, at $Q^2 = 6$ GeV^2, $s = 11$ GeV^2 ($x_{\rm Bj} = 0.37$). Statistics are for 400 hour at $\mathcal{L} = 10^{37}/\mathrm{cm}^2/\mathrm{s}$. The horizontal error bands are the widths of the bins. The ratio B/A was fixed at 0.05 in the simulation.

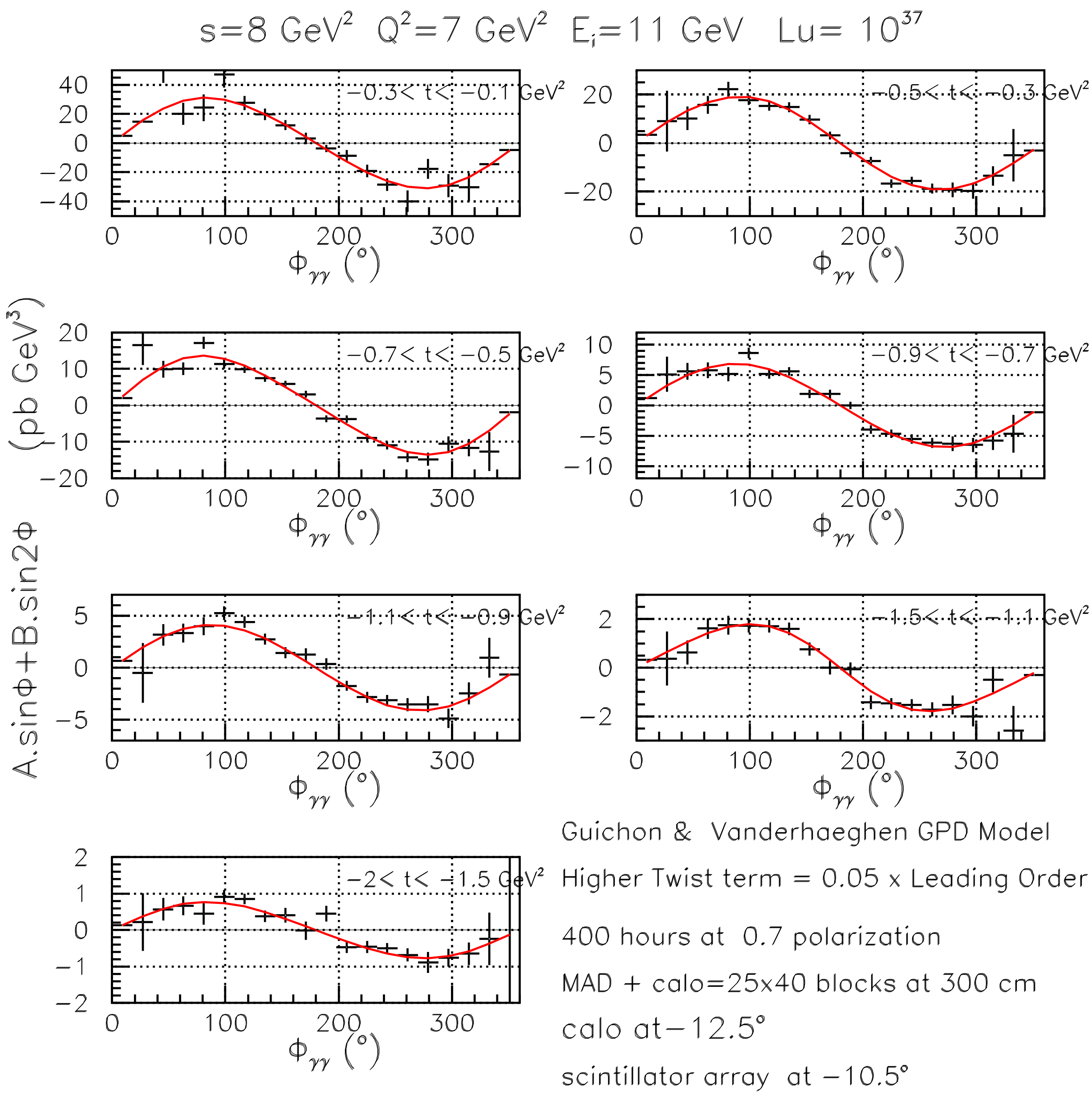

Figure 3.31: Helicity dependent cross sections $\tilde{s}\tilde{u}[d\sigma(\vec{e}, e'p\gamma) - d\sigma(e, e'p\gamma)]$ in 7 bins in t at $\langle x_{\rm Bj}\rangle = 0.50$, weighted by Bethe-Heitler propagator. Statistics are for 400 hour at $\mathcal{L} = 10^{37}/\text{cm}^2/\text{s}$. The central values of the kinematics are listed on the figure.

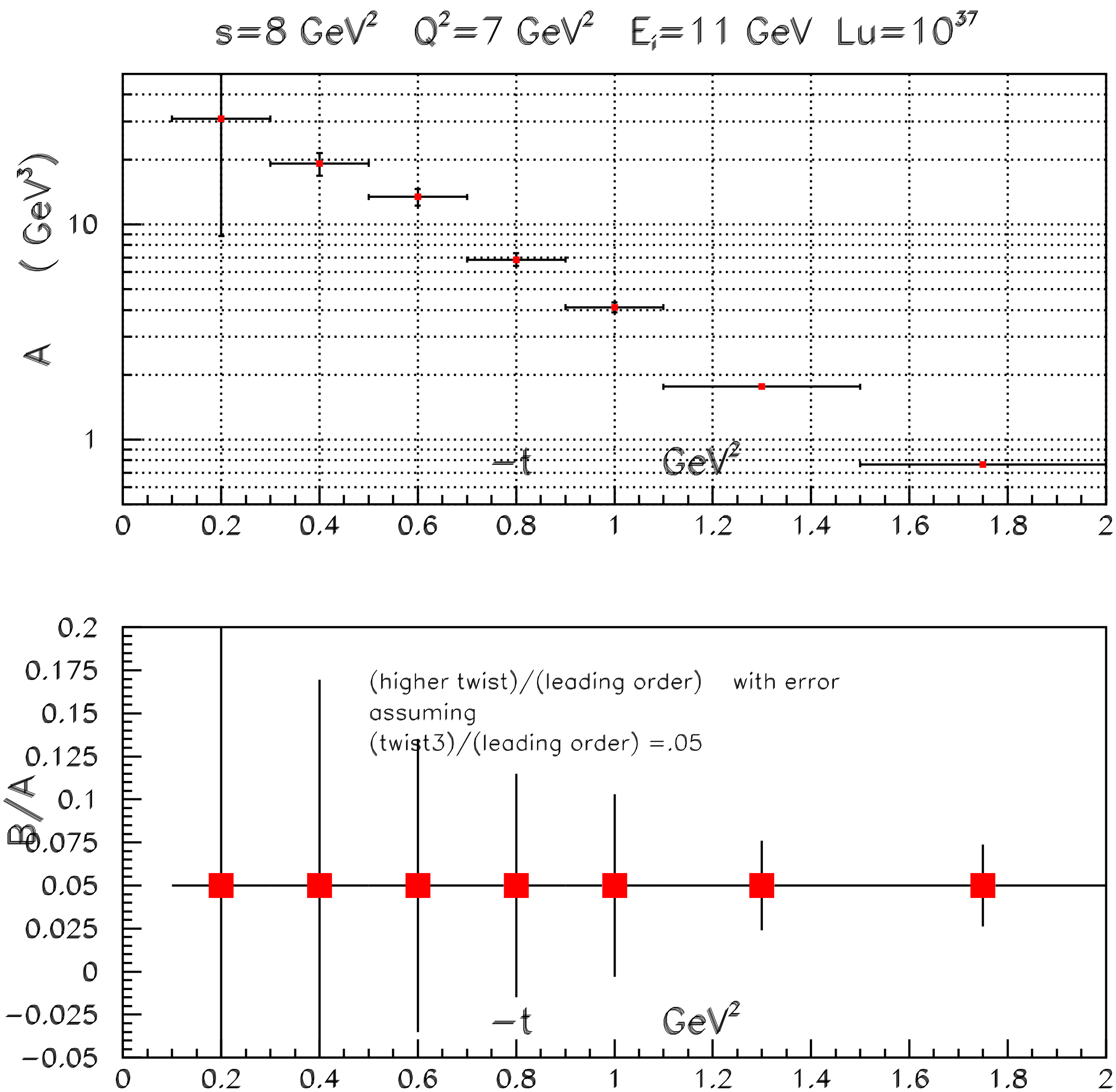

Figure 3.32: Anticipated precision of the extraction of the leading twist $\sin\phi$ and higher twist $\sin 2\phi$ terms as a function of t, at $Q^2 = 7$ GeV^2, $s = 8$ GeV^2 ($\langle x_{\rm Bj}\rangle = 0.5$). Statistics are for 400 hour at $\mathcal{L} = 10^{37}/\text{cm}^2/\text{s}$. The horizontal error bands are the widths of the bins. The ratio B/A was fixed at 0.05 in the simulation.

Thus high-Q^2 measurements of the Generalized Polarizabilities would provide novel new information about the quark structure of the proton.

3.3.6 Virtual Compton Scattering at Large t

The soft overlap mechanism for RCS can be extended to Virtual Compton Scattering $ep \to ep\gamma$. Even low Q^2 gives us additional tests of the reaction mechanism. At fixed (large) t, the Q^2 behavior of the cross section is determined by the Klein-Nishina cross section, and not the nucleon form factors $R_{V,T,A}(t)$.

Some kinematics and count rates are illustrated in Table 3.3.6. The separation of the $ep \to ep\gamma$ and $ep \to ep\pi^0$ channels requires a triple coincidence. This requires a large calorimeter close to the target at large angles. The kinematics, and isolation of the exclusive channel via triple coincidence are illustrated in Fig. 3.33

θ_e	s	Q^2	$\frac{d\Gamma}{dk'd\Omega_e}$	$\theta_p^{\rm lab}$	$p_p'^{\rm lab}$	$\theta_\gamma^{\rm lab}$	$q'_{\rm lab}$	$\theta_{\gamma\gamma}^{\rm CM}$	rate
(deg)	(GeV^2)	(GeV^2)	$\left(\frac{1}{\text{GeV sr}}\right)$	(deg)	(GeV)	(deg)	(GeV)	(deg)	(hr^{-1})
Polarizabilities, $k = 8.8$ GeV, $k' = 5.4$ GeV									
20.4	1.2	6.0	$4.1 \cdot 10^{-5}$	−25	3.2	−33	0.97	−45	16
				−29	3.1	−21	0.99	45	54
Soft-Overlap Mechanism, $k = 8.8$ GeV, $k' = 3.1$ GeV									
17.3	9.0	2.5	$5.9 \cdot 10^{-5}$	−15	5.9	86	0.57	155	8
				−23	4.9	36	1.65	120	6

Table 3.7: Kinematics and Rates for Virtual Compton Scattering. Rates are calculated assuming a luminosity of $4.0 \cdot 10^{38}$/cm^2/s $\times 4$ GeV/k_e (fixed total beam power of 100 μA $\times 4$ GeV= 0.4 MW. For polarizabilities, only the Bethe-Heitler plus Born contribution is calculated. Based on calculations at $Q^2 = 4$ GeV^2, we expect actual rates to be a factor of 4 higher, with a factor of 2 sensitivity to the polarizabilities. The rates in the "Soft-Overlap" section assume s^{-6} scaling, extrapolated from RCS, with a virtual photon flux factor.

3.3.7 Nucleon Photopion Production at 11 GeV in Hall A

Mapping the transition from strongly interacting, non-perturbative Quantum Chromodynamics (QCD) region, where nucleon-meson degrees of freedom are effective to perturbative QCD (pQCD) is one of the most fundamental, challenging tasks in nuclear and particle physics. Exclusive processes are essential in studies of transitions from non-perturbative to perturbative QCD region. Differential cross sections for many exclusive reactions [155] at high energy and large momentum transfer appear to obey the quark counting rules. The quark counting rule was originally obtained based on dimensional analysis [156, 157, 158]. Although it was later confirmed by a short-distance perturbative QCD approach up to calculable powers of the running coupling constant[159], the hadron helicity conservation selection rules predicted in the same approach tend not to agree with data in the similar energy and momentum transfer region. In recent years, a similar trend has been observed in deuteron photo-disintegration experiments at SLAC and JLab [160] - [161]. An onset of the scaling behavior has been observed in deuteron photo-disintegration [161] at a surprisingly low momentum transfer of 1.0 $(\mathrm{GeV/c})^2$ to the nucleon involved. However, a recent polarization measurement on deuteron photo-disintegration [162] shows disagreement with hadron helicity conservation at the kinematics where the quark counting behavior is observed in the differential cross section.

Apart from the early onset of scaling and the disagreement with hadron helicity conservation rules, several other striking phenomena have been observed in pp elastic scattering. This includes: the oscillation of the differential cross-section about the scaling behavior predicted by quark counting rules (s^{-10} for pp elastic scattering) and the anomalous spin correlation coefficient A_{nn} observed in pp elastic scattering [163, 164], i.e. it is ~ 4 times more likely for protons to scatter when their spins are both parallel and normal to the scattering plane than when they are anti-parallel at the largest momentum transfer measured (${p_T}^2 = 5.09$ $(\mathrm{GeV/c})^2$, $\theta_{c.m.} = 90°$). Theoretical interpretation for such an oscillatory behavior and the striking spin-correlation in pp elastic scattering was attempted by Brodsky, Carlson, and Lipkin [165] within the framework of quantum chromodynamic quark and gluon interactions, where interference between hard pQCD short-distance and long-distance (Landshoff [166]) amplitudes was discussed for the first time. Lastly, Carroll *et al.* [167] reported the anomalous energy dependence of nuclear transparency from the quasi-elastic $A(p, 2p)$ process: the nuclear transparency first rises followed by a decrease. This intriguing result was confirmed recently at Brookhaven [168] with improved experimental technique in which the final-state was completely reconstructed. Ralston and Pire [169] explained the free pp oscillatory behavior in the scaled differential cross section and the $A(p, 2p)$ nuclear transparency results using the ideas of interference between the short-distance and long-distance amplitudes and the QCD nuclear filtering effect. Carlson, Chachkhunashvili, and Myhrer [170] have also applied such an interference concept to the pp scattering and have explained the pp polarization data. On the other hand, Brodsky and de Teramond [171] claimed that the structure seen in $s^{10}\frac{d\sigma}{dt}(pp \to pp)$, the A_{NN} spin correlation at $\sqrt{s} \sim 5$ GeV, and large c.m. angles [163, 164], and the $A(p, 2p)$ transparency result can be attributed to $c\bar{c}uuduud$ resonant states.

The $\gamma n \to \pi^- p$ and $\gamma p \to \pi^+ n$ photopion reactions are essential probes of the transition from meson-nucleon degrees of freedom to quark-gluon degrees of freedom. The cross sections of these processes are also advantageous for the investigation of the oscillatory behavior around the quark counting rule prediction. The relatively higher rates for these processes will also allow angular scans to investigate the t and p_T dependence of the scaling behavior in addition to the usual energy scan investigating the s dependence. Recent results from deuteron photo-disintegration (E96-003) [161] have shown the importance of doing such angular scans. Moreover, these photoreactions in nuclei allow the search for the QCD nuclear filtering and color transparency effects. The nuclear filtering effect refers to the suppression of the long distance amplitude in the strongly interacting nuclear environment, which is complementary to color transparency effect in which large momentum transfers select out short distance amplitudes which are then free to propagate through the passive nuclear medium.

An experiment studying these reactions (E94-104) was completed recently in Hall A. The preliminary E94-104 results in a rather coarse step of $\sqrt{s}$, seem to suggest oscillatory behavior in $s^7 \frac{d\sigma}{dt}$ in both the $\gamma p \rightarrow \pi^+ n$ and the $\gamma n \rightarrow \pi^- p$ processes. An experiment (E02-010) to perform a fine scan in the center-of-mass energy region of 2.3 GeV $\leq \sqrt{s} \leq$ 3.4 GeV with photopion productions from nucleons was approved recently at JLab. With the 12 GeV energy upgrade, such measurements can be extended to 11 GeV. This extension is crucial because it allows detailed investigation of the scaling/oscillatory scaling behavior both **below** and **above** the charm threshold.

For the coincident $d(\gamma, \pi^- p)$ measurements from deuterium and other nuclear targets the requirement of two spectrometers capable of reaching high momenta of about 6.5 GeV, make these measurements ideal in Hall C using the HMS and the planned Super-HMS. However, for the $\gamma p \rightarrow \pi^+ n$ process, the detection of the π^+ particle alone is sufficient for the two-body process, thus making Hall A advantageous by employing the planned Medium Acceptance Spectrometer (MAD). Furthermore, using the combination of the MAD spectrometer and the Hall A large acceptance photon calorimeter which was used successfully in the recently completed real Compton scattering experiment, the $\gamma p \rightarrow \pi^0 p$ process can be studied by detecting the proton (MAD) and the π^0 particle (calorimeter) in coincidence. These measurements can be carried out using a 50 μA electron beam impinging on a 6% copper radiator, and a liquid hydrogen target.

In our estimates we have used realistic angular acceptance for the MAD spectrometer (25 msr for angle setting greater than 25°, and 4.5 msr at the most forward angle, 12°) and 15-cm LH2 and LD2 targets. The time estimated includes time for running without a radiator. Fig. 3.34 shows the projected result for an energy (s) scan of $\gamma p \rightarrow \pi^+ n$ together with a 3% point-to-point systematic uncertainty and a 2 % statistical uncertainty. According to our estimate the projected result can be achieved in 35 hours, which does not include the estimate of the overhead required for such a measurement. Fig. 3.35 shows the projected result for an energy (s) scan of $\gamma p \rightarrow \pi^0 p$ together with a 5% point-to-point systematic uncertainty and a 2 % statistical uncertainty. This measurement will be carried out in coincidence mode and the required beam time is 100 hours, which does not include any overhead. In the above beam time estimates, we assumed 100% for the overall data taking efficiency.

3.3.8 Polarization in Meson Photoproduction with MAD

Polarization measurements can play a crucial role in understanding the reaction mechanism of wide angle meson photoproduction at high energy. The scattering amplitude at asymptotic energies is dominated by multi-gluon exchange within the minimal Fock-state of the nucleon and meson. The section on Real Compton Scattering describes the soft overlap process that likely dominates at high energies below the asymptotic limit. In the case of RCS, these two mechanisms predict large, but opposite, polarization observables. Similar phenomena are expected in the meson production case.

There are several photoproduction reactions that are quite attractive, in that they allow determination of both cross sections and polarizations to large values of s and $-t$. The reactions of interest include $\vec{\gamma} p \rightarrow \vec{p} \pi^0$, $\vec{\gamma} p \rightarrow K^+ \vec{\Lambda}^0$, with $\Lambda^0 \rightarrow p \pi^-$, and $\vec{\gamma} \vec{n} \rightarrow p \pi^-$ with the neutron polarized within a polarized ^{3}He target.

Neutral Pion Photoproduction: Recoil polarimetry of the proton allows a determination of the induced polarization p_y and the polarization transfers C_x and C_z, for a longitudinally polarized electron beam. The $\vec{\gamma}p \to \vec{p}\pi^0$ reaction can be measured with singles protons at lower energies or forward proton angles, because of the kinematic separation from ep elastic scattering, and because the cross sections are much larger than those for real Compton scattering (RCS). At higher energies and more backward angles, the ep peak and its radiative tail dominate the spectrum. During the recent Hall A G_{Ep} [172] and RCS [173] experiments, data were taken with an HRS spectrometer to detect protons, and with calorimeter arrays to detect the coincident electrons and photons, respectively. These experiments have both demonstrated the feasibility of using a calorimeter for coincidence measurement of the two photons from the π^0 decay, allowing a clean measurement of $\vec{\gamma}p \to \vec{p}\pi^0$.

Fig. 3.36 shows the expected induced polarization that could be obtained with a polarimeter installed in MAD, and coincident π^0 detection to reduce background. By measuring a kinematically complete final state, it is not necessary to limit data to be near the photon endpoint, and the need for multiple beam energies is reduced. This procedure detects only the π^0 decays in which the photons are near 90° in the π^0 rest frame, reducing efficiency ≈50%, but removing almost all backgrounds. Cross sections were assumed to follow the scaling rules. Times estimates used 1 day of beam time spent at each angle. The electron beam energy was 7 GeV. The momentum acceptance of MAD allows data to be taken over a wide range of incident photon energies at the same time, almost 2 GeV, but the range is limited for backward angle π^0s by the angular range of the coincident π^0, about 10°. Uncertainties of about 0.1 on C_x, p_y, and C_z are generally achievable in this time, for each 200 MeV bin of incident photon energy. The variation in uncertainty with angle results largely from spin transport in the MAD spectrometer, with some influence from the variation in cross section and solid angle with angle and the polarimeter figure of merit with proton momentum. Thus, in about 2 weeks, 15 angles are taken every 5 degrees in the c.m., to allow the determination of the contribution of any high spin resonances. This leads to about 15 angles × 10 energy bin × 3 polarization observables = 450 data points for E_γ = 5 - 7 GeV. Good data can be taken in reasonable beam times for beam energies up to about 9 GeV. The angle range is constrained by the forward angle limits of MAD and the calorimeter.

$K^+\Lambda^0$ Photoproduction: The $\vec{\gamma}p \to K^+\vec{\Lambda}^0$ reaction is detected through coincidence measurements of the outgoing K^+ and the proton from the $\Lambda^0 \to p\pi^-$ decay. The decay has a 64% branching ratio, and is also self analyzing. In the Λ^0 rest frame, the decay distribution has the form $1 + AP\cos\theta$, where θ is the angle between the polarization direction and the proton momentum vector, and the analyzing power $A = 0.64 \pm 0.01$. Because the proton is heavier, it covers a smaller phase space in the lab than does the π^-. Once the Λ^0 momentum exceeds ≈2 GeV/c, most of the decay cone can be captured in a single setting of the MAD spectrometer.

Test measurements in Hall A in 1999 showed that the major backgrounds come from real π^+p coincidences, which appear to arise from ω photoproduction, and from random π^+p coincidences. The Hall A measurements at 3.3 GeV and $90^\circ_{\rm cm}$ successfully determined the Λ^0 polarization without the use of any particle identification in the spectrometers - true coincidences were determined only from coincidence time of flight, and the true to random ratio was about 1. Much cleaner measurements are possible with Cherenkov detectors, preferably a RICH, to remove a large fraction of the π^+ background.

The uncertainties for $K^+\Lambda^0$ photoproduction are similar to those for π^0 photoproduction. While the polarimetry is much more efficient, needing only a few percent as many counts, and cross sections are roughly similar, it is not possible in general to detect the π^- from the Λ^0 decay. Since the measurement is not kinematically complete, only data near the endpoint are useful, and multiple beam energies are needed. Also, the limited maximum momentum of the HRS spectrometer restricts kinematics in which the K^+ goes forward at high energies.

π^- Photoproduction on the Neutron: The reaction $\vec{\gamma}\vec{n} \to p\pi^-$ also allows easy access to polarization observables. If the recoil polarization is not measured, the cross section has the form [174]:

$$\begin{aligned} \frac{d\sigma}{dt} &= \frac{d\sigma}{dt}_{\text{unpol}}\Big[1 - P_T\Sigma\cos 2\phi + P_x(-P_T H\sin 2\phi + P_\circ F) \\ &\quad + P_y(T - P_T P\cos 2\phi) - P_z(-P_T G\sin 2\phi + P_\circ E)\Big]. \end{aligned} \tag{3.43}$$

Here, ϕ is the angle between the linear polarization of the beam and the reaction plane, P_x, P_y, and P_z are the target polarization components, P_T and $P_\circ$ represent the degree of linear and circular polarization of the photons, and Σ, H, F, T, P, G, and E are the seven polarization observables. Unless one uses an oriented crystal radiator, or detects the low energy forward electron that produced the Bremsstrahlung, all directions of linear polarization are averaged over and $P_T = 0$. The figure of merit for these observables is slightly less than that for $\gamma p \to \pi^0 p$ recoil polarizations. The polarimetry figure of merits are about equal, with $A^2\epsilon$ about $0.1^2 \times 0.3 = 0.003$ for the polarimeter, and $P^2\epsilon$ about $0.4^2 \times 0.01 = 0.0016$ for the polarized target. Large coincidence efficiency is possible if the momentum of the proton or pion to be captured by MAD is a few GeV/c. The $p\pi^-$ kinematic correlation, spread out by the initial state Fermi momentum of the neutron, then remains mostly within the acceptance of MAD.

The use of cryogenic ^{3}He instead allows $p\pi^-$ coincidences at sufficient rates that recoil polarimetry measurements are feasible. The reduced rate, from the smaller solid angles of HRS + MAD combined, as compared to the MAD + calorimeter measurement, reduces the feasible range of the experiment. However, if both beam-target and beam-recoil polarizations are measured, model independent determinations of the reaction amplitudes are possible - see [175] for details.

3.3.9 Deuteron Photodisintegration

The deuteron photodisintegration reaction, $\gamma d \to pn$, is one of the simplest reactions for studying explicit quark effects in nuclei. A discussion of this is presented in detail in a recent review [176]. Here, we briefly summarize the argument.

Fig. 3.37 shows the induced polarization in deuteron photodisintegration. For clarity, only data from Stanford [177], Tokyo [178, 179], and Jefferson Lab [180] are shown. In the meson–baryon calculations, resonance–background interferences are generally expected to lead to large polarizations. This is shown in the calculation from Kang *et al.* [181]. The more recent, technically superior calculation of Schwamb and Arenhövel [182, 183] indicates the difficulty understanding p_y, even at low energies at which only the Δ resonance should have a significant effect. Explicit inclusion of all resonances for energies up to 4 GeV is unlikely, given the 286 channels needed for currently known four–star resonances. Indeed, within this framework it appears that somehow the combined effects of all resonance conspire to make the induced polarization largely vanish.

Using quark degrees of freedom naturally averages over all the baryon resonances. There is currently only one available calculation of polarizations in a quark framework. Sargsian [184] relates photodisintegration to the photo-quark coupling, the deuteron wave function, and nucleon-nucleon scattering. The physical picture is that the photon is absorbed on quarks being exchanged between the two nucleons. Sargsian estimates that the induced polarization and the polarization transfer observables are all small for beam energies up to 4 – 5 GeV.

Cross section data allow the reaction to be studied to much higher energy. Fig. 3.38 shows cross sections measured at high energies, from JLab [185, 161] and SLAC [186, 187, 188], along with the lower energy Mainz data [189]. At sufficiently high energies at each angle, the cross sections start to fall about as s^{-11}. The threshold for this behavior corresponds to a transverse momentum slightly over 1 GeV.

Meson-baryon model calculations from Kang *et al* [181] and from Lee [190] are shown in Fig. 3.38 only at 90°, and have only been carried out for lower energies. The shaded region is the calculation from Sargsian [184]; a region is indicated since uncertainties in the nucleon-nucleon data base, along with needed interpolations, lead to uncertainties in the prediction. The green dashed line shows the quark gluon string model [191, 192], which uses Regge trajectory methods to treat the high energy, low t data as arising from 3-quark exchange. The dotted purple line is the reduced nuclear amplitudes model of Brodsky and Hiller [193], which attempts to extend perturbative QCD expectations to lower energies by incorporating aspects of the soft physics in the reaction mechanism. (The lines shown assume a fixed, angle–independent normalization. The actual angle dependence is unknown, and could be taken from the data.) The dash dot purple line represents an estimate from Raydushkin [194] that absorption of the photon on exchanged quarks should lead to a kinematic dependence proportional to the nucleon elastic form factor to the fourth power times phase space factors. While none of the theories agree with all of the data as well as one would like, they do indicate that quark models can approximately reproduce the cross section data.

At this point, is is extremely difficult to extend either the cross section or polarization measurements to higher energies at JLab with existing equipment. Experimental considerations for measurements of $\gamma d \rightarrow pn$ are dominated by the small cross sections and by the high momentum of the outgoing proton, relative to other reaction products. The increased solid angle of the proposed MAD spectrometer would allow cross sections and polarization to be measured at higher energies, if backgrounds are low, as they have been for existing Hall A experiments. Even so, raw data rates will only be a few Hz.

The MAD spectrometer will allow cross section measurements to photon energies near 8 GeV; this is a straightforward extension of the latest Hall C singles measurements [161].

The Hall A polarization data can be extended to about 4 GeV.

Current data are taken as singles proton measurements. The use of a ≈50% efficient coincident neutron detector would allow rejection of 3-body final states from pn kinematic correlations. In this case, the full momentum acceptance of MAD could be used to obtain at the same time polarizations over a range of ≈1 GeV of incident photon energies. Fig. 3.39 shows projected results for the induced polarization, using MAD plus a coincident neutron detector. Similar uncertainties are obtained at the same time for the polarization transfer data, if a polarized electron beam is used. Care must be used about calibrating the neutron detector if it is to be used for cross section measurements. Its efficiency can be determined with the much higher cross section $\gamma p \to \pi^+ n$ reaction, after correctly treating the electroproduction background contributions.

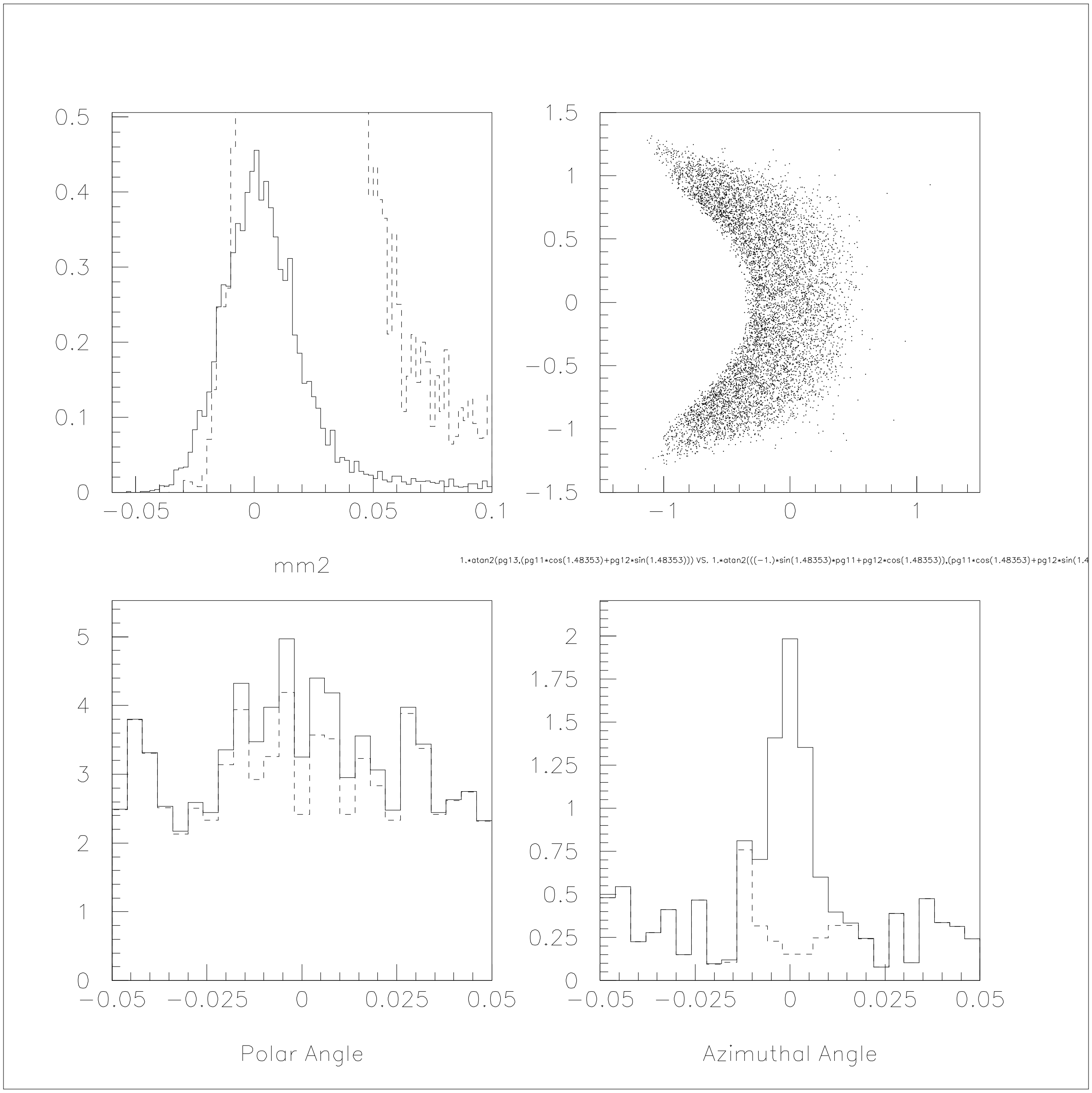

Figure 3.33: Virtual Compton Scattering in the "soft-overlap" region, with HRS-MAD-calorimeter coincidences. Kinematics are $Q^2 = 2.5$ GeV^2, $s = 9$ GeV^2, and $\theta_{\gamma\gamma}^{\rm CM} = 155°$. Except for the scatter plot, the vertical axis is counts per bin per hour at a luminosity of $2 \cdot 10^{38}$. Upper left: Missing mass-squared in $p(e, e'p)X$; Solid is VCS, dashed is π^0, divided by 10. Upper right, scatter plot of transverse coordinates (m) of VCS photons in a plane 1 m from the target, centered at 85 degrees from the beamline. Lower plots: Difference between expected and detected photon positions for VCS and π^0 decay photons (solid) and π^0 decay photons only (dash). Left plot is polar angle relative to beam axis. Right plot is (laboratory) azimuthal angle. In both plots, a cut $M_X^2 < 0.02$ GeV^2 is imposed. In the right plot, a cut of ± 0.015 is imposed on the left plot.

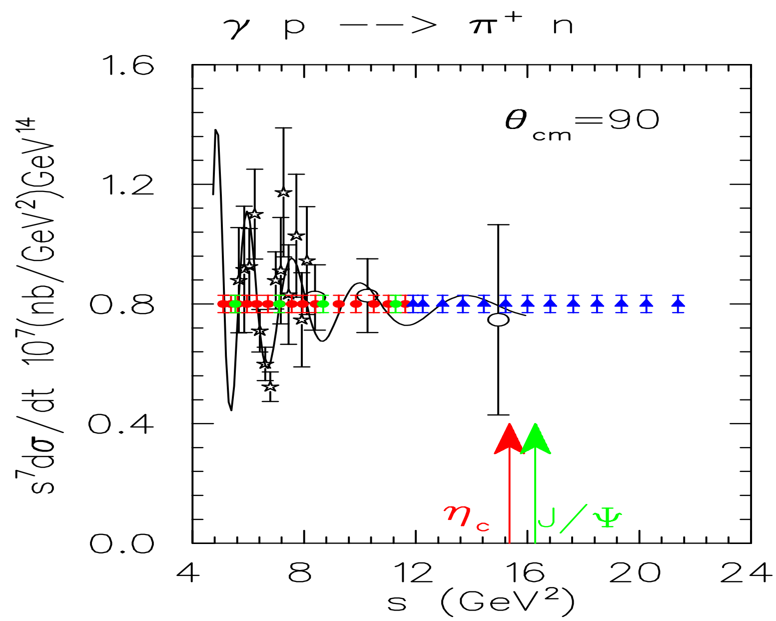

Figure 3.34: The scaled differential cross-section for the $p(\gamma, \pi^+)n$ process at C.M. angle of 90°, as a function of cms energy squared s in GeV^2 along with the projected measurements for JLab at 11 GeV (blue solid points). The red solid points are the projected results from E02-010 and the green solid points show the completed E94-104 data points.

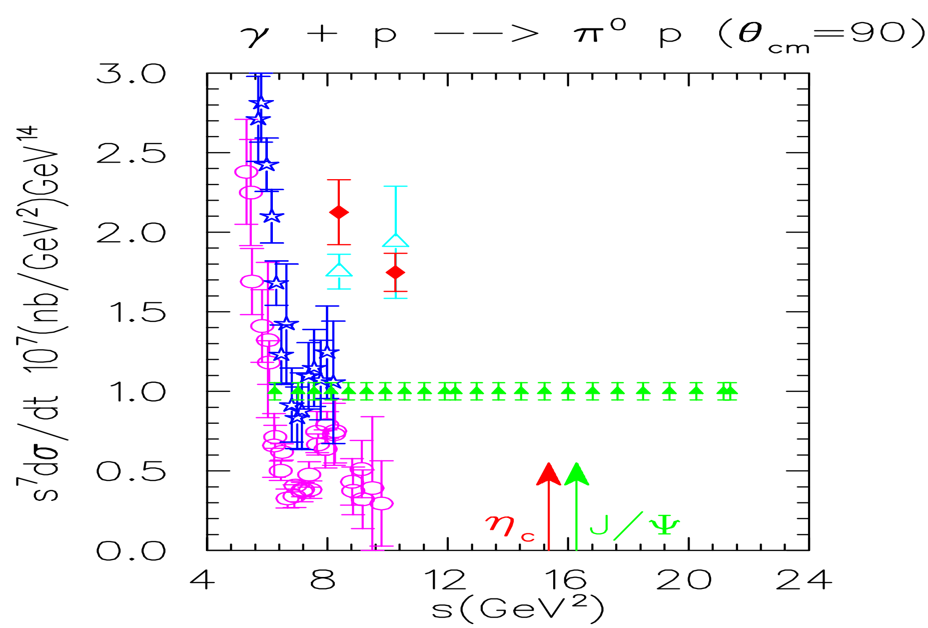

Figure 3.35: The scaled differential cross-section for the $p(\gamma, \pi^0)p$ process at C.M. angle of 90°, as a function of cms energy squared s in GeV^2 along with the projected measurements for JLab at 11 GeV (blue solid points).

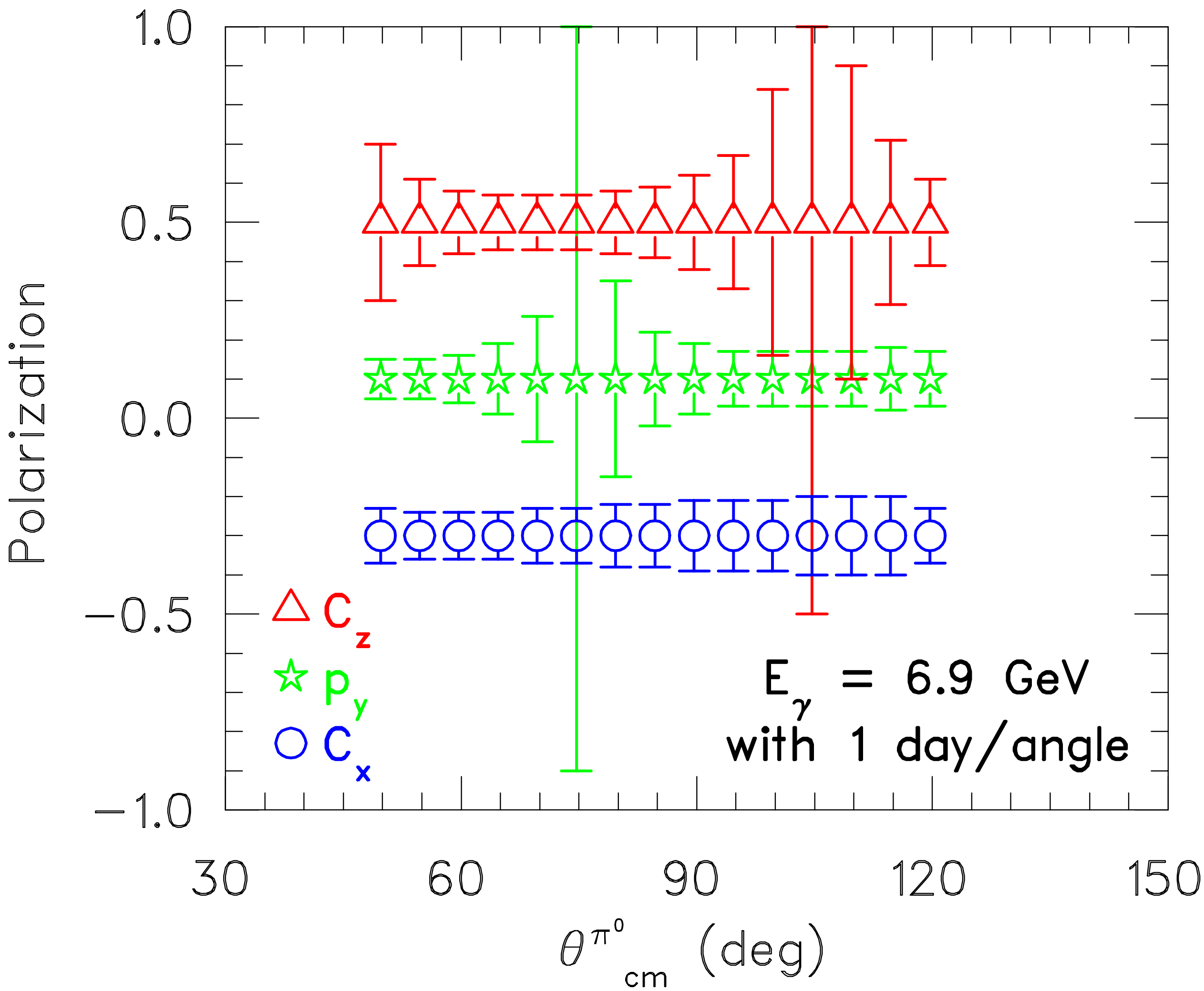

Figure 3.36: Estimated uncertainties for the induced polarization in $\vec{\gamma}p \to \vec{p}\pi^0$, for E_γ = 6.9 GeV, as a function of π^0 angle. The value chosen for the polarizations is arbitrary. One day of beam time at each angle is assumed. Similar quality angular distributions would be obtained at at the same time for several additional 200 MeV bins in photon energy. See text for further details.

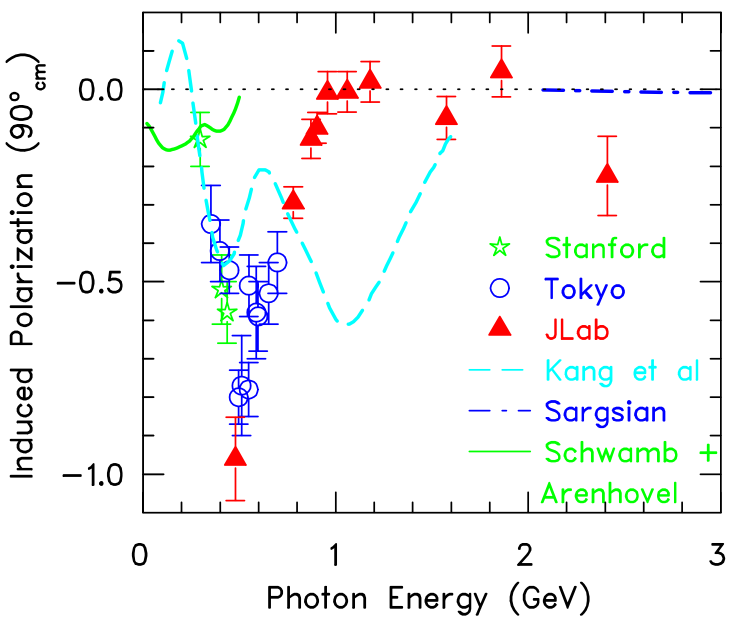

Figure 3.37: Induced polarization in deuteron photodisintegration at $\theta_{\rm cm} = 90°$, as a function of photon energy.

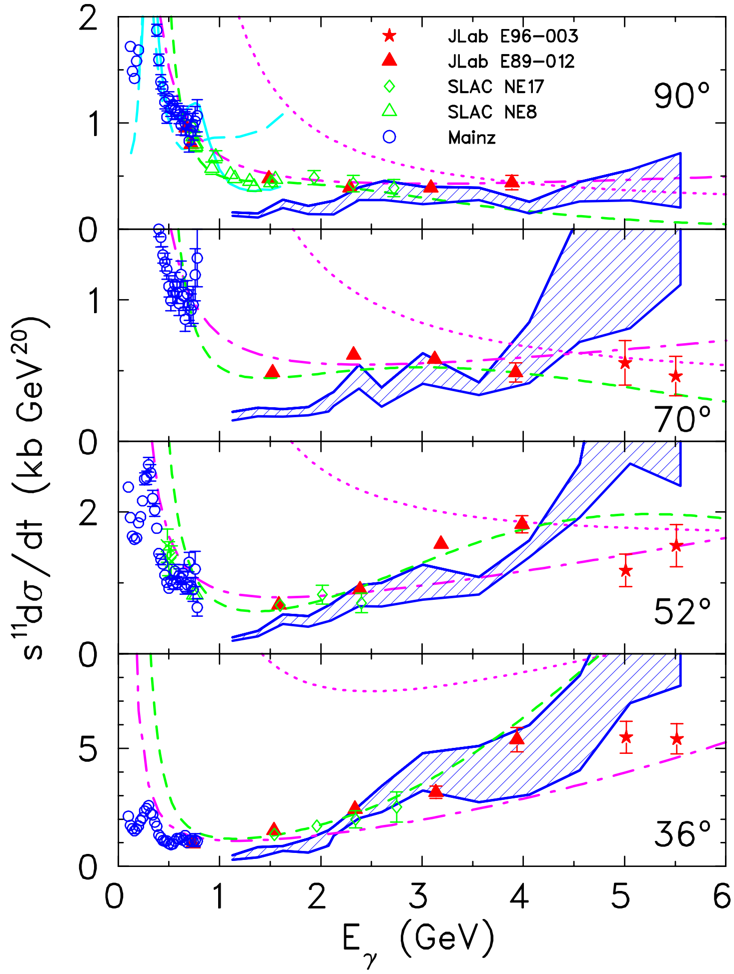

Figure 3.38: High energy deuteron photodisintegration cross sections.

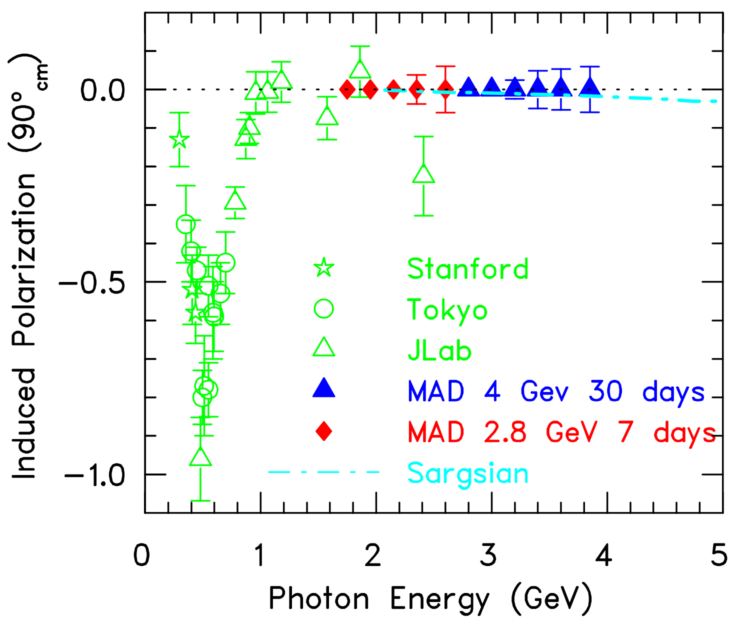

Figure 3.39: Projected results for deuteron photodisintegration polarizations with MAD.

3.4 Hadrons in the Nuclear Medium

One of the main motivations in studying hadrons in the nuclear medium at high energies is to probe the nucleon-nucleon interaction at sub-fermi separations. Because of the existence of the nuclear core one needs considerably higher momentum transfer than the average excitation of the baryonic states ($\sim 0.3 - 1\ GeV$) in order to probe separations smaller than the nucleon size. The Jefferson Lab 12 GeV upgrade will allow the exploration of the high momentum transfer regime where the following questions can be addressed:

- What happens during the brief time intervals when two or more nucleons overlap in space?
- Does new physics emerge in these states where the densities can amount to as much as three to four times the standard nuclear density ρ_0? It is worth noting that these studies would help understand the physics of neutron stars and will have relevance in the investigation of the super-dense nuclear matter at zero temperatures,.
- What is the mechanism of the exchange forces in sub-fermi distances? Can one continue to account for the interactions using meson exchanges or will explicit quark exchange forces start to play a dominant role?
- If densities are high, can one detect the presence of super-fast quarks (quarks carrying momenta greater than those of a nucleon)?

Investigating these questions will allow scientists for the first time to address the more general question of what is the role of Quantum Chromodynamics in the microscopic structure of nuclei.

The main kinematic characteristic needed to address these issues is the large value of the transfered momenta and energies to the nucleus. In order to probe the quark degrees of freedom in nuclei the transfered four momentum in the reaction should exceed the typical hadronic masses in the nucleus, i.e. $Q^2 \gg m^2$. The next kinematic requirement is defined by the specific configuration one wants to probe at small distances. If we are interested in the structure of the exchange interaction at small distances, one has to look for kinematical situations where the high transferred momentum is equally shared between two outgoing particles (e.g. nucleons). This leads to disintegration reactions in light nuclei, like the deuteron and A = 3 systems, at large momentum transfer and fixed C.M. angle As the existing data from JLab shows these reactions are particularly sensitive to the dynamics of the exchanged interactions between two nucleons. If we are interested in the structure of the two nucleons pre-existing at very small space-time separation, then we have to choose the so called "knocked-out" kinematics in which the virtual photon will knock out a nucleon while the correlated nucleons will be detected in the nucleon fragmentation region. In these reactions the knock-out nucleon carries the whole momentum of the virtual photon and, the recoil nucleons will carry the preexisting momenta in the correlations. In deep inelastic kinematics, if short-range nucleon correlations are identified, one may expect the existence of the super-fast quarks which carry momenta exceeding those of individual nucleons. Deep inelastic inclusive scattering at $x > 1$ will kinematically identify those quarks.

Based on the above kinematic requirements one can specify the reactions which will ideally facilitate the above mentioned studies.

- Deep inelastic inclusive scattering at $x > 1$ and large Q^2 for a wide range of the nuclei. The observation of the Bjorken scaling in $x > 1$ region and the measurement of the x distribution of super-fast quarks in this region will be the major objectives in the studies of these reactions. These measurement will use the property of the QCD evolution equation - that with an increase of Q^2 at fixed x, the contribution from higher and higher $x' > x$ become dominant in the DIS cross section. This is a feature of QCD which can be used to study nuclei at very short distances.

- High Q^2 (e, e', N) knock-out reactions. By making measurements of the cross section and asymmetries in this reaction, evidence of color transparency should become apparent.

- Exclusive quasielastic photo/electrodisintegration of light nuclei will search for both color transparency and nuclear filtering effects.

- Semi-inclusive deep inelastic scattering experiments to further our understanding of effects such as fragmentation.

- Elastic scattering experiments to study the short-range nucleon-nucleon interaction, few-body wave functions, isobar and three-body force contributions, and effects from possible quark-cluster admixtures.

3.4.1 Studying Short-Range Correlations via A(e,e')X at $x_B > 1$

When scattering electrons off a nucleon, the range of $x_B \leq 1$. However, for scattering off a nucleus, it is possible for x_B to be larger than unity. At low transfered momenta, where the hadronic description of nuclei is valid, such scattering corresponds to that of a correlated two- or multi-nucleons cluster. In deep inelastic scattering (DIS) x_B is a measure of the fraction of the longitudinal momentum carried by the struck quark. Hence, $x > 1$ indicates that the electron scatters off a super-fast quark that carries more momentum than the nucleon. This corresponds to the DIS description of short-range correlations (SRC) in nuclei and therefore will manifest itself at high transfered momenta by the onset of scaling. Figure 3.40 indicates that for $x_B = 1.5$, only around $Q^2 = 15(\text{GeV/c})^2$, a significant contribution to the cross section comes from the tail of the inelastic scattering.

The contribution of DIS increases with Q^2 and for a fixed (but high enough) Q^2, the relative contribution of the DIS tail increases with decreasing x_B. For larger values of x_B, even higher transfered momenta will be needed to observe DIS. Indeed, Fig. 3.41 displays calculations by M. Sargsian [195] and data from Hall C [196] which indicate that for $^{56}Fe(e, e')X$ at $x_B = 1.5$, two-body correlations are observed. Yet, up to $Q^2 = 7$ (GeV/c)^2, the structure

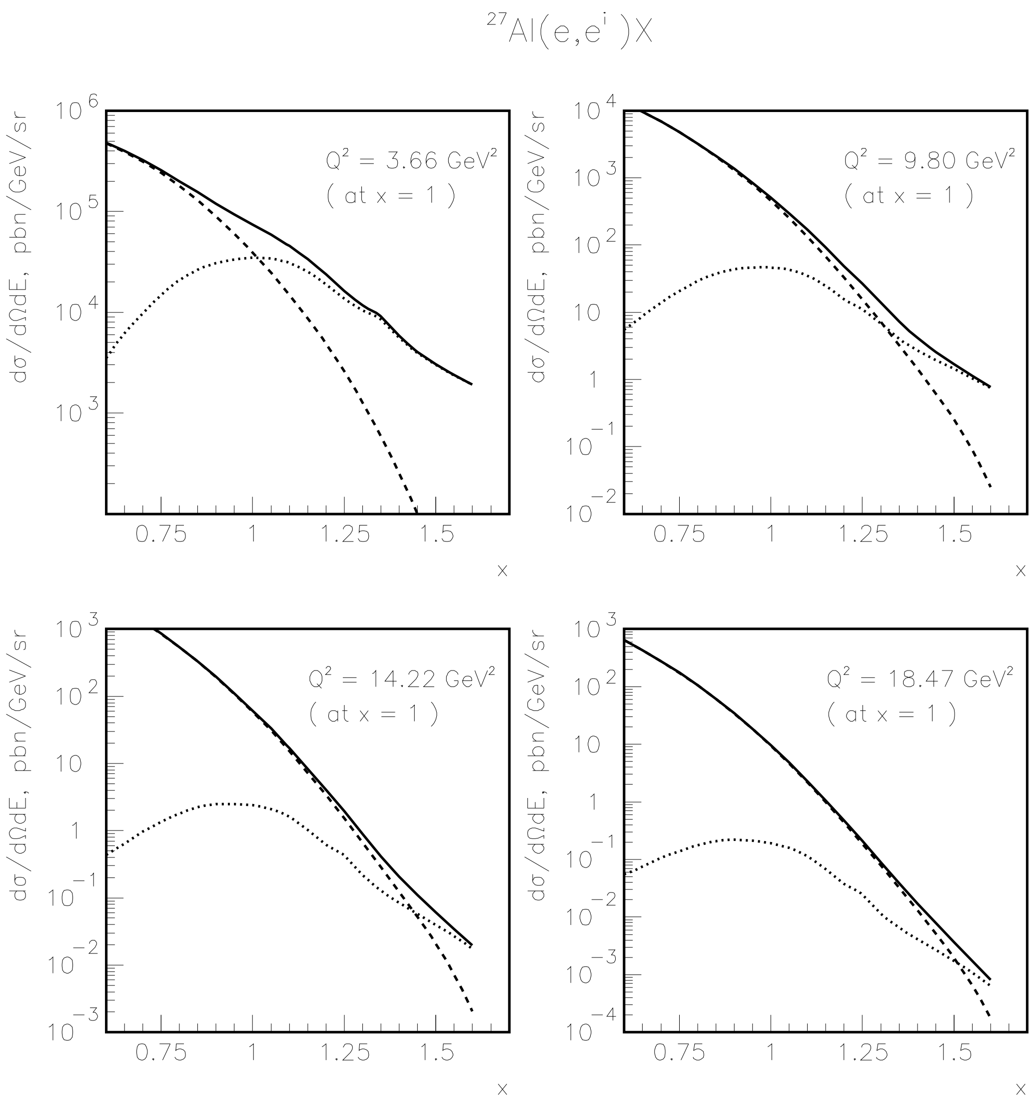

Figure 3.40: Differential cross section for ${}^{27}Al(e,e')X$ as a function of x_B. Solid line is the sum of the quasielastic contribution (dotted line) and the inelastic contributions (dashed line).

function F_2 falls roughly as the form factor and scaling is not observed. According to these calculations, the relative contribution from DIS increase with Q^2, as displayed by the flattening of the curve. Also included in the figure are projected data that can be obtained in Hall A with a 11 GeV beam and the MAD spectrometer.

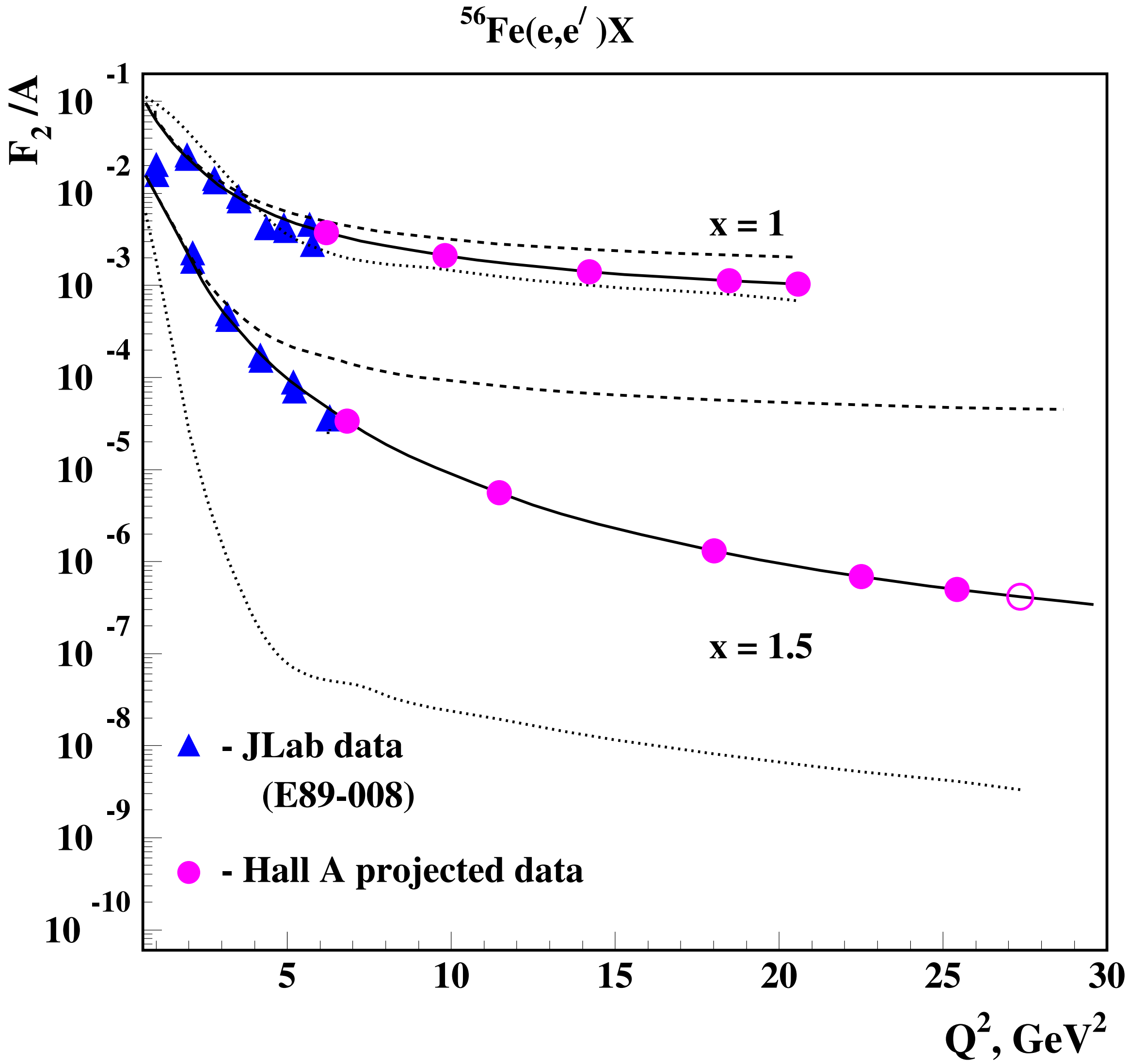

Figure 3.41: Predictions for the onset of scaling for ^{56}Fe(e,e')X. Dotted line - mean-field predictions (no correlations) Solid line includes two-body correlations. Dashed line include two- and multi-body correlations. The data are from Jefferson Lab experiment E89-008 [196].

It should be noted that these calculations assume the onset of SRC at nucleon momentum within the nucleus of about 400 MeV. Within this assumption, at $x_B = 1.5$, the data are consistent with contributions from two-body SRC only. If the onset of correlation is set at a higher nucleon momentum, the multi-nucleon correlations curve will deviate from that of the two-nucleon correlations at a higher Q^2. Hence, multi-nucleon correlations are excluded by these data only if the onset of correlations is at $p_i \simeq 400$ MeV/c. Thus data at higher momentum transfers will not only test the predictions of two-body correlations, but if deviation from preditions are observed, they will determine the nucleon momentum range in which correlations are significant. Moreover, by comparing $F_2(x = const., Q^2)/\mathrm{A}$ extracted from a nucleus to a similar curve extracted from deuterium (where multi-nucleon correlations are not possible), contributions from multi-nucleon correlations can be extracted.

To obtain a good understanding of SRC we plan to measure the structure function $F_2(x_B, Q^2)$ for a fixed $x_B = 1.5$, and for a range of Q^2 up to the point where we are limited by count rates. Similar measurements will be performed on aluminum and deuterium. As of now, there are no data on deuterium. We expect to be able to measure up to Q^2 of at least 25 (GeV/c)^2 for aluminum, and 23 (GeV/c)^2 for deuterium. We anticipate that the onset of scaling will be observed within this range of Q^2. In terms of nucleonic degrees of freedom, the calculated curves for both nuclei will have to be consistent with the values of nucleon momentum corresponding to the onset of SRC. The difference between the F_2/A of the two nuclei will thus be due to multinucleon correlations. Figure 3.42 displays the projected data that can be obtained on deuterium.

The following estimated count rates assume incident beam energy of 11 GeV and the beam current of $60\mu A$. We used a 20 cm long deuterium target which corresponds to 3% of a radiation length and a luminosity of $3.8 \cdot 10^{38} s^{-1} cm^{-2}$. For the aluminum target we assumed a thickness of 1 cm which corresponds to an 11% radiator and a luminosity of $2.3 \cdot 10^{37} s^{-1} cm^{-2}$. This target will have to be cooled which should not pose any special problem. These luminosities are currently used in experiments in Hall A and do not pose any technical problems either.

We use the designed solid angles of the MAD spectrometer: 6 msr at 12°, 18 msr at 20° and 28 msr at angles 35° and larger. The momentum acceptance is ±15% and the momentum resolution is $\approx 10^{-3}$. Because of the large momentum acceptance, the data can be simultaneously obtained for a wide range of x_B, and binned appropriately. Hence, the proposed measurement will produced simultaneously $F_2(Q^2)$ curves for $1.2 \leq x_B \leq 1.6$ with good statistics, and up to $x_B \approx 1.8$ with lesser statistics. The time estimates are based on 1000 counts per bin size of $\Delta x_B = \pm 0.1$ at $x_B = 1.5$. Most importantly, all calculated cross sections assume only two-body short range correlations. For aluminum, if multi-nucleon correlations are present, the cross-section could be significantly larger.

We also estimated backgrounds from pions using the code EPC and a code from SLAC where measured pion yields have been parameterized. Currently these estimates have large uncertainties stemming from the fact that both the kinematics measured at SLAC and the parametrization of EPC have a very small overlap with the kinematics studied here. We therefore use the pion yields obtained only as a rough guide. According to our estimates, the pion background grows with scattering angle (and Q^2), and the pion/electron ratio is approximately 25 for Aluminum at $Q^2 = 23(GeV/c)^2$. This background is easily manageable with the MAD spectrometer which expects to have a pion rejection ratio of at least 10^{-4}. The obtained rates for Deuterium are listed in Table 3.8 and the ones for Aluminum in Table 3.9. For the beam time estimate we assume a statistical error of 3%. At this time we have not included losses due to radiative processes.

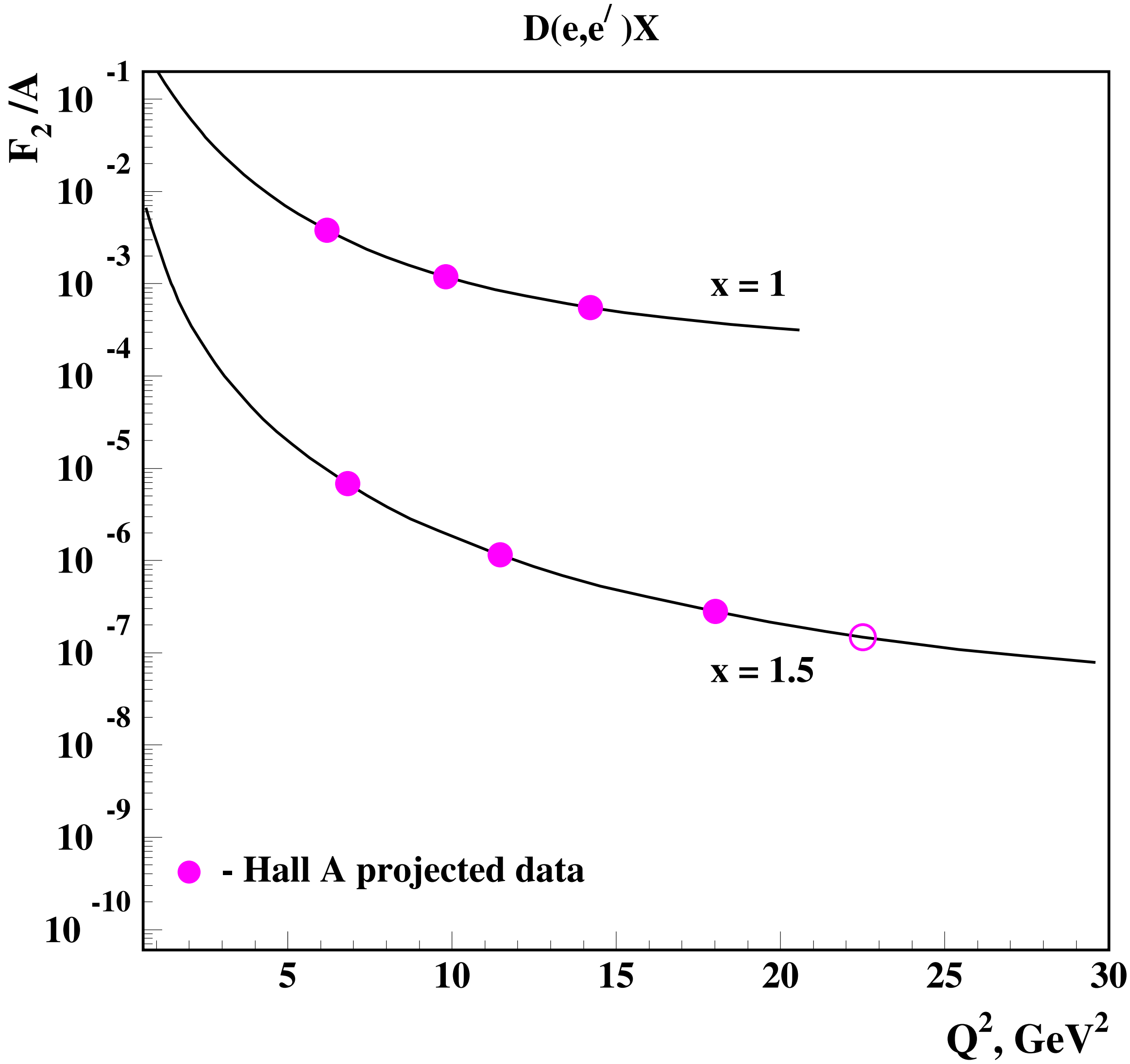

Figure 3.42: Projected data for $d(e, e')X$.

θ_e	$Q^2(GeV/c)^2$	$\frac{d\sigma}{d\Omega d\nu}[\frac{pb}{sr \cdot GeV/c}]$	events/hour	beam-time [hours]
10	3.87	4.48E+1	4.7E+4	2
20	11.47	3.74E-2	1.25E+2	8
30	18.01	2.07E-3	0.85E+1	120
40	22.5	4.37E-4	2.3	500

Table 3.8: Cross sections and rates for deuterium, $x = 1.5$, including two-body correlations.

θ_e	$Q^2(GeV/c)^2$	$\frac{d\sigma}{d\Omega d\nu}[\frac{pb}{sr \cdot GeV/c}]$	events/hour	beam-time [hours]
20	11.47	2.8	0.6E+3	2
25	15.00	5.1E-1	1.2E+2	8
30	18.01	1.5E-1	5.0E+1	20
40	22.5	3.3E-2	1.0E+1	100
50	25.4	1.3E-2	5.0E-2	200
60	27.36	6.8E-3	2.0E-2	400

Table 3.9: Cross sections and rates for aluminum, $x = 1.5$, including two-body correlations only.

The results indicate that for deuterium and within the conditions described above the highest practical Q^2 value is about $Q^2 = 23$ $(GeV/c)^2$ while aluminum can be measured up to $Q^2 = 25$ (GeV/c)^2. At these attainable Q^2 values we expect to observe x-scaling. If multi-body correlations are present, the count rates should be significantly higher and the measurement can be extended to even higher Q^2.

3.4.2 Color Transparency in Few Body (e,e'p) Reactions

Color Transparency (CT) has emerged as a promising tool for the understanding of the nucleon structure in terms of quarks and gluons [197]. Its basic concepts involve the selection, via a hard exclusive reaction at sufficiently high momentum transfer (Q^2), of a very special quark configuration in a hadron: the minimal valence state where all quarks are close together and constitute a small size color neutral (or mini-hadron) configuration. Such a color singlet system cannot emit or absorb soft gluons and therefore experiences much reduced strong interaction with other nucleons when traveling through the nuclear medium.

While CT as a direct consequence of the Quantum Chromo-Dynamics (QCD) physics in hard exclusive processes is not questionable, its applicability and its manifestation in a given experiment remain open problems. Indeed, a non-ambiguous evidence of CT not only requires the selection of a small size configuration but also a clear signature of the subsequent reduced interaction. The main parameter that governs the CT phenomenon is the momentum transfer of the virtual photon that controls the transverse size and part of the coherence length of the mini-hadron. The latter corresponds to the distance required for the mini-hadron to evolve from its minimal valence state toward its asymptotic wave function.

There are several ways to look for CT effects in nuclei. The study of quasiexclusive hard reactions A(p,2p) and A(e,e'p) can shed light on the range of Q^2s necessary for the wavefunctions of nucleons to be dominated by point like configurations (PLC) [198, 199]. If Q^2 is large enough, one expects both the projectile and the scattered particle travel through the nucleus in pointlike configurations. A straightforward way is to determine the transparency ratio $T = \sigma_{exp}/\sigma_{PWIA}$ in (e,e'p) reactions as a function of Q^2 and various nuclei A. Experiments at SLAC [200] and JLab [201] did not find any such effects when they studied these reactions for various nuclei but their range in Q^2 was limited to $\sim 8(\mathrm{GeV/c})^2$. It is possible that these color transparency effects will start showing up at higher values of Q^2 possible with the 12 GeV upgrade. In Hall A with the MAD spectrometer and a central momentum of 6 (GeV/c), it is possible to determine the transparency ratio T for various nuclei upto Q^2 values of 11 $(\mathrm{Gev/c})^2$. By decreasing the bend angle of the spectrometer, a central momentum of $\sim$ 8 (GeV/c) can be obtained and Q^2 of 13.5 $(\mathrm{GeV/c})^2$ can be achieved.

A more sensitive way to observe the onset of CT in nuclei is to look for processes where the ejectile interacts with other nuclei on its passage within the nucleus [202, 203, 204, 205]. A large portion of the (e,e'p) cross section beyond $p_{recoil} \geq 300$ MeV/c originates from recoil nucleons with lower momenta rescattering. With the advent of CT, this rescattering should decrease as a function of increasing Q^2, and produce a more significant effect than just measuring the transparency ratio T, even at low values of Q^2. Another important advantage of studying this reaction process is that the effect can be studied even in the lightest nuclei $({}^2H, {}^3He, {}^4He)$ for which wave functions are known much better and the eikonal approximation which accounts for all orders of rescattering[203, 204, 205] can provide a reliable base line calculation.

A suitable measure of this effect can be studied in the (e,e'p) reaction as a ratio R of the cross section in kinematics where this rescattering term is dominant ($p_{recoil} \sim 400MeV/c$) to the cross section in kinematics where single scattering is dominant ($p_{recoil} \leq 200MeV/c$) and Glauber screening is important. Figure 3.43 shows these regions clearly in the recent ${}^3He(e,e'p)d$ reaction cross section as a function of the missing momentum [206] for a low value of $Q^2 = 1.55(Gev/c)^2$. In Table 3.10, we show the kinematics and the estimated running times in studying the ${}^2H(e,e'p)n$ reaction with a combination of the MAD detector and the 4 GeV/c HRS spectrometer up to Q^2 values of $\sim 13.5(Gev/c)^2$. The predicted value of this ratio $R = \sigma(p = 400MeV/c)/\sigma(p = 200MeV/c)$ for the case of D(e,e'p) and the effect of color transparency is quite dramatic even at low values of Q^2. In all cases, the CT effects are estimated within the quantum diffusion model (QDM) of Ref. [207] utilizing two values for the expansion parameter $\Delta M^2 = 0.7$ and 1.1 GeV^2, which characterize the time development of the PLC during the propagation in the nuclear medium. These two values of ΔM^2 give the upper and lower limit of CT predictions within the QDM model.

We estimate 100 hours for the D(e,e'p) and approximately 200 hours each for ^{3,4}He(e,e'p) reactions for studying the the dependence of R as a function of Q^2 in the range 4 to 13.5 $(Gev/c)^2$ in intervals of 2 $(Gev/c)^2$ as shown in Table 3.10). For the three lightest nuclei $({}^2H, {}^3He, {}^4He)$, where this effect is supposed to be quite pronounced, the total running time would be approximately 500 hours.

3.4.3 Recoil Polarization in $(e, e'p)$ Reactions at Large Q^2.

Another straightforward way to examine the nucleon for point like configurations, PLC, is the use of quasi-free $(\vec{e}, e'\vec{p})$ reactions on nuclei. Here, we propose to investigate both CT, and nuclear filtering (NF) in the same experiment, by measuring recoil proton polarizations; at the same time cross sections with extremely high statistics will be obtained parasitically. The large solid angle and momentum acceptance of MAD coupled with a focal plane polarimeter

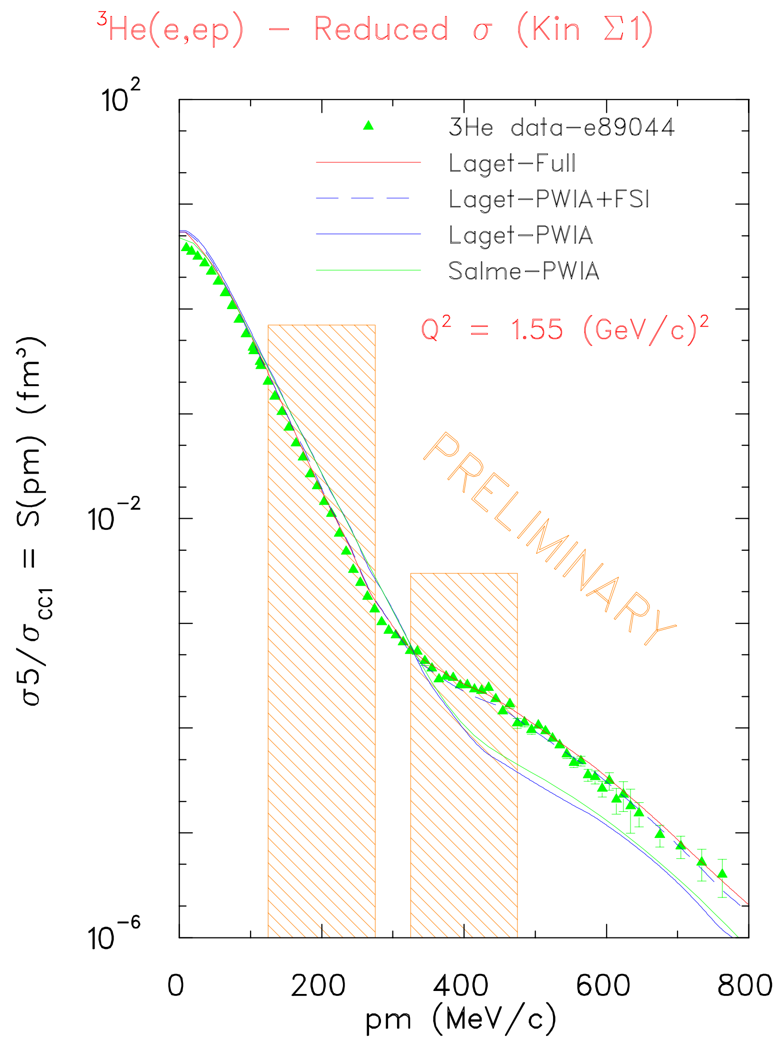

Figure 3.43: $^3He(e,e'p)d$ [206]

Table 3.10: Kinematics and Run Time Estimate for $R = \sigma(p = 400\ MeV/c)/\sigma(p = 200\ MeV/c)$ for ${}^2H(e,e'p)n$ reaction. The total estimated running time is $\leq$ 100 hours for a $\leq$ 5% uncertainty in the ratio R for all Q^2 points.

Q^2	E_i	E_f	θ_e	$p(=q)$	$p_R = 200MeV/c$			$p_R = 400MeV/c$			Total
$(GeV/c)^2$	GeV	GeV	deg	GeV	θ_p deg	cts/hr	Time	θ_p deg	cts/hr	Time	hours
4.0	6.6	4.468	21.22	2.90	37.51	7.2e+4	1	41.37	6150	1	2
6.0	6.6	3.403	29.96	4.00	27.78	6000	1	30.57	500	1	2
8.0	6.6	2.337	42.21	5.09	20.10	665	2	22.29	53	8	10
10.0	8.8	3.471	33.25	6.17	19.73	710	2	21.53	57	8	10
12.0	8.8	2.405	44.23	7.25	14.91	131	10	16.44	10	40	50
13.5	11.0	3.806	32.99	8.06	16.28	250	4	17.65	20	20	24

allow studies that are not feasible with existing experimental equipment, or with Hall C HMS equipped with a focal plane polarimeter. The main point here is that, from moderate to large Q^2, MAD can capture the entire Fermi cone of coincident protons in a single setting. This allows nuclear quasi-free *ep* coincidences to be measured over nearly the same kinematic range as elastic *ep* scattering.

Simultaneous polarization measurements can be made of:

- P_n: The induced polarization in quasi-free kinematics results from final state rescattering. With the onset of CT, P_n will vanish.

- $P_{x,z}$: In a simple interpretation, the polarization transfer observables reflect the electric and magnetic form factors of the nucleon in the nucleus. The onset of CT leads to F_1 being a PLC, but F_2 always involves a finite impact parameter and orbital angular momentum. Thus, at high Q^2, nuclear filtering leads to a decrease in F_2, corresponding to an increase in G_E. This effect should be particularly noticeable near Q^2 of about 7 GeV^2; although G_{Ep} has only been measured up to 5.6 (GeV/c)^2, it now appears likely that it goes through 0 and changes sign near this Q^2.

The parasitic cross section measurements will also determine the transparency ratio, σ_A/σ_{PWIA}, and the missing momentum dependence of the cross sections. The transparency will probably be measured to high Q^2, perhaps 18 GeV^2, in Hall C. The missing momentum dependence is modified by CT; the reduction of rescattering that results from CT leads to a decrease in the strength of the cross section at large missing momentum. The ratio $\sigma_{400MeV/c}/\sigma_{200MeV/c}$ for example is expected to decrease from about 0.1 to 0.05 at Q^2 of 8 - 10 (GeV/c)^2.

The simultaneous measurement of the polarization observables and cross sections in a single spectrometer setting puts the most complete possible constraints on any models. This optimizes beam time and provides enormous statistics for the cross section determination, typically tens of millions of events, for each kinematic setting.

The top panel of Fig. 3.44 shows the free proton form factor ratio $\mu G_{Ep}/G_{Mp}$, and a modified ratio. The expected increase in the transparency from CT leads to an enhancement of F_1 relative to F_2, resulting in a modified ratio $\mu G_{Ep}/G_{Mp}$. Expected changes in the cross section of several percent correspond to large changes in G_{Ep} with only small changes in G_{Mp}; thus polarization transfer to look at the form factor ratio is a very sensitive observable. The bottom panel of Fig. 3.44 shows expected values of the polarization transfer observables as a function of beam energy, for fixed $Q^2 = 0.8$ GeV^2. The estimates have been done for ^{12}C, using the usual relations between the free nucleon form factors and the polarization transfer observables; for quasi-free scattering the polarizations are slightly different, from kinematic effects as well as various dynamical effects. Using MAD for protons plus HRS for electrons, a one month experiment would allow both the ep elastic and $^{12}C(e, e'p)$ quasi-free scattering to be determined to ± 0.01, as compared to the estimated 0.04 difference. Similarly sized effects can be seen at smaller Q^2, as increased count rate generate smaller uncertainties, compensating for the slightly smaller expected differences.

3.4.4 Pion Photoproduction in the Nuclear Medium

Pion photoproduction in the nuclear medium is an integral part of the effort to map the transition from the strongly interacting, non-perturbative regime where the nucleon-meson degrees of freedom are relevant to the perturbative regime of QCD where quarks and gluons are the appropriate degrees of freedom. Photoproduction of pions in the nuclear medium is a natural extension of the program on pion photoproduction from nucleons, which is one of the key programs for JLab at 12 GeV. In pion production from nucleons the agreement with the scaling behavior predicted by the constituent quark counting rules will be studied in detail and the oscillatory scaling behavior will be verified. Oscillatory scaling refers to the dramatic oscillations about the quark counting rule prediction, seen in the scaled cross-section of some exclusive process such as pp elastic scattering. The theoretical interpretation of this oscillatory behavior [208] involves the idea of interference between the hard pQCD, short distance amplitudes and the long distance (Landshoff) amplitudes. This QCD process is analogous to the QED effect of Coulomb-nuclear interference observed in low energy charged particle scattering. On extending these ideas to processes occurring in the nuclear medium it has been suggested that these long distance amplitudes are suppressed in the strongly interacting nuclear environment [209]. Large quark separations tend not to propagate in the nuclear medium while small quark separations propagate with small attenuation. This leads to suppression of the oscillation phenomena arising from interference of the long distance amplitude with the short distance amplitude (as seen in pp scattering, mentioned earlier). This is called the nuclear filtering effect. The experimental manifestation of this effect is predicted to be in the form of oscillations in nuclear transparency measurements, which are 180° out of phase with the oscillations in the free cross-section. This is because the transparency is formed by dividing the nuclear cross-section by the free cross-section scaled by the proton number Z of the nuclear target.

The experimental support for nuclear filtering comes from the nuclear transparency measurements in A(p,2p) experiments carried out at Brookhaven [167] which have shown a rise in

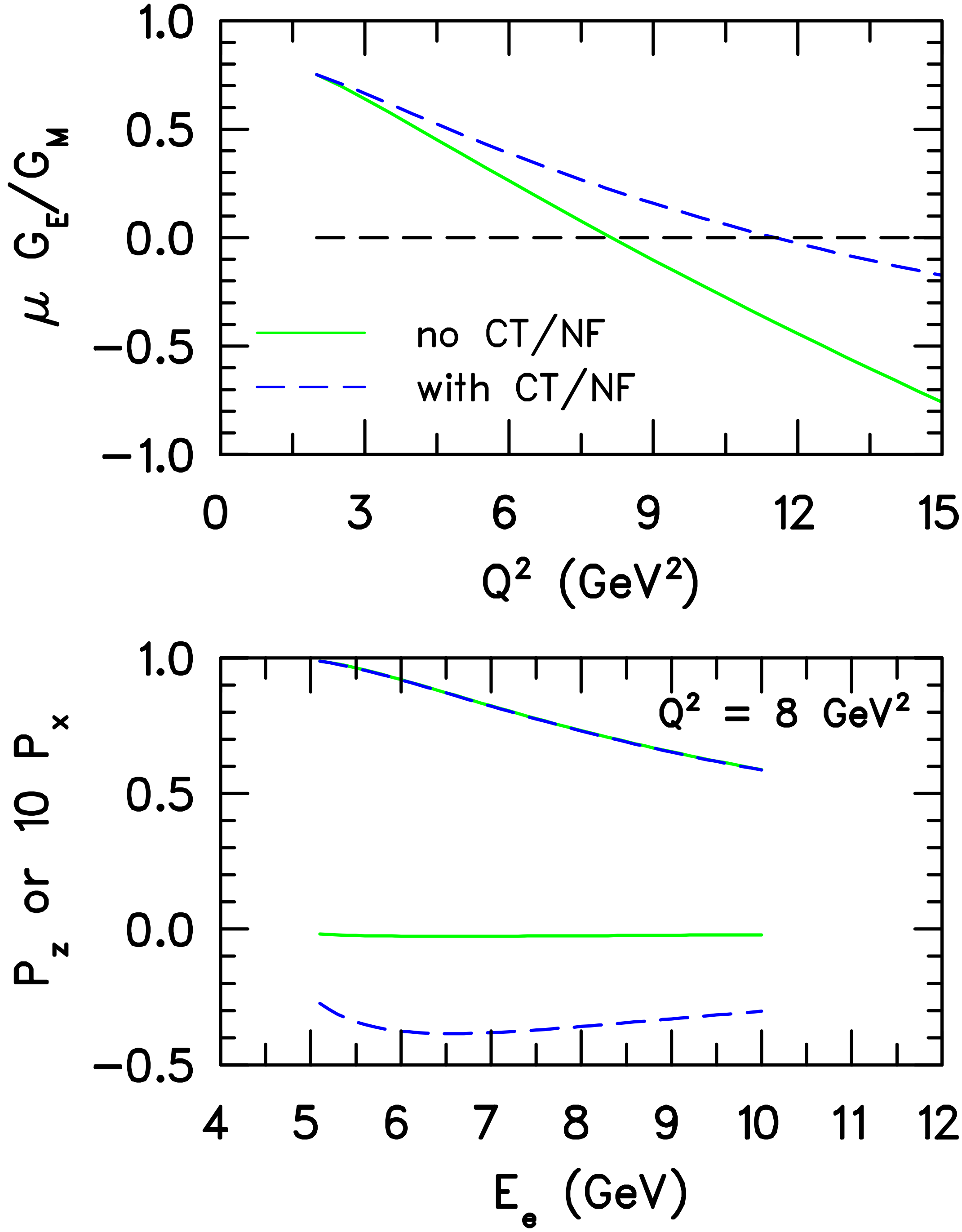

Figure 3.44: Top: Estimated $\mu G_{Ep}/G_{Mp}$ as a function of Q^2. The solid line indicates the behavior determined by high Q^2 polarization measurements in Hall A, and extrapolates the data assuming QF_2/F_1 is constant. The dashed line indicates the effects of CT/NF which enhance F_1 relative to F_2. Bottom: The longitudinal polarization transfer is positive and largely independent of the form factor ratio at small Q^2, but will change sign once G_E changes sign. The transverse polarization transfer is negative and depends strongly on the form factor ratio, thus it is greatly affected by CT/NF.

transparency for $Q^2 \approx 3$ - 8 $(GeV/c)^2$, and a decrease in the transparency at higher momentum transfers has been observed. A more recent experiment [168], completely reconstructing the final-state of the A(p,2p) reaction, confirms the validity of the earlier Brookhaven experiment. Nuclear filtering is one of the possible explanation for this effect [209], an alternative explanation put forward by Brodsky and de Teramond [171] claimed that the structure seen in the $A(p, 2p)$ transparency result and the oscillation in the scaled pp cross-section, can be attributed to $c\bar{c}uuduud$ resonant states. Thus the experimental verification of the nuclear filtering effect would be a very interesting confirmation of this QCD based approach in the transition region. A nuclear transparency measurement of the $\gamma n \to \pi^- p$ process from a ^{12}C target will allow the investigation of the nuclear filtering effect. These measurements involve coincidence detection of π^- and p produced by bremsstrahlung photons incident on a ^{12}C target. With the upgrade of JLab to 12 GeV and the MAD spectrometer one can extend these measurements up to just below the charm threshold. This would help confirm the nuclear filtering effect below the charm threshold, and also be complementary to a Hall C program extending these measurements to above the charm threshold.

Color Transparency (CT) is another phenomenon which can be studied with pion photoproduction in the nuclear medium. Color transparency is an effect which is complementary to nuclear filtering, and refers to the suppression of final (and initial) state interactions of hadrons with the nuclear medium in exclusive processes at high momentum transfers [210]. CT occurs when exclusive processes proceed via the selection of hadrons in the so-called point-like-configuration (PLC) states. Furthermore this small configuration should be "color screened" outside its small radius and the compact size should be maintained while it traverses the nuclear medium. While nuclear filtering uses the nuclear medium actively, in CT large momentum transfers select out the short distance amplitude which are then free to propagate through the passive nuclear medium. The expansion time relative to the time to traverse the nucleus is an essential factor for the observation of the CT effect, based on the quantum diffusion model by Farrar, Liu, Frankfurt and Strikman [211]. Thus, while the large A limit provides a perturbatively calculable limit for the nuclear filtering effect, one expects to observe the onset of CT effect sooner in light nuclei compared to heavier nuclei. Hence, a measurement of the $\gamma n \to \pi^- p$ process from a ^{4}He target will allow the investigation of the color transparency effect. These measurements would also involve coincidence detection of the π^- and p, produced from a ^{4}He target. Once again these measurements would be complementary to a Hall C program extending these measurements to higher energy.

In our estimates we have used realistic MAD and HRS angular acceptance, a 250 mg ^{12}C target and a 10 cm ^{4}He target. We have used a 50μA electron beam incident on a 6% copper radiator. The time estimated includes time for running without a radiator. The projected results for nuclear transparency of photo-pions from a ^{12}C target is shown in Fig. 3.45 and from a ^{4}He target is shown in Fig. 3.46. In these figures a 3% point-to-point systematic uncertainty along with 2.5 (2.0)% statistical uncertainty for ^{12}C (^{4}He)is shown. According to our estimates the projected results can be achieved with 350 hours of beam time for ^{12}C and 90 hours for ^{4}He.

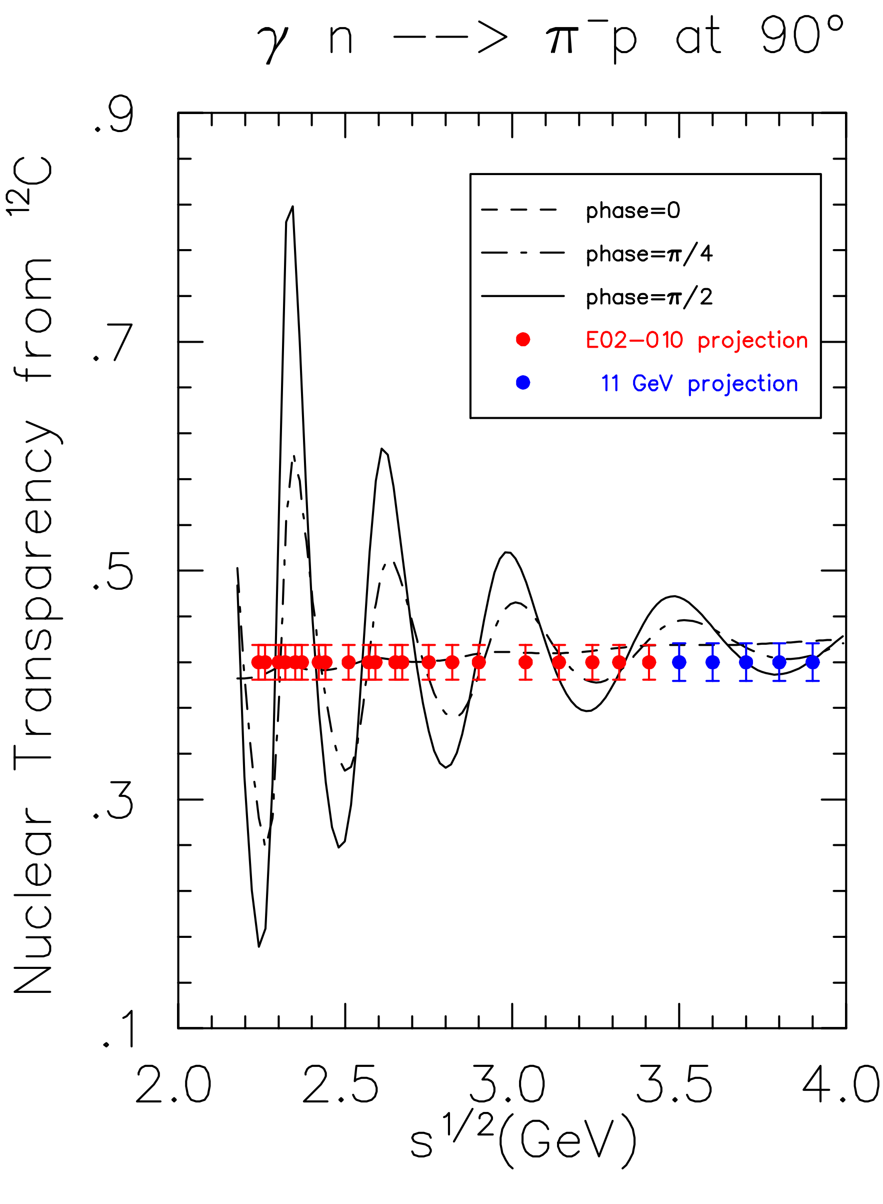

Figure 3.45: The projected results for nuclear transparency for photo-pions production from a ^{12}C target. The lines are calculations from Ref [212] using the two component model and and additional nuclear phase.

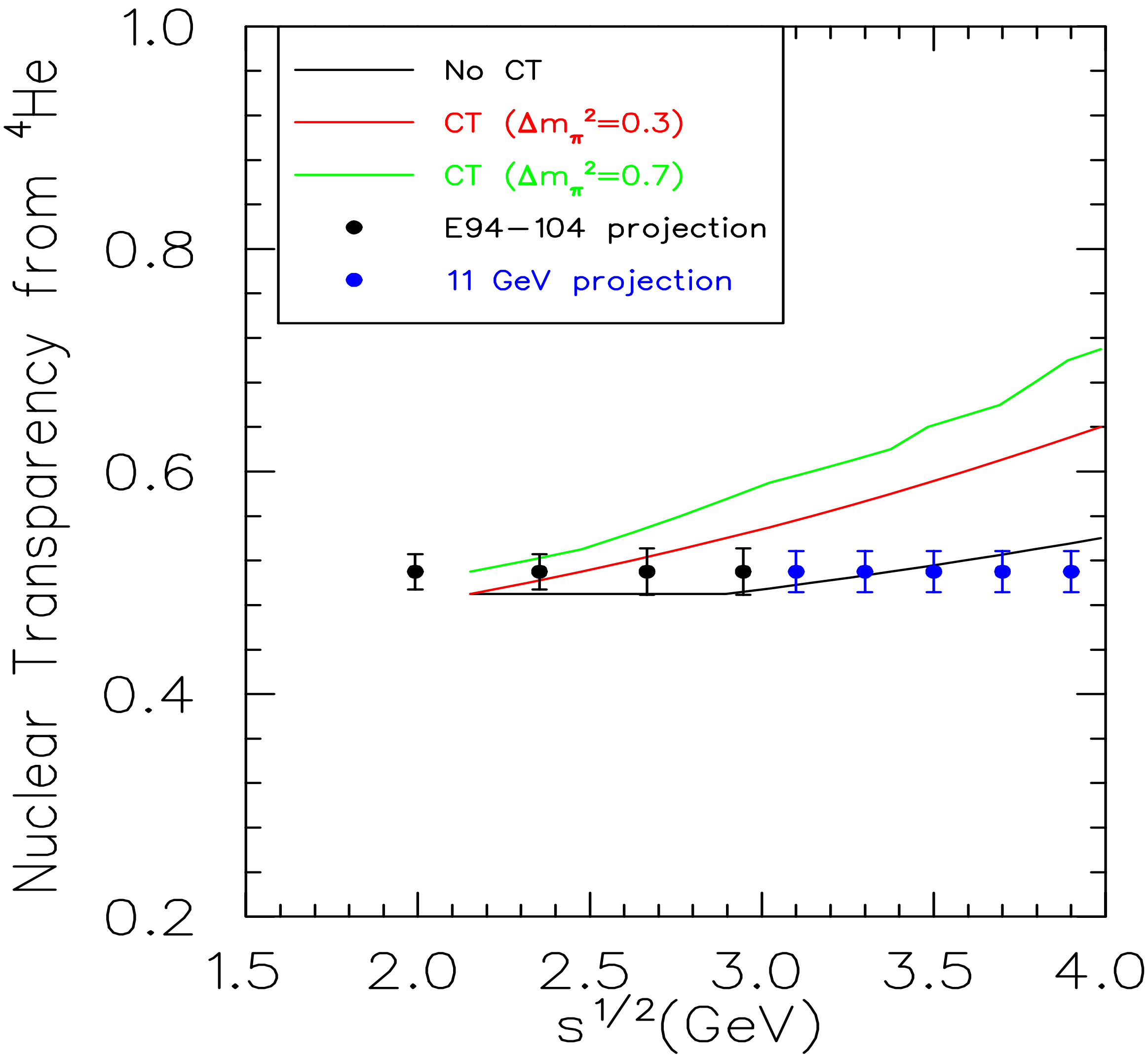

Figure 3.46: The projected results for nuclear transparency for photo-pions production from a ^{4}He target. The lines are CT calculations from Ref [213].

3.4.5 Nuclear Effects in Hadronization by Deep Inelastic Electron Scattering

Nuclear effects have been determined in quasi-elastic electron scattering by comparing data from a nucleus to a proton target. The shift of the peak position reflects the binding energy of the nucleon, the broadening of the peak is caused by Fermi motion, and the quenching of the longitudinal response has stimulated a great number of various theoretical approaches. However, since the quasi-elastic scattering is a coherent process, information which can be derived is rather limited.

By applying the same methodology to higher Q^2 so that the scattering happens in Bjorken scaling region, our understanding of nuclear effects can be pushed to a deeper level. Since the process is incoherent, all different hadron species can be generated. Moreover, an extra degree of freedom will permit an investigation of the dependence of nuclear effects on different energy scale. By detecting an energetic hadron product in coincidence with the scattered electron, a lot more valuable knowledge can be extracted.

Due to the weakness of electromagnetic (EM) interaction, in deep inelastic scattering (DIS), the virtual photon can deliver a huge amount of momentum into a small definite region of the nucleon, consequently a constituent quark can be knocked out. According to QCD, quarks are confined by the color field, the striking quark has to go through a fragmentation process and to be materialized into a hadron or a hadron jet, which is called current fragmentation. In the case of a nucleus target, the hadron needs to travel through the nuclear medium. By comparing the data to that from a deuterium target, nuclear effects can be revealed.

The evolution from the leading quark to a hadron can be described by a formation length, Λ_h, which is the distance extended in the hadronization process. As an approximation, Λ_h can be scaled by ν, the energy transfered by the virtual photon, with a conversion factor 1 fm/GeV. Thus, if ν is large, say 50 GeV, the quark is materialized most likely at a distance well outside a heavy nucleus. In this case, the observed effect is between the leading quark and rest part of the nucleus, which has been shown to be small by the EMC[214] and TMC[215] data. However, as ν is decreased, the hadron will be formed inside the target nucleus, and an attenuation of the hadron spectra is experienced. In the SLAC data [216] at 20.5 GeV beam energy with positive and negative hadrons measured at Q^2 from 0.35 to 5 $(GeV/c)^2$, and the invariant mass of the hadron system W^2 from 7 to 31 GeV^2, the attenuation of forward hadron is observed and the effect is large for larger nuclei. Albeit low statistics and no particle identification, these data opened a door for studying nuclear physics right inside the nucleus, which is unreachable by any hadron beam available in laboratory.

More recently, the HERMES collaboration examined the nuclear effect by scattering 27.5 GeV positrons from deuterium and nitrogen target [217]. The data covered a range of ν from 7-23 GeV. The detector can single out π^+ and π^-, while all the other hadrons are unidentified except their electric charge. Beside an attenuation of the hadron spectra, the data also showed a different attenuation of the positive and negative hadrons. Apparently, a complete particle identification will help to understand this difference.

With 11 GeV CW beam at Jlab, the nuclear effect study in semi-inclusive experiment will provide important data near the low energy limit which will expand the hadron spectra into a complete set, in addition to the data from TMC, EMC, SLAC and HERMES. First, at 11 GeV, ν can be pushed down as low as 5 GeV, where nuclear effect will be stronger. Second, due to the smaller energy scale, gluon effects and anti-nucleon yields will be low, which will make the data analysis simplifier, since the nuclear effects can be deduced with less uncertainties. Finally, at 11 GeV, potentially the experiment can scan over a large region from coherent to incoherent allowing different physics aspects in the transition phase to be mapped out.

In order to see the nuclear effects of hadronization, the scattering has to be done in the DIS region, where the point-like structure of the nucleon can be probed. However, there is no clear mark to separate the coherent and incoherent process. The SLAC-MIT data [218] with 7 to 16 GeV beam at 0.8 to 2.2 (GeV/c)^2 Q^2 showed that the structure function began scaled behavior at $\nu = 3GeV$, and fully scaled after $\nu = 4$ GeV. Hence, the minimum Q^2 requirement should be around 1 GeV. In reality, the Q^2 dependence of scaling is relative to x. For larger x at the same W, Q^2 needs to be higher; while for smaller x the high Q^2 requirement can be less rigorous.

The other concern is that W has to be large, so that the quark can have enough energy to be materialized and to break up the binding of the target nucleus. The minimum value should be set at 2 GeV, which will help cutting off background from resonance. In order to see the hadronization, W has to be large enough so that the current fragmentation can be separated from the recoiled remnant part of the nucleon for such a purpose, a Feynman variable is introduced, which defined by

$$x_F = P_L/P_{Lmax},$$

where P_L and P_{Lmax} are the longitudinal momentum of the hadron and its maximum in the hadron center mass system. For current fragmentation, x_F should be positive and large, so that P_L will be greater than P_T, the transverse momentum of the hadron. As a qualitative estimation, we take $P_{Lmax} = W/2$, $P_T = 0.5GeV/c$, and ask $P_L > P_T$, this will give a minimum W of 2.4 GeV. Like the Q^2 limit is relative to x, the W dependence is relative to P_T. By taking data at small x, but $x > 0.1$, and low P_T, good quality hadronization data will be selected.

To perform the measurement, we will use the Medium Acceptance Detector (MAD) for hadron arm and the High Resolution Spectrometer (HRS) as the electron arm. HRS will be oriented at an angle facing the recoil momentum of the hadron system. The detector will be arranged in five different configurations as shown in Table 3.11, in order to cover many values of ν, namely 4,5,6 and 7 GeV. The highest ν is overlapped to the HERMES coverage, the three lower values will be an extension to the previous data. Deuterium, nitrogen and argon targets will be measured.

When compared to large acceptance detectors, such as CLAS, the HRS-MAD combination has the advantage for background rejection. In addition to DIS, scattering also happens in the resonance region, as well as in the Vector Meson Dominance (VMD) region. The resonance data located between W= 1 and 2 GeV, and the VMD data are dominating at large ν and low Q^2, or equivalently small x. By locating the two detector at specific angles

Setting	I	II	III	IV	V
E_0 (GeV)	11	10	9	9	8
$\theta_{HRS}(deg.)$	24	22	19	27	15
$W(GeV)$	2.5	2.5	2.5	2.5	2.5
$E_1(GeV)$	4.0	4.0	4.0	3.0	4.0
$\nu(GeV)$	7	6	5	6	4.0
$Q^2(GeV/c)^2$	7.7	5.9	4.0	5.9	2.2
$\theta_{MAD}(deg.)$	13	13	14	12	14
x	0.59	0.52	0.42	0.52	0.29
$d\sigma/dx/dy$ (nb)	10	16	32	13.5	50

Table 3.11: Kinematic parameters in four different setups.

and setting the magnet for a limited region of momentum, these background will be automatically cut off. The disadvantage of small solid angle detector is the lower event rate, while this can be compensated by increasing the beam current, since the above background and high rate low Q^2 events are fully suppressed.

The rate estimation is based on 100 μA beam current and 10 cm liquid deuterium target, which gives a luminosity of $3 \times 10^{38}/cm^2/sec$. Using a cross section 10 nb and dx=0.1, dy=0.05, azimuthal acceptance of HRS 5%, the electron rate at HRS will be about 750 Hz, or 2.7M/hour. Assuming 4 hours for each run, the electrons will count to 10.8 M.

According to the prediction of Venus and the MAD angular acceptance, there will be 620k positive hadrons and 210k negative hadrons during a 12 hours runs with three magnet settings. Assuming the events are uniformly distributed on momentum, for each 4 hours run (one magnet set up), there will be 155k positive hadrons and 52.5k negative hadrons in average. These estimation will cause about 10Hz coincidence rate for each single run.

For each detector set up and a fixed target, measurements will be repeated with a reverse field in the HRS magnet in order to detect negative hadrons. The deuteron, nitrogen and argon targets are to be measured for all values of ν. If half day beam time is assigned to each detector-target-charge configuration, 12 days beam time will be requested. Including 6 days set up for detector tuning and target changing, in total 20 days will be enough for this experiment at 1% precision in most cases. Figure 3.47 shows a tentative project result on the π^+ multiplicity ratio as a function of ν from 10% of the anticipated data. The blue diamonds are for $z = 0.5$ and nitrogen; the red boxes are for $z = 0.5$ and argon; and the black 'X' are for $z = 0.2$ and nitrogen. The blue circle are data from HERMES [217] for $z > 0.2$ and nitrogen. All the other data points and the fitting curve are from the yellow diamond is the SLAC data on carbon. The curves are from a calculation [219], the dotted (black) is for $z = 0.2$ and nitrogen, the dashes (blue) is for $z = 0.5$ and nitrogen, and the solid (red) is for $z = 0.2$ and argon.

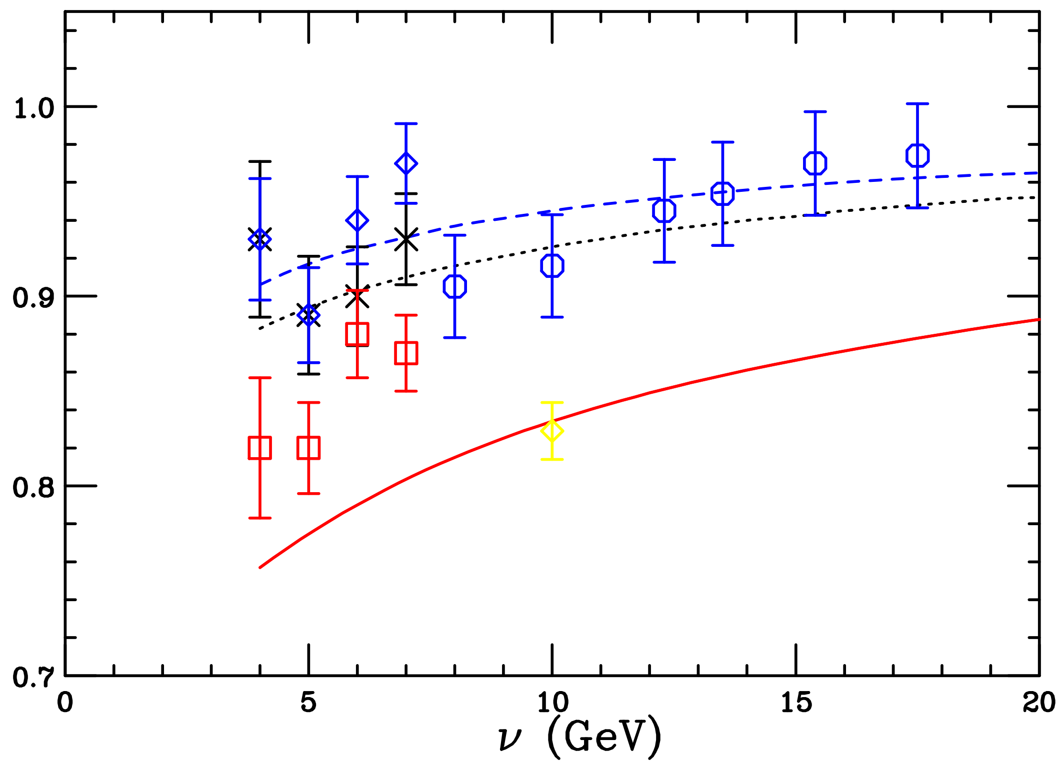

Figure 3.47: Shown are the tentative project results on the π^+ multiplicity ratio as a function of ν from 10% of the total events. The blue diamonds are for $z = 0.5$ and nitrogen; the red boxes are for $z = 0.5$ and argon; and the black 'X' are for $z = 0.2$ and nitrogen. The blue circle are data from HERMES [217] for $z > 0.2$ and nitrogen. All the other data points and the fitting curve are from the yellow diamond is the SLAC data on carbon. The curves are from a calculation [219], the dotted (black) is for $z = 0.2$ and nitrogen, the dashes (blue) is for $z = 0.5$ and nitrogen, and the solid (red) is for $z = 0.2$ and argon.

3.4.6 Few-Body Form Factors

In addition to measurements particles emitted from the nuclear medium, measurements of the elastic form factors of the deuteron and the helium isotopes are of crucial importance in understanding their electromagnetic structure and testing the "standard model" of light nuclei that is based on the meson-nucleon framework, the impulse approximation (IA), and meson-exchange currents (MEC) [220]. Such measurements offer unique opportunities for studying the short-range nucleon-nucleon interaction, few-body wave functions, isobar and three-body force contributions, and effects from possible quark-cluster admixtures. Large momentum transfer measurements can test "nuclear chromodynamics" predictions based on quark dimensional scaling (QDS) and perturbative QCD (pQCD) [221].

The starting point of the conventional theoretical approach of elastic scattering from few-body systems is the impulse approximation, where the incident electron interacts with one of the nucleon constituents of deuterium or helium. The form factors of light nuclei are then convolutions of the nuclear wave function with the form factors of the constituent nucleons. At large momentum transfers the effects of relativity cannot be ignored, and either corrections to the IA or fully relativistic approaches, as in the deuteron case [222], have been developed. It has long been understood and overwhelmingly supported by the available data that the few-body form factors are sensitive to the presence of meson-exchange currents and isobar configurations that augment the IA picture [220].

At distances much less than the nucleon size, the underlying quark substructure of the nucleons cannot be ignored. This has lead to the formulation of so-called hybrid quark models [223] that treat few-body nuclei as quark clusters when the inter-nucleon separation becomes smaller than $\sim$1 fm. At sufficiently "large" momentum transfers, the few-body form factors are expected to be calculable in terms of only quarks and gluons within the framework of pQCD. The first attempt at a quark-gluon description of the few-body elastic form factors was based on the dimensional-scaling quark model (DSQM) [156], where the underlying dynamical mechanism during elastic scattering is the hard rescattering of the constituent quarks via exchange of hard gluons. The Q^2 dependence of this process is then predicted by simply counting the number n of gluon propagators (n=5 for deuterium, 8 for ^{3}He, and 11 for ^{4}He), which implies that the elastic structure functions $A(Q^2)$ of the few-body systems should follow the power law: $\sqrt{A(Q^2)} \sim (Q^2)^{-n}$. This prediction was later substantiated, for the deuteron case, in the pQCD framework, where it was shown [224] that to leading-order:

$$\sqrt{A(Q^2)} = \left[\alpha_s\left(Q^2\right)/Q^2\right]^5 \sum_{m,n} d_{mn} \left[\ln\left(\frac{Q^2}{\Lambda^2}\right)\right]^{-\gamma_n-\gamma_m},$$

where $\alpha_s(Q^2)$ and Λ are the QCD strong coupling constant and scale parameter, and $\gamma_{m,n}$ and d_{mn} are QCD anomalous dimensions and constants.

The 12 GeV energy upgrade of the JLab electron beam and the proposed spectrometer facilities upgrades will be ideal for improving and extending the existing elastic structure function measurements of light nuclei to higher momentum transfers. These measurements will test the limits of the standard model of few-body nuclei, and may uncover a possible transition to a quark-gluon description of the few-body form factors, as predicted by quark-dimensional scaling and perturbative QCD.

Figure 3.48 shows the recent JLab Hall A and older SLAC and Saclay data [225] on the deuteron form factor, $F_d(Q^2) \equiv \sqrt{A(Q^2)}$, multiplied by $(Q^2)^5$. It is evident that the data show an approach to a scaling behavior consistent with the power law of DSQM and pQCD. Although several authors have questioned the validity of QDS and pQCD at the momentum transfers of this experiment [226], similar scaling behavior has been reported in deuteron photodisintegration at moderate photon energies [227]. It is extremely important to test this apparent scaling behavior by extending the deuteron $A(Q^2)$ measurements to higher momentum transfers. Higher JLab beam energies in the range of 9-11 GeV are essential for such measurements. To separate elastic from inelastic scattering and to suppress backgrounds, recoil deuterons should be detected in coincidence with scattered electrons. A

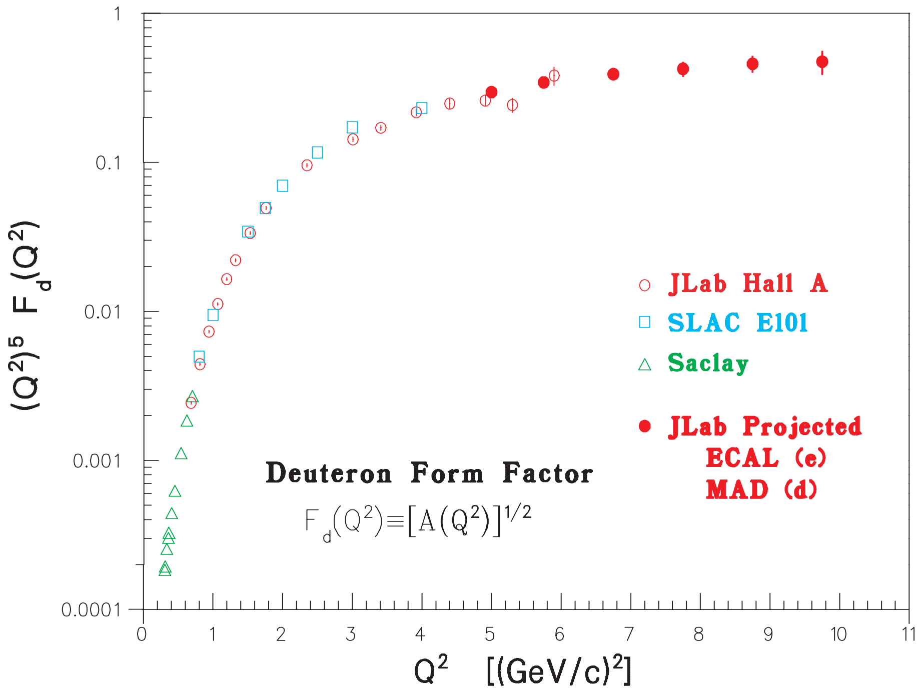

Figure 3.48: Projected data for the deuteron form factor $F_d(Q^2)$ with an 11 GeV JLab beam. Also shown are existing JLab, SLAC and Saclay data.

possible scenario would be to use the proposed Medium Acceptance Device (MAD) to detect recoiling deuterons and a segmented electromagnetic calorimeter (ECAL) to detect scattered electrons. Assuming a 20 cm long liquid deuterium target and beam current of 70 μA, $A(Q^2)$ can be measured up to ~ 10 $(\mathrm{GeV/c})^2$ in one month of beam time, as shown in Fig. 3.48. Such an experiment will double the Q^2 range of the existing data, which has been acquired over a period of 40 years. This measurement will undoubtedly resolve the question of the applicability of the QDS and pQCD ideas at moderate momentum transfers. The observation of a diffractive structure (which cannot be ruled out from the existing data) would settle the above question once and for all.

The existing data [30] on the ^{3}He form factor, $F(Q^2) \equiv \sqrt{A(Q^2)}$ (shown in Fig. 3.49), are in good agreement with the standard model (IA+MEC) calculations [1] at low Q^2 but are fairly inconclusive at the largest momentum transfers. They are consistent with a change in slope at ~ 55 fm^{-2}, indicative of an onset of quark scaling [2], but, at the same time, cannot exclude the presence of a second diffraction minimum as predicted by conventional meson-nucleon theory. As in the case of the deuteron, more measurements at higher Q^2 would be crucial in testing the quark-scaling prediction and a possible breakdown of the meson-nucleon framework. The energy upgrade of JLab will also allow new ^{3}He measurements that could double the Q^2 range of the existing data (taken also over a period of 40 years) in a single experiment with a ten-fold better sensitivity. As in the case of the deuteron, recoiling nuclei will be measured with the MAD spectrometer and scattered electrons with a calorimeter.

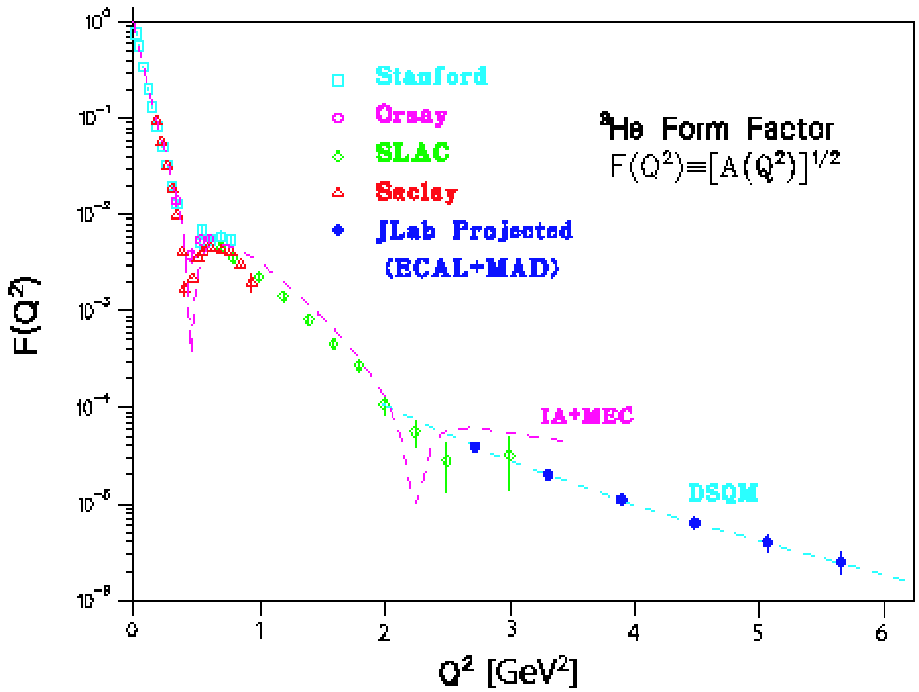

Figure 3.49: Projected data for the ^{3}He elastic form factor $F_(Q^2)$ with an 11 GeV beam. Also shown are existing data and predictions of the standard model (IA+MEC) [228] and the dimensional scaling quark model (DSQM) [2].

Assuming a 20 cm long ^{3}He gas cryogenic target and an electron beam of 11 GeV with current of 70 μA, the ^{3}He $F(Q^2)$ can be measured up to ~ 150 fm^{-2} in one month of beam time, as shown in Fig. 3.49. It is evident that this experiment will be able to show whether the apparent change in slope of the SLAC data can be attributed to a classical diffraction minimum, or a quark-scaling approach as argued in Ref. [2].

3.5 Charm Production near Threshold

3.5.1 General motivations

With the 11 GeV beam an area for research, new to JLab, becomes available, namely studies of charm production. The properties of charmed particles have been thoroughly studied elsewhere at higher energies and they are not the topic of the program presented here. Rather, charm photoproduction close to threshold can be used as a tool to study properties of the nuclear target, opening a new window into QCD dynamics, particularly multi-quark, gluonic and hidden color correlations in nucleons and nuclei. In contrast to diffractive charm production at high energy which tests the behavior of the gluon structure functions at small x, charm production near threshold tests the structure of the target near $x = 1$ and its short range behavior.

This difference results from the kinematics of the reaction products. For J/ψ production off the nucleon, the threshold energy is $E_\gamma = 8.20$ GeV and, due to the large mass of the charmed quark ($m_c \approx 1.5$ GeV), the $c\bar{c}$ fluctuation of the photon travels over $l_c \cong 2E_\gamma/4m_c^2 =$ .36 fm (see Fig. 3.50). The large mass of the charmed quark imposes also a small transverse size $r_\perp \sim 1/m_c = 0.13$ fm of this fluctuation. The minimum value allowed for the momentum transfer is large ($t_{min} \sim 1.7$ GeV^2 at threshold, and ~ 1 GeV^2 at $E_\gamma = 10$ GeV). Thus charm production near threshold implies a small impact distance ($b \sim 1/m_c \sim 0.13$ fm). All the five valence quarks (the two heavy charm quarks in the probe and the three light quarks in the target) must be in the same small interaction volume.

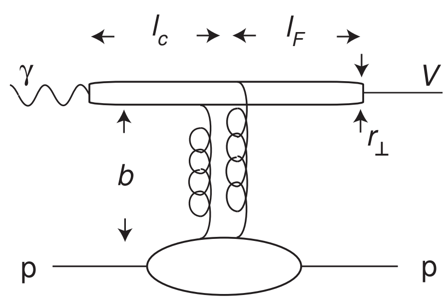

Figure 3.50: The characteristic time scales in J/ψ production on proton.

As a consequence, all the quarks must be involved in the reaction mechanism. On nucleon targets, this implies that three gluon exchange may take over two gluon and one gluon exchange, and open the way to the study of correlations between valence quarks.

Relying on the short-distance behavior of hadronic matter [229, 230, 231] shows that the charm production cross-section can be cast in a simple form using general properties of perturbative QCD. For two-gluon exchange, the cross-section of the $\gamma p \to J/\psi p$ reaction takes the form:

$$\frac{d\sigma}{dt} = \mathcal{N}_{2g} v \frac{1}{16\pi} \frac{(1-x)^2}{R^2 \mathcal{M}^2} F_1(\frac{t}{4})(s-m^2)^2 \tag{3.44}$$

while for three-gluon exchange it takes the form:

$$\frac{d\sigma}{dt} = \mathcal{N}_{3g} v \frac{1}{16\pi} \frac{(1-x)^0}{R^4 \mathcal{M}^4} F_1(\frac{t}{9})(s-m^2)^2 \tag{3.45}$$

where $x \approx (2m\mathcal{M} + \mathcal{M}^2)/(s-m^2)$ and $\mathcal{M}$ is the mass of the $c\bar{c}$ pair. The relative weight of the two- and three-gluon exchange terms is controlled by the probability $1/R^2\mathcal{M}^2$ that two quarks in the proton (of radius $R \sim 1$ fm) are bound within a transverse distance $1/\mathcal{M}$ (see [232]). $F_1(t)$ is the isoscaler proton form factor. This argument takes into account the fact that the momentum transfer is shared between two or three valence quarks in the proton. This implies that the t distributions for the three-gluon exchange cross-section is flatter than the t distributions for the two-gluon exchange cross-section. The upper limit of the normalization coefficient, $\mathcal{N}$, was estimated by assuming that each channel saturates the experimental cross-section measured at SLAC [233] and Cornell [234] around $E_\gamma = 12\,GeV$. As depicted in Fig.3.51, this conjecture is consistent with the limited data that are available [233, 234, 235]. Clearly 12 GeV beams from an upgraded CEBAF will allow a more comprehensive determination of the J/ψ photoproduction cross section between threshold and 12 GeV.

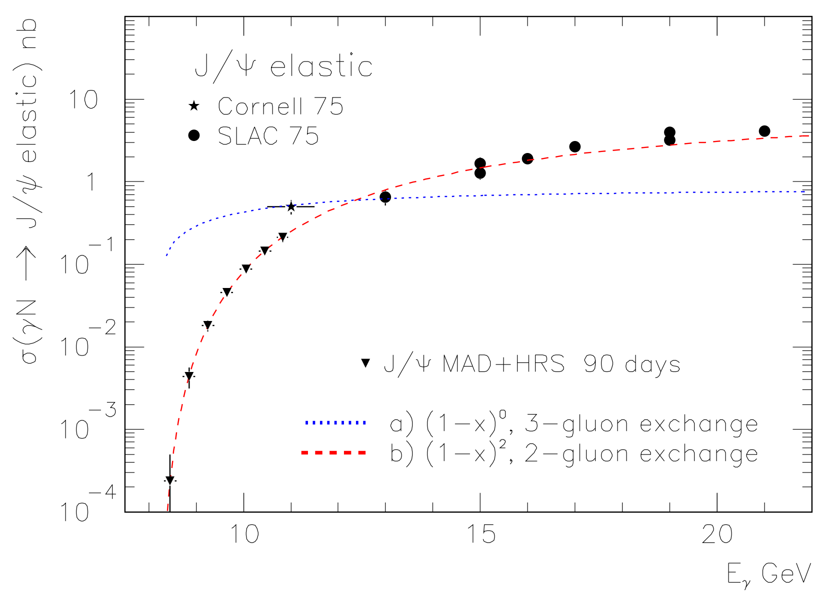

Figure 3.51: Variation of the cross sections of J/ψ photoproduction near threshold, for two or three gluon exchange mechanisms. The inverted triangles show the expected accuracy at CEBAF at 11 GeV beam.

In a different approach it is argued that the t-dependence of the elastic photo-production of J/ψ via the two-gluon exchange should be given by $d\sigma/dt \propto (1 - t/m_{2g}^2)^{-4}$, where $m_{2g} \approx 1$ GeV, as a theoretical expectation for the t-dependence of gluon GPD. The convolution of GPD with other functions is simplified by the small size of the meson produced.

This would explain the flatter t-dependence of the cross section at lower energies and indicate that the two-gluon exchange mechanism remains dominating down to lower energies. It is pointed out that a better data at low energies are needed to verify this approach and stressed that the knowledge of the transverse gluon distribution is important as a key ingredient for the understanding of relative importance of soft and hard processes for high energy nucleon-nucleon collisions at different impact parameters and is needed for description of data from hadron colliders.

On few body targets, each exchanged gluon may couple to a colored quark cluster and reveal the hidden color part of the nuclear wave function, a domain of short range nuclear physics where nucleons lose their identity (Fig. 3.52). It is striking that in $\gamma d \to J/\psi pn$ the $|8_c 8_c>$ hidden color state of the deuteron couples so naturally by two gluons to the $J/\psi pn$ final state [236]. Such exotic configurations are more likely to appear below the threshold for charm creation on a nucleon at rest, where quasi free production is suppressed. On deuterium the threshold for J/ψ production is ~ 5.65 GeV, while on heavy nuclei the threshold is simply the J/ψ mass 3.1 GeV.

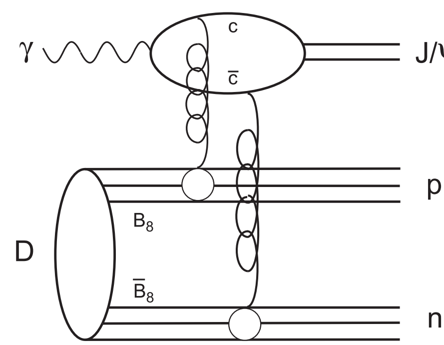

Figure 3.52: The simplest diagram to reveal hidden color state in deuterium [236].

The formation length, l_F, over which the $c\bar{c}$ pair evolves into a J/ψ after its interaction with a nucleon, is given by:

$$l_F \cong \frac{2}{m_{\psi'} - m_{J/\psi}} \left[\frac{E_{J/\psi}}{2m_c} \right] \cong 0.22 E_\gamma \tag{3.46}$$

Near threshold l_F is about 1 fm, closer to the size of the nucleon than to the size of the nucleus.

This is the ideal situation for determining the scattering cross section of a full sized charmed meson on a nucleon, in contrast to the situation at high energies where the cross section is sensitive to the interaction of a compact $c\bar{c}$ pair with the entire nucleus. There is an interest in knowing the cross section $\sigma_{\psi N}$ due to several reasons. Since there is no Pauli blocking for charm quarks in nuclei, a large attractive Van der Waals potential binding the pair to the nucleus may occur [237]. This potential may yield a relatively large value of the ψ-nucleon cross section of $\sigma_{\psi N} \approx 7\ mb$ at low energies [238]. Such a gluonic potential between color-neutral states would open up a possibility to trace part of the short-range nucleon-nucleon interaction to such a color force. Its observation would play a very important role in understanding the nucleon-nucleon force.

On the other hand, QCD calculations along with using the VM model and the existing data on gluon structure functions lead to $\sigma_{\psi N} \approx 0.3\ mb$ [239] at 20 GeV, rapidly falling toward lower energies.

Besides of its own interest, the ψ-nucleon cross section is an important parameter in the search for QGP.

So far, the single measurement of $\sigma_{\psi N}$ from SLAC [240], gave $\sigma_{\psi N} = 3.5 \pm 0.8 \pm 0.5\ mb$. Unfortunately, the need to subtract a large calculated background and the lack of information on the J/ψ kinematics makes it impossible to disentangle coherent and incoherent photoproduction in the experiment. The first estimates of $\sigma_{\psi N}$ derived from J/ψ hadroproduction, gave a value of $\approx$ 7 mb[241], but after correction [242] for the energy loss and coherence effects this value went down to $\approx$ 3.6 mb.

An approved experiment at SLAC E159 is aiming at measuring $\sigma_{\psi N}$ in a photon beam at 15,25 and 35 GeV. Due to the low duty cycle at SLAC and the energy dependence of the production cross section, this coincidence experiment would not be able to use a lower beam energy. Using the lower energy at JLab would be complimentary, because of the smaller formation length.

Finally, intrinsic charm components in the proton ground state and possible penta-quark resonances or charmonium bound states may be revealed near threshold. The discovery of such qualitatively new states of matter would be a major success for CEBAF at 11 GeV.

Since no quantitative predictions exist for charm production near threshold, we will rely on interesting conjectures on the short distance behavior of hadronic matter, inferred from properties of perturbative QCD. Experiments are mandatory to explore this virgin frontier of our knowledge.

3.5.2 Experimental program

The program includes a measurement the energy dependence of J/ψ photoproduction cross section on protons, in the energy range above threshold up to 11 GeV. These results should demonstrate whether the production mechanism at threshold is the same as at 150-20 GeV, or a new mechanism (a three-gluon contribution in the scheme discussed above) plays a significant role. If the two-gluon exchange should stay dominant down to low energies, the measurement of the t-dependence of the cross section could be used to constrain the gluon GPD of the nucleon. These data will also be used for the A-dependence measurement, in order to take into account the Fermi motion effect on the production cross section.

The issue of experimental feasibility has been worked out in detail [243]. Three options were evaluated for the detector: Hall D, MAD+HRS of Hall A and a dedicated, calorimeter - based experiment called here "ECAL" for brevity. These three options provide the resolutions for the key physics variables as shown in Table 3.12. The mass resolution affects the level of background, while the t resolution is important for removing the coherent production on nuclei.

setup	$\sigma(M)/M$	$\sigma(E_\Psi)/E_\Psi$	$\sigma(E_\gamma)/E_\gamma$	$\sigma t(GeV/c)^2$
Hall D, tagged beam	0.010	0.004	0.001	0.03
HRS+MAD	0.002	0.001	0.002	0.014
ECAL	0.035	0.007	0.01	0.11

Table 3.12: Experimental resolutions of the possible charm experiments at JLab

The expected event rates and exposition times are shown in Table 3.13.

process	setup	recoil	BG/sig	$d\sigma/dt \propto (1-x)^2$		$d\sigma/dt \propto (1-x)^0$	
				events/ 90 days	days needed	events/ 90 days	days needed
$\gamma p \to J/\psi(1S)p$							
$J/\psi(1S) \to e^+e^-$	ECAL	yes	0.10	$0.6 \cdot 10^5$	10	$3.0 \cdot 10^5$	0.2
$J/\psi(1S) \to l^+l^-$	HRS+MAD	no	<0.02	$2.4 \cdot 10^3$	190	$2.8 \cdot 10^4$	45
$J/\psi(1S) \to l^+l^-$	D tag	yes	0.07	$2.6 \cdot 10^2$	640	$2.1 \cdot 10^3$	40
$\gamma p \to \Lambda_c^+ \overline{D}^0$							
$\overline{D}^0 \to K^+\pi^-$	HRS+MAD	no	0.05	$2.9 \cdot 10^3$	-	$2.9 \cdot 10^4$	-
$\overline{D}^0 \to K^+\pi^-$	D tag	yes	0.25	$5.4 \cdot 10^2$	-	$3.4 \cdot 10^3$	-

Table 3.13: Comparison of the experimental options to study charm at JLab. The background to signal ratio was estimated for 11 GeV photons. The last column shows the number of days of data taking needed to achieve an average relative statistical accuracy of the cross-section measurement of 10%, in an energy range of 0.4 GeV above the threshold. This estimate has not been done for open charm since the background is at the moment uncertain.

The best opportunity to obtain a large statistics in short time are given by the “ECAL” option. This setup would require additional efforts in comparison with the other options, that are driven by various different projects. MAD+HRS provide a reasonable sensitivity for a pilot measurement on the cross-section and the A-dependence measurement. The latter can not be done by Hall D which does not plan to use nuclear targets.

The expected yields from nuclear targets for MAD+HRS are presented in Table 3.14.

The systematic error of such a measurement will be better than in [240]. The statistical error was estimated using the same model for nuclear transparency as was used for the SLAC experiment[240]. This model, based on a semi-classical Eikonal approximation for the re-scattering [244, 245], predicts the values for nuclear transparency $T = \sigma_{\gamma A}/(A \cdot \sigma_{\gamma N})$, given in Table 3.15.

target		^{1}H	^{2}H	Be	C	Al	Cu	Ag	Pb
J/ψ(1S)	$(1-x)^2$	160	320	550	360	210	110	80	60
/day	$(1-x)^0$	$\times 5.4$							

Table 3.14: The expected yields of MAD+HRS setup per day on nuclear targets 7.7% radiation length thick, and from a 15 cm liquid hydrogen target

A	9	12	27	63	108	207	$\sigma(\sigma_{\psi N})$, mb
T for $\sigma_{\psi N}$=1.0 mb	0.982	0.980	0.974	0.963	0.952	0.929	0.28
T for $\sigma_{\psi N}$=3.5 mb	0.938	0.931	0.908	0.870	0.833	0.751	0.24
T for $\sigma_{\psi N}$=7.0 mb	0.876	0.863	0.816	0.740	0.665	0.502	0.17

Table 3.15: The values of nuclear transparencies for J/ψ(1S), calculated in the model used by the SLAC measurement[240], for 3 values of $\sigma_{\psi N}$. The last column presents the expected statistical error for a $\sigma_{\psi N}$ measurement, assuming a statistical error of 3% for the yields on every target.

3.6 Search for New Physics Using Parity Violation

The weak mixing angle, θ_W is one of the fundamental parameters of the Standard Model. The tangent of the weak mixing angle represents the relative coupling strength of the SU(2) and U(1) groups (g and g'). At the Z resonance, the value of $\sin^2(\theta_W)$ has been well established through a number of measurements; however, there have been very few measurements made of $\sin^2(\theta_W)$ away from $Q^2 = M_Z^2$. One important consequence of the Standard Model is that the value of $\sin^2(\theta_W)$ will vary (run) as a function of Q^2. Deviations from the predicted running are sensitive to possible extensions of the Standard Model. The running of $\sin^2(\theta_W)$ is illustrated in Fig. 3.53 [246].

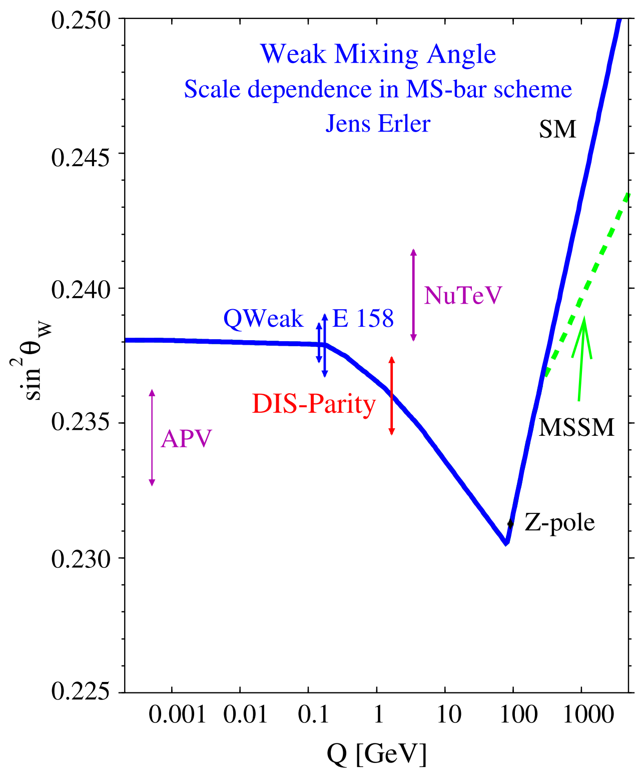

Figure 3.53: The running of $\sin^2\theta_W$ shown as a function of Q^2. The proposed combined statistical and systematic precision of the DIS parity violation experiment (DIS-Parity) is shown in red. Also shown are the existing APV cesium [247, 248] and neutrino DIS (NuTeV) [249] measurements along with expected uncertainty of the approved Jefferson Laboratory Q_{weak} [250] and running SLAC E-158 Møller [251] experiments.

Two measurements which have been made away from the Z-pole come from atomic parity violation (APV) and νA scattering. In APV the most sensitive measurements come from the cesium atom [247, 248]. Unfortunately, the interpretation of APV results have been somewhat controversial and the extracted value for the weak charge, $Q_W = 1 - 4\sin^2(\theta_W)$, has changed as the understanding of atomic structure has advanced. The most recent calculations of cesium APV appear to disagree with the measured values by approximately two standard deviations [252]; however, this conclusion is by no means universal and there is still considerable ongoing discussion in the literature about these values [253, 254, 255, 256, 257, 258, 259, 260]. At higher energies using neutrino scattering on iron, the NuTeV collaboration at Fermilab recently reported $\sin^2\theta_W^{\mathrm{on-shell}} = 0.2277 \pm 0.001(\mathrm{stat}) \pm 0.0009(\mathrm{syst})$, three standard deviations above the Standard Model predictions [249]. Naturally, this deviation has been interpreted in terms of physics beyond the Standard Model (new propagator or couplings, dimension six operators, extra U(1) gauge bosons, etc) [261]. However, there are also more conventional explanations, including nuclear effects in the iron target [262] and QCD effects [261]. Clearly, in order to observe and understand deviations from the standard model, more and theoretically better-understood high precision measurements are needed.

One such measurement is SLAC Experiment 158, which is using parity non-conservation in Møller scattering to measure $\sin^2(\theta_W)$ at an average Q^2 of 0.03 $(\mathrm{GeV/c})^2$. This experiment has complete its first run with an expected uncertainty of $\delta\left[\sin^2(\theta_W)\right] \approx 0.0025$ By the completion of its second run in 2003, E-158 should achieve a precision corresponding to $\delta\left[\sin^2(\theta_W)\right] \approx 0.0007$ [251]. The Jefferson Laboratory experiment Q_{weak} will provide a complimentary measurement of $\sin^2(\theta_W)$. Q_{weak} will determine the weak charge on the *proton* by measuring the parity violating asymmetry in elastic *ep* scattering, also at an average Q^2 of 0.03 $(\mathrm{GeV/c})^2$. The experiment anticipates a precision of 4% in Q_W, roughly corresponding to $\delta\left[\sin^2(\theta_W)\right] \approx 0.0005$ [250].

Here we present another possible measurement of $\sin^2(\theta_W)$ using parity non-conserving deep inelastic electron-deuterium scattering. The measurement would use the upgraded 11 GeV beam at Jefferson Lab, and could be staged in either Hall A or Hall C. The relative merits of each are under study. Since this experiment would use a deuterium target, it will not suffer from the uncertainties in nuclear effects and nuclear parton distributions that the NuTeV measurement on iron did. It is important to note that the sensitivity to different "new physics" scenarios of the three new experiments, Møller, Q_{weak} and this proposed measurement, is not the same [263], and to fully explore the range of possible extensions to the Standard Model, these experiments form a complementary program.

3.6.1 Formalism for DIS

The parity-violating asymmetry for scattering longitudinally polarized electrons from an unpolarized isoscalar target such as a deuteron (assuming isospin symmetry) is given by [264, 265]

$$\begin{aligned} A_d &= \frac{\sigma_L - \sigma_R}{\sigma_L + \sigma_R} \\ &= -\left(\frac{3G_F Q^2}{\pi\alpha 2\sqrt{2}}\right)\frac{2C_{1u} - C_{1d}\left[1 + R_s(x)\right] + Y(2C_{2u} - C_{2d})R_v}{5 + R_s(x)} \end{aligned}$$

where, taking $\sin^2(\theta_W) \approx 0.23$,

$$\begin{array}{rcrcrl} C_{1u} & = & -\frac{1}{2} + \frac{4}{3}\sin^2(\theta_W) & \approx & -0.19, & \\ C_{1d} & = & \frac{1}{2} - \frac{2}{3}\sin^2(\theta_W) & \approx & 0.35, & \\ C_{2u} & = & -\frac{1}{2} + 2\sin^2(\theta_W) & \approx & -0.04 & \text{and} \\ C_{2d} & = & \frac{1}{2} - 2\sin^2(\theta_W) & \approx & 0.04. & \end{array}$$

Also

$$Y = \frac{1-(1-y)^2}{1+(1-y)^2 - y^2R/(1+R)} \text{ and}$$
$$y = \nu/E.$$

Here, $\nu = E - E'$ is the energy lost by an incident electron of energy E scattering to an electron of energy E', and the ratio $R = \sigma_L/\sigma_T \approx 0.2$ depends on x and Q^2. The ratios $R_s(x)$ and $R_v(x)$ depend on the quark distribution functions:

$$R_s(x) = \frac{2s(x)}{u(x)+d(x)} \text{ and } R_v(x) = \frac{u_v(x)+d_v(x)}{u(x)+d(x)}.$$

At high x, where sea quark contributions vanish, $R_v = 1$ and $R_s = 0$, and using $\sin^2(\theta_W) \approx 0.23$ for C_{1u}, C_{1d}, C_{2u} and C_{2d} from above, we find

$$A_d \approx 10^{-4} Q^2 (0.72 + 0.12Y).$$

The sensitivity to $\sin^2(\theta_W)$ is approximately given by

$$\frac{d\sin^2(\theta_W)}{\sin^2(\theta_W)} = \left(\frac{dA}{A}\right)\left(\frac{0.96+0.16Y}{1.0+1.8Y}\right).$$

Even for large Y, for which the sensitivity is greatest, competitive measurements of $\sin^2(\theta_W)$ require a combined systematic and statistical error on (dA/A) below 2%.

In the above formalism, $C_{1u(d)}$ represents the axial Z-electron coupling times the vector Z-u quark (d quark) coupling, while the $C_{2u(d)}$ are the vector Z-electron coupling times the axial Z-u quark (d quark) coupling. Each of the C_{ia} terms is sensitive to physics beyond the Standard Model in different ways.

3.6.2 Counting Rates and Expected Uncertainties

To have good sensitivity to new physics beyond the Standard Model, we would like $x > 0.2$ so that uncertainties in the sea quark distributions are sufficiently small, $Q^2 > 2$ GeV^2 to minimize higher twist contributions, Y as large as possible to improve the sensitivity to $\sin^2(\theta_W)$, and a deuterium target to avoid the uncertainty due to the $d(x)/u(x)$ ratio. It is also important to keep $E'/E > 0.3$ to avoid large rates of pions and pair-symmetric backgrounds in the detectors.

It is quickly apparent that the highest available beam energy is optimal. Assuming 11 GeV, one finds the best figure-of-merit for an electron scattering angle of 10 to 15 degrees.

Picking a typical value of 12.5 degrees, the optimum central momentum is about 5.5 GeV, corresponding to $x = 0.27$, $Q^2 = 2.8$ GeV^2, $W^2 = 8.6$ GeV^2 (well above the resonance region), and $Y = 0.64$. This happens to be quite well matched to the combination of the existing HMS and planned SHMS spectrometers in Hall C or to the MAD spectrometer in Hall A. The target length acceptance at 12.5 degrees is about 60 cm, corresponding to 10 g/cm^2 and 8% radiation length of LD2. It is not desirable to use a much longer target than this because radiative corrections become difficult to calculate.

Assuming a beam current of 90 μA corresponding to the maximum power level for the planned $Q_{\rm weak}$ target in Hall C, a momentum bite of $\pm 12\%$, and an solid angle of 6 msr for the MAD spectrometer, (or average solid angle of 11 msr for the combined HMS and SHMS spectrometers), the total count rate is on the order of 1 MHz. Assuming a beam polarization of 0.8, this leads to a relative statistical error on the asymmetry of 0.5% in about 450 hours (or 250 hours for Hall C) of "perfect" data collection. The resulting statistical error on $\sin^2(\theta_W)$ would be about 0.0006, or a 0.25% relative error. To help understand systematic effects, especially to find out if higher twist effects are sizable corrections or not, it is necessary to also take data at higher (x, Q^2) by going to approximately 15 degree scattering angle, and at fixed x but lower Q^2 by lowering the beam energy to 8 GeV. At 15 degree, the solid angle of MAD spectrometer increases to about 15 msr. For the central point, it is desirable to take additional data with a proton target to look for nuclear effects in deuterium that are larger than the uncertainty in the d/u ratio of the proton. Approximately 50 days of running time would be needed for the complete program.

The largest systematic error is expected to be from the beam polarization (of order 1%). Experience using a Compton polarimeter at the SLD at SLAC has shown the error can be reduced to below 1% with sufficient effort. The error due to radiative corrections should be well under 1%, and the error due to the determination of the average Q^2 should be under 0.5%. The error due to R is about 0.2%. A more difficult class of systematic error relates to the interpretation, because higher twist effects may not be negligible at the relatively low Q^2 of about 3 GeV^2. This will be partially addressed by making an additional measurement at lower Q^2, and another at higher Q^2 and x. Possible breaking of isospin symmetry in the deuteron could lead to corrections, as could effects such as nuclear shadowing, and the "EMC Effect" in the deuteron. These can be addressed by also making measurements with a proton target, if the d/u quark ratio is sufficiently well known at the desired kinematics from other experiments. Significant theoretical support will be needed to control all of these uncertainties to the desired level. Because the asymmetry is several orders of magnitude larger than the $Q_{\rm weak}$ and G0 experiments, control of helicity-correlated beam parameters should be adequate if they can be maintained at G0 levels when the beam energy is upgraded.

The combined statistical and systematic uncertainties for the measurement of the asymmetry, A_d are at the 1.2% level. This gives a uncertainty on $\sin^2(\theta_W)$ of roughly 0.6%. This uncertainty is shown in Fig 3.53. This experiment is sensitive to "new physics" in both $2C_{1u} - C_{1d}$ and $2C_{2u} - C_{2d}$. The sensitivity to the $2C_{2u} - C_{2d}$ makes the experiment quite unique. Assuming the successful completion of the $Q_{\rm weak}$ experiment, an absolute uncertainty of $\Delta C_{1u(d)} = 0.005$ may be obtained. With this, the proposed experiment places an absolute uncertainty of $\delta(C_{2u} - \frac{1}{2}C_{2d}) = 0.012$. When taken together with the results from the SAMPLE experiment [266] much tighter bounds are placed on C_{2u} and C_{2d} than were previously available [267] as illustrated in Fig. 3.54.

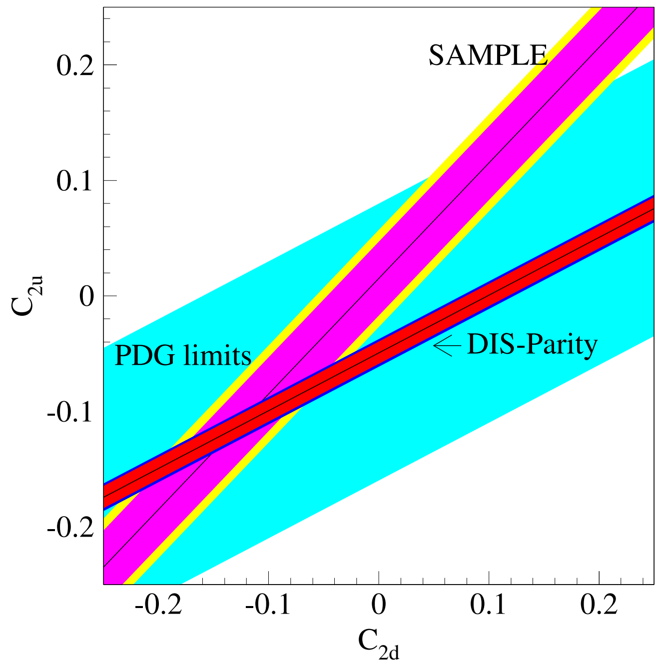

Figure 3.54: The limits on C_{2u} and C_{2d} listed by the particle data group [267], by the SAMPLE experiment [266] and by the proposed experiment.

3.6.3 Detection of Electrons

At the above kinematics the principal additional source of particles will be pions, at about 0.8 the rate of inelastic electrons. Thus the total rate will be about 2 MHz, which is tolerable for the lead glass spectrometer detectors. To separate pions from electrons, it is probably sufficient to demand a coincidence between the Čerenkov and lead glass counters, and ignore the wire chamber and time-of-flight information. The Čerenkov counter will have to be adjusted (gas mixture, pressure) to have a threshold about 6 GeV for pions. For each lead glass plus Čerenkov coincidence, the pulse height information would be recorded so that cuts could be placed off-line to optimize the efficiency versus purity, and for optimizing the lead glass energy resolution.

The equipment planned for Hall A (the MAD spectrometer) has smaller acceptance at the angle of 12.5 degree but higher acceptance at 15 degree than the HMS plus SHMS. There is no compelling reason to prefer one Hall over the other, at this stage of planning. It is worthwhile to take advantage of both hall's capability to have complimentary measurements.

3.6.4 Conclusion

A competitive search for physics beyond the Standard Model can be made using DIS parity violation at Jefferson Lab using the upgraded 11 GeV beam. An experiment has been presented which would measure $\sin^2(\theta_W)$ to an 0.5% relative error. The proposed experiment is complimentary to both the Møller and Q_{weak} experiments in its sensitivity to extensions of the Standard Model.

Chapter 4

Instrumentation

4.1 Introduction

The Jefferson Lab 12 GeV (11 GeV for Halls A, B and C) upgrade opens several new windows of opportunity for physics. In particular, a large kinematics domain in deep inelastic scattering becomes available. Coupled to the high luminosity and high polarization of beam and targets, Jefferson Lab will be in an unique position to make a significant contribution in the understanding of nucleon and nuclear structure, and the strong interaction in the high x_{bj} region.

Theoretically, the high x_{bj} region is relatively clean, where it provides a testing ground for our understanding of the nucleon structure in terms of a simple valence quark picture. Due to the fact that the quark distribution drops fast when x_{bj} becomes large, few precision data exist in this region (especially for the spin-dependent nucleon structure). Precision data in this region (at relatively low Q^2) are not only important for understanding the structure there, but also have a significant impact on a search of new physics beyond the standard model at very high energies. A high luminosity is crucial for getting precise information in this region to test our understanding. However, the high luminosity of CEBAF alone is not enough to fully explore the high x_{bj} region. A well matched spectrometer is crucial for the high impact physics program in the high x_{bj} region.

Figure 4.1 lists the requirements of a number of experiments discussed in the previous chapter, including a few in the high x region (1-5). Other inclusive experiments discussed are the spin structure in the high energy region and a DIS parity violating experiment to test standard model.

With the high luminosity and well matched spectrometers, another window opens in the study of the nucleon structure and strong interaction: the semi-inclusive reaction to probe the structure of the parton distributions. The experiments 8-12 are examples of a very rich program using semi-inclusive reactions to test the factorization, to study the flavor decomposition of the nucleon spin structure, the asymmetry of the sea quark distribution, the transversity, and the π structure function.

With an 11 GeV beam, another threshold is crossed: charm production. Threshold charm

Experimental Requirements for MAD

No.	Exp's	Pmax (GeV/c)	Angle (degrees)	Acc(angle) (msr)	Acc(mom) (%)	Res(mom) (%)	Res(ang) H, V(mr)	Luminos-ity (10^37)	e or h?
1	d/u (3H/3He)*	6	15-30	15-30	30	0.3	1-3	10	e
2	A1n,g1n	6-7	15-30	15-30	30	0.3	2-3	0.1	e
3	g2n	6	15-30	15-30	30	0.3	2-3	0.1	e
4	A1p,g1p	6-7	15-30	15-30	30	0.3	2-3	0.01	e
5	spin duality	6-7	12-25	12-25	30	0.3	2-3	0.1	e
6	g1 at high E	6-7	12	12	30	0.3	1-3	0.1	e
7	DIS-Parity	6-7	12-15	12-15	30	0.3	1-3	100	e
8	semi-pi+/pi-	6	15-25	15-25	30	0.3	2-3	5	e
9	d_bar/u_bar	6	15-25	15-25	30	0.3	2-3	40	e
10	delta_u, d, s	6	15-25	15-25	30	0.3	2-3	0.1	e
11	transversity	6	15-38	15-30	30	0.3	2-3	0.1	e
12	pi struc. fun.	3	15-22	15-25	30	0.3	2-3	0.1	e
13	charm	6-7	12-15	12-15	30	0.3	1-3	40	e
14	hadronization	6	12-30	12-30	30	0.3	2-3	40	e
15	x>1	7	12-60	12-30	30	0.2	1-3	40	e
16	Gen	6	15-20	15-20	30	0.3	2-3	0.1	e
17	Gep/Gmp	7-8*	15-35	15-30	30	0.3	2-3	40	p, FPP
16	CT (e,e'p)	7-8*	15-35	15-30	30	0.3	2-3	40	p
17	CT with FPP	7	15-40	15-30	30	0.3	2-3	10	p, FPP
18	CT in pion prod	6	12-30	12-30	30	0.3	2-3	20	pi
19	pi+- photoprod	6	12-30	12-30	30	0.3	2-3	20	pi
20	pi0 photoprod	7	12-90	12-30	30	0.3	2-3	20	p, FPP
21	KLambda	6	12-90	12-30	30	0.3	2-3	20	p
22	gamma-d	4	20-40	20-30	30	0.3	2-3	20	p, FPP

.

Figure 4.1: The list of experiments along with their experiment requirements.

production (experiment #13) opens another window to study the role of gluons in nucleon structure and some other novel phenomena, such as hidden color. Also a measurement of the charm-nuclear cross sections will provide important information for RHIC physics.

Taking advantage of the 11 GeV beam, experiments on nuclei with DIS conditions become possible (experiments #14 − 15). Also, measurements of fundamental quantities, such as nucleon form factors, can be extended to higher Q^2 regime (experiments #16 − 17). 11 GeV also opens up the possibility to reach high enough Q^2 (or s) to study novel QCD phenomena, such as color transparency (18-20). Photoproduction (21-24) at high energy provides a powerful tool to investigate the transition from the non-Perturbative QCD region to the pQCD region by studying the onset of scaling and interference phenomena.

¿From the listed experiments, it is concluded that a spectrometer with the following parameters will be well suited to this physics program:

Angular acceptance of about 30 msr (at a scattering angle of 35°) to 15 msr (at 15°);
Momentum acceptance of about 30%;
Maximum central momentum of 6 GeV/c;
Minimum scattering angle of 12-15° (reduced solid angle at small angles);
Moderate resolutions of 0.3% *in momentum, 1 mr (3 mr) in horizontal (vertical) angle.*

About two thirds of the experiments considered require detection of electrons. Electron detection will be the primary consideration for initial detector design. For electron detection, good pion electron separation is needed. Pion rejection as good as a few times 10^{-5} is needed at low momenta, with a reduced requirement at higher momenta. Higher luminosity and large acceptance makes background an important consideration in design of detectors. All these considerations have been taken into account in the new spectrometer and detector design.

The remaining one third of the experiments require hadron detection. A number of them will need a focal plane polarimeter (FPP). The hadron detection will be implemented in the second stage.

Some experiments will need parameters that go beyond the initial design specifications. An effort has been made to keep the spectrometer relatively easy to upgrade, at a later stage, to suit these experimental needs.

Another important area of physics with 12 GeV upgrade is the study of the Generalized Parton Distributions (GPDs). Wide Angle Compton Scattering and Deeply Virtual Compton Scattering are examples of experiments which will study the GPDs. These experiments require the construction of a large, highly segmented, electromagnetic calorimeter. It is planned to be constructed after the initial stage of the upgrade.

4.2 MAD Super Conducting Spectrometer

4.2.1 General

In order to perform the experimental program, the Medium Acceptance Device, MAD, spectrometer has been designed. MAD is a 6 GeV/c super conducting spectrometer with a moderately large acceptance of about 35 msr. This device consists of two large 120 cm warm bore, super conducting, combined function magnets that are 4 meters long. These magnets and the shield house are supported by a welded steel structure with steel drive wheels. The shield house is a composite of concrete, steel, and lead. The cryogenics are proven systems using standard JLab components. A schematic of how the MAD spectrometer would look in Hall A is shown in Fig. 4.2.

4.2.2 Combined Function Magnet

The MAD spectrometer requires two similar combined function super conducting magnets that can simultaneously produce 1.5 T dipole fields and 4.5 T/m quad fields for Mad CF#1the first magnet and 3.1 T Dipole and 1.8 T/m Quad for MAD CF#2 the second magnet inside a warm bore of 120 cm. A magnetic design using TOSCA 3D has been performed to establish the basic magnetic requirements, provide 3D field maps for optics analysis and produce basic engineering information about the magnets. A two sector nested cosine theta/cosine two theta design with low current density coils (4111/5750Amp/cm2 MAD #1)(4100/2800 Amp/cm2 MAD #2), warm bore and warm iron design has been selected and analyzed. These low current densities are consistent with the limits for a cryostable winding. Coils of this type are generally the most conservative that can be built and the large size and modest field quality requirements (3e-3) insure that construction tolerances (1-2 mm) are easily achievable. See tables 4.1 and 4.2 for other relevant parameters of the magnets.

The magnetic design uses TOSCA generated cosine theta type coils with “constant perimeter” ends. These coils closely approximate the ideal cosine geometry that is well established as a “perfect” generator of high purity fields. Practical considerations, finite current distributions, limited number of sectors and TOSCA’s internal approximations all contribute to deviations from the ideal geometry and are the sources of higher order field errors in the design. The yoke is modeled as truly non-linear iron with the nominal properties of 1010 steel. This steel is a commonly available alloy with properties suitable for the less demanding simple return yoke function of a Cosine style magnet. The present design yoke has an elliptical outside shape to permit closer approach to the beam line and a circular inner shape to fit the cryostat. Table 4.2 contains the present yoke dimensions. Several yoke shapes have been studied so far and further shape refinements are expected to yield an optimized shape and size. Compromises in yoke shape to improve the smallest angles attainable by MAD do not in general have a significant effect on field quality rather the effect is most felt in the integral strength. The MAD magnets have significant stability margins so small increases in current to make up for iron that is removed can be easily accommodated

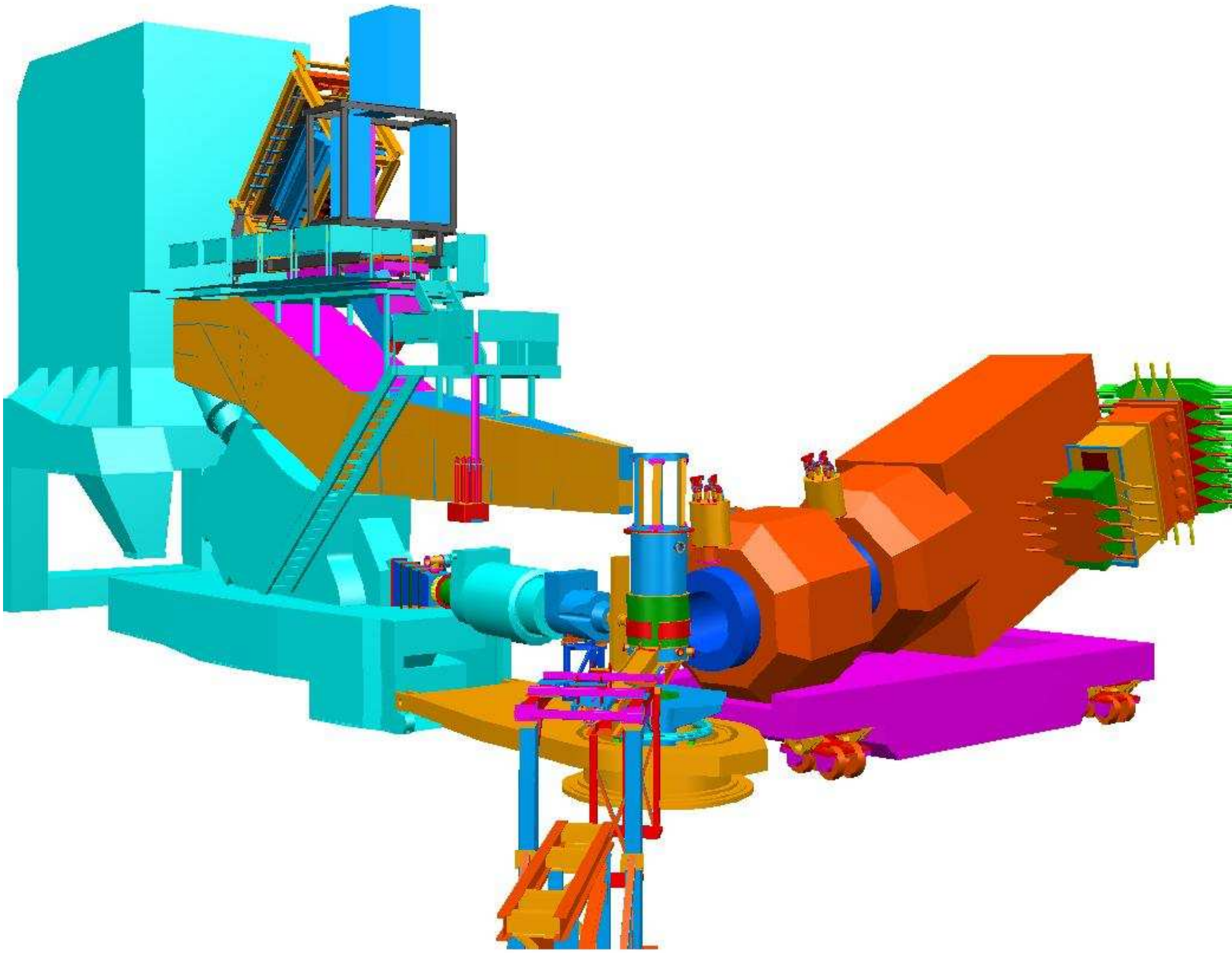

Figure 4.2: Shown is a schematic of how the MAD spectrometer would look in Hall A. The MAD spectrometer is on the right and one of the present Hall A high resolution spectrometers is shown on the left.

without sacrificing reliability.

The combined function magnets produce peak fields in the warm bore of 4 T and peak fields in the windings of 5 T. These fields are comparable to those achieved in large bore magnets produced 20 years ago for MHD research. There are significant differences as well between the present magnet and these prototypes for example the stored energy and average forces of these magnets are typically less even though the field volumes are comparable. This is due to the fact that the superposed quadrupole field produces significantly less stored energy for a given maximum field. The combined fields also produce a very asymmetric field and force distribution. The fields add on the bottom of the magnet and subtract on the top for example , so the fields across the bore range from -1 to 4 T. Similarly the fields in the windings are highest where the fields add giving 5 T winding fields and nearly -2 T where they subtract. There is thus a net force between the yoke and coil that must be dealt with due to the asymmetry. The MAD magnets must operate in both relative polarities so the magnets must be designed to accommodate the forces arising from both relative polarities. The peak linear force densities are 39,000 pounds per inch for the quadrupole winding and 36,000 pounds per inch for the dipole winding.. These forces add on one side and subtract on the other yielding peak pressures that range from 2400psi to -300 psi. Simple pressure vessel computations for 20KSI material stress yields a 4.5 inch thickness for the cold mass. Due to the large radial thickness of the windings (5 inches) and cryostat (16 inches) the required 4.5 inch pressure shell is easily accommodated without stressing the coil cold mass. Obviously in a real cold mass the stress will be distributed and the resulting stress lowered. The large size of the cryostat will allow separate fluid pressure vessels in accordance with the ASME code. This will greatly simplify the final design and result in a much more conservative magnet. A fully clamped winding is planned for the final construction. This combined with the very conservative cryo-stability will result in a very reliable design MAD spectrometer.

The cryogenics for the MAD combined function magnets will be based on the very successful thermal syphon cooling that has been incorporated in nearly all the SC magnets at JLab. The very high (100g/sec) internal flow rates and simple reservoir level control insure very reliable operation with simple controls. These magnets have approximately 100 liters of Helium in a reservoir over the magnet coils and thus have are capable of about 1 hour of isolated operation when refrigerator shutdowns occur.

The heart of this system is a somewhat complex control reservoir that contains JT valves, bayonet connections, phase separating reservoirs, current leads, relief valves and instrumentation including level sensors. There are four of these control reservoirs at JLab and three more being delivered. The standardization of design and function and use of standardized components insures compatibility and reliability. The efficiency of common design results ultimately in cost and operational savings. The control reservoir will be mounted on the downstream ends of the MAD magnets and will be located on the side to keep the overall profile of the MAD magnets low enough to fit through the truck access door. The cryogenic valving allows for top and bottom fill of Helium and Nitrogen for level operation and cool down respectively. There will also be a separate valve for variable temperature cool down gas made locally in a LN2 to He gas Heat exchanger (also standard design). This will be used to cool down and warm up the MAD magnets to minimize thermal stress due to relative contraction and increase the overall efficiency of cryogenic operations. Helium at 3.0 atm and 4.5 K is supplied from the ESR and JT expanded in the magnet to fill the reservoir. The on board phase separator allows efficient return of cold gas to the ESR while filling the reservoir without disturbing level indication. A cold return shut off valve and a warm return shutoff valve are included to allow smooth transition from cool down to regular closed cycle operation. Similarly LN2 is supplied at 80 K and 2 to 4 atm resulting in a very high quality liquid after expansion. Gaseous N2 is vented at the magnet to a sealed exhaust line. Separate flow control and measurement for each current lead is a normal part of this design. Finally, the reservoirs contain dual relief devices, an ASME coded mechanical relief and a rupture disc set at a 25% higher pressure. Exhaust lines for relief separate from cool down lines are used so that there is no chance of a contamination blockage in these all important pressure relief paths. The reservoirs contain temperature sensors, liquid level sensors and voltage taps. Generally all internal instrumentation is routed to the reservoir to a set of vacuum feed through's. Strain gauges in the cold to warm support system will be essential due to the force between yoke and coil especially considering the asymmetry of these forces. Vacuum gauging and system pressure sensors will also be located in the control reservoir. JLab owns the design for the installed and to be delivered control reservoirs all of which were built commercially, thus a repeat order on a small PO could be easily accomplished.

DC power for the MAD magnets is presently designed around low voltage high current commercial power supplies. A nominal DC current of about 5000 amps at 10 volts would be a safe choice for MAD due to the relatively low inductance (less than 1H) and provide easily for a charge time under 30 minutes. It is anticipated that 4 identical power supplies with the same rating (10 V,5000 A) would be obtained from a commercial source. Fast discharge voltages under 500 volts are easily obtained with a high current design thus reducing the risk of exposure to high voltages. The very large cold mass and low current density insures that sufficient material is available in the cold mass to absorb a large fraction of the stored energy at a low temperature during a quench discharge resulting in a safer overall magnet. Cryostable magnets are in general extremely safe and reliable but the presence of Liquid Helium in the windings is essential. The open windings characteristic of a cryostable coil exposes the coil to risk of high temperature during a quench if the windings are uncovered due to the small residual heat conduction through the insulated spacers. The MAD coils would not be self protecting and therefore a reliable fast discharge system is essential. Twelve of the thirteen large super conducting magnets presently at JLab are cryostable. These systems all have dual quench detection systems and fail safe energy dump switches.

Table 4.1 lists the parameters of the evaluation of the Steckly criteria (Alpha) for cryogenic stability. Alpha is the ratio of Joule heating in an adiabatic unit length of conductor to the heat removed by surface conduction from the same unit length.

$$Alpha = I^2 * Rho/(area * perimeter * (T_c - T_o) * H_c) \tag{4.1}$$

The condition of stability is that alpha must be less than one. Alpha less than one also means that the velocity of spread of the normal zone is negative, therefore a normal zone will always shrink. This evaluation of alpha ignores heat that is conducted along the conductor so

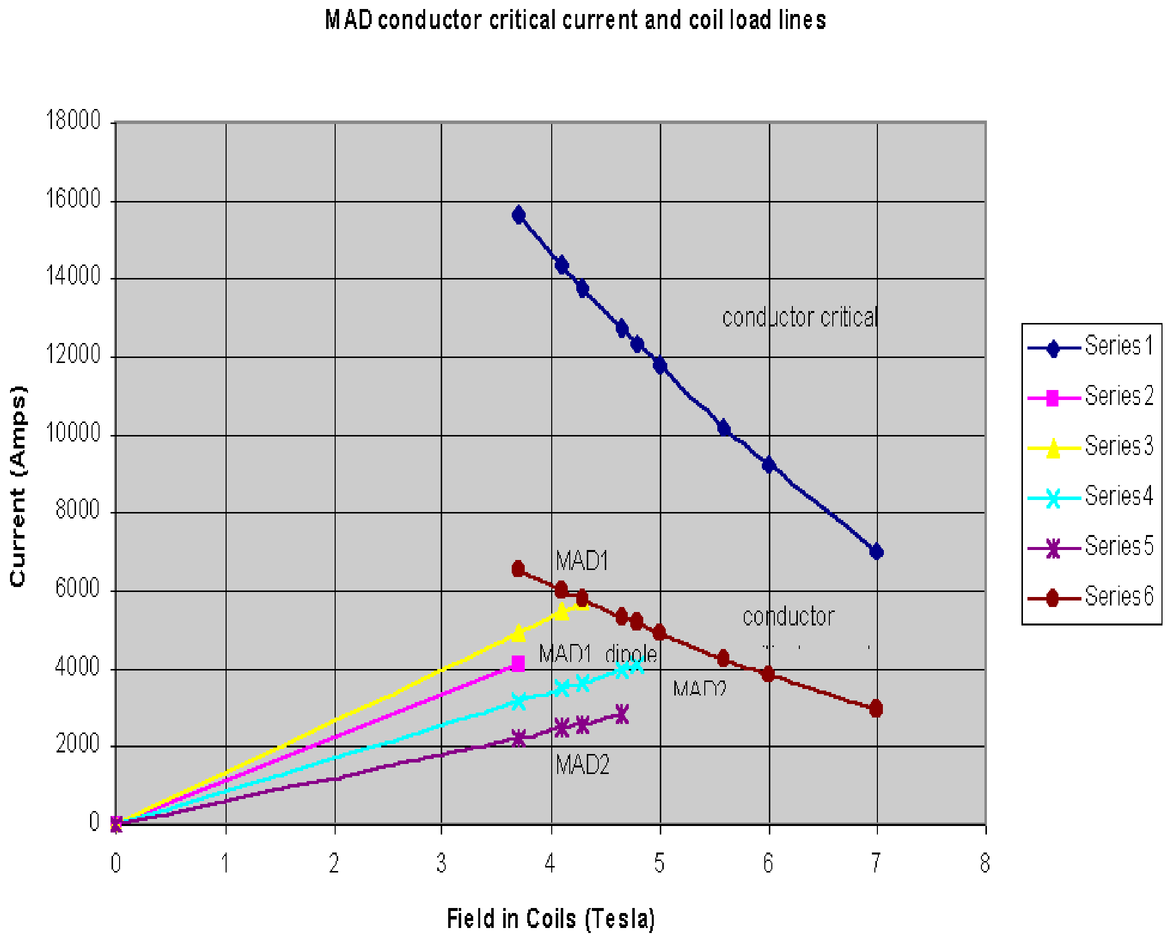
MAD conductor critical current and coil load lines
Current (Amps)
Field in Coils (Tesla)
18000
16000
14000
12000
10000
8000
6000
4000
2000
0
0
1
2
3
4
5
6
7
8
conductor critical
MAD1
conductor
MAD1 dipole
MAD2
MAD2
Series1
Series2
Series3
Series4
Series5
Series6

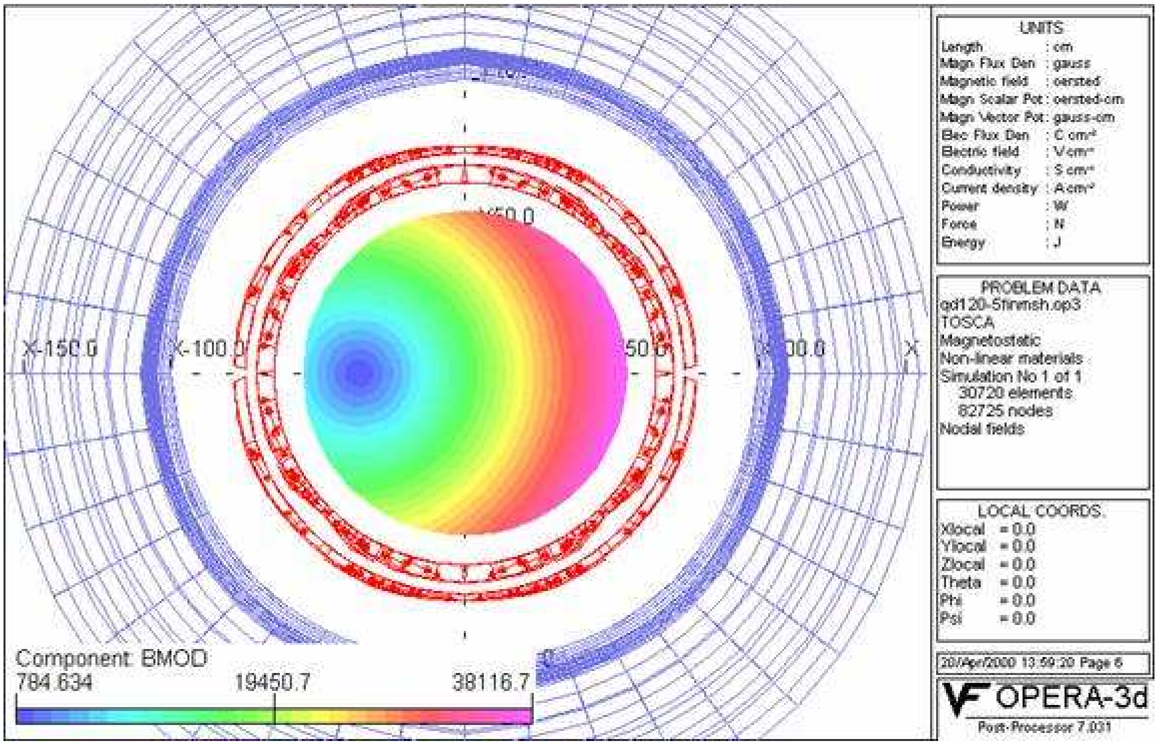

UNITS
Length : cm
Magn Flux Den : gauss
Magnetic field : oersted
Magn Scalar Pot : oersted-cm
Magn Vector Pot : gauss-cm
Elec Flux Den : C cm⁻²
Electric field : V cm⁻¹
Conductivity : S cm⁻¹
Current density : A cm⁻²
Power : W
Force : N
Energy : J
PROBLEM DATA
qd120-5finmsh.op3
TOSCA
Magnetostatic
Non-linear materials
Simulation No 1 of 1
30720 elements
82725 nodes
Nodal fields
LOCAL COORDS.
Xlocal = 0.0
Ylocal = 0.0
Zlocal = 0.0
Theta = 0.0
Phi = 0.0
Psi = 0.0
20/Apr/2000 13:59:20 Page 6
OPERA-3d
Post-Processor 7.031
Component: BMOD
784.634
19450.7
38116.7
X-150.0
X-100.0

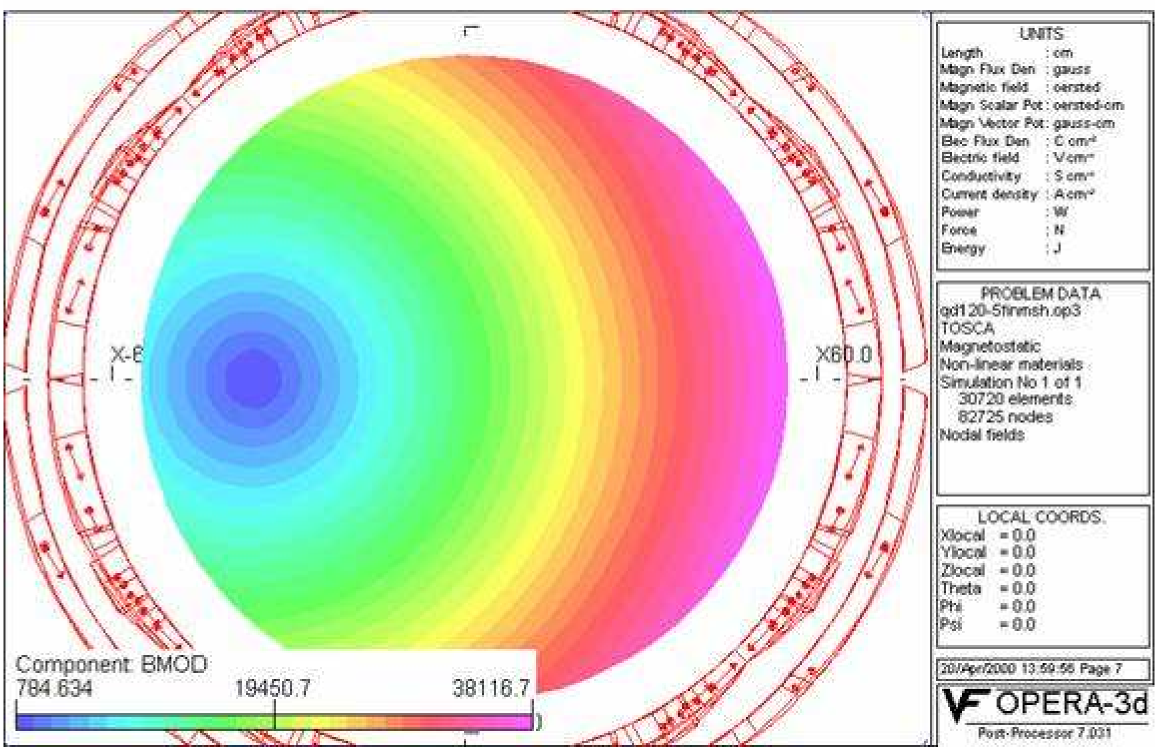

UNITS
Length : cm
Magn Flux Den : gauss
Magnetic field : oersted
Magn Scalar Pot : oersted-cm
Magn Vector Pot : gauss-cm
Elec Flux Den : C cm⁻²
Electric field : V cm⁻¹
Conductivity : S cm⁻¹
Current density : A cm⁻²
Power : W
Force : N
Energy : J
PROBLEM DATA
qd120-5finmsh.op3
TOSCA
Magnetostatic
Non-linear materials
Simulation No 1 of 1
30720 elements
82725 nodes
Nodal fields
LOCAL COORDS.
Xlocal = 0.0
Ylocal = 0.0
Zlocal = 0.0
Theta = 0.0
Phi = 0.0
Psi = 0.0
20/Apr/2000 13:59:56 Page 7
OPERA-3d
Post-Processor 7.031
Component: BMOD
784.634
19450.7
38116.7
X60.0

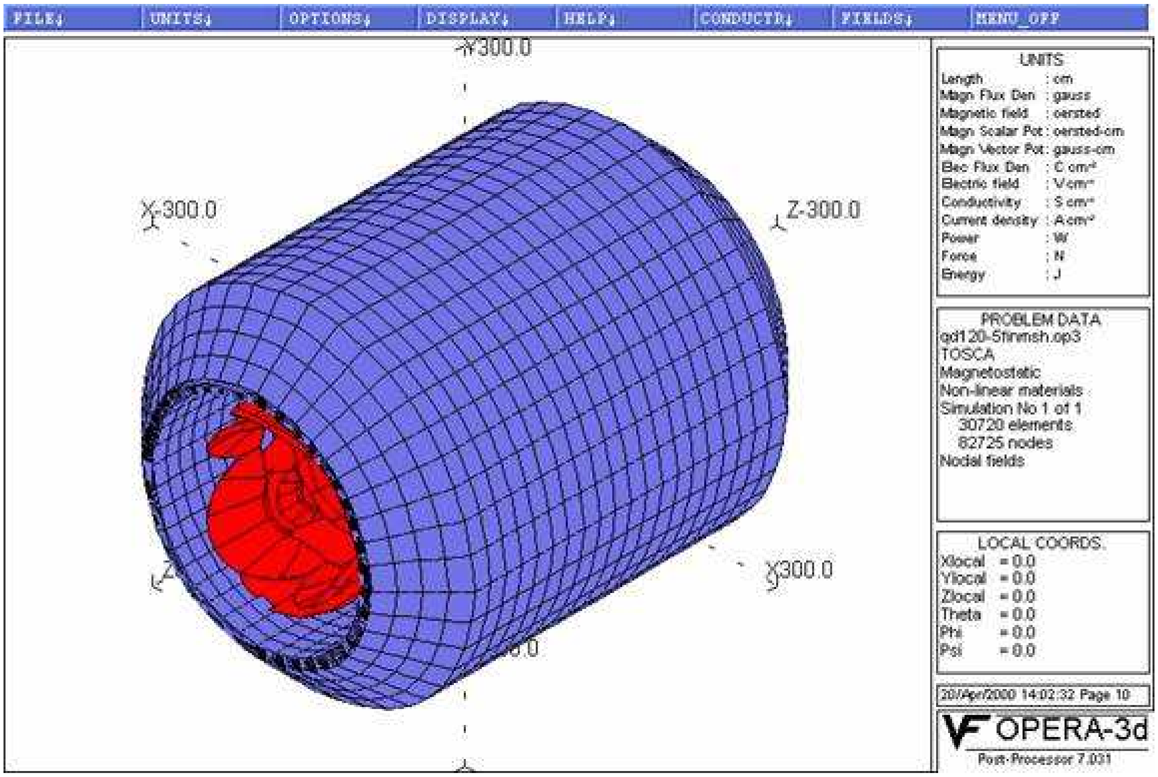
FILE
UNITS
OPTIONS
DISPLAY
HELP
CONDUCTR
FIELDS
MENU_OFF
Y300.0
X-300.0
Z-300.0
X300.0
UNITS
PROBLEM DATA
qd120-5finmsh.op3
TOSCA
Magnetostatic
Non-linear materials
Simulation No 1 of 1
30720 elements
82725 nodes
Nodal fields
LOCAL COORDS.
20/Apr/2000 14:02:32 Page 10
OPERA-3d
Post-Processor 7.031

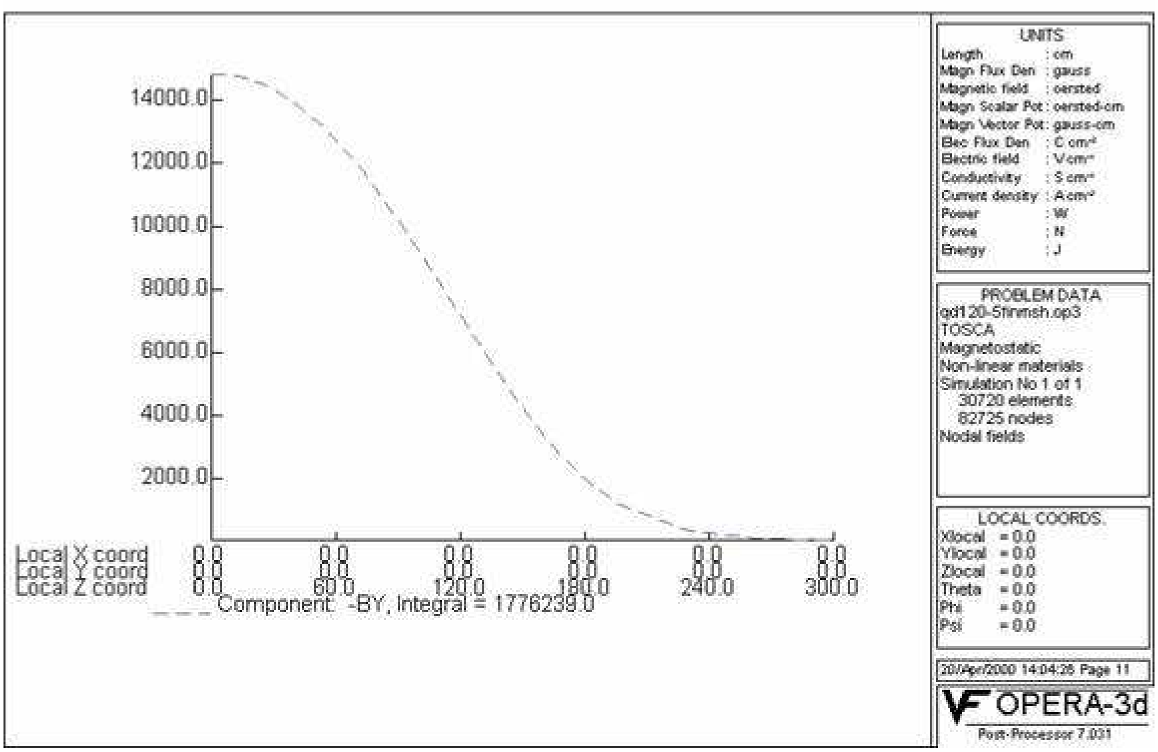
14000.0
12000.0
10000.0
8000.0
6000.0
4000.0
2000.0
Local X coord
Local Y coord
Local Z coord
0.0
60.0
120.0
180.0
240.0
300.0
Component: -BY, Integral = 1776239.0
UNITS
PROBLEM DATA
qd120-5finmsh.op3
TOSCA
Magnetostatic
Non-linear materials
Simulation No 1 of 1
30720 elements
82725 nodes
Nodal fields
LOCAL COORDS.
20/Apr/2000 14:04:28 Page 11
OPERA-3d
Post-Processor 7.031

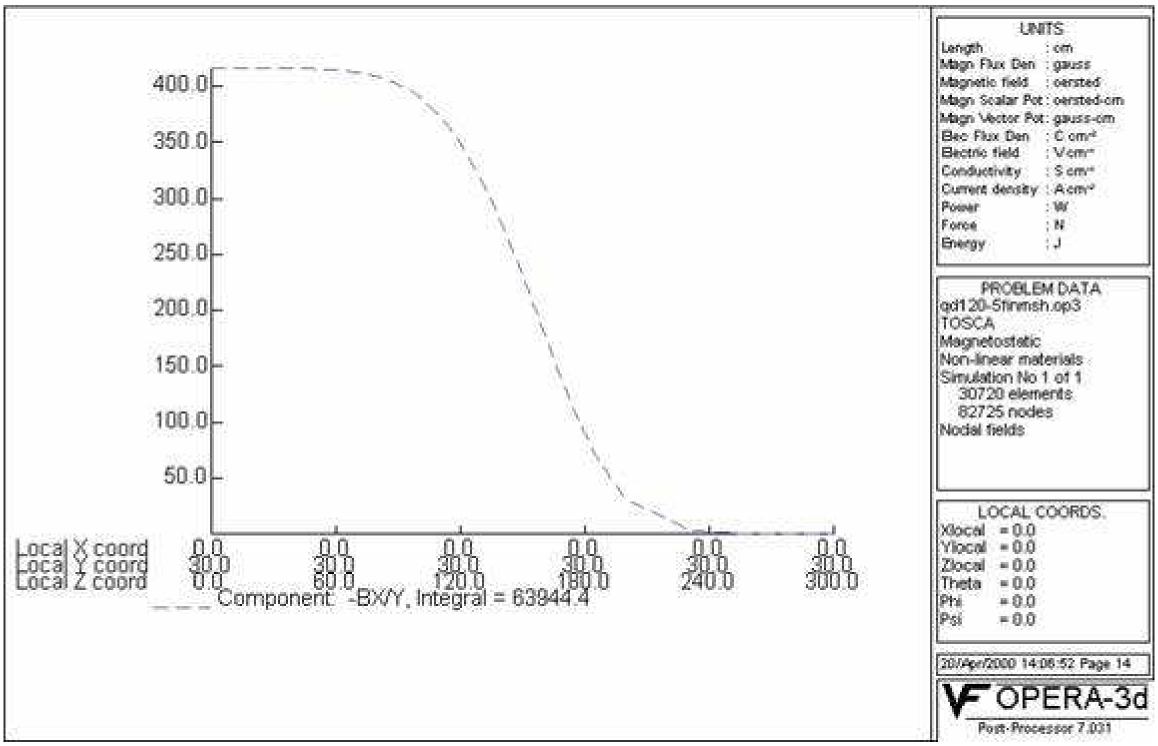
400.0
350.0
300.0
250.0
200.0
150.0
100.0
50.0
Local X coord 0.0 0.0 0.0 0.0 0.0 0.0
Local Y coord 30.0 30.0 30.0 30.0 30.0 30.0
Local Z coord 0.0 60.0 120.0 180.0 240.0 300.0
Component: -BX/Y, Integral = 63944.4
UNITS
Length : cm
Magn Flux Den : gauss
Magnetic field : oersted
Magn Scalar Pot : oersted-cm
Magn Vector Pot : gauss-cm
Power : W
Force : N
Energy : J
PROBLEM DATA
qd120-5finmsh.op3
TOSCA
Magnetostatic
Non-linear materials
Simulation No 1 of 1
30720 elements
82725 nodes
Nodal fields
LOCAL COORDS.
Xlocal = 0.0
Ylocal = 0.0
Zlocal = 0.0
Theta = 0.0
Phi = 0.0
Psi = 0.0
20/Apr/2000 14:06:52 Page 14
OPERA-3d
Post-Processor 7.031

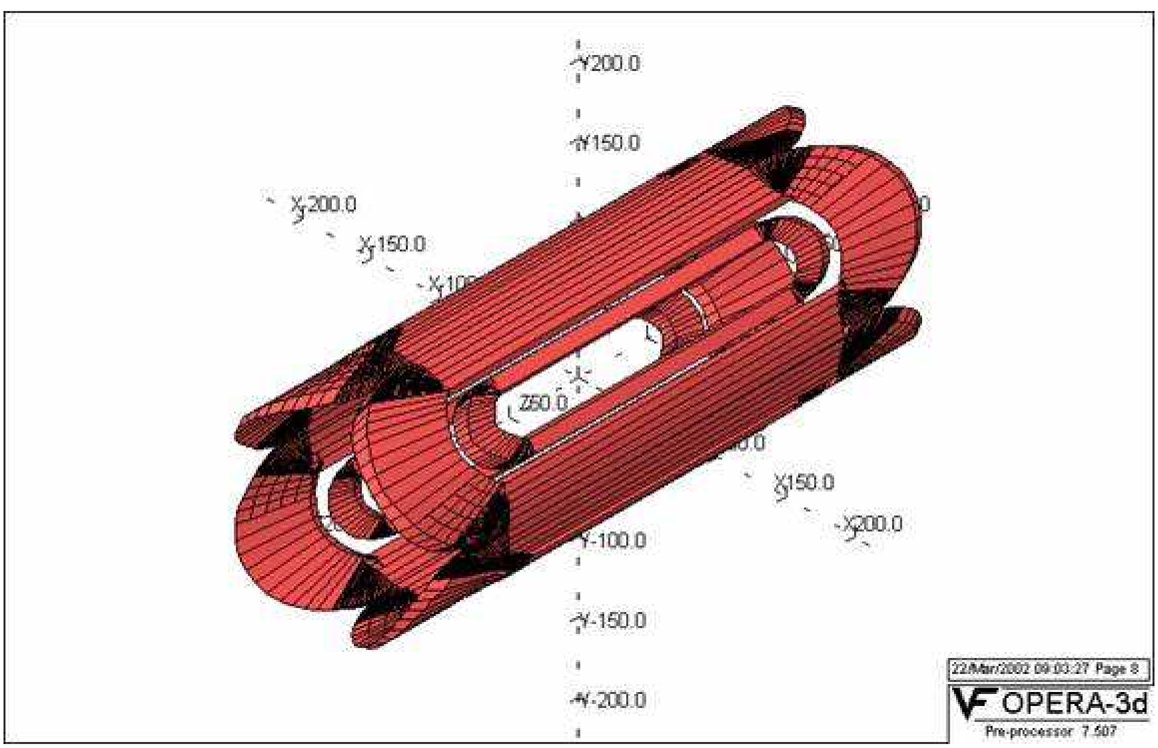
Y200.0
Y150.0
X200.0
X150.0
Z50.0
X150.0
X200.0
Y-100.0
Y-150.0
Y-200.0
22/Mar/2002 09:03:27 Page 8
OPERA-3d
Pre-processor 7.507

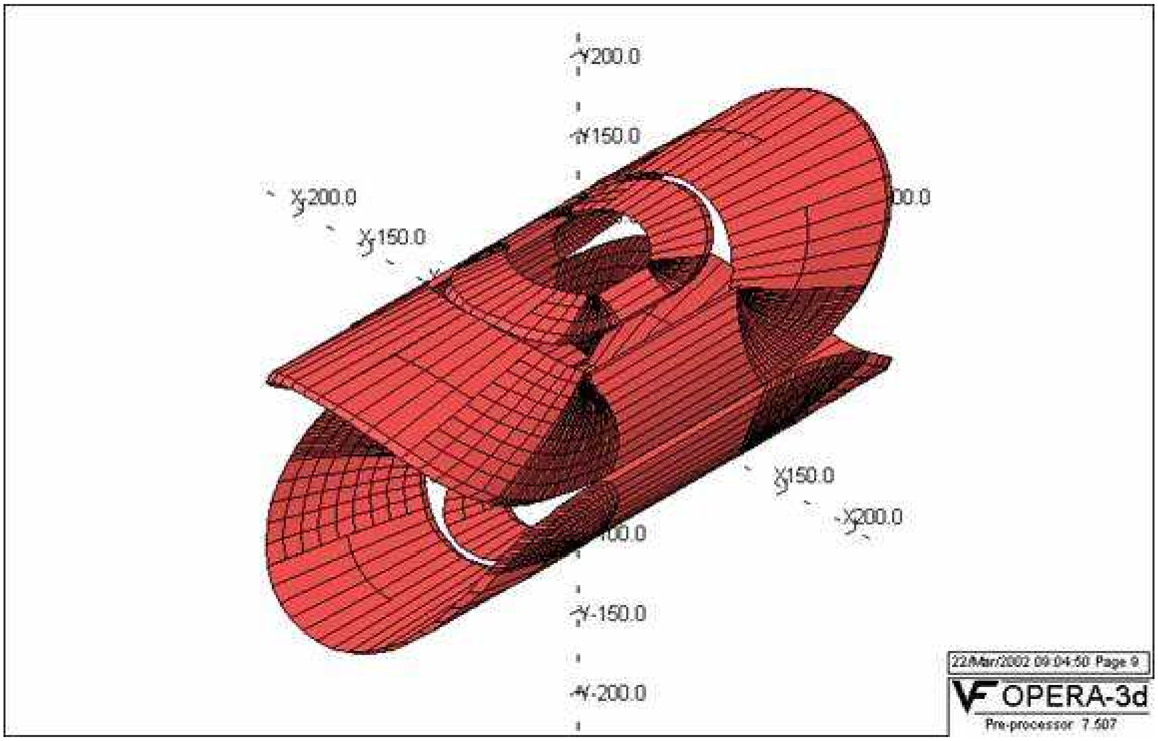
Y200.0
Y150.0
X200.0
X150.0
00.0
X150.0
X200.0
100.0
Y-150.0
Y-200.0
22/Mar/2002 09:04:50 Page 9
OPERA-3d
Pre-processor 7.507

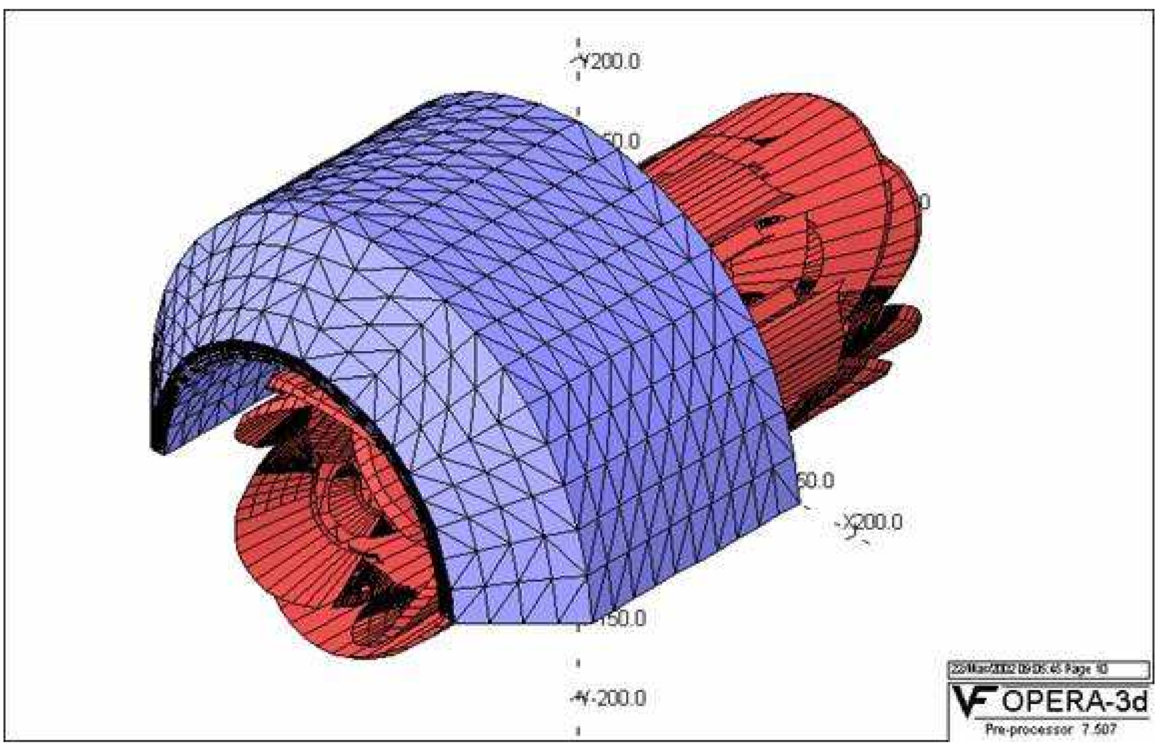
Y200.0
50.0
X200.0
150.0
Y-200.0
OPERA-3d
Pre-processor 7.507

	MAD1 Dipole	MAD1 Quadrupole	MAD2 Dipole	MAD2 Quadrupole
B_{max}	3.7	4.3	4.8	4.65
Area	0.8	0.8	0.8	0.8
Perimeter	5	5	5	5
gamma	0.6	0.6	0.6	0.6
Rho(5T,4.4K)	2.58E-8	2.86E-8	3.10E-8	3.03E-8
H_c	0.2	0.2	0.2	0.2
T_c	7.87	7.15	7.54	8.07
T_o	4.42	4.42	4.42	4.42
$T_c - T_o$	3.45	2.73	3.12	3.65
I_{max}	4111	5750	4100	2800
alpha	0.26	0.72	0.35	0.14

Table 4.1: The table lists the parameters of the evaluation cryogenic stability. B_{max} is the maximum field, Area is conductor cross section, perimeter is that fraction exposed to Helium, gamma is the per cent of the perimeter that is covered with liquid helium, Rho is the resistivity corrected for the magnetic field via the Kohler Plot, H_c is the surface nucleate boiling heat transfer, $(T_c - T_o)$ is the temperature difference between the current sharing temp and operating temp, I_{max} is the maximum design operating current.

this criteria is satisfied by an arbitrary length of conductor as long as the surface is wetted by Liquid Helium. A slightly less conservative approach known as "cold end recovery" achieves some further current margin from conduction along the conductor to the super conducting (non heating) cold end of the normal zone. This extra margin comes at the cost of finite length of applicability. That is a long enough normal zone will eventually have a positive velocity. All of these stability criteria depend on a constant supply of liquid Helium so a normal disturbance that lasts long enough will eventually use up the local supply of Helium and the quench will propagate. Cryostable magnets must be protected from operation when the Helium Liquid level is low and there is risk of exposed (non-wetted) coils. Therefore in addition to quench voltage detection a low liquid level condition is also cause for a fast discharge.

4.2.3 Magnet DC Power and Energy Dump System

The DC power for the MAD magnets will consist of four independent power supplies. These supplies will be 12 pulse SCR supplies with a final stage transistor regulator and stability of 10 PPM. These devices are readily available from Danfysik and others. The power supplies will provide 10 volts for ramp up or down, have polarity switches and the possibility of NMR control for the Dipole coils. The energy dump systems will consist of a 10 volt ramp down, a slow dump and a fast dump resistor. The fast dump will apply a voltage of 150 volts to the dipole coils and 250 volts to the quad coils to reduce the current to zero in 150 seconds. These voltages may increase as the design progresses to maintain a reasonable final coil temperature near 80 Kelvin. The dipole and quad have dump resistances such that the time

MAD magnet #1	Combined function Quadrupole-Dipole
Nominal Bend	10 degrees
Aperture	120 cm warm bore
NI dipole	2.33 E 6 amp turns 4111 amp/cm2 2 sector - cosine theta
NI quad	4.9 E 6 amp turns 5750 amp/cm2 2 sector - cosine 2 theta
Bend strength	3.5 T.M Central field 1.48 T Eff length Dip 2.4 M
Quad strength	12.8 (T/Mm)m Gradient 4.17 T/m Eff length Quad 3.1 m
dB/B - dG/G	3 e -3
LOA	4.0 m
Yoke	1010 steel 291 K# warm iron 3.2 m OD 2.0 m ID 3.0 M long
Coil and cryostat	55 K# Stainless 4.0 m Long 1.99 m OD 1.20 m ID
Stored Energy	15.0 MJ
Peak linear force density dipole coil	36,000#/in. peak pressure 1100 psi
Peak linear force density Quad coil	39,000 Win. Peak pressure 1300 psi

MAD magnet # 2	Combined function Quadrupole-Dipole
Nominal Bend	22 degrees
Aperture	120 cm warm bore
NI dipole	4.72 E 6 amp turns 4100 amp/cm2 2 sector - cosine theta
NI quad	2.2 E 6 amp turns 2800 amp/cm2 2 sector - cosine 2 theta
Bend strength	8.8 TM Central field 3.08 T Eff length Dip 2.8 m
Quad strength	5.4 (T/m)m Gradient 1.82 T/m Eff length Quad 2.97 m
LOA	4.0 m
Yoke	1010 steel 409 K# warm iron 3.2 m OD 2.0 m ID 4.0 m long
Coil and cryostat	55 K# St.StI 4.0 m Long 1.99 m OD 1.20 m ID
Stored Energy	26.3 MJ
Peak linear force density dipole coil	48,300 Win. peak pressure 2300 psi
Peak linear force density Quad coil	14,700 Win. Peak pressure 1500 psi

Table 4.2: Properties of the medium resolution, high acceptance spectrometer magnets.

constants are equal so that both coils discharge equally. The design of the MAD magnets is such that in the event of a discharge of one coil set the second coil set will see a voltage which will mimic a quench and a discharge of the second coil will be initiated anyway. The possibility of a real second coil quench is also possible due to eddy current heating in the stabilizer material.

4.2.4 Magnet Control System

The MAD magnets will have a control system that is self contained and able to be operated by an EPICS control screen. The magnets internal controls will take care of interlocks, operating valves by PID, and processing information from the magnet into engineering units. The EPICS system will allow user operation from GUI screens, archival data logging, and graphic display. A dual processor PLC of a type produced by Mitsubishi for critical fail safe process control will be used. These dual processor PLC's can switch the process control from primary to secondary in 50 milliseconds in the event that the primary processor fails. These processors can also be switched manually or by software for routine software maintenance. The use of dual processor PLC's can reduce if not eliminate the nuisance of radiation induced local processors.

The PLC will use a combination of commercial electronics for and PLC I/O modules for signal acquisition. Typically Liquid level control is by commercial AMI units and cryogenic thermometry is by Commercial Lakeshore electronics modules. Readouts of magnet voltages, pressures, strain gauges, and valve position LVDT's is by standard PLC plug ins. These systems are in wide use and all PLC's support them.

4.2.5 Support Structure

The MAD support structure is a welded steel frame riding on steel wheels. The structure will be fabricated from pre-fabricated sections that must be welded together in the Hall. The steel structure will have a main beam section that will carry the entire spectrometer. The entire beam and spectrometer will ride on large steerable steel wheel bogies that permit radial motion and scattering angle changes. This system is similar to the other large spectrometers at JLab. The steel fabrications will be hollow welded structures similar to ship hull sections. As such they will have internal access to permit complete welding of all seams and joints. The wheel sections which will also be similar to those already in use will be driven by motors and reducers with variable frequency drives. The wheels will have to be capable of radial motion so the use of tapered conical wheels may not be possible. The wheels are planned to be flat cylindrical wheels that are steered while in motion to control the radius of rotation. These wheels can be steered 90 degrees and then used to position the spectrometer radially for either the lower acceptance small angle regime (12-28 degrees) or the large acceptance (greater than 28 degrees) regime.

4.2.6 Spectrometer Motion System

The MAD spectrometer has a required range of motion from 28 degree to 135 degrees at the nominal large acceptance distance from the pivot and from 15 to 28 degrees in the small angle configuration. This requires radial motion superimposed on the angular motion. A concept involving steerable wheels is being pursued to accomplish the range of motion desired. The MAD rotates and translates as a free body. That is there is no pivot connection. Pointing is achieved by slewing the front wheels relative to the rear wheels and using a laser retro reflector system to achieve the desired pointing accuracy. The retro reflector is mounted on a reference circular stage on the scattering chamber. The MAD has an auto collimated laser that achieves the desired pointing and an angle measure. The distance off the pivot is determined by the same system. Proximity detectors insure that the system always moves in a safe angular range and that obstacles are avoided. Positioning accuracy consists of three components: angular measurement, pointing, and distance from pivot. The scattering angle positioning accuracy is 0.1 degrees, the pointing is +/- 2 mm and the distance off the pivot is +/- 0.5 cm. It may be possible to measure these quantities more accurately but these are the spectrometer setting tolerances. A scale etched into the floor at the radius of the rear drive wheels and viewed by a video camera with a gratical lens is used to confirm the scattering angle setting.

The motion of the MAD spectrometer is coordinated by a stand alone PLC that integrates the drive wheel motion, laser system read back, proximity sensors and the laser scan (light curtain) obstacle detection. The rotation motion is limited to a preprogrammed range set in EPROM in the PLC and by the proximity detection. The slew drive system is a maximum +/- 1 cm. and a minimum +/- 1 mm jog type system that acts on the front drive wheels only. Shaft encoders on the drive wheels are used to control the motion. Pointing accuracy is confirmed by the laser retro reflector system with the spectrometer at rest. The final distance off the pivot is measured when all angle adjustments are made.

4.2.7 Shield House

The MAD spectrometer shield house is a reinforced cast concrete structure that is built on the steel carriage. The concrete is confined by a steel housing that is up to 4 inches in thickness. The concrete thickness is varied to optimize the shielding in all directions. The concrete is 80 cm. thick in the sides toward the beam, back, and bottom. The sides away from the beam and the top are 40 cm thick and the front toward the target is 70 cm thick. The concrete is formed and poured in place including the two door sections. The concrete is a conventional mix with added borate to absorb thermal neutrons. The interior walls, floor, and ceiling will have a minimum 1 inch thick lead lining except for the front wall which has 3 inches of lead. The lead is covered and constrained by a system of Aluminum plates and C channels. The MAD detectors will be mounted on a transverse rail system so that the detectors may be easily removed for servicing and relocated accurately. The shield house will be accessed by doors that are hinged to open outward on the side away from the beam. The transverse rails will allow the entire detector package to roll out for servicing. There will be a limited amount of space inside the shield to allow some access to one side.

4.2.8 MAD Vacuum Systems

The MAD Spectrometer has three vacuum systems that are dedicated to the operation of the Magnets, the MAD spectrometer vacuum, and the Čerenkov detector. The MAD Cryogenic system is presumed to be leak tight and cryo-pumping so a dedicated vacuum system is not included. The magnets are also assumed to be leak tight but a vacuum system tailored to leak testing, commissioning, and bi-annual vacuum servicing is included as a dedicated vacuum system. This system can be used to commission and service the cryogenic system as needed. This system is assumed to be portable, self contained, and fully instrumented. The Spectrometer vacuum system and the Čerenkov vacuum systems are dedicated to these two systems and are permanently installed on the MAD.

The pumping system for the magnets consists of a Leybold-Heraus Turbo pump backed by a direct drive roughing pump. A 1000 liter per second turbo pump with a full port gate valve, roughing bypass manifold, and leak testing manifold are required. The wheeled pump station would have a mechanical 30-0-30 vacuum gauge, high range and low range TC gauges, and a Cold Cathode Ion gauge. A dedicated RGA for system commissioning is assumed. A large full port cold trap that can be piped in for system startup and mounted on a separate wheeled cart is included. Appropriate auxiliary vacuum hoses, valves, and flanges to facilitate connecting to all the MAD vacuum systems are also included.

A Spectrometer vacuum-air changing system that is dedicated to partial evacuation and rapid air change from normal atmosphere to helium is required. This system consists of either an "un-backed" Roots type blower pump or a ducted fan type pump and a high volume low pressure Helium gas delivery system. The pump discharge is ported outside Hall A to prevent introducing a large quantity of Helium gas to the Hall during system startup. The spectrometer gas system will have pressure gauges and differential pressure relief valves to prevent over and under pressure. A spectrometer gas system operating range from 0.9 atmosphere to 1.1 atmosphere is planned. An Arc Cell system to monitor Helium purity is assumed. The Arc Cell system will measure the presence and quantity of Nitrogen in the Helium atmosphere by spectroscopically measuring the light from Nitrogen. This system is similar to existing systems used to monitor the nitrogen contamination in cryogenic systems but is optimized for use at high relative initial concentrations of nitrogen. The detection range for Nitrogen is assumed to be from 80% down to 1%. A hygrometer to measure water vapor may also be included as a quality control check against air leaks.

The system would first introduce dry Nitrogen in a drying cycle until the water vapor is removed and then Helium is introduced to displace the Nitrogen. A continuous low volume Helium purge is maintained and monitored with both the Arc Cell and Hygrometer to monitor the system.

The Čerenkov vacuum and gas system is similar to the above but includes the capability of introducing other gases besides Helium. This system is dedicated to providing the correct Čerenkov atmosphere and has differential pressure relief valves to limit the operating pressure range to 0.9 atmospheres to 1.1 atmospheres. Appropriate monitoring equipment to verify that the correct index has been achieved will be used including a Michelson Refractometer. An arc cell system and a hygrometer are used for quality control of the process. The Čerenkov system operates first with a Nitrogen purge to dry the system, then the Nitrogen is displaced with the detection gas. A small volume purge of detection gas is maintained to permit monitoring by refractometer. The Hygrometer and arc cell may also be used for quality control of the process.

4.2.9 Cryogenic Systems

The MAD magnets will be designed with a cryogenic interface similar to the existing HRS and HMS magnets. Internally the magnets will have thermal syphon circulation from Helium and Nitrogen reservoirs. The magnets will have liquid level control and valves to permit independent warm up or cool down using a local heat exchanger. The cryogenic supply will use the existing Hall A transfer line, Septum adapter box, vacuum jacketed return lines, flex gas lines, and cool down heat exchanger. The MAD cryogenic system requires a new cryogenic distribution box that rides on the back of MAD and a flexible transfer line similar to that constructed for the G0 experiment. The magnets will be connected by JLab standard u-tubes similar to those used on HMS/HRS quads. A set of gas manifolds installed on the back of the MAD will collect and return cryogenic gases to the existing Hall A gas system. A stand to hold up the new equipment and a platform are required for support and personnel access. The system is completed by automated cool down valves and actuators identical to those used on HMS.

4.2.10 Operating Modes

During normal operation and liquid level control the MAD magnets are fed helium gas at 4.5 K and 3 atmospheres. This gas is JT expanded at each magnet by a valve that is controlled by the Mad Magnets control system to maintain liquid level. Boil off gas and JT flash are returned to the local refrigerator cold at 1.2 atmospheres and 4.2 K. Nitrogen is fed to the Mad at 85 K and 4 atmospheres where it is expanded into the N2 reservoir by a local valve under local control. Boil off N2 is vented outside. Vapor cooled current leads are controlled by local valves that servo on current in the MAD magnet and adjust the Helium gas flow accordingly. No burnout current leads are specified. The Helium gas from the vapor cooled leads (VCL's) is returned warm to the ESR compressor suction. The cool down gas return and N2 gas return lines are vacuum jacketed to prevent ice and water from accumulating near the magnets.

Internally the MAD magnets use thermal syphon circulation. An insulated supply line or "down comer" feeds helium to the bottom of the MAD magnet cryostat and a return line collects the slightly less dense fluid at the top of the cryostat and returns top the Helium reservoir through a standpipe. The Mad Magnets heat leak provides the energy to drive the circulation. The pipes are sized for 10 times the design heat load to insure stable thermal syphon flow under all conceivable conditions. The LN2 system is similar except that the LN2 shield is composed of stainless steel inflated panels.

During cool down and warm up 4 atmosphere Helium gas at 300 K is blended on the MAD in a "cool down heat exchanger" (CDHXR) with a pre-cooled 80- K Helium stream. This variable temperature source is controlled by the MAD magnet control system to provide a 70 K delta temperature for either warming or cooling and maintain an internal temperature difference in the MAD magnet of no more than 50 K. This CDHXR provides an independent and precise method of warming and cooling the Mad magnets independently.

4.3 MAD Optics

4.3.1 General Characteristics

The device is a magnetic spectrometer built from two combined function, quadrupole and dipole, superconducting magnets. The quadrupole components provide the focusing necessary to achieve the desired solid angle while the dipole components provide the dispersion needed for momentum resolution. The maximum central momentum is 6 GeV/c. The total bend angle is 32° with a 10° bend in the first magnet and a 22° bend in the second. The larger bend in the second magnet was chosen to prevent direct line of sight between the target and the detectors while keeping the dispersion reasonably small thereby reducing the size requirements on the detector package. Extra versatility can be achieved by varying the drift distance to the first magnet. Larger drift distances allow smaller scattering angles at the cost of reduced acceptance. Depending on the details of the detector package, scattering angles as small as 12° are possible.

Configuration	35°	20°	12°
Central Momentum	6 GeV/c	6 GeV/c	6 GeV/c
$\Delta P/P_0$	± 15%	± 15%	± 15%
y_0	±¿6cm	±¿6cm	±¿6cm
θ_0	± 198 mrad	± 138 mrad	± 68 mrad
ϕ_0	± 35 mrad	± 32 mrad	± 23 mrad
$\Delta\Omega$	~ 28 msr	~ 18 msr	~ 6 msr
δy_0	2.6 mm	3.6 mm	4.6 mm
$\delta\theta_0$	1.9 mrad	1.3 mrad	0.6 mrad
$\delta\phi_0$	0.5 mrad	0.5 mrad	0.5 mrad
$\delta\sigma$	1.3E-3	1.0E-3	0.7E-3

Table 4.3: The table shows the estimated performance parameters based on Transport calculations of the optical properties. For y_0, as much as ± 20 cm makes it through the spectrometer, but the ϕ_0 centroid shifts. The error estimates assume a 0.5 mrad angle determination and 100 μm position determination.

-3.72	0.00	0.00	0.00	3.54
-1.03	-0.27	0.00	0.00	103.0
0.00	0.00	1.00	5.15	0.00
0.00	0.00	-1.05	-4.43	0.00

Table 4.4: The first order Transport matrix in natural units (m, radians) for the 35 configuration.

-2.51	0.00	0.00	0.00	3.29
-0.70	-0.40	0.00	0.00	90.2
0.00	0.00	1.00	7.10	0.00
0.00	0.00	-0.79	-4.58	0.00

Table 4.5: The first order matrix for the 20 configuration.

The optics is very much that of a quadrupole pair. The large acceptance is achieved by keeping the magnets as short as possible and as close together as possible. The first order transfer matrices for the 35° and 20° configurations are shown in tables 1.4 and 1.5 In both cases $< x|\theta\delta >\sim 17$, which drives the expected momentum resolution at $\delta\pm$ 15/

-2.51	0.00	0.00	0.00	3.29
-0.70	-0.40	0.00	0.00	90.2
0.00	0.00	1.00	7.10	0.00
0.00	0.00	-0.79	-4.58	0.00

Table 4.6: The first order matrix for the 12° configuration.

The first order transfer matrix for the 12° configuration is shown in table 1.6. In this case, $< x|\delta\theta >\sim 25$

4.3.2 Raytracing Studies

A working model of the MAD has been developed using the raytracing code SNAKE. The magnetic fields in the magnets are determined using TOSCA generated maps (see section on Magnet design considerations). Those maps were created by running TOSCA on the magnet with only the quadrupole coil energized and with only the dipole element energized. Two maps are thereby generated. Those two maps are then added together with scale factors to simulate tuning the various elements. Once the first order properties expected from the Transport studies are achieved a large number (2000) of random trajectories spanning the full acceptance of the spectrometer are traced through the spectrometer. These trajectories are then used as input to a fitting program (MUDIFI) that determines the best-fit polynomials reconstructing the target parameters (δ, θ_0, y_0, and ϕ_0) of the trajectories based on their positions and angles (x_f, y_f, θ_f, and ϕ_f) in the detectors. The sensitivity to measurement errors in the detectors can then be explored in a Monte-Carlo fashion using a new set of trajectories generated in the same manner as those used in the fitting.

The following figures show the resolutions δ, θ_0, y_0, and ϕ_0 generated in the Monte Carlo analysis for three case:

- No measurement error: (labeled fit $+x_0\pm$ 100 microns) This demonstrates how well the optics is understood at this point and the effect of a 200 micron beam spot.
- Standard Errors: Here a "standard" set of conservative detector errors $\sigma_x = \sigma_y = 100$ microns and $\sigma_\theta = \sigma_{phi} = 0.5$ mrad is folded into the analysis.

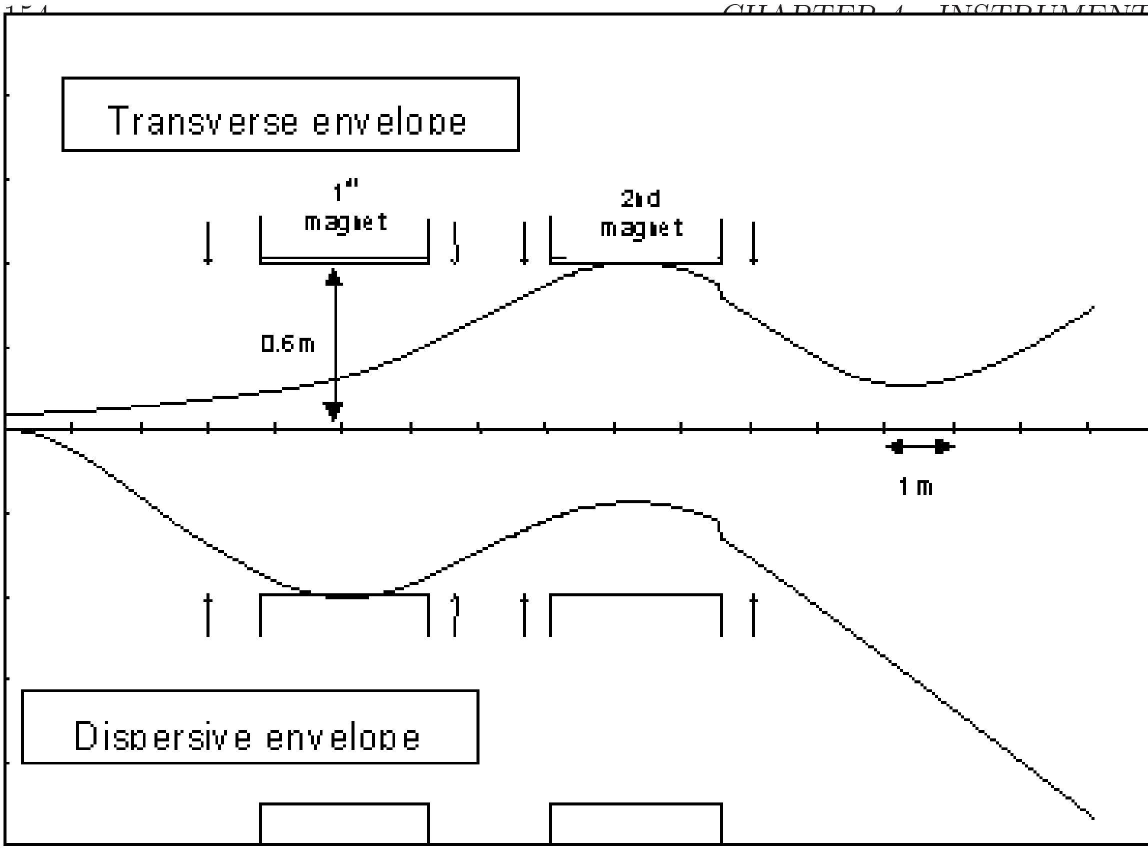

Figure 4.3: Shown is the beam envelope, transverse and dispersive, calculated with 2^{nd} order TRANSPORT for the 35° configuration.

- 0.5 * Standard Errors: The same as 2. But with the detector errors reduced by a factor of 2.

In general there is a reasonable match between the Monte-Carlo analysis and the Transport based predictions with some degradation particularly at large positive δ's. This is most likely a consequence of higher order aberrations not accounted for in the Transport analysis and still reasonable for the anticipated experimental program. Further tuning of the optics by adjusting the admixture of quadrupole and dipole in each magnet may improve the situation as well.

In order to evaluate the sensitivity of the optics to tuning errors, sets of trajectories were generated using the same setup as that above except that the quadrupole strength in each of the two magnets was varied by 0.1%. Resolutions achieved using the reconstruction tensor generated from trajectories with the correct tune on trajectories generated with the incorrect tune are compared in the following figures.

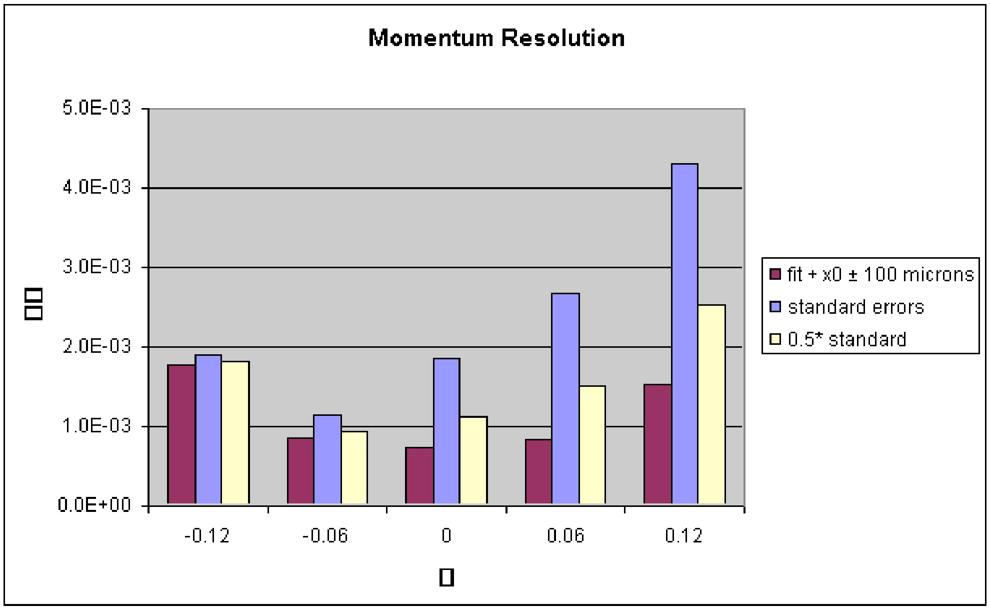

Figure 4.4: Momentum resolution in 6% δ bins.

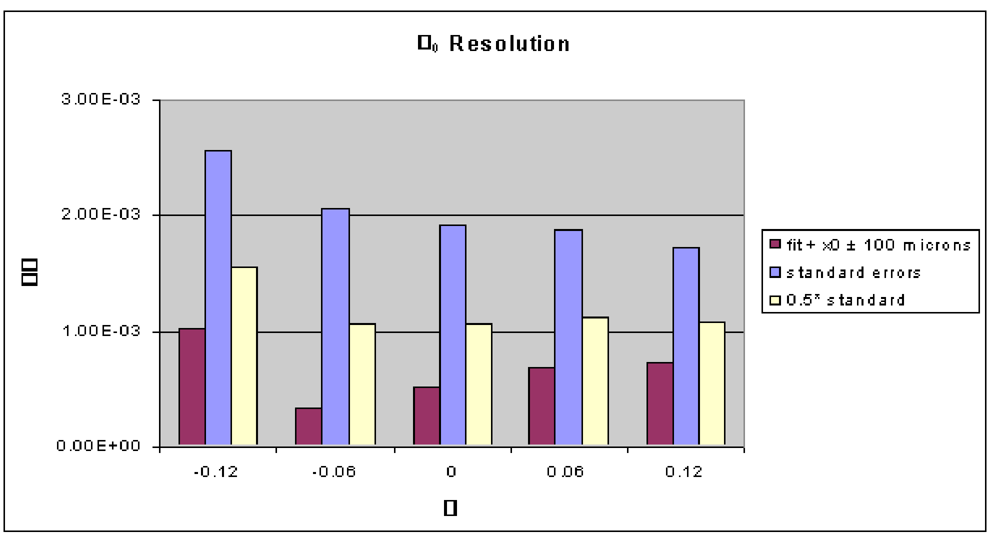

Figure 4.5: θ resolution in 6% δ bins.

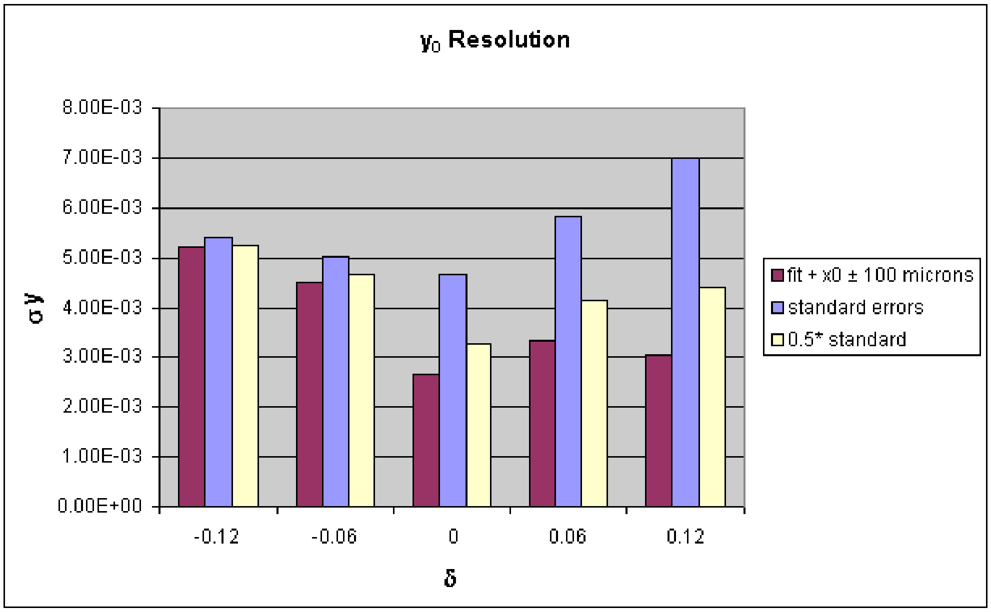

Figure 4.6: y0 resolution in 6% δ bins.

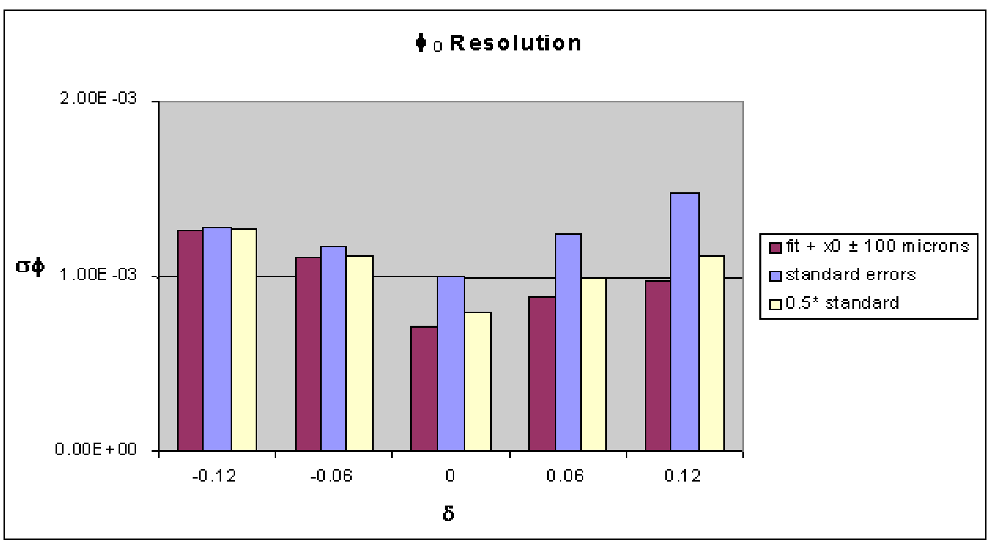

Figure 4.7: ϕ resolution in 6% δ bins.

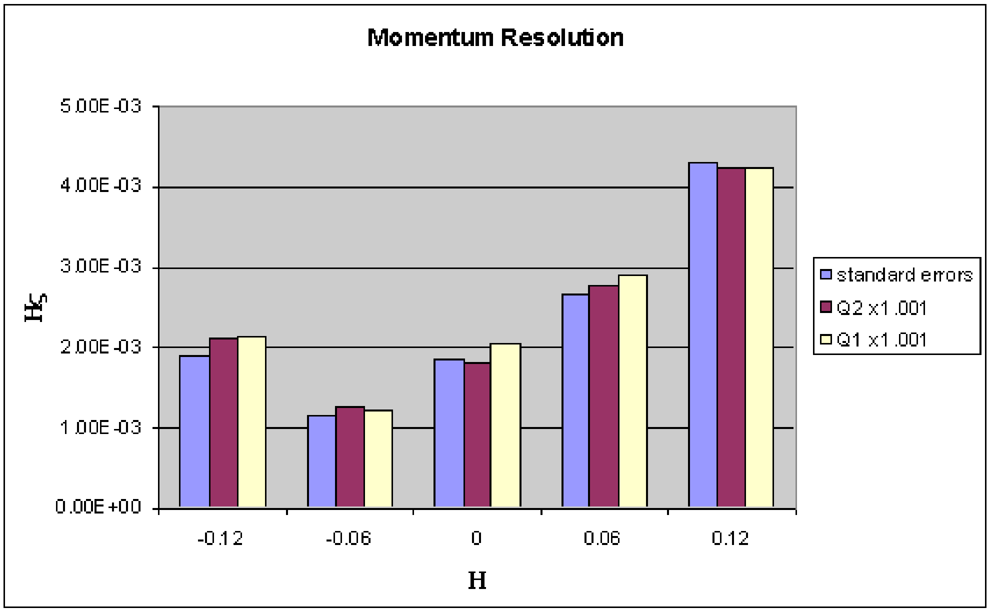

Figure 4.8: Effect on δ resolution after mistuning the quadrupole component in each magnet by 0.1%

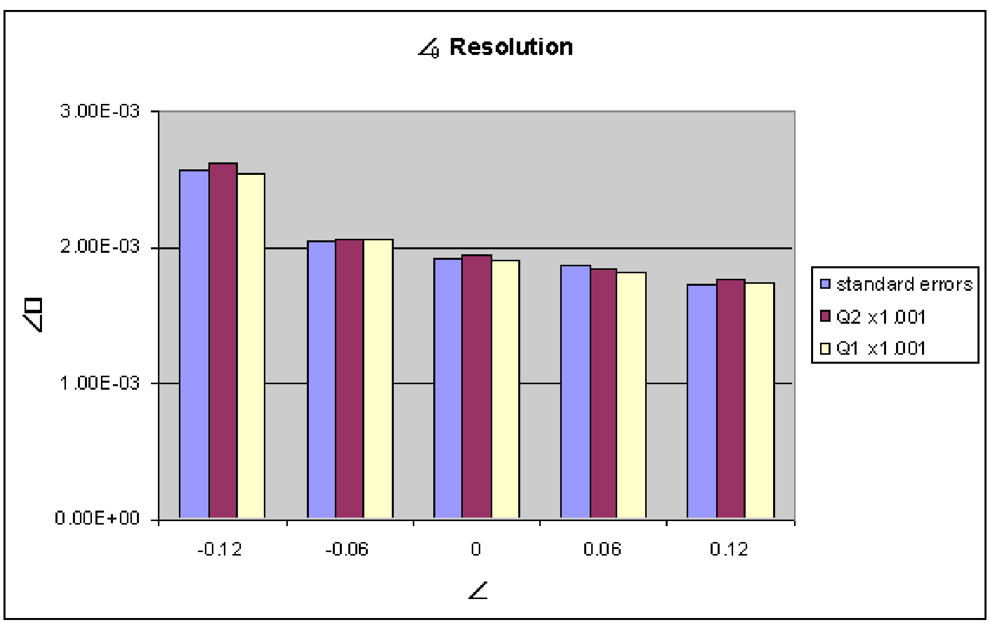

Figure 4.9: Effect on θ resolution after mistuning the quadrupole component in each magnet by 0.1%

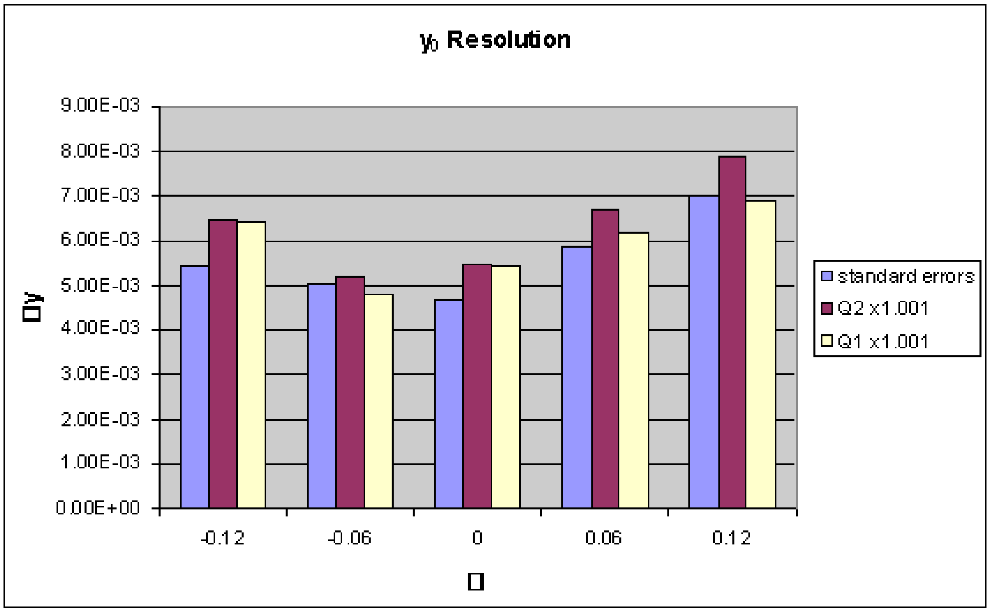

Figure 4.10: Effect on y resolution after mistuning the quadrupole component in each magnet by 0.1%

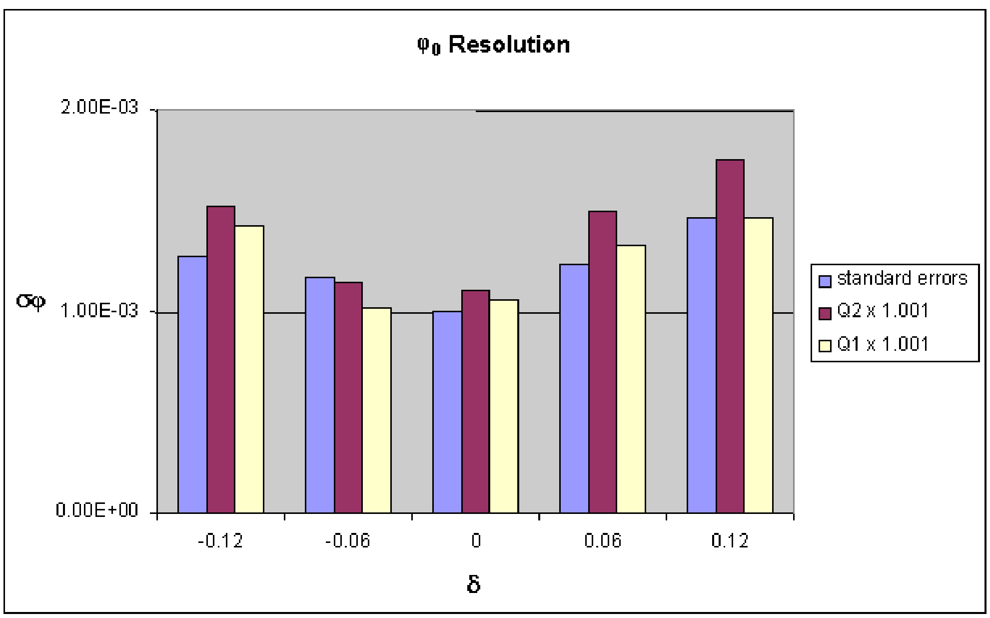

Figure 4.11: Effect on ϕ resolution after mistuning the quadrupole component in each magnet by 0.1%

4.4 MAD Simulations

Three different software packages were used for simulations. They are described below. The first two, MCEEP and SIMC, were employed mainly to simulate expected physics results such as counting rates and distributions. Results of these simulations can be found in the various physics sections of this document. Here we describe only the general features of and specific modifications made to the programs. The third software package, GEANT, was used to simulate the realistic spectrometer performance in terms of backgrounds and resolution. Results of the GEANT simulations are given in section 4.4.3 below.

4.4.1 MCEEP

MCEEP [268] is a program designed to simulate (e,e'X) experiments by averaging theoretical models over an experimental acceptance. The current version includes cross section models for the proton, deuteron, triton, ^{3}He, ^{4}He, ^{12}C, and ^{208}Pb. Both scattering to bound states and to the continuum can be studied. The program can also simulate (e,e') elastic scattering. A general three-dimensional interaction region can be specified to evaluate the effects of rastered or diffuse beams and extended targets. Internal and external radiative effects and multiple scattering can be simulated. Spin transport and precession inside magnetic elements of the spectrometer can be taken into account. Output can be in the form of histograms or ntuples. Data in histograms can be filtered with a variety of cuts.

MCEEP was originally designed for the study of sub-1GeV (e,e'N) reactions. The event generator includes various PWIA and DWIA spectral functions for the standard target nuclei (see above) as well as more sophisticated models for the d(e,e'p)n reaction. There is also support for pion and kaon electroproduction from hydrogen.

MAD is described within MCEEP via a set of transfer functions, which are essentially TRANSPORT matrices generalized to higher orders. Both forward and reverse functions have been incorporated in MCEEP. Coefficients up to 5th order and sometimes higher were included. The transfer functions were obtained as follows: Field maps for the MAD magnets were calculated using TOSCA and given as input to the raytracing code SNAKE. SNAKE was then used to trace a large number ($\approx$2000) of random trajectories through the spectrometer. Finally, polynomials were fitted to the target and focal-plane parameters of these trajectories. The fits were performed using the program MUDIFI. The resulting polynomials represent the transfer functions.

4.4.2 SIMC

SIMC [269] is a program similar to MCEEP. It can simulate elastic and quasi-elastic (e,e'p) scattering from hydrogen, deuterium, carbon, iron, and gold, as well as (e,e'π) and (e,e'K) from hydrogen, deuterium, and ^{3}He. Other targets can be incorporated by supplying an appropriate spectral function. Single-arm experiments can also be simulated. It was originally developed for (e,e'p) experiments at SLAC and has since been modified for the experimental setup in Halls A and C at JLab. Rastered beam profiles and target energy loss can be simulated, and kinematic, spectrometer, and beam offsets can be taken into account. One particular strength of the program is the treatment of radiative corrections. Many target and spectrometer parameters are hardwired into the code, and so a special version had to be created for the MAD simulations.

MAD was incorporated in SIMC in a similar manner as MCEEP. The spectrometer is described by a set of transfer functions that were derived from magnetic field maps. These functions are used to compute focal plane coordinates from generated target variables and to trace focal plane events back to the target.

(Add description of any addt'l modifications made.)

4.4.3 GEANT Simulation of Backgrounds

A thorough simulation of the expected backgrounds in MAD detectors is particularly important because of its large aperture and momentum acceptance. Simulation was used to optimize the optics and collimators in order to reduce the backgrounds to acceptable levels. The background consists of high energy particles, like electrons from DIS and pions from photoproduction by quasi-real photons, as well as a low energy photon background stemming from cascades of electromagnetic interactions of the electron beam in the target and windows. The latter background in MAD was simulated using GEANT 3.21. The geometry used included the target vacuum chamber with all relevant details of the construction, the windows and the target cell, as well as the MAD geometry including the distribution of the materials and magnetic field maps. The beam interaction with the material on its way and the interactions of the secondary particles was done with GEANT, which includes the most important electromagnetic reactions, such as Møller scattering, Bremsstrahlung, Compton scattering etc. The main source of background is a cascade of processes involving low energy photons going inside the spectrometer aperture, scattering (via Compton scattering) one or more times on the walls of the spectrometer chamber, and finally deflecting toward the detector. There are several ways to reduce this background:

a) Increase the bending angle of the spectrometer. It turns out that increasing the bending angle from 22 to 32° reduces the background by a factor of 5. This change has already be incorporated into the design.

b) Place collimators inside the spectrometer in its focal areas. The spectrometer optics accepts particles crossing the entrance to the first magnet of MAD in a relatively narrow vertical band. A collimator (COL1) with a rectangular opening 30 cm wide and 100 cm high does not affect the useful particles while reducing the background. Additionally, a collimator (COL3) close to the target chamber and leaving only the particles coming directly from the target, helps. In the vertical projection, MAD focuses the particles at about the center of the second magnet. A collimator (COL2) 30 cm upstream of the center of the second magnet with a hole about 30 cm high and as wide as the magnet bore helps to reduce the background. All three collimators reduce the soft photon background by a factor of 3.

c) Trap the photons on a special profile of the spectrometer chamber surface. The hole in COL2 is in the direct line of sight from the target. Nearly half on the background left is photons passing directly from the target through this hole and rescattering on the bottom side of the magnet chamber behind the collimator. A periodic structure on the surface of the chamber can reduce the background by a factor of about 1.5.

With MAD positioned at 25°, with a 50 μA beam impinging on a 15 cm liquid hydrogen target the calculated photon flux in the detector area is about 100 MHz with the average photon energy of $\sim$0.7 MeV. The photon energy spectrum is well described by the function $\frac{dN}{dE} \propto e^{-\alpha \cdot E}$, where α=1.5 MeV^{-1}. This flux can create a serious background in thick detectors. This was taken into account in the detector design.

4.5 MAD Detectors

With a maximum central momentum of 6 GeV/c for the spectrometer and a momentum bite of ±15% a wide range of momenta (0.7-7 GeV/c) must be considered in the design of a detector package. The proposed detector package for the spectrometer has three major functions: triggering, tracking, and particle identification. They are accomplished by using scintillator counters, multi wire drift chambers (MWDC), different Čerenkov counters, and an electromagnetic calorimeter. The Figure 4.12 shows the side view of the detector package in the configuration for electron and hadron detection. The trigger will be formed from the signals of scintillators, gas (aerogel) Čerenkov counters, and the electromagnetic calorimeter. Two MWDCs separated by 100 cm will provide tracking information for momentum and angle reconstruction. A multi-wire proportional chamber (MWPC) will be installed between MWDCs to improve the high rate capability of the tracking system.

The main parameters of the detector package are presented in Table 4.7 (without aerogel Čerenkov counters and Focal Plane Polarimeter).

Table 4.7: MAD detector parameters

	Scintillators	Drift Chamber	Gas Čerenkov	Calorimeter
sensitive area	$0.5(0.6) \times 2.0(2.5)$ m^2	0.5×2.5 m^2	0.6×2.5 m^2	1.0×3.0 m^2
space used	10,10,20 cm	100 cm	250 cm	100 cm
segmentation	16 paddles, 4 planes	1200	12 PMTs	192 PMTs
resolution	0.15 ns	75 μm	$>$ 7.5 ph.electrons	$10\%/sqrt(E)$

Particle identification will based on the long (250 cm) low refraction index gas Čerenkov counter and the electromagnetic calorimeter in the electron configuration. A variable refraction index will be achieved by using mixture of helium and nitrogen. The pion rejection factor, which is a product of rejection by the electromagnetic calorimeter (100) and gas Čerenkov counter (200), will be sufficient to reduce the pion contamination to the 1% level in the inclusive electron scattering experiments. A higher rejection factor, required at lower momentum settings, will be achieved by using gas with a higher index of refraction.

Two aerogel Čerenkov counters and a short (100 cm), high index, gas Čerenkov counter will be used in the hadron configuration. The Čerenkov counters for the hadron configuration will use the same space as the low index gas Čerenkov counter in the electron configuration.

Expected counting rates in the spectrometer are shown in Table 4.8. They were calculated for a beam energy of 11 GeV and a beam current of 70 μA on the 15 cm^2 hydrogen target (the luminosity is of 2.5×10^{38} Hz/cm^2). The required pion rejection factor is dictated by the e/π ratio in inclusive electron scattering. It varies from less then 10^3 at high momentum up to 10^5 at low momentum and forward angles.

The operation of the detectors in an environment of high flux of low energy photons is discussed in the section on Monte Carlo simulations.

Table 4.8: Single rates in MAD detector (kHz)
$E_{beam} = 11$ GeV , $J_{beam} = 70\ \mu$A, 15 cm long liquid hydrogen target.

P(GeV/c)	$\theta = 15$ degree				$\theta = 25$ degree				$\theta = 35$ degree			
	e	π^-	π^+	p	e	π^-	π^+	p	e	π^-	π^+	p
1.5	1	780	830	360	500	290	300	290	0.1	21	120	330
3.0	3	90	90	170	0.4	5	100	270	0.02	0.04	130	270
4.5	4	9	70	170	0.1	0.03	30	280	—	—	—	—

The following sections present the details of proposed detectors and their expected performance.

4.5.1 Scintillators

The trigger package for the MAD detector system will consist of four segmented planes of scintillators designated S_0, S_1, $S_2.V$, and $S_2.H$. The S_0 and S_1 planes will be located immediately before and after the drift chambers respectively. The S_2 package will consist of two planes ($S_2.V$ and $S_2.H$), oriented orthogonal to each other in a hodoscope configuration, and located just before the electromagnetic calorimeter. The primary DAQ trigger will be formed by a coincidence between the S_1 and S_2 planes, with timing set by $S_2.V$. The S_0 plane will primarily be used for trigger efficiency studies and can be removed when it is necessary to reduce multiple scattering which would degrade the angular resolution of the spectrometer. Each plane will be segmented into 16 elements to keep the total rate in a given paddle at an acceptable level.

Based on GEANT simulations, the background rate due to low energy photons will be approximately 10^8 Hz under typical running conditions. The fraction of these gammas that interact is 4% for S_0 and S_1, and 30% in each plane of S_2. Using discriminator thresholds of 0.5 MeV for S_0 and S_1, and 5 MeV for S_2 provides high efficiency for electron detection while reducing the background singles rate per paddle to approximately 50 kHz in S_0 and S_1, and 100 Hz in each plane of S_2. Requiring a coincidence between S_1 and one of the S_2 planes yields a background trigger rate of approximately 10 Hz. Requiring S_1 and both planes of S_2 in coincidence makes the background trigger rate negligible.

The scintillator elements in the S_0 and S_1 planes will be stacked horizontally (segmentation in the dispersive direction). The thickness of each element is 0.5 cm for S_0 and S_1, with a 1 cm overlap between adjacent elements. Each of the S_2 planes will contain 16 scintillator elements, with one plane oriented vertically and the other horizontally. The scintillator elements in S_2 be 5 cm thick to provide good timing resolution ($\sigma < 150$ ps). Approximate geometrical dimensions for each element are given in Table 4.9.

The detectors will be built of Bicron BC-408 or Eljen Technologies EJ-200 with a typical pulse width of FWHM ~ 2.5 ns and long attenuation lengths. Each scintillator will have light guides attached to both ends which will channel the light onto 2 inch diameter photomultiplier tubes (PMTs). For S_0 and S_1, which are 0.5 cm thick, a high gain PMT such as the Photonis XP2262 is appropriate. For S_2, the light output is expected to be high and a fast, 8-stage tube such as the Photonis XP2282B is suitable.

Table 4.9: Geometrical specifications for scintillator planes.

Plane	Location (z)	Active Area (H x V)	Number of Elements	Element Dimensions, cm (L x W x T)
S_0	0.0-0.1m	0.50m x 2.0m	16	50 x 13.5 x 0.5
S_1	1.3-1.4m	0.50m x 2.0m	16	50 x 13.5 x 0.5
$S_2.V$	4.1-4.2m	0.60m x 2.5m	16	60 x 16 x 5
$S_2.H$	4.2-4.3m	0.64m x 2.5m	16	4 x 250 x 5

4.5.2 Drift chambers

A system of two drift chambers and a multi-wire proportional chamber is proposed to instrument the MAD focal plane. The first drift chamber will be located at 0.1 m from the exit of the last MAD magnet while the second drift chamber will be located 1 m further downstream. The MWPC will be located at the mid-point between the chambers. Simulations of particle tracks through the MAD spectrometer indicate that the active area of the second chamber needs to be only about 20% larger than the active area of the first chamber. The design and construction considerations make it more cost-effective and convenient to make all three chambers with the same dimensions, 0.6 m $\times$2.5 m. The two drift chambers are proposed to have identical design, each with three groups of wire-planes with wires oriented at +45° (u) , -45° (v) ,and +90° (x). Each group of wire planes will consist of four planes separated by 1 cm each. The four planes in each direction are essential to reconstruct good tracks in a high rate environment. Furthermore, the four planes provide high resolution and high efficiency: single wire plane resolutions of roughly 100 – 150 μm have been achieved in the past, having four planes will improve this resolution to the required 75 μm value. In case of inefficiencies, at least two wire planes in the same direction is required to resolve the left-right ambiguity of drift times. With the single wire inefficiency for a drift chamber usually very low (usually $< 3\%$), the inefficiency for a chamber with four planes, resulting from the absence of two out of four planes, is extremely small. The low energy photon background at the MAD focus is estimated to be as high as 3 GHz. Assuming a conversion efficiency of 0.1% we can estimate a low energy electron rate of 3 MHz at the drift chambers. Some of these electrons will give random hits in the wire planes while the others will make tracks through one of both wire chambers. In a much worse case scenario of 60 MHz background electrons, each wire in the chamber will see about 1 MHz of these electrons. The dead-time per drift cell, mainly arising from the drift of positive ions away from the region around the sense wire, electronic dead-time and pulse-widths, is usually limited to several hundred ns.

As a result, a 1 MHz per wire rate does not pose any danger of high dead-time. Furthermore, four wire planes in each direction combined with the high position resolution and hence, the high timing resolution of the drift chamber can be used to suppress hits and tracks from background electrons. The per-wire position resolution of roughly 100 μm corresponds to a timing resolution of about 2 ns. Thus a comfortable 5σ timing window of 10 ns can be used to select good tracks. This will easily separate the real track that registered the scintillator trigger from background tracks coming at 1 MHz per wire. A complete track reconstruction simulation in a high background rate environment is under development. The extra group of planes (x) enhances high rate operation and further improves resolution. In the rare case where two out of the four planes in a (u), or (v) group fails to fire, the hits on the (x) planes can be used to ensure that the chamber has almost 100% efficiency. A wire spacing of 30 mm between sense wires is proposed to give a drift distance of 15 mm. This drift distance corresponds to a drift time of roughly 300 ns. This corresponds to an extremely high limit on the rate *per wire* around 3 MHz. For this inter-wire spacing, each plane will consist of 65 sense wires (about 1600 sense wires for the two chambers). Sensitive planes will contain alternating sense and field wires. Each sensitive plane will be between two field-shaping planes consisting of only field wires separated by 5 mm.

Chamber Design

The chamber will be constructed out of planer frames. This design is popular in wire chamber construction as it allows convenient wire stringing and easy access to each wire plane. The HERMES drift chambers, which are comparable in size to the chambers proposed here, are based on a similar design. Furthermore, multi wire proportional chambers for Hall A Big-Bite spectrometer, which will be constructed at University of Virginia in the near future, are also based on planer frames. The experience gathered in the design, wire stringing, construction, and operation of the Big-Bite MWPC will be invaluable for the MAD drift chamber project.

Chamber Simulations

The wire-chamber simulation package GARFIELD is used for a complete simulation of the the electric field configurations, drift parameters, and resolutions of the proposed drift chambers. Figures 4.13 and 4.14 show the simulated drift lines in the chambers and electron drift lines for a typical track.

4.5.3 Gas Čerenkov counter

The gas Čerenkov counter will be placed at about 1.5 m from the exit of the magnet, just after the S_1 scintillator counter. In the electron configuration (Figure 4.12) the length of the counter is 2.5 m. The mixture ratio of two gases (He and N_2) will be used to adjustment the index of refraction, so that the number of photo-electrons (ph.e.) for high energy electrons is maximized for the given momentum and length of the radiator while keeping the pion speed

Table 4.10: Collection efficiency of photons for each phototube.

Tube Number	Efficiency(%)	Tube Number	Efficiency(%)
1	97.6	7	97.6
2	99.7	8	99.4
3	99.9	9	99.9
4	97.3	10	97.4
5	91.4	11	92.4
6	82.5	12	82.6
Average		96.3	

for the same momentum below the threshold of Čerenkov radiation. Figure 4.15 shows the parameters of the counter vs. particle momentum. At 6 GeV/c central momentum of the spectrometer the fraction of N_2 will be 60% giving about 8 ph.e.

In the hadron configuration the length of the counter will be reduced to 1 m. Here, the counter will be used to reject electrons. Depending on the needs of the particular experiment, the momentum threshold for pions can be adjusted by changing the partial pressure of Freon 114. In the momentum range above 2.7 GeV/c this detector can be used for positive identification of the pion.

The back surface of the Čerenkov counter is covered by 12 mirrors in 2×6 arrangement. Each mirror is tilted by 15 degrees so that the reflected photons can be collected at the side wall of the chamber. Including the tilt, each mirror measures 62 cm×50 cm. Since we need to allow a small overlap between mirrors, the size of the actual mirror will be a little larger than this, probably about 63 cm×52 cm, which is still reasonable for manufacturing.

Each mirror will have a spherical shape with a radius of 1 m (the focal length of 50 cm).

Figure 4.16 shows the geometry of the Čerenkov counter with schematic diagrams for mirrors and phototubes.

Using the transfer functions of MAD, emission of photons, reflection on the mirror and collection in the phototubes have been simulated. Figure 4.17 shows the distribution of the actual impact points of reflected photons on the plane of phototubes. In the figure, each circle represents 5 inch phototube. Black dots are a projection of particle trajectories at the back surface of the chamber.

Except for the bottom four tubes, we can collect almost all of the photons reflected by each mirror. For the bottom four tubes, we need to use "Winston Cones" to increase collection efficiency. Due to the small profile of the particle trajectories at the bottom of the chamber, there is enough space to put Winston cones.

Photon collection efficiency has been quantified for each mirror in Table 4.10 and averages about 96%. With Winston cones, this efficiency will increase slightly.

4.5.4 Aerogel Čerenkov counters

Hadron identification, mainly π, K, and p, will be accomplished by a combination of time-of-flight measurement and threshold Čerenkov counters. Two aerogel Čerenkov counters, with indices 1.008 and 1.030, are required to cover the momentum range, as shown in Table 4.11 and Figure 4.18.

Table 4.11: The momentum threshold to produce Čerenkov radiation.

Index	P_π (GeV/c)	P_K (GeV/c)	P_p (GeV/c)
1.030	0.58	2.06	3.92
1.008	1.11	3.93	7.46
1.00143	2.61	9.24	17.6

A design similar to the current aerogel detectors in Hall A, A1 and A2, will be employed. All the inner surface of the detector will be covered with millipore paper, including the inactive edge of the PMT's. The detector will be made of two separable assemblies for PMTs and aerogel. However, some differences do exist:

- Dimensions: The MAD aerogel Čerenkov counters will be 0.6 m(H)$\times$2.5 m(V), determined by the beam envelope at z=1.5-3.0 m. This is much larger than the dimension of A1, 0.32 m(H)$\times$1.70 m(V) and that of A2, 0.30 m(H)$\times$1.94 m(V). Due to the wider horizontal dimension, the photons will be subject to more diffusions and losses on their way to the PMTs located on the sides of the detector. The height of the detector has to be increased too, which requires 2-3 layers of PMTs.

- Magnetic field: A magnetic shield is required as the magnetic field is on the level of 10 Gauss. There are two possible ways to add a magnetic shield. One is to add an enclosed shield for the whole detector, i.e. to insert an 0.50 mm iron planes before and after the aerogel detector with thicker iron on the sides. This will introduce more δ electrons and nuclear absorptions. The other option is to add individual shields for each PMT. This will affect the photon collection.

- Aerogel thickness: Fewer photo-electrons are expected when the refractive index get closer to 1, which is nearly proportional to $n - 1$. To get enough photo-electrons, the aerogel thickness must be increased for index n=1.008. But due to the absorption and scattering in the aerogel, the number of photo-electrons will saturate at a certain thickness, on the level of 15 cm.

Based on the performance of A1($n = 1.015$), as shown in Figure 4.18(b), the number of photon-electrons at different momenta were estimated for indices of 1.008 and 1.030, as shown in Figure 4.18(c,d). The value of the rejection factor for a given momentum was estimated to be 30 based on an experimental result for A1, where the rejection factor was about 30 at 2 GeV/c.

4.5.5 Electromagnetic Calorimeter

An electromagnetic calorimeter is planned as the most downstream detector in the MAD detector stack. The main purpose of the calorimeter is separation between electrons and charged pions. Electrons, producing showers, have nearly all their energy absorbed in the calorimeter, whereas, only a small fraction of the energy of a hadron will be absorbed. Comparing the energy release in the calorimeter with the momentum of the particle provides pion/electron discrimination. The longitudinal profiles of the signals produced by electrons and hadrons in a calorimeter also differ. The maximum energy density of an electromagnetic shower is occurs at about 5 radiation lengths into the calorimeter. Hadrons do not produce such a pattern.

The size of the calorimeter was selected using the GEANT simulation of MAD at 25 and 35° and at the mean energy of 6 GeV. The initial particle was produced in a 10 cm long liquid hydrogen target with uniform distributions of the angles and momentum in the range of MAD acceptance. The results depend considerably on the optics applied, in particular in Y-projection (perpendicular to the dispersive direction), since the calorimeter is close to the transverse focus of MAD.

The results for "MAD-2" optics are presented on Fig.4.19.

A newer version of the optics, "MAD-3", provides better spectrometer resolution and more compact particle profiles in the calorimeter area (see Fig.4.20).

In the Hall A HRS spectrometers, lead glass arrays of about 1.8 m^2 surface are used for the electromagnetic calorimeters. Since further modifications of the optics may occur, a slightly larger detector size than needed for the "MAD-3" optics, 3.2×1.0 m^2, is being considered for the present purposes.

Since most of the events in MAD will contain only one high energy particle, only a coarse transverse segmentation of the calorimeter is required.

It is proposed to build a lead-plastic scintillator sandwich calorimeter, about 22 radiation lengths deep, divided along the dispersion direction in 32 bars. Each bar is 10 cm wide and 100 cm long. The bar is divided in three segments along its depth in order to improve the e^-/π separation. Since the light attenuation in the scintillator sheets along the bar length of 100 cm is considerable, each segment is read out by two photomultiplier tubes from both sides of the bar, each PMT seeing a half of the scintillator sheets. In the first approximation, in the case of low attenuation losses, such an arrangement cancels out the effect of attenuation. In total the detector will include 196 PMTs.

A similar design[270] is used in Hall B at JLab, although with three projections readout from triangular shaped detector modules, employing the same compensation of the attenuation losses. With longitudinal segmentation in two segments an energy resolution of about $\sigma_E/E \sim 0.1\ GeV^{0.5}/\sqrt{E}$ and a e^-/π suppression factor of about 100 was obtained. The sandwich contained 2.2 mm lead sheets and 10 mm plastic scintillator sheets. The light was collected with the help of optical fibers. For the design proposed a similar result is expected. To estimate the cost of such a detector the Hall B experience is used, scaling the cost to the size of the detector. One module in Hall B, costing about $1M, is about four times larger in weight than the detector proposed for MAD, and contains about the same number of PMTs.

4.5.6 Focal Plane Proton Polarimeter

The large solid angle and momentum acceptance of MAD coupled with a focal plane polarimeter allow a range of studies that are essentially impossible with existing experimental equipment, or with the Hall C HMS equipped with a focal plane polarimeter. Possible proposals include determination of the recoil proton polarization in deuteron photo disintegration, meson photo production, elastic scattering, resonance electro production, and quasi free scattering. These are discussed elsewhere in this document (see section ?).

Conventional polarimeters measure an azimuthal asymmetry from the scattering of the protons in an analyzer to determine the polarization. The incoming trajectory will be determined by the focal plane HDCs, while the outgoing trajectory will be determined by tracking chambers specific to the polarimeter. The polarimeter figure of merit, ϵA^2, is enhanced by large efficiency for detecting scattered protons. This requires both large polarimeter chambers - the existing Hall A polarimeter can measure scatters up to about 70° - and thick analyzers, up to about 1 m, to increase the scattering efficiency. Because the thick analyzers also absorb a significant fraction of the protons, up to about 50% at 3 – 4 GeV/c, it is further desirable to segment the polarimeter, alternating layers of analyzer with chambers. A double analyzer, as has been used in the Hall A RCS experiment, is a reasonable compromise between increased costs and increased efficiencies.

The polarimeter measurements are inclusive, based on a single outgoing charged particle track, with no further information. In principle further information about the outgoing particle or nuclear scattering could improve the analyzing power determination, as different reactions have different analyzing powers. There is insufficient information at this time however to justify implementing such schemes in the polarimeter.

Due to the large beam envelope with MAD, an alternate detector stack to the conventional design is desirable. In the experiments considered so far, the only significant background is π^+ mesons, which can be sufficiently reduced through the use of a single Čerenkov detector. Use of smaller tracking detectors further forward in the detector stack reduces the cost of the FPP.

The layout of the focal plane polarimeter is shown in Fig. 4.21. Use of a CH_2 analyzer with density near 1000 kg/m^3 leads to a total analyzer mass of 4500 kg. A carbon analyzer of similar volume would yield a similar figure of merit, with about 60 – 70% greater density. To capture scatterings from the analyzer with good geometric efficiency, the tracking chambers would need to extend about $\pm$50 cm beyond the analyzer, leading to active areas near 2.5 m wide by 4 m high.

We propose to construct a set of 4 multilayer straw-tube chambers, very similar in design to the existing Hall A FPP, to cover the above active area. With 2 cm drift cell diameter, the number of channels will be about 5000.

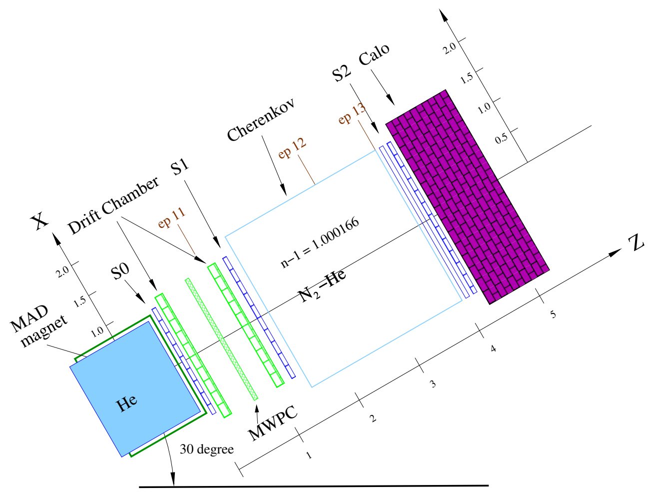

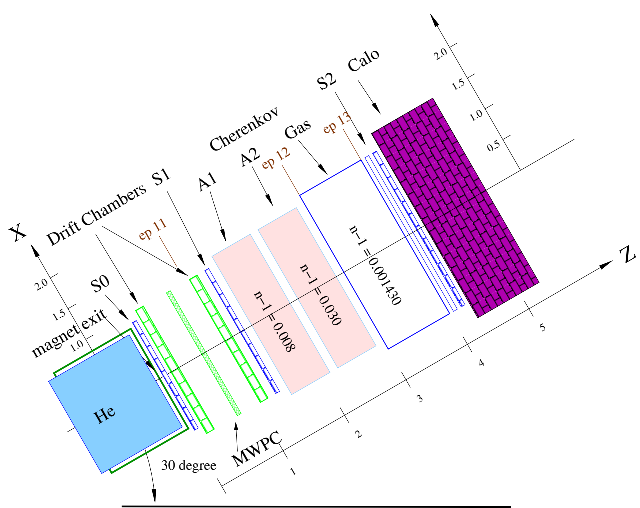

Figure 4.12: Configuration of the detector package.

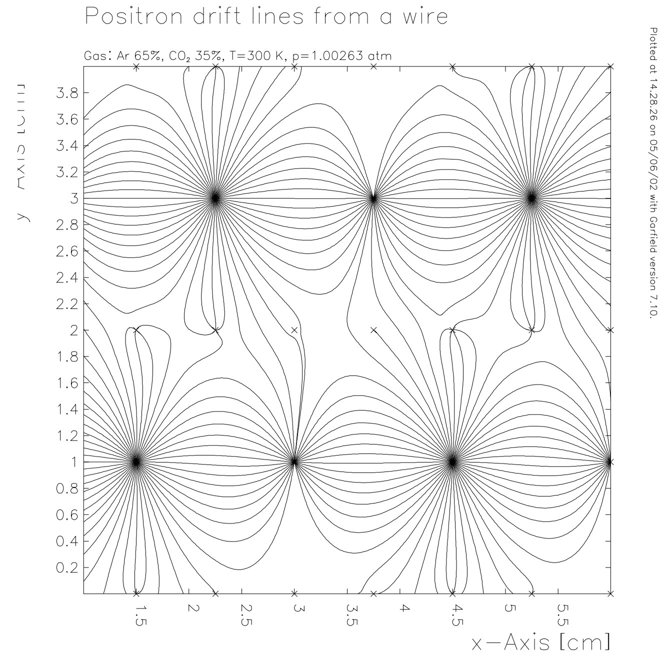

Figure 4.13: The GARFIELD simulation of drift lines for the proposed configuration. The wire planes located at y= 0, 2 and 4 cm consist of 100 μm wires separated by 5 mm and maintained at -2000 V. The filed shaping wires located at (3,1), (6,1) and (3.75,3) are 100 μm wire maintained at -3000 V. The sense wires located at (1.5,1), (4.5,1), (2.25,3) and (5.25,3) are 20 μm wire at ground potential.

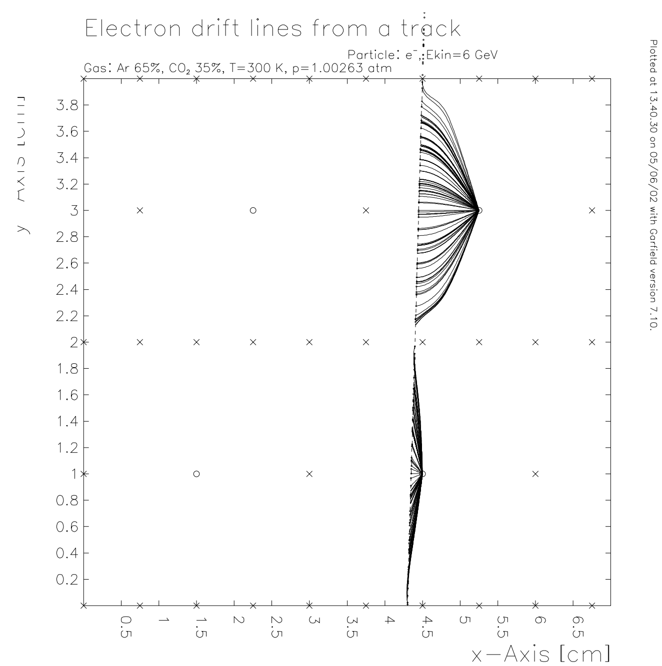

Figure 4.14: The GARFIELD simulation of a typical track through the chamber.

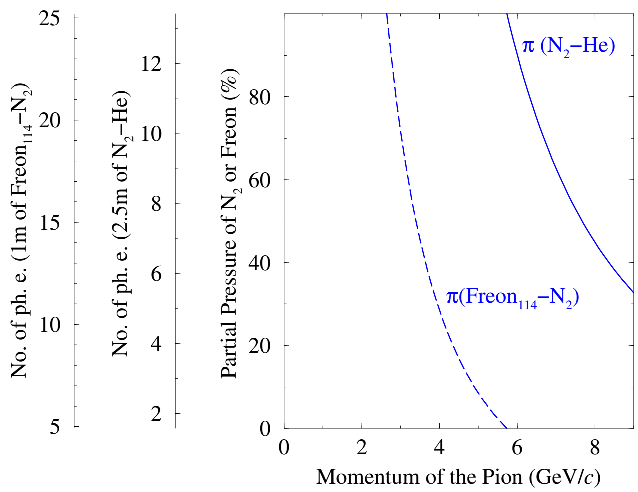

Figure 4.15: Number of photo-electrons expected for high energy electrons in the gas Čerenkov counter. Partial pressure corresponding to the threshold of Čerenkov radiation for pion at given momentum. The solid line represents the N_2-He mixture and the dashed line shows threshold for the mixture of Freon 114 and N_2.

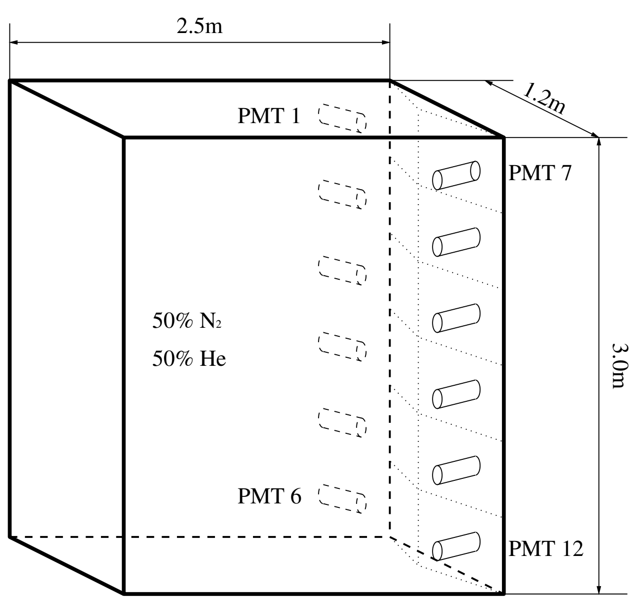

Figure 4.16: Geometry of the Čerenkov counter with schematic diagrams for mirrors and phototubes.

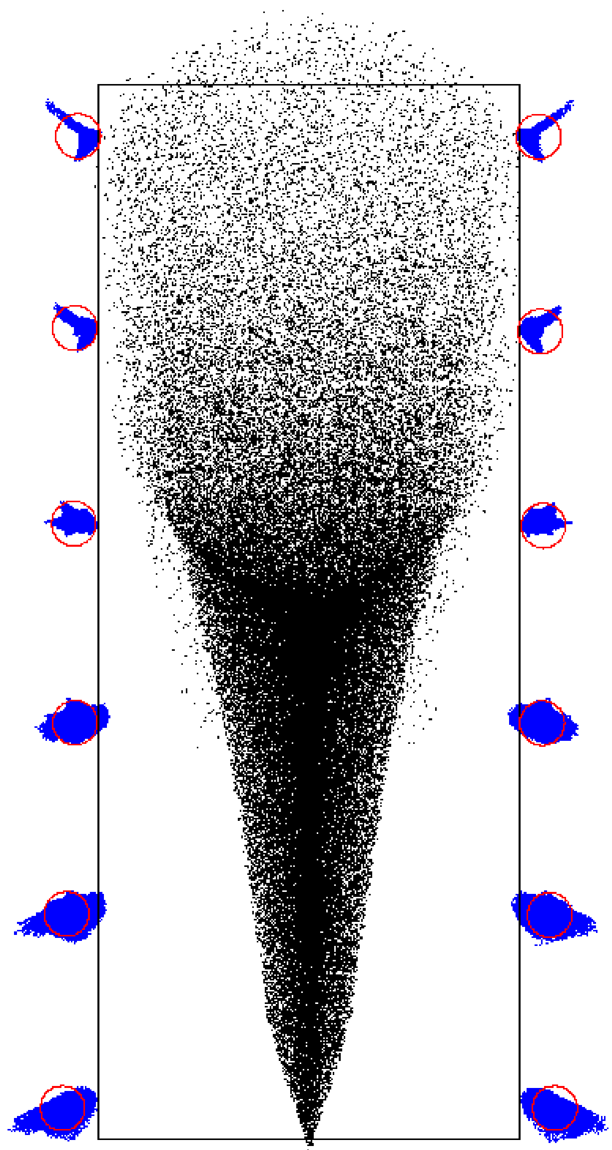

Figure 4.17: Simulation of photon collection by each phototube. The black points are a projection of the actual trajectories on the back surface of the chamber and the blue dots are the impact points of the reflected photons on the phototube surface with red circles for 5 inch phototubes.

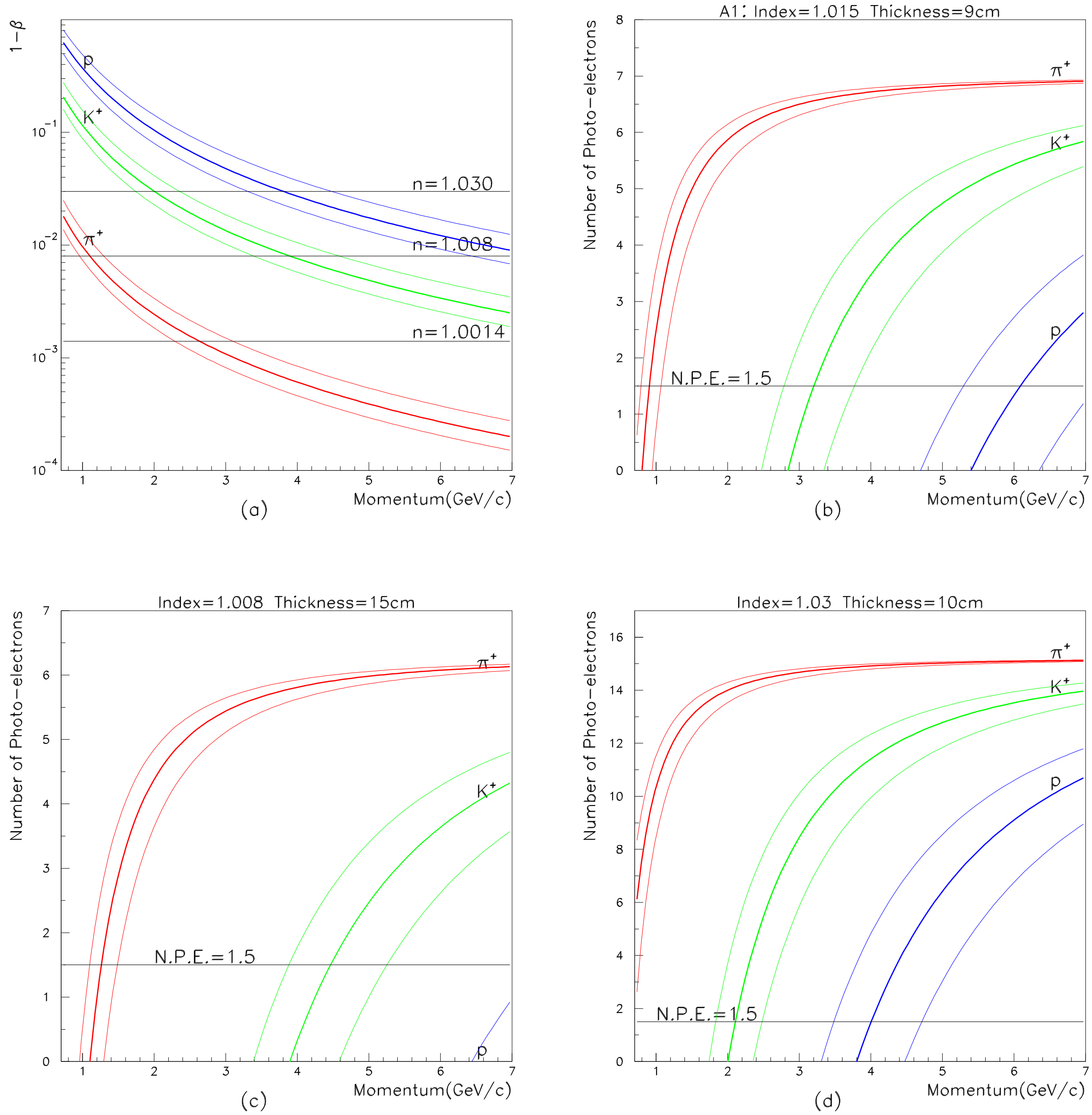

Figure 4.18: **(a)** The deviation of velocity from 1 vs. momentum for the proton, pion and kaon. Side lines represent the momentum bite of the spectrometer. **(b)** A1 performance with index of 1.015 and thickness of 9 cm. **(c)** Estimated number of photo-electrons vs. momentum for index of 1.008 and thickness of 15 cm. **(d)** Estimated number of photo-electrons vs. momentum for index of 1.030 and thickness of 10 cm.

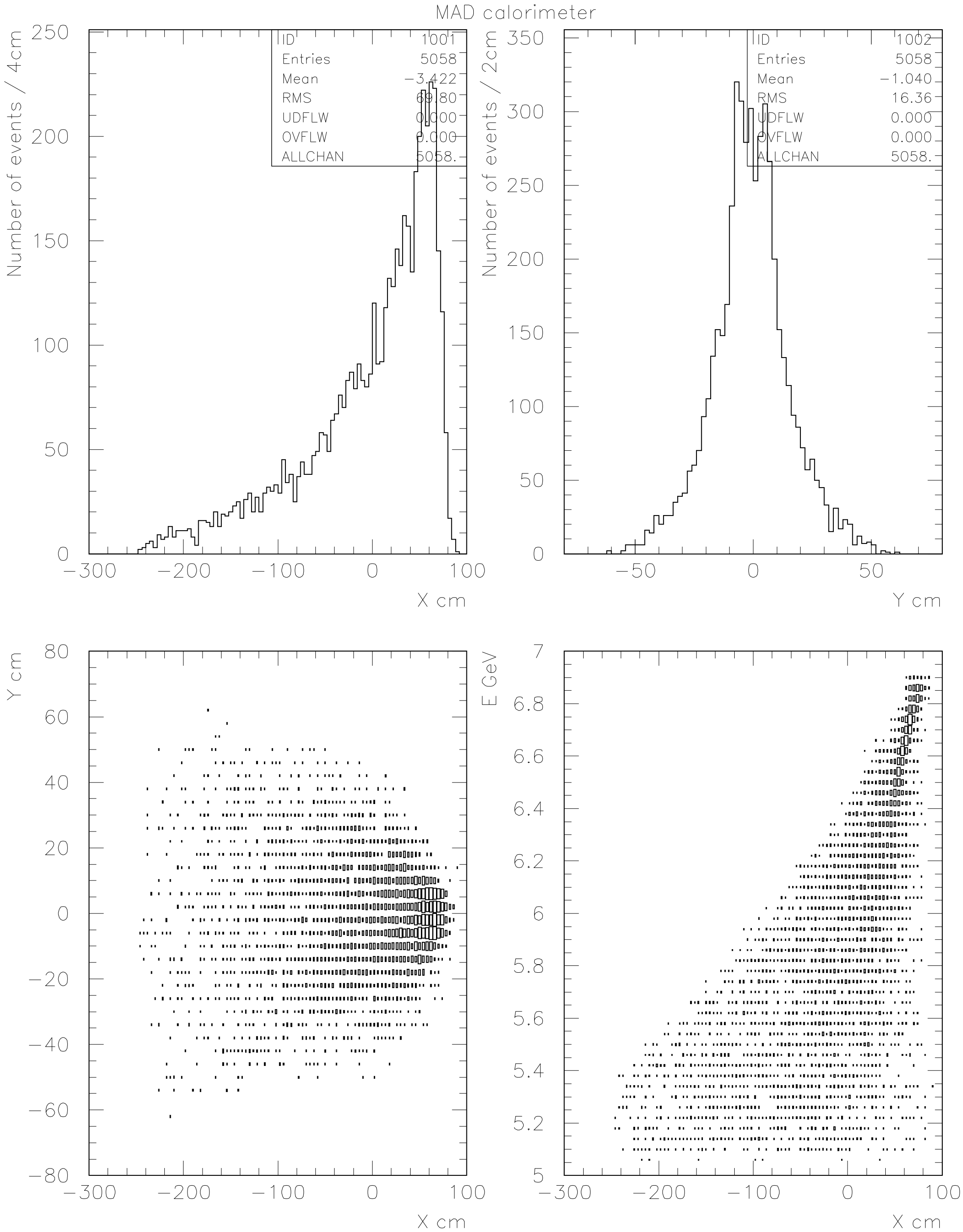

Figure 4.19: Simulation of the particles spectra in the plane of the MAD calorimeter at 25°, with "MAD-2" optics used. The top histograms represent the X and Y distributions, while the bottom ones represent the correlations of two projections and of the dispersive projection with the momentum.

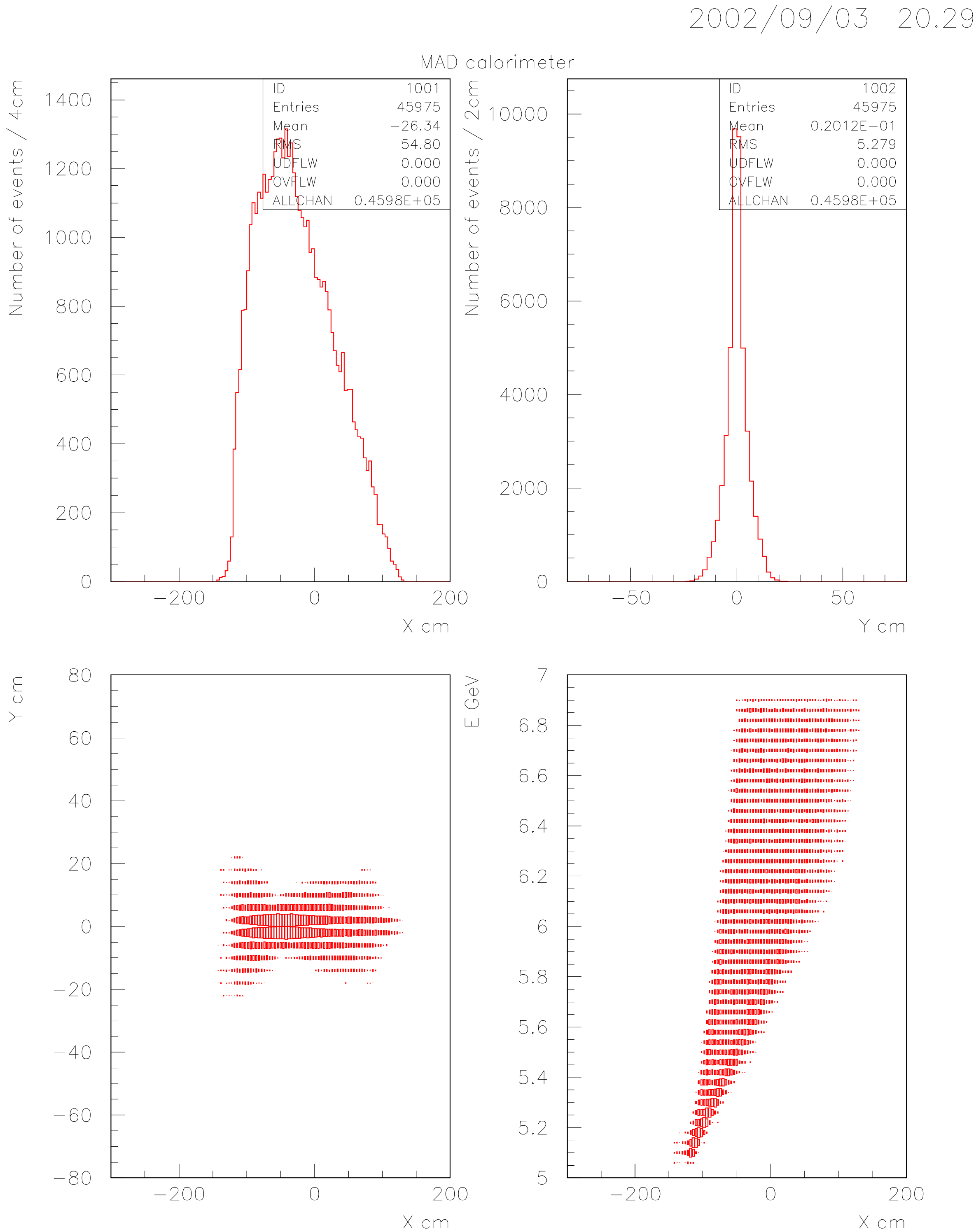

Figure 4.20: Simulation of the particles spectra in the plane of the MAD calorimeter at 35°, with "MAD-3" optics used. The top histograms represent the X and Y distributions, while the bottom ones represent the correlations of two projections and of the dispersive projection with the momentum.

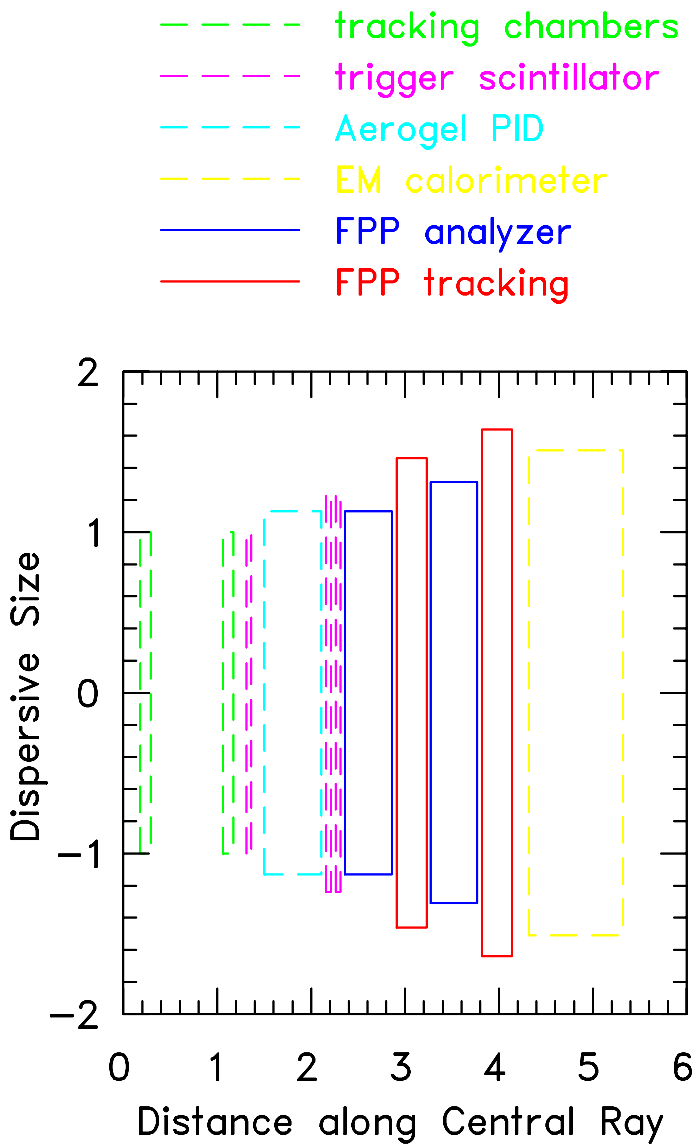

Figure 4.21: Layout of the MAD focal plane polarimeter.

4.6 Trigger Electronics

In this section the electronics and equipment needed to form a first level trigger out of the detector signals of the MAD spectrometer are described.

The proposed system will be built using commercially available components which follow VME, NIM and/or CAMAC standards. The described system will work as well with a DAQ system in a conventional environment or with a DAQ system based on Flash ADCs and Pipelined TDCs. To accomplish high singles rates in some of the detector subsystems, only modules capable of handling rates of 100 MHz or more are acceptable.

As described in section 2.4, the detector package of the HRS includes up to four scintillator planes, each made of 16 long scintillator paddles equipped with photo-multiplier tubes (PMTs) on each end. Although usually the main trigger will be formed by the signals of two planes only, all four planes will be built in the same fashion. Then, the trigger definition is very flexible and can be adjusted for the individual needs of each experiment.

The analog signal of each PMT will be split passively on the base of the tube. One signal will be fed into a pipleline Flash ADC, requiring no delay cable. The second signal will be fed into a leading edge discriminator (e.g. CAEN V895 or C894). The specific modules mentioned parenthetically are examples of presently available off-the-shelf units. The discriminators listed above provide two copies of the logical signal. One will be used for timing purposes and put into a TDC. A programmable delay (e.g. CAEN C211) is used to adjust small timing differences within the different channels. A 16 channel meantimer (e.g. CAEN C561 or V706) is used to combine the signals of the two PMTs of each scintillator paddle, and make this signal independent of the point of intersection. Finally the logical "or" of the 16 signals will be formed in a logic module (e.g. CAEN C561 or V706). This signal is the trigger for each scintillator plane. Using Gate and Delay Generators (GDG, e.g. CAEN 469) and Programmable Logic Units (PLU, e.g. CAEN C542 or V495), the signals from the four scintillator planes can form various triggers, the definition of the trigger can be changed easily and other detectors, for example the Čerenkov detector, can be incorporated if needed.

Some additional modules, Fan-in/Fan-Out modules, Level Converters and Coincidence Units, are needed to provide retiming signals, gates for the digitizing modules and scalers.

4.6.1 DAQ for MAD

In this section the data acquisition system (DAQ) for the MAD spectrometer. The system is built in VME using commercial components like scalers, ADCs, and TDCs where available, plus new custom built modules that are presently under development by collaborators. The system will have a high performance that will exceed FASTBUS standards. The existing HRS DAQ, or other existing detector DAQ systems, could remain the same and be connected to the new DAQ for experiments that use MAD in conjunction with other equipment; however, to take full advantage of the new technology the HRS DAQ should be upgraded as well.

Accommodating the detector design will require approximately 400 ADC channels, 2000 TDC channels, and 400 scaler channels. For the scintillators 60 psec resolution TDCs can be

Table 4.12: Equipment needed for the triggering system of the MAD detector package

Device	Typical Module	Form Factor	Units (inclu spare)
LE Discriminator	Caen C 894	Camac	15
Prog. Delay	Caen C 211	Camac	10
Meantimer	Caen C 561	Camac	6
Gate and Delay	Caen C 469	Camac	4
PLU	Caen C 542	Camac	2
ECL-Nim-ECL	Caen C 467/468	Camac	6
Fan-Out	Caen C 211	Camac	5
Coinc Unit	Caen V 512	VME	4
Camac Crates			3
VME Crates			2
VME CPUs			2
Camac Controllers			3
Cables			

used, while for drift chambers and other detectors poorer resolution (0.5 nsec) is adequate.

A new generation of pipeline digitizing front-end devices can be used for experiments that require speeds in excess of 5 kHz, and up to 20 kHz. For pipelined ADCs, there are two foreseeable alternatives. One is a custom built pipelined Flash ADC being prototyped by Indiana University, which might be manufactured at JLab. Another possibility is a similar ADC being built by the SISGmbH company in Germany. In the pipeline approach, detector data are continuously digitized and stored in a pipeline, which is a dual port memory. When a trigger condition is satisfied, the data are extracted from the pipeline and read out on the VME backplane. This scheme has two attractive features: 1) The pipeline approach introduces no deadtime; and 2) Delay cables can be avoided. However, a possible disadvantage with respect to ADCs is that if the sampling frequency is not sufficiently high, one may suffer loss of resolution. In tests at Indiana University [271], it was found that with 250 MHz and 8 bits resolution, the Flash ADC samples resulted in an energy resolution much better that the intrinsic resolution of lead glass.

A new high resolution pipelined VME TDC is being designed and prototyped by the Jefferson Lab DAQ group. This TDC has 60 psec resolution with 32 channels on a single slot 6U form factor, or 120 psec for 64 channels. The TDC can either run in a common start mode or a trigger matching mode. In the common start mode, a trigger starts and clears the hit counters, and a subsequent trigger initiates read-out of data since the start time. Of course, this mode will introduce deadtime. In the "trigger matching" or pipelined mode, a trigger is used to define a window in time to pull data out of a hit counter. The hit counter runs continuously even as the desired data is buffered in memory, and therefore produces very little deadtime.

4.6.2 DAQ upgrade for the HRS

(NOTE: This section probably will be dropped for the final CDR, but we include it here to explain the issues around an HRS upgrade to complement MAD.)

To take full advantage of the pipelined DAQ approach for the MAD spectrometer during coincidence experiments, the DAQ of the HRS should be upgraded as well. In a mixed environment, the pipelined TDCs and the Flash ADCs would be essentially used like conventional modules, eliminating their advantageous dead time behavior. In that case the rate capability of the HRS and the MAD spectrometer would be limited to the present situation of roughly 2 kHz with 20% computer dead time.

For an upgrade the existing Fastbus based ADCs and TDCs need to be replaced by their VME based successors. Because of the switch from Fastbus to VME, also crates, CPUs and CODA related modules need to be exchanged. The trigger logic and the scaler units can remain the same.

In the following table the needed equipment for an HRS upgrade is summarized. This system would be sufficient to run the VDCs, the existing trigger scintillators S0, S1 and S2, one gas and two aerogel Čerenkov detectors and the pion rejector in pipelined mode at the the same time. The shower/preshower detector is included, but not the FPP nor RICH detectors. For experiments that require FPP or RICH, their existing DAQ could be integrated into the new DAQ with performance limited by the existing DAQ.

Table 4.13: DAQ needs for an upgrade of the HRS spectrometer to an pipelined readout scheme.

Device	Resolution	Req Channels	Units (inclu spare)
ADC	12 bit, 250 MHz	280	11
TDC	100 psec	88	5
TDC	500 psec	1500	25
Crates	VME		4 $
CPU			4 $
CODA Items			

4.7 High Performance Calorimeter

High intensity 11 GeV beams in CEBAF's Hall A offer unique possibilities for studying both Real and Virtual Compton Scattering. These experiments require the construction of a large acceptance, high resolution, electromagnetic calorimeter, capable of withstanding high levels of background. Other experiments, particularly high P_T photo-production of neutral mesons will also benefit from such a detector.

We will use Deeply virtual Compton scattering (DVCS) to illustrate the requirements for EM calorimetry with 11 GeV beams[272]. DVCS (on the proton) refers to the $H(e, e'p\gamma)$ reaction in kinematics of $Q^2 = -q^2 = (k - k')^2$ large and $-t = -(P' - P)^2 << Q^2$. The initial and final electron momenta are k and k', respectively, and the initial and final proton momenta are P and P', respectively. DVCS kinematics in the fixed target frame produce an energetic forward photon in the direction of the $\vec{q}$-vector. It is important to discriminate the exclusive DVCS process from competing inelastic processes (such as $e + p \to e'p\pi^0 \to e'p\gamma\gamma$ or $e + p \to e'N^*\gamma \to e'N\pi\gamma$. This requires either high resolution $p(e, e'\gamma)X$ coincidences, or a triple coincidence experiment, with detection of the electron in a high resolution spectrometer, detection of the photon with high angular resolution, and detection of the proton with angular resolution approximately a factor of 10 less stringent than the photon angular resolution. The kinematical accessibility with different colorimeter resolutions for exclusive DVCS measurements via the $p(e, e'\gamma)X$ technique are illustrated in Fig. 4.22.

For DVCS, the photons must be detected at angles as small as 10°, with luminosity of at least 10^{37}. This requires a calorimeter material that is radiation hard. It is also important to have a very fast time response to make it possible to suppress pile-up and random coincidences.

PbF_2 is an attractive Čerenkov medium for electromagnetic calorimetry. Some basic properties of PbF_2 are listed in Table 4.7 and compared with the Pb-Glass in use for the calorimeter for the Real Compton Scattering experiment 99-114.

The primary distinction of PbF_2 is its very high Z^2 weighted density, resulting in much smaller individual element sizes. The transverse dimension of each element should be slightly larger than the Moliere radius, to optimize spatial resolution, and the longitudinal dimension should be 20 radiation lengths to fully contain the shower.

Nuclear absorption cross sections scale approximately as A, δ-ray production scales as Z, and the EM shower production scales as Z^2. Therefore the high density PbF_2 will have lower background from hadrons (including neutrons than Pb-Glass. Of course any Čerenkov medium will have much lower hadronic background than a scintillating shower counter.

A secondary benefit of the high density of PbF_2 is the low mass per detector element. Thus the total calorimeter will be much lighter than a comparable calorimeter constructed from Pb-Glass.

The small size of the PbF_2 will also result in very narrow intrinsic time spread in the collected light. R.D. Appuhn, et al.[273], quote a precision of 0.6 ns r.m.s. on leading edge timing of the light pulse from an array 21x21x175 mm3 PbF_2 blocks, coupled to a high

	Pb-Glass TF-1	PbF_2	$PbWO_4$
Index of Refraction	1.65	1.85	1.85
Radiation Length X_0 (cm)	2.5	0.93	0.89
Moliere Radius r_0 (cm)	3.3	2.2	2.2
Density ρ (g/cm^3)	3.86	7.77	8.28
Photoelectrons/GeV	1100	1600	5000
Critical Energy (MeV)	15	8.6	

Table 4.14: Comparison of Pb-Glass, PbF_2, and $PbWO_4$ calorimeter properties. The photo-electrons per GeV for TF-1 Pb-Glass are obtained with a photo-cathode covering 36obtained with a UV sensitive mesh PMT covering 45% of the cross section. The critical energy is the energy at which electron energy losses by ionization and radiation are equal. The element size chosen for Pb-glass is 40x40x400 mm^3, for PbF_2, 30x30x150 mm^3.

speed mesh PMT (Hamamatsu R4722). The MAMI A4-collaboration has obtained a total pulse width of 20 ns, dominated by PMT time jitter and dispersion in 23 m of cable.[274] The leading edge time resolution and the total pulse width are both critical parameters for suppression of accidental coincidences and pile-up rejection. Small blocks makes it practical to couple the crystals to very fast photo-tubes.

For radiation doses from 200 Gy (20 kRad) to 1 kGy (100 kRad) the radiation damage to PbF_2 is a factor of 10 less than SF5 Pb-Glass.[274] Radiation damage reduces the transmittance of the crystals, with the greatest effects at short wavelengths. For doses of 200 Gy and 200 kGy the transmittance was reduced by 5has been easily annealed with blue light as well as natural light.

R.D. Appuhn et al.[273] report a electromagnetic shower energy resolution for small a test array of $5.6\%/\sqrt{GeV/E}$ for 1 to 6 GeV electrons. More recently, P. Achenbach *etal.*,[274] report a resolution of 3% at 1 GeV. It may be surprising that PbF_2 can yield superior energy resolution to Pb-Glass, since both are Čerenkov media. However, there are a number of differences between PbF_2 and Pb-Glass that influence energy resolution

- The higher index of refraction for PbF_2 lowers the electron energy threshold for Čerenkov radiation and therefore reduces the fluctuations in light output.
- The enhanced UV transmission of PbF_2 increases the light output. Coupled to UV sensitive photomultiplier tubes the light yield for PbF_2 is higher.
- The lower critical energy of PbF_2 reduces the fluctuations in the number of e^+e^- pairs produced.
- Fluctuations in the longitudinal development of the shower can contribute to the energy resolution, due to differential attenuation of the light. The smaller PbF_2 crystals will

generally have less light attenuation than Pb- Glass, contributing to the improved energy resolution.

R.D. Appuhn[273] achieved a transverse position resolution of 1 mm$\sqrt{GeV/E}$ with a test array of 20 x 20 x 175 mm^3 PbF_2 crystals. The spatial resolution may be degraded slightly with larger crystals, but it is clear that the very high spatial resolution will allow a PbF_2 array to be placed very near the target, without limiting the photon angular resolution.

High density scintillators offer an alternative to PbF_2. These scintillators can achieve much higher energy resolution, as illustrated in Fig. 4.22. However, as scintillators, they are much more sensitive to neutrons and other hadronic background. Also, the light output is generally much slower for scintillators than for a Čerenkov medium-resulting in much greater pile-up problems. $PbWO_4$ crystals have recently been produced with light decay constants of 5 ns [7]. The Radiation length and Moliere radius of $PbWO_4$ are 0.89 cm and 2.2 cm, respectively. Thus $PbWO_4$ is a possible alternate medium to PbF_2. Additional tests are required to evaluate the feasibility of a scintillator calorimeter. For comparison, properties of $PbWO_4$ are shown in Table 4.7

- **Conceptual Design**

The optimal DVCS signal is obtained in a cone of approximately 150 mr (half angle) around the $\vec{q}$-vector. The direction of q is smeared out by the electron acceptance: typically this smearing is approximately equal to the electron solid angle. In addition, it is important to detect the double photon coincidence from deeply virtual π^0 production: $p(e, e'\pi^0)$ when the lab energies of the two π^0-decay photons are approximately equal. In deep virtual kinematics with electron beams up to 11 GeV, the electron energy transfer $k - k'$ will be from 3 to 7 GeV. Almost all of this energy will be converted into the fast forward particle (photon, π^0...). For a 3 GeV π^0 the symmetric decay corresponds to a laboratory opening angle of roughly 50 mr relative to the π^0 direction, with the cone getting narrower as the π^0 energy increases.

Including both the DVCS photon angular range, and the π^0 decay solid angle, a calorimeter of solid angle 0.1 sr is desired.

The optimal transverse size for PbF_2 blocks is 20-30 mm, depending upon achieved spatial resolution and availability of suitable PMTs.

We assume an array of 26 x 26 mm^2 blocks and a transverse spatial resolution of 1.5 mm.

The photon angular resolution is determined as follows:

$$\sigma(\theta_\gamma = \frac{\sigma(x_b)}{L_\gamma)} + \frac{\sigma(y_{sp})}{L_\gamma} . \frac{\sin\theta_\gamma}{\sin\theta_{sp}} \tag{4.2}$$

L_γ is the distance of the calorimeter from the target, $\sigma(x_b)$ is the resolution on the instantaneous transverse position of the beam (100 μm r.m.s.), $\sigma(y_{sp})$ is the vertex reconstruction resolution from a magnetic spectrometer viewing the event in coincidence (1 mm rms for HRS, 4mm for MAD) at angle θ_{sp}. In DVCS kinematics, typical angles for the calorimeter are 10-20 deg with an electron spectrometer at 10-30 deg. In High P_T real or virtual photo-production of photons, π^0-mesons, or η-mesons, at 90° in the CM, the proton spectrometer and photon calorimeter are approximately symmetrically placed around the beam at angles decreasing from 40° to 25° as the incident photon energy increases from 3 to 9 GeV.

To achieve large solid angle coverage and high angular resolution, we propose a 1296 element array with 26 mm cell size. In DVCS kinematics, with the calorimeter 3 m from the target, the design acceptance of 0.1 sr can be achieved with a photon angular resolution of 0.5 mr.

Individual crystal will be 26x26x200 mm^3 rectangular blocks coupled to UV transmitting 25 mm fast PMT's. While several solutions for PMT's are possible we take the EMI 9111WB 8-stage photomultiplier as a baseline solution. With a photo-cathode of 22 mm diameter, the PMT will cover 72% of the surface of the crystal. In addition, the PMT offers high quantum efficiency of about 28% and spectral response down to 180 nm. Simulations suggests light yields with the above solution to be about 2500 pe/GeV. The calorimeter will be arranged in a square matrix of 36x36 elements. However, the array will be flexible in design so that it can be easily reconfigured for a different geometry. A blue laser based light source coupled to each crystal will provide calibration, timing, and gain monitoring signal. Using standard integrating ADC's for the readout and programmable high voltage supplies currently used in Hall A.

In summary, We propose that the physics program of 11 GeV electron beams in Hall A will require a flexible, high performance calorimeter. We believe these requirements can be met with a 1296 element array of 26 x 26 x 200 mm^3 PbF_2 crystals, coupled to 25 mm UV optimized fast PMT's.

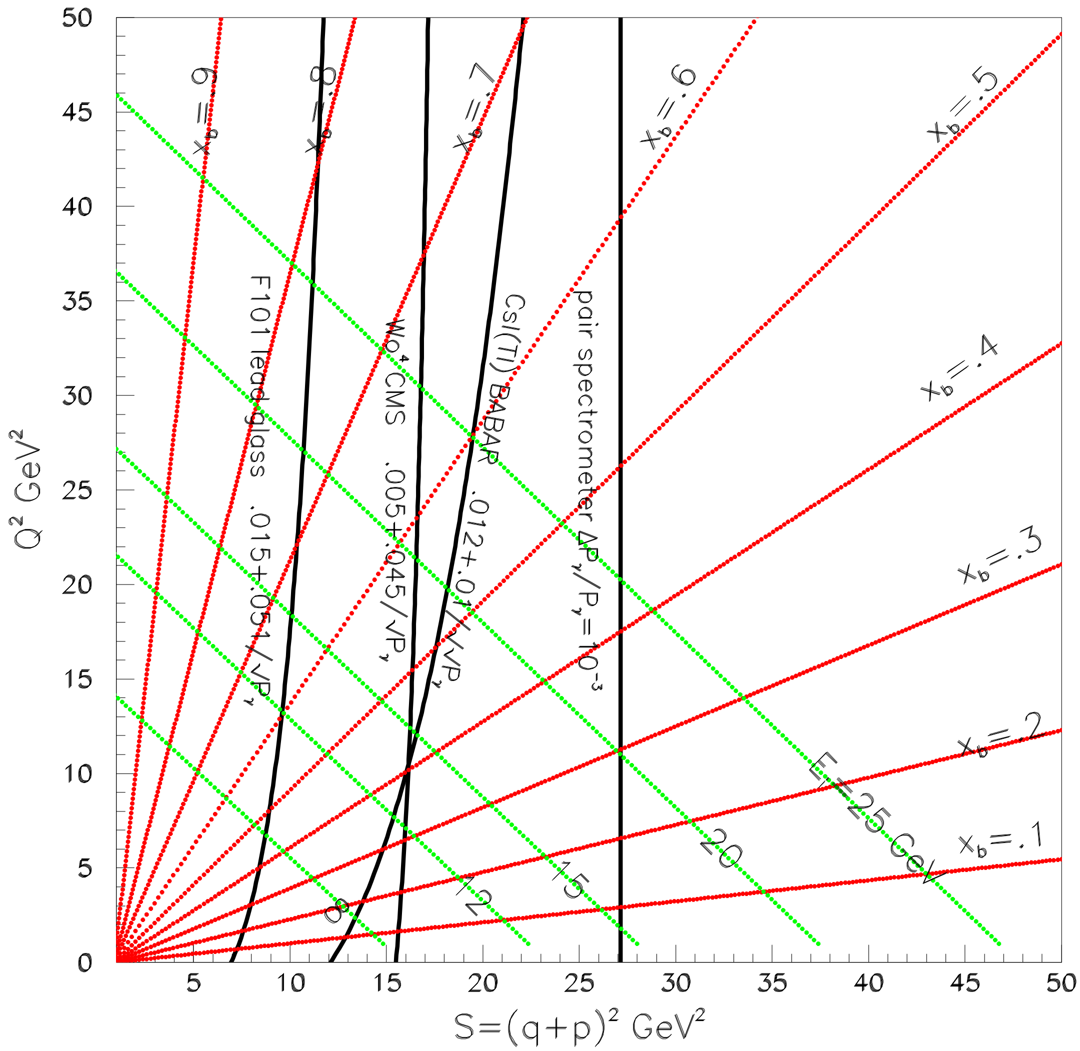

Figure 4.22: Photon resolution on a plot Q^2 vs. s. The curves labeled by different photon energy resolution values correspond to the kinematic limit at which the $p(e, e'\gamma)$ and $p(e, e'\gamma)N\pi$-threshold are separated by 1-σ in the forward (DVCS) limit. For each resolution curve, the entire kinematic region to the left is accessible with the exclusive channel resolved without a triple coincidence. The curve labeled WO4 corresponds to $PbWO_4$, a high density scintillator.

4.8 The Hall A Beam Line

For the 12 GeV upgrade, the basic plan is to keep the present layout of the accelerator and utilize the existing tunnel and beamline. As regards Hall A, the basic layout of the beamline and beamline instrumentation will remain the same. A schematic layout of the present beamline in Hall A with its instrumentation is shown in Figure 1.

The quality of the beam will be somewhat compromised by going to the higher energies, and this reduction in beam quality has been endorsed by the User Group Board of Directors. Table 1 gives a comparison of the presently achievable beam parameters at 6 GeV and the expected beam parameters in going to the higher energy. The highest energy in Hall A will be 11 GeV (2.2 GeV per pass) with the upgrade.

Table 4.15: Key parameters of Beam Quality - present and with upgrade

Parameter	Present @6 GeV	With Upgrade @12 GeV
Horizontal emittance ϵ_x	$2.9 * 10^{-7}$ m.rad	$9 * 10^{-6}$ m.rad
Vertical emittance ϵ_y	$2.9 * 10^{-7}$ m.rad	$1.9 * 10^{-6}$ m.rad
Energy Spread $\delta p/p$	$1 * 10^{-4}$	$2 * 10^{-4}$

No changes are envisaged regarding the primary diagnostic and beamline instrumentation [275, 276]. This includes the present SEE Beam Position Monitors, the Hall A target OTR and the Scanners for beam profile measurements, the two rf cavity monitors (BCMs) and the Unser Monitor for beam current monitoring, and the present fast feedback system to maintain the stability of the beam in both position and energy. The fast rastering system may have to be upgraded to operate at the higher energies with the same amplitudes as presently available up to 6 GeV. The only possible addition to the instrumentation may be the installation of a Synchrotron Light Interferometer for beam profile determination and the beam energy width monitoring.

The beam optics and layout will also basically remain the same in going to the higher energies. Most of the modifications involved ensure that the various beam focusing and deflecting elements can reach the requisite higher fields. All the beamline magnets will remain resistive, not superconducting. The present plans for the dipoles (especially in the Hall A Arc section) will be modified from C-type magnets to H-type magnets by adding a return path to the yoke in order to reach the higher fields without saturation. The present beamline quadrupoles have enough margin that they are able to reach 170% of their design current (enough to reach 11 GeV) with acceptable field quality. Higher current power supplies for both will be needed for the upgrade.

4.8.1 Beam Polarimeters

Møller Polarimeter

The Hall A beam line is equipped with a Møller polarimeter, whose purpose is to measure the longitudinal polarization of the electron beam delivered to the hall. The polarimeter exploits the process of Møller scattering $\vec{e}^- + \vec{e}^- \rightarrow e^- + e^-$. Its cross-section depends on the beam and target polarizations $\mathcal{P}_{beam}$ and $\mathcal{P}_{target}$ as: $\sigma \propto (1 + (A(\theta_{CM}) \cdot \mathcal{P}_{targ} \cdot \mathcal{P}_{beam}))$. The analyzing power A depends on the scattering angle in the CM frame θ_{CM} and has its maximum of 7/9 at $\theta_{CM} = 90°$. A ferromagnetic foil, magnetized in an external magnetic field of about 0.03T is used for the target. Both electrons, scattered close to the the horizontal plane, are detected with the help of a spectrometer consisting of three quadrupole magnets, focusing the electrons onto two vertical slits in a dipole magnet, which provides a horizontal field. The dipole magnet deflects the electrons downward, away from the beam line, toward the detector. The beam also passes this dipole magnet, through an area shielded against the magnetic field. The polarimeter can measure the beam polarization in about 30min with a relative error of about 0.2% statistical and 3% systematic.

Two factors limit the useful beam energy range of the polarimeter: a) the spectrometer acceptance, defined by the positions of the magnets and the available field strength, and also the positions of the collimators; b) the beam deflection in the Møller dipole caused by the residual field in the shielding insertion. At the moment, the first factor gives the lower limit for beam energy of 0.8 GeV, while the second factor gives the upper limit at about 6. GeV. In order to operate at 11 GeV an upgrade of the polarimeter is proposed, keeping the target and the dipole magnet at the same positions along the beam line: [1]

- Reduce the bend angle of the dipole from 11 to 7.3°, thereby reducing the maximum field needed in the dipole.
- Lift the detector by 10 cm.
- Add the 4-th quadrupole magnet at 70 cm from the Møller target. This magnet exists and is stored at JLab.
- Move the 1-st quadrupole magnet 40 cm downstream.
- Add a shielding pipe to the magnetic shielding insertion in the dipole magnet.

The four quadrupole design provides a sufficiently large spectrometer's acceptance on the scattering angle $\Delta\theta_{CM} \approx 20°$, presented on a Fig. 4.23.

The residual field in the beam area inside the dipole is reduced both by reducing the requirements for the magnetic field strength and by using the additional magnetic shielding. The latter was optimized using a TOSCA simulation. The present diameter of the bore in the shielding insertion is 4.0 cm. The diameter of the electron beam line before and after the Møller polarimeter is 2.54 cm. It is possible to increase the attenuation of the shielding

[1] The detailed proposal can be found in URL http://www.jlab.org/m̃oller/docs/upgrade_11gev.ps.gz

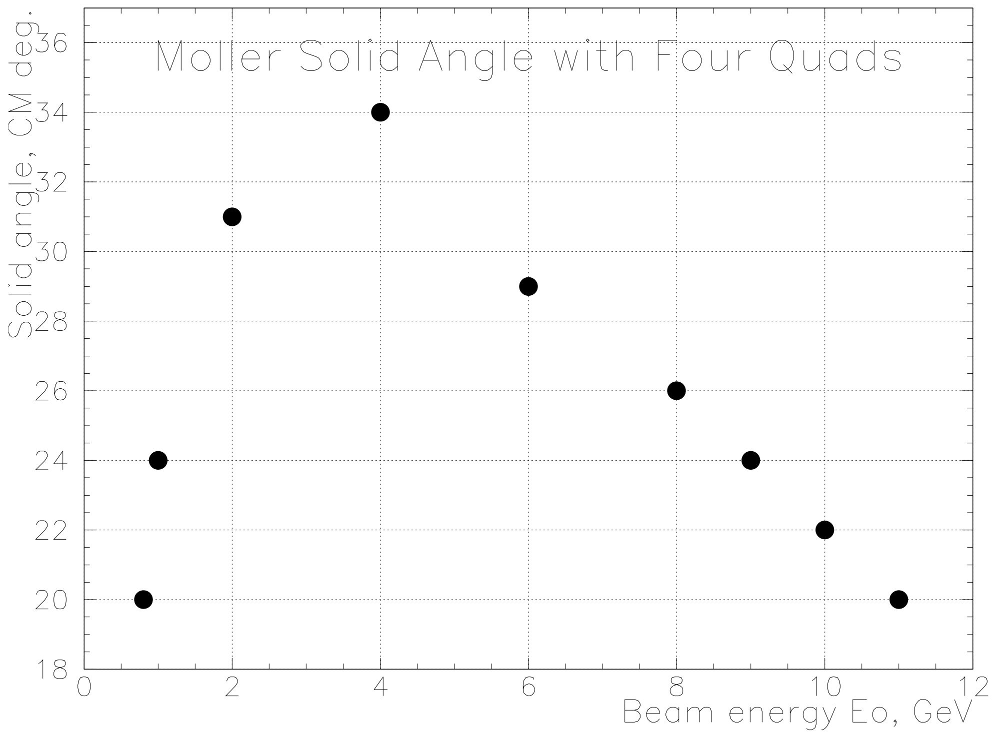

Figure 4.23: Møller polarimeter acceptance of θ_{CM}, with four quadrupole magnets

insertion by placing a coaxial magnetically isolated pipe with the inner/outer diameters of 2.54/3.4 cm, made of magnetic steel AISI-1006, inside the bore. The shielding pipe is centered in the shielding insertion bore with an additional external isolating pipe of a non-magnetic material. The shielding pipe length should be 10 cm longer than the shielding insertion length in order to reduce the influence of the fringe field outside of the shielding insertion. The new design attenuates to an acceptable level the dipole magnetic field up to 14.8 kGs, corresponding to a beam energy of 11 GeV and a dipole bending angle of 7.3°. This field can be provided with the power supply currently used for the dipole. The expected electron beam shift on the Hall A target and in the beam dump are shown in Fig. 4.24.

Compton Polarimeter

The Hall A Compton polarimeter, designed and built by CEA, Saclay, determines the absolute polarization of the electron beam by measuring Compton backscattering asymmetry of polarized light from polarized electrons. A detailed description of the existing Compton polarimeter can be found in Ref [277]. In brief, the Compton polarimeter consists of a magnetic chicane made of 4 dipole magnets over about 15 m. The chicane displaces the beam downward by 300 mm where it interacts with polarized light confined in a High-Finesse

Fabry-Perot cavity. The polarized light is injected from a 1064 nm infrared laser. The backscattered photons and the recoil electrons are detected in a $PbWO_4$ electromagnetic calorimeter and silicon strip detector, respectively.

The Compton polarimeter chicane has been designed to operate up to a maximum beam energy of 8 GeV. This limit is due to the 1 m long dipoles in the chicane which have a maximum pole-tip field of 1.5 T.

There are two possible solutions to upgrading the maximum beam energy of the chicane to 11 GeV:

- Increase the $\int$B.dl of the chicane dipole to 2.0626 Tm
- Decrease the chicane displacement to 218 mm

The first option has the advantage of keeping the geometry of the Compton polarimeter intact. The available real estate in the Hall A tunnel precludes increasing the length of each dipole from 1 m to 1.37 m. Hence the field of each dipole must be increased to 2.062 T This might require a superconducting magnet solution which may be prohibitively expensive.

The second alternative is to keep the present dipoles intact, and to raise the bottom two dipoles along with the optics cavity and the photon calorimeter by 82 mm. This option, although labor intensive, might be more efficient in terms of capital cost.

4.8.2 Beam Energy Measurement Devices

There are at present two independent devices to measure the absolute energy of the beam in Hall A, the arc and ep methods. The present ep design enables measurement of the beam energy to about 6 GeV. Major redesign of the device is necessary to implement it for energies above 6 GeV. To implement the Arc method for higher energies, the assumption is made that the arc dipoles will be modified from C-type magnets to H-type magnets by adding a return path to the yoke in order to reach high fields without saturation. This will necessitate remeasurement of the 8 modified H-style arc dipoles as well as the 9th dipole. The mapper for the 9th Dipole will also have to be modified.

The beam energy width monitoring can still be done with the OTR and harp at the middle of the arc section (1C12 location) of the Hall A beamline. The proposed new Synchrotron Light Interferometer could also be used for monitoring the beam energy width.

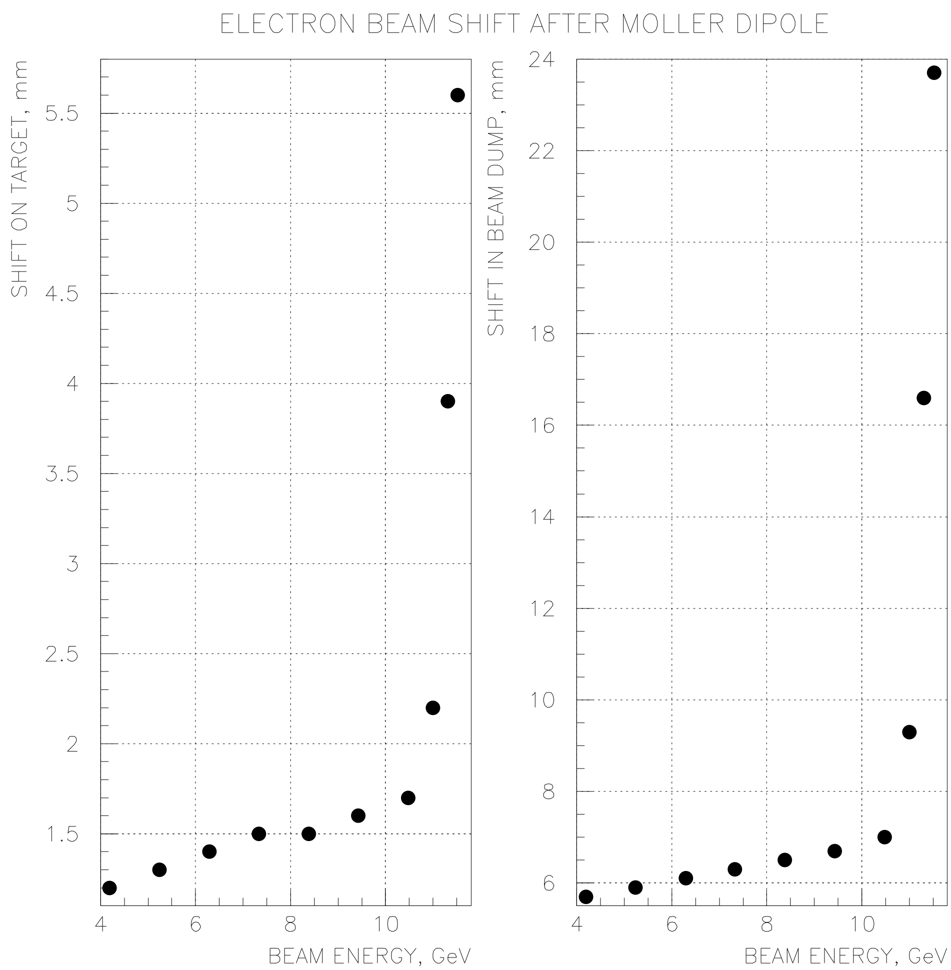

Figure 4.24: The dipole with the 10 cm extended shielding pipe. The electron beam shift on the Hall A target (left picture) and in the Hall A beam dump (right picture).

Bibliography

[1] A.W. Schreiber, A.I. Signal and A.W. Thomas, Phys. Rev. D **44** (1991) 2653.

[2] B. T. Chertok, Phys. Rev. Lett. **40** (1976) 1429.

[3] S. Capstick *et al.*, *Key Issues in Hadronic Physics*, Report presented at the APS Division of Nuclear Physics Town Meeting on Electromagnetic and Hadronic Physics, Jefferson Lab (2000), arXiv:hep-ph/0012238.

[4] L.W. Whitlow *et al.*, Phys. Lett. **B282** (1992) 475.

[5] W. Melnitchouk and A.W. Thomas, Phys. Lett. **B377** (1996) 11.

[6] S. Kuhlmann *et al.*, Phys. Lett. **B476** (2000) 291.

[7] E.D. Bloom and F.J. Gilman, Phys. Rev. Lett. **16** (1971) 1140.

[8] I. Niculescu *et al.*, Phys. Rev. Lett. **85** (2000) 1182.

[9] J. Ashman *et al.*, Phys. Lett. **B206** (1988) 364.

[10] B. Lampe and E. Reya, Phys. Rep. **332** (2000) 1.

[11] F.E. Close, Phys. Lett. **43** (1973) 422.

[12] A. Bodek and J.L. Ritchie, Phys. Rev. D **23** (1981) 1070.

[13] L.L. Frankfurt and M.I. Strikman, Phys. Rep. **160** (1988) 235.

[14] R.P. Feynman, Photon Hadron Interactions (1972) Reading, Massachusetts.

[15] R.D. Carlitz, Phys. Lett. **58** (1975) 345.

[16] N. Isgur, Phys. Rev. D **59** (1999) 034013.

[17] N.I. Kochelev, Proceedings of Workshop on Physics with Polarized Protons at HERA (1997) Hamburg, arXiv:hep-ph/9711274.

[18] G.R. Farrar and D.R. Jackson, Phys. Rev. Lett. **35** (1975) 1416.

[19] H. Georgi A. de Rújula and H.D. Politzer, Ann. Phys. **103** (1975) 315.

[20] W. Melnitchouk, Phys. Rev. Lett. **86** (2001) 35.

[21] T. Uchiyama and K. Saito, Phys. Rev. C **38** (1988) 2245.

[22] C. Ciofi degli Atti and S. Liuti, Phys. Rev. C **41** (1990) 1100.

[23] I.R. Afnan, F. Bissey, J. Gomez, A.T. Katramatou, W. Melnitchouk, G.G. Petratos and A.W. Thomas, Phys. Lett. **B493** (2000) 36.

[24] G. Salme E. Pace and S. Scopetta, Phys. Rev. C **64** (2001) 055203.

[25] M.M. Sargsian, S. Simula and M.I. Strikman, arXiv:nucl-th/0105052.

[26] F. Bissey *et al.*, private communication.

[27] J. Gomez *et al.*, Phys. Rev. D **49** (1994) 4348.

[28] S. Dasu *et al.*, Phys. Rev. D **49** (1994) 5641.

[29] L. Tao *et al.*, Z. Phys. **C70** (1996) 387.

[30] A. Amroun *et al.*, Nucl. Phys. **A579** (1994) 596.

[31] D. Beck *et al.*, Nucl. Instr. and Meth. **A277** (1989) 323.

[32] See for instance, B. Adeva *et al.* (SMC), Phys. Lett. **B412**, (1997) 414; K. Ackerstaff *et al.* (HERMES Collaboration), Phys. Lett. **B404**, (1997) 383; P.L. Anthony *et al.* (E142 Collaboration), Phys. Rev. D **54**, (1996) 6620; K. Abe *et al.* (E143 Collaboration), Phys. Lett. **B364**, (1995) 61; K. Abe *et al.* (E154 Collaboration), Phys. Lett. **B405**, (1997) 180; P.L. Anthony *et al.* (E155 Collaboration), Phys. Lett. **B463**, (1999) 339.

[33] P.L. Anthony *et al.*, Phys. Lett. **B493** (2000) 19.

[34] K. Abe *et al.*, Phys. Rev. D **58** (1998) 112003.

[35] J. P. Chen, Z.-E. Meziani and P. Souder, spokespersons, JLab Experiment E99-117.

[36] J.L. Friar *et al.*, Phys. Rev. C **42** (1990) 2310.

[37] R.M. Woloshyn, Nucl. Phys. **A496** (1989) 749.

[38] C. Ciofi degli Atti, S. Scopetta, E. Pace and G. Salme, Phys. Rev. C **48** (1993) 968.

[39] R.W. Schulze and P.U. Sauer, Phys. Rev. C **48** (1993) 38.

[40] F. Bissey, A.W. Thomas and I.R. Afnan, Phys. Rev. C **64** (2001) 024004.

[41] F. Bissey, V. Guzey, M. Strikman and A. Thomas, Phys. Rev. C **65** (2002) 064317.

[42] C.E. Carlson and N.C. Mukhopadhyay, Phys. Rev. D **41** (1998) R2343.

[43] X. Ji and P. Unrau, Phys. Rev. D **52** (1995) 72.

[44] X. Ji and W. Melnitchouk, Phys. Rev. D **56** (1997) 1.

[45] F.E. Close and N. Isgur, Phys. Lett. **B509** (2001) 81.

[46] N. Isgur, S. Jeschonnek, W. Melnitchouk and J.W. Van Orden, Phys.Rev. D **64** (2001) 054005.

[47] F.E. Close and Q. Zhao, arXiv:hep-ph/0202181.

[48] S. Liuti *et al.*, arXiv:hep-ph/0111063.

[49] Jefferson Lab experiment 94-010, G.D. Cates, J.P. Chen and Z.E. Meziani spokespersons; Jefferson Lab experiment 01-012, J.-P. Chen, S. Choi and N. Liyanage spokespersons; Jefferson Lab experiment 91-023, V. Burkert, D. Crabb and R. Minehart spokespersons; Jefferson Lab experiment 93-009, G. Dodge, S.E. Kuhn and M. Taiuti spokespersons; Jefferson Lab experiment 96-002, O.A. Rondon spokesperson.

[50] S. Wandzura and F. Wilczek, Phys. Lett. **B72** (1977) 195.

[51] E. Stein, P. Gornicki, L. Mankiewicz and A. Schafer, Phys. Lett. **B353** (1995) 107.

[52] K. Abe *et al.* (E143 Collaboration), Phys. Rev. Lett. **76** (1996) 587.

[53] P.L. Anthony *et al.* (E155 Collaboration), arXiv:hep-ex/0204028.

[54] B. Adeva *et al.* (SMC), Phys. Lett. **B302**, (1993) 533; D. Adams *et al.* (SMC), Phys. Lett. **B329**, (1994) 399; B. Adeva *et al.* (SMC), Phys. Lett. **B357**, (1995) 248.

[55] X. Song, Phys. Rev. **D54** (1996) 1955.

[56] M. Stratmann, Z. Phys **C60** (1993) 763.

[57] X. Ji and P. Unrau, Phys. Lett. **B333** (1994) 228.

[58] E. Stein *et al.*, Phys. Lett. **B343** (1995) 369.

[59] I. Balitsky *et al.*, Phys. Lett. **B242**, (1990) 245; **B318**, (1993) 648 (Erratum).

[60] B. Ehrnsperger and A. Schager, Phys. Rev. D **52** (1995) 2709.

[61] M. Göckeler *et al.*, Phys. Rev. D **63** (2001) 074506.

[62] H. Weigel *et al.*, Phys. Rev. D **55** (1997) 6910.

[63] M. Göckeler *et al.*, Phys. Rev. D **63** (2001) 074506.

[64] *Nuclear Theory with Lattice QCD*, N. Isgur and J.W. Negele, principal investigators, (March, 2000), http://www.jlab.org/~dgr/lhpc/march00.pdf.

[65] J.D. Bjorken, Phys. Rev. **148** (1966) 1467.

[66] S.B. Gerasimov, Sov. J. Nucl. Phys. **2** (1966) 430.

[67] S.D. Bass and A. De Roeck, Nucl. Phys. Proc. Suppl. **105** (2001) 1.

[68] K. Helbing *et al.*, Nucl. Phys. Proc. Suppl. **105** (2002) 113.

[69] S.D. Bass and P.V. Landshoff, Phys. Lett. **B336** (1994) 537.

[70] F.E. Close and R.G. Roberts, Phys. Lett. **B336** (1994) 257.

[71] R. P. Feynman, *Photon-Hadron Interactions* (Benjamin, Reading, MA, 1972); F. E. Close, *Introduction to Quarks and Partons* (Academic, New York, 1978).

[72] L. L. Frankfurt, M. I. Strikman, L. Mankiewicz, A. Schafer, E. Rondio, A. Sandacz and V. Papavassiliou, Phys. Lett. **B230**, (1989) 141; F. E. Close and R. G. Milner, Phys. Rev. D **44**, (1991) 3691.

[73] J. Levelt, P.J. Mulders and A.W. Schreiber, Phys. Lett. **B263** (1991) 468.

[74] E. Christova and E. Leader, Phys. Lett. **B468** (1999) 299.

[75] R. L. Jaffe and X. Ji, Nucl. Phys. **B375** (1992) 527.

[76] P. Amaudraz *et al.*, Phys. Rev. Lett. **66** (1991) 2712.

[77] A. Baldit *et al.*, Phys. Lett. B **332** (1994) 244.

[78] K. Ackerstaff *et al.*, Phys. Rev. Lett. **81** (1998) 5519.

[79] E.A. Hawker *et al.*, Phys. Rev. Lett. **80** (2001) 3715.

[80] J. Speth and A.W. Thomas, Adv. Nucl. Phys. **24** (2001) 83.

[81] A.W. Thomas, Phys. Lett. B **126** (1983) 97.

[82] W. Melnitchouk A.W. Thomas and F.M. Steffens, Phys. Rev. Lett. **85** (2000) 2892.

[83] J.-C. Peng *et al.*, Phys. Rev. D **58** (1998) 092004.

[84] J. Speth W. Melnitchouk and A.W. Thomas, Phys. Rev. D **59** (1999) 014033.

[85] E. Henley M. Alberg and G.A. Miller, Phys. Lett. **B471** (2000) 396.

[86] R.D. Field and R.P. Feynman, Phys. Rev. D **15** (1977) 2590.

[87] R.J. Fries and A. Schafer, Phys. Lett. **B443** (1998) 40.

[88] K.G. Boreskov and A.B. Kaidalov, Eur. Phys. J. **C10** (1999) 143.

[89] F.-G. Cao and A.I. Signal, Eur. Phys. J. **C21** (2001) 105.

[90] D. Diakonov, V.Yu. Petrov, P.V. Pobylitsa, M.V. Polyakov and C. Weiss, Phys. Rev. D **56** (1997) 4069.

[91] M. Gluck and E. Reya, Mod. Phys. Lett. A **15** (2000) 883.

[92] F.M. Steffens, arXiv:hep-ph/0204094.

[93] J. Wendland (HERMES Collaboration), `http://www-hermes.desy.de/notes/pub/trans-public-index.html`.

[94] J.F. Donoghue and E. Golowich, Phys. Rev. D **15** (1977) 3421.

[95] D.A. Ross and C.T. Sachrajda, Nucl. Phys. **B149** (1979) 497.

[96] F.M. Steffens and A.W. Thomas, Phys. Rev. C **55** (1997) 900.

[97] J.S. Conway *et al.*, Phys. Rev. D **39** (1989) 39.

[98] J. Badier *et al.*, Z. Phys. **C18** (1985) 281.

[99] C. Adloff *et al.*, Eur. Phys. J. **C6**, 587 (1999); C.-P. Fagerstroem, Ph.D. Thesis, Univ. of Toronto (1999); G. Levman, Proc. of Workshop on Lepton Scattering, Hadrons and QCD, Univ. of Adelaide (2001).

[100] E.L. Berger and S.J. Brodsky, Phys. Rev. Lett. **42** (1979) 940.

[101] A.I. Signal and A.W. Thomas, Phys. Lett. **B191** (1987) 205.

[102] S.J. Brodsky and B.-Q. Ma, Phys. Lett. **B381** (1996) 317.

[103] W. Melnitchouk and M. Malheiro, Phys. Rev. C **55** (1999) 431.

[104] S. Aoki, M. Doui, T. Hatsuda and Y. Kuramashi, Phys. Rev. D **56**, (1997) 433; S. Sasaki, T. Blum, S. Ohta and K. Orginos, arXiv:hep-lat/0110053; D. Dolgov *et al.*, arXiv:hep-lat/0201021.

[105] J.C. Collins, Nucl. Phys. **B396** (1994) 161.

[106] R. Ent, H. Mkrtchyan and G. Niculescu, JLab Proposal E00-004 (2000).

[107] H. Avagian, Talk at JLab seminar, March 2002.

[108] C. E. Carlson A. Afanasev and C. Wahlquist, Phys. Rev. D **62** (2000) 074011.

[109] Proposal for Drell-Yan Measurements of the Nucleon and Nuclear Structure with the FNAL Main Injector, spokespersons: D.F. Geesaman and P.E. Reimer.

[110] G. Ingleman, A. Edin and J. Rathsman, DESY Report 96-057 (1996).

[111] H.L. Lai *et. al.*, Phys. Rev. D **55** (1997) 1280.

[112] T. Sjöstrand, Comp. Phys. Comm. **83** (1994) 74.

[113] K. Ackerstaff *et al.*, Phys. Lett. **B464** (1999) 123.

[114] K. Suzuki and W. Weise, Nucl. Phys. **A634** (1998) 141.

[115] K. Suzuki T. Shigetani and H. Toki, Phys. Lett. **B308** (1993) 383.

[116] R.M. Davidson and E. Ruiz Arriola, Phys. Lett. **B348** (1995) 163.

[117] C.D. Roberts M.B. Hecht and S.M. Schmidt, Phys. Rev. C **63** (2001) 025213.

[118] C. Best *et al.*, Phys. Rev. D **56** (1997) 2743.

[119] S.D. Drell and T.-M. Yan, Phys. Rev. Lett. **24** (1970) 181.

[120] W. Melnitchouk, private communication (2002) .

[121] J.D. Sullivan, Phys.Rev. D **5** (1972) 1732.

[122] J. Soffer G. Bunce, N. Saito and W. Vogelsang, Ann. Rev. Nucl. Part. Sci. **50** (2000) 525.

[123] O.G. Smirnova A.V. Efremov and L.G. Tkachev, Nucl. Phys. Proc. Suppl. **74** (1999) 49.

[124] A. Airapetian HERMES Collaboration *et al.*, Phys. Rev. Lett. **84** (2000) 4047.

[125] A. Airapetian HERMES Collaboration *et al.*, Phys. Rev. **D64** (2001) 097101.

[126] K. A. Oganessian, H. R. Avakian, N. Bianchi and A. M. Kotzinian, arXiv:hep-ph/9808368.

[127] W.-D. Nowak E. De Sanctis and K. A. Oganessian, Phys. Lett. **B483** (2000) 69.

[128] A. Bravar for the SMC Collaboration, Nucl. Phys. Proc. Suppl. **79** (1999) 520.

[129] W.-D. Nowak V.A. Korotkov and K.A. Oganessian, Eur. Phys. J. **C18** (2001) 639.

[130] J.J. Aubert *et al.*, Phys. Lett. **B160** (1985) 417.

[131] O. Gayou *et al.*, Phys. Rev. Lett. **88** (2002) 092301.

[132] M. Jones *et al.*, Phys. Rev. Lett. **84** (2000) 1398.

[133] J. C. Collins and A. Freund, Phys. Rev. D **59** (1999) 074009.

[134] A. V. Radyushkin, Phys. Rev. D **59** (1999) 014030.

[135] J. P. Ralston and B. Pire, arXiv:hep-ph/0110075.

[136] M. Diehl, arXiv:hep-ph/0205208.

[137] X. D. Ji, Phys. Rev. Lett. **78** (1997) 610.

[138] A. V. Afanasev, arXiv:hep-ph/9808291.

[139] L. Andivahis *et al.*, Phys. Rev. D **50** (1994) 5491.

[140] A. F. Sill *et al.*, Phys. Rev. D **48** (1993) 29.

[141] W.K. Brooks, spokesperson, JLab proposal E94-017.

[142] A. Lung *et al.*, Phys. Rev. Lett. **70** (1993) 718.

[143] T. Eden *et al.*, Phys. Rev. C **50** (1999) R1749.

[144] R. Schiavilla and I. Sick, Phys. Rev. C **64** (2001) 041002.

[145] G. Cates, K. McCormick, B. Reitz, B. Wojtsekhowski, spokespersons, JLab proposal E02-013.

[146] A. V. Radyushkin, Phys. Rev. D **58** (1998) 114008.

[147] H. W. Huang, P. Kroll and T. Morii, Eur. Phys. J. **23** (2002) 301.

[148] M. A. Shupe *et al.*, Phys. Rev. D **19** (1979) 1921.

[149] M. Vanderhaeghen, P. A. Guichon and M. Guidal, Phys. Rev. D **60** (1999) 094017.

[150] B. Pire M. Diehl, T. Gousset and J. P. Ralston, Phys. Lett. **B411** (1997) 193.

[151] P. A. Guichon and M. Vanderhaeghen, Prog. Part. Nucl. Phys. **41** (1998) 125.

[152] P. A. Guichon, G. Q. Liu and A. W. Thomas, Nucl. Phys. **A591** (1995) 606.

[153] B. Pasquini, M. Gorchtein, D. Drechsel, A. Metz and M. Vanderhaeghen, Eur. Phys. J. **A11** (1995) 185.

[154] J. Roche *et al.*, Phys. Rev. Lett. **85** (2000) 708.

[155] R.L. Anderson *et al.*, Phys. Rev. **D14** (1994) 679.

[156] S.J. Brodsky and G.R. Farrar, Phys. Rev. Lett. **31** (1973) 1153.

[157] S.J. Brodsky and G.R. Farrar, Phys. Rev. D **11** (1975) 1309.

[158] V. Matveev *et al.*, Nuovo Cimento Lett. **7** (1973) 719.

[159] G.P. Lepage and S.J. Brodsky, Phys. Rev. D **22** (1980) 2157.

[160] J. Napolitano *et al.*, Phys. Rev. Lett. **61** (1995) 2530.

[161] E.C. Schulte *et al.*, Phys. Rev. Lett. **87** (2001) 102302.

[162] K. Wijesooriya *et al.*, Phys. Rev. Lett. **86** (2001) 2975.

[163] D.G. Crabb *et al.*, Phys. Rev. Lett. **41** (1978) 1257.

[164] G.R. Court *et al.*, Phys. Rev. Lett. **57** (1981) 507.

[165] S.J. Brodsky, C.E. Carlson and H. Lipkin, Phys. Rev. D **20** (1979) 2278.

[166] P. V. Landshoff, Phys. Rev. D **10** (1974) 1024.

[167] A.S. Carroll *et al.*, Phys. Rev. Lett. **61** (1988) 1698.

[168] Y. Mardor *et al.*, Phys. Rev. Lett. **81** (2001) 5085.

[169] J.P. Ralston and B. Pire, Phys. Rev. Lett. **61** (1990) 1823.

[170] C.E. Carlson, M. Chachkhunashvili and F. Myhrer, Phys. Rev. D **46** (1992) 2891.

[171] S. J. Brodsky and G. F. de Teramond, Phys. Rev. Lett. **60** (1988) 1924.

[172] O. Gayou *et al.*, Phys. Rev. Lett. **88** (2002) 092301.

[173] C. Hyde-Wright, A. Nathan, B. Wojtsekhowski, *et al.*, Jefferson Lab Hall A experiment 99-114.

[174] I.S. Barker, A. Donnachie and J.K. Storrow, Nucl. Phys. **B95** (1975) 347.

[175] W.-T. Chiang and F. Tabakin, Phys. Rev. C **55** (1997) 2054.

[176] R. Gilman and Franz Gross, J. Phys. G **28** (2002) R37.

[177] F.F. Liu, D.E. Lundquist and B.H. Wiik, Phys. Rev. **165** (1968) 1478.

[178] T. Kamae *et al.*, Phys. Rev. Lett. **38** (1977) 468; T. Kamae *et al.*, Nucl. Phys. **B139** (1978) 393.

[179] H. Ikeda *et al.*, Phys. Rev. Lett. **42** (1979) 1321; H. Ikeda *et al.*, Nucl. Phys. **B172** (1980) 509.

[180] K. Wijesooriya *et al.*, Phys. Rev. Lett. **86** (2001) 2975.

[181] Y. Kang, P. Erbs, W. Pfeil and H. Rollnik 1990 *Abstracts of the Particle and Nuclear Intersections Conference*, (MIT, Cambridge, MA); Y. Kang 1993 Ph.D. thesis Bonn.

[182] M. Schwamb and H. Arenhövel 2001 arXiv:nucl-th/0105033; M. Schwamb and H. Arenhövel, Nucl. Phys. **A690** (2001) 682;M. Schwamb and H. Arenhövel, Nucl. Phys. **A690**(2001) 647; M. Schwamb, H. Arenhövel, P. Wilhelm, and Th. Wilbois Phys. Lett. **B420** (1998) 255.

[183] M. Schwamb and H. Arenhövel, Nucl. Phys. **A690** (2001) 682.

[184] L. L. Frankfurt, G. A. Miller, M. M. Sargsian and M. I. Strikman Phys. Rev. Lett. **84** (2000) 3045; L. L. Frankfurt, G. A. Miller, M. M. Sargsian and M. I. Strikman, Nucl. Phys. **A663** (2000) 349; M. M. Sargsian, private communication.

[185] C. Bochna *et al.*, Phys. Rev. Lett. **81** (1998) 4576.

[186] J. Napolitano *et al.*, Phys. Rev. Lett. **61** (1988) 2530.

[187] S. J. Freedman *et al.*, Phys. Rev. C **48** (1993) 1864.

[188] J. E. Belz *et al.*, Phys. Rev. Lett **74** (1995) 646.

[189] R. Crawford *et al.*, Nucl. Phys. **A603** (1996) 303.

[190] Lee T-S H, FBSS **6** (1992) 526.

[191] L.A. Kondratyuk *et al.*, Phys. Rev. C **48** (1993) 2491.

[192] V. Yu Grishina *et al.*, Eur. Phys. J. **A10** (2001) 355.

[193] S. J. Brodsky and J. R. Hiller, Phys. Rev. C **28** (1983) 475.

[194] A. Radyushkin, private communication.

[195] J. Arrington *et al.*, to be published in J. of Phys.

[196] J. Arrington *et al.*, Phys. Rev. Lett. **82** (1999) 2056.

[197] J.-M. Laget, Proc. of the Workshop on Color Transparency (1998) Grenoble.

[198] S.J. Brodsky, in Proceedings of the Thirteenth International Symposium on Multiparticle Dynamics, ed. W. Kittel, W. Metzger and A. Stergiou (World Scientific, Singapore, 1982) 963.

[199] A. H. Mueller, in Proceedings of the Seventh Rencontres de Moriond, ed. J. Tran Thanh Van (Editions Frontieres, Gif-sur-Yvette, France, 1982) Vol. I, 13.

[200] T.G.O'Neill *et al.*, Phys. Lett. **B351** (1995) 87.

[201] K. Garrow *et al.*, arXiv:hep-ex/0109027.

[202] L.L. Frankfurt and M. Strikman, Prog. in Part. and Nucl. Phys. **27** (1991) 135.

[203] K.S. Egiyan, L.L. Frankfurt, W.R. Greenberg, G.A. Miller, M.M. Sargsyan and M.I. Strikman, Nucl. Phys. **A580** (1994) 365.

[204] L.L. Frankfurt, W.R. Greenberg, G.A. Miller, M.M. Sargsyan and M.I. Strikman, Zeit. für Phys. **A352** (1995) 97.

[205] J.-M. Laget in *Proc. of the Workshop on Color Transparency*, Grenoble (France), Edt. E. Voutier, (1997) `http://isnwww.in2p3.fr/ct97.html`.

[206] JLab Experiment E89-044, preliminary results (Contact: A. Saha).

[207] G.R. Farrar, H. Liu, L.L. Frankfurt and M.I. Strikman, Phys. Rev. Lett. **61** (1988) 686.

[208] J.P. Ralston and B. Pire, Phys. Rev. Lett. **61** (1992) 1823.

[209] J.P. Ralston and B. Pire, Phys. Rev. Lett. **65** (2000) 2343.

[210] S.J. Brodsky and A.H. Mueller, Phys. Lett. **B206** (1988) 685.

[211] G.R. Farrar, H. Liu, L.L. Frankfurt and M.I. Strikman, Phys. Rev. Lett. **61** (1988) 686.

[212] P. Jain and J. Ralston, to appear in Phys. Rev. D, arXiv:hep-ph/0005126.

[213] H. Gao, R. J. Holt and V. R. Pandharipande, Phys. Rev. C. **54** (1996) 2779.

[214] J. Ashman *et al.*, Z Phys. **52** (1991) 1.

[215] M. R. Adams *et al.*, Phys. Rev. D **50** (1994) 1836.

[216] L. S. Osborne *et al.*, Phys. Rev. Lett. **40** (1978) 1624.

[217] A. Airapetian *et al.*, Eur. Phys. J. **C20** (2001) 479.

[218] R. E. Taylor, Inelastic electron-proton scattering in the deep continuum region, in *4th Int Symp. on the electron and photon int. at high energies*, page 253, 1969.

[219] A. Bialas, Phys. Lett. **B133** (1983) 241.

[220] J. Carlson and R. Schiavilla, Rev. Mod. Phys. **70** (1998) 743.

[221] C. E. Carlson, J. R. Hiller and R. J. Holt, Ann. Rev. Nucl. and Part. Sci. **47** (1997) 395.

[222] E. Hummel and J. A. Tjon, Phys. Rev. Lett. **63** (1989) 1788.

[223] H. Dijk and B. L. G. Bakker, Nucl. Phys. **A494** (1990) 438.

[224] C. Ji S. J. Brodsky and G. P. Lepage, Phys. Rev. Lett. **51** (1983) 83.

[225] L.C. Alexa *et al.*, Phys. Rev. Lett. **82** (1999) 1374.

[226] N. Isgur and C. H. Llewellyn Smith, Phys. Rev. Lett. **52** (1995) 1080.

[227] C. Bochna *et al.* (E89-012 Collaboration), Phys. Rev. Lett. **81** (1998) 4576.

[228] R. Schiavilla and D. O. Riska, Phys. Rev. C **43** (1991) 437.

[229] P. Hoyer, Nucl. Phys. **A622** (1997) 284c.

[230] A. H. Mueller S. J. Brodsky, P. Hope and W. Tang, Nucl. Phys. **B369** (1992) 519.

[231] P. Hoyer S. J. Brodsky, E. Chudakov and J. M. Laget, Phys. Lett. **B498** (2001) 23.

[232] E. L. Berger and S. J. Brodsky, Phys. Rev. Lett. **42** (1979) 940.

[233] U. Camerini *et al.*, Phys. Rev. Lett. **35** (1975) 483.

[234] B. Gittelman, K. M. Hanson, D. Larson, E. Loh, A. Silverman and G. Theodosiou, Phys. Rev. Lett. **35** (1975) 1616.

[235] R. L. Anderson, SLAC-PUB-1741 *Invited talk presented at Int. Conf. on Production of Particles with New Quantum Numbers*, Wisconsin U., Madison, Apr 22-24, 1976.

[236] J. M. Laget and R. Mendez-Galain, Nucl. Phys. **A581** (1995) 397.

[237] M. Luke, A. V. Manohar and M. J. Savage, Phys. Lett. **B288** (1992) 355.

[238] S. J. Brodsky and G. A. Miller, Phys. Lett. **B412** (1997) 125.

[239] A. Syamtomov D. Kharzeev, H. Satz and G. Zinovjev, Eur. Phys. J. **C9** (1999) 459.

[240] R. L. Anderson *et al.*, Phys. Rev. Lett. **38** (1977) 263.

[241] C. Gerschel and J. Hufner, Z. Phys. **C56** (1992) 171.

[242] J. Hufner and B. Z. Kopeliovich, Phys. Lett. **B426** (1998) 154.

[243] E. Chudakov *et al.*, Letter of Intent for CEBAF12, JLab technical note: JLAB-TN-01-007, January 2001.

[244] K. Gottfried and D.R. Yennie, Phys. Rev. **182** (1969) 1595.

[245] J.M. Laget, Nucl. Phys. **A194** (1972) 81.

[246] J. Erler, private communication; J. Erler, arXiv:hep-ph/0005084.

[247] C.S. Wood *et al.*, Science, **275** (1997) 1759.

[248] S.C. Bennet and C.E. Wieman, Phys. Rev. Lett. **82** (1999) 2484.

[249] G.P. Zeller and the NuTeV Collaboration, Phys. Rev. Lett. **88** (2002) 091802.

[250] R. Carlini *et al.* (Q_{weak} Collaboration) "The Q_{weak} Experiment: A Search for New Physics at the TeV Scale via a Measurement of the Proton's Weak Charge," (2001).

[251] K.S. Kumar *et al.* (SLAC E-158–Møller Collaboration) "A Precision Measurement of the Weak Mixing Angle in Møller Scattering," SLAC Proposal E-158.

[252] V.A. Dzuba, V.V. Flambaum and J.S.M. Ginges, arXiv:hep-ph/0204134.

[253] V.A. Dzuba, V.V. Flambaum and J.S.M. Ginges, arXiv:hep-ph/0111019.

[254] A.I. Milstein and O.P. Sushkov, arXiv:hep-ph/0109257.

[255] W.R. Johnson, I. Bednyakov and G. Soff, Phys. Rev. Lett. **87** (2001) 233001.

[256] W.R. Johnson, I. Bednyakov and G. Soff, Phys. Rev. Lett. **88** (2002) 079903.

[257] M.G. Kozlov, S.G. Porsev and I.I. Tupitsyn, Phys. Rev. Lett. **86** (2001) 3260.

[258] V.A. Dzuba *et al.*, Phys. Rev. A **63** (2001) 044103.

[259] A. Derevianko, Phys. Rev. Lett. **85** (2000) 1618.

[260] V.A. Dzuba, V.V. Flambaum and O.P. Sushkov, Phys. Rev. A **56** (1997) R4357.

[261] S. Davidson *et al.*, JHEP **37** (2002) 202.

[262] G.A. Miller and A.W. Thomas, arXiv:hep-ex/0204007.

[263] M.J. Ramsey-Musolf, Phys. Rev. C **60** (1999) 015501.

[264] R. Cahn and R. Gilman, Phys. Rev. D **17** (1978) 1313.

[265] P.E. Bosted *et al.* (SLAC E-149 Collaboration) "DIS-Pairty: Parity Violation in Deep Inelastic Electron Scattering, " SLAC Proposal E-149 (1993).

[266] R. Hasty *et al.*, Science **290** (2000) 2117.

[267] D.E. Groom *et al.* (Particle Data Group), Eur. Phys. J. **C15** (2000) 1.

[268] "MCEEP — Monte Carlo for Electro-Nuclear Coincidence Experiments", User Manual, version 3.6, by P.E. Ulmer, Old Dominion University, unpublished (2001). Available from `http://www.physics.odu.edu/~ulmer/mceep/mceep.html`.

[269] "A-B-SIMC", SIMC Primer, by J. Arrington, Argonne National Lab, unpublished (2001). Available from `http://www.jlab.org/~johna/SIMC_documents/simc.ps`.

[270] M. Amarian *et al.*, Nucl. Instr. and Meth. **A460** (2001) 239.

[271] Indiana University test results at `http://dustbunny.physics.indiana.edu/~paul/hallDrd`.

[272] Hall A DVCS Collaboration proposal, Experiment 00-110, `http://www.jlab.org/exp_prog/proposals/00/PR00-110.pdf`.

[273] R. D. Appuhn *et al.*, Nucl. Instr. and Meth. **A350** (1994) 208.

[274] P. Achenbach *et al.*, Nucl. Instr. and Meth. **A416** (1998) 357.

[275] B.D. Anderson *et al.*, Basic Instrumentation for Hall A Beamline preprint.

[276] Hall A Operational Manual (2000).

[277] G. Bardin *et al.*, Conceptual Design Report of a Compton Polarimeter for Hall A at CEBAF, DAPNIA/CEA Report, `http://www.jlab.org/compton/Documentation/Technical/1996/proposal.ps`.